Development and Application of *Operando* TEM to a Ruthenium Catalyst for CO Oxidation

by

Benjamin Kyle Miller

A Dissertation Presented in Partial Fulfillment
of the Requirements for the Degree
Doctor of Philosophy

Approved March 2016 by the
Graduate Supervisory Committee:

Peter Crozier, Chair
Jingyue Liu
Martha McCartney
Peter Rez

ARIZONA STATE UNIVERSITY

May 2016

ABSTRACT

Operando transmission electron microscopy (TEM) is an extension of *in-situ* TEM in which the performance of the material being observed is measured simultaneously. This is of great value, since structure-performance relationships lie at the heart of materials science. For catalyst materials, like the SiO_2-supported Ru nanoparticles studied, the important performance metric, catalyst activity, is measured inside the microscope by determining the gas composition during imaging. This is accomplished by acquisition of electron energy loss spectra (EELS) of the gas in the environmental TEM while catalysis is taking place. In this work, automated methods for rapidly quantifying low-loss and core-loss EELS of gases were developed. A new sample preparation method was also established to increase catalytic conversion inside a differentially-pumped environmental TEM, and the maximum CO conversion observed was about 80%. A system for mixing gases and delivering them to the environmental TEM was designed and built, and a method for locating and imaging nanoparticles in zone axis orientations while minimizing electron dose rate was determined.

After atomic resolution images of Ru nanoparticles observed during CO oxidation were obtained, the shape and surface structures of these particles was investigated. A Wulff model structure for Ru particles was compared to experimental images both by manually rotating the model, and by automatically determining a matching orientation using cross-correlation of shape signatures. From this analysis, it was determined that most Ru particles are close to Wulff-shaped during CO oxidation. While thick oxide layers were not observed to form on Ru during CO oxidation, thin RuO_2 layers on the surface of Ru nanoparticles

were imaged with atomic resolution for the first time. The activity of these layers is discussed in the context of the literature on the subject, which has thus far been inconclusive. We conclude that disordered oxidized ruthenium, rather than crystalline RuO_2 is the most active species.

To Peter Crozier, my advisor, my mentor, and my friend,
without whom none of this would have been possible.

ACKNOWLEDGMENTS

I must first and most importantly thank Dr. Peter Crozier whose dedication, encouragement, and passion for research at the cutting edge pushed this project forward despite our many setbacks. I thank him for frequently pushing me past where I thought myself capable of going. As a mentor and advisor, Peter modeled in many respects what I would someday like to achieve.

I would also like to thank the members of my committee. Dr. Peter Rez encouraged me (likely more than he realized) at several points in my work with just the right words of affirmation. Dr. Jimmy Liu helped me to examine the value of my work, and induced me to make it better than I thought it could be. Dr. Molly McCartney enhanced my understanding of electron optics early in my work and taught me a simple trick which ultimately saved me hours of tedium over the course of my PhD.

I am also grateful to Karl Wiess who helped me with some very practical aspects of my work, and whose trust in me gave me confidence. I must also thank Dr. Pierre Stadelmann who advanced my understanding of electron optics and image simulation in the last few years of my PhD, and helped me to take full advantage of his software. He also wrote several additions to the JEMS software which I had specifically requested for the completion of this work, and which were greatly appreciated.

I must also acknowledge the hard work of several undergraduate students whom I co-supervised with Peter over the course of my PhD. Trevor Barker developed the process for forming *operando* pellets. Russell Wisniewski analyzed some of the earliest images produced in this work, and built several crystal models. Chelsea McAlpin worked on image

processing. Nolan Walker performed some of the image simulations and also built advanced particle models. Jayse Langdon worked on *ex-situ* reactor measurements and modelling of kinetics.

I would also like to thank the other members of Peter's research group who taught me many little tricks and techniques in the lab, often inspired me to do better work, and generally made my life as a PhD student fun.

Finally, I would like to thank my wonderful wife Rachael who encouraged me and helped me in many ways, patiently allowing me to focus on my project, especially during the arduous writing of this dissertation.

I also gratefully acknowledge the funding of the National Science foundation (NSF-CBET 1134464) without which this work could not go forward, and the excellent facilities at the LeRoy Eyring Center for Solid State Science at Arizona State University.

TABLE OF CONTENTS

Page

LIST OF FIGURES ix

LIST OF TABLES xv

CHAPTER

1. INTRODUCTION 1

1.1. Motivation: The Value of CO Oxidation Catalysis 1

1.2. *In-Situ* and *Operando* Determination of Structure-Property Relationships 3

1.3. Introduction to CO Oxidation 19

1.4. Summary 40

1.5. Research Objectives and Outline 41

2. CATALYST SYNTHESIS AND *EX-SITU* EXPERIMENTS 45

2.1. Catalyst Synthesis 45

2.2. Ex-Situ Experiments 47

2.3. Estimating ETEM Conversions 55

2.4. Summary 59

3. *OPERANDO* EXPERIMENTAL TECHNIQUE 65

3.1. The *Operando* Challenge: Quantifying Product Gases in the ETEM 65

3.2. Existing Methods 66

3.3. New Developments 78

3.4. Summary 100

4. IMAGE ANALYSIS METHODS FOR STRUCTURE DETERMINATION 117

4.1. Existing Methods 117

4.2. Methods Created or Enhanced for this Work 121

4.3. Summary 130

CHAPTER Page

5. CO OXIDATION OVER Ru/RuO_2: CATALYTIC ACTIVITY AND PARTICLE SHAPE 142

5.1. Confirmation of *Ex-Situ* Results 142

5.2. Nanoparticle Shape 145

5.3. The Shape of Nanoparticles in a High-Activity State 147

5.4. The Shape of Nanoparticles in Single-Gas Environments 150

5.5. Shape Analysis Conclusions and Discussion 152

5.6. Summary 158

6. CO OXIDATION OVER Ru/RuO_2: CATALYTIC ACTIVITY AND PARTICLE SURFACE STRUCTURES 174

6.1. Early Evidence for RuO_2 Surface Layers 174

6.2. Thin RuO_2 Observed During CO Oxidation 175

6.3. Correlation Between Activity and Surface Layers 179

6.4. Surface Structure Discussion 182

6.5. Summary 187

7. SUMMARY AND FUTURE WORK 199

7.1. Summary 199

7.2. Future Work 200

REFERENCES 210

APPENDIX

I RIG 150 TEMPERATURE GRADIENT 236

II GC METHOD PARAMETERS 240

III GC DATA ANALYSIS 243

IV TITAN GAS HANDLING SYSTEM DESIGN 256

V LOW-LOSS EELS CODE 263

APPENDIX Page

VI CORE-LOSS EELS CODE..... 283

VII DIFFRACTOGRAM ANALYSIS AND IMAGE REGISTRATION CODE..... 298

VIII PARTICLE OUTLINING AND ELLIPSE FITTING CODE..... 331

IX PARTICLE ORIENTATION ESTIMATION CODE..... 340

X IMAGE REFERENCE TABLES..... 362

LIST OF FIGURES

Figure Page

1-1 *Operando* TEM..... 43

1-2 Proposed Active Structures. 44

2-1 SiO_2 Spheres.. 60

2-2 Ru-SiO_2..... 60

2-3 GC Raw Data. 61

2-4-*Ex-Situ* Conversion. 61

2-5 *Ex-Situ* Conversion. 62

2-6 *Ex-Situ* Conversion Data. 62

2-7 *Ex-Situ* Arrhenius Plot. 63

3-1 Ta Heating Holder. 102

3-2 *Operando* Sample Prep. 102

3-3 Titan ETEM Window. 103

3-4 RGA-EELS *Operando* Data. 104

3-5 Raw RGA Data. 104

3-6 EELS Basics. 105

3-7 EELS Low-Loss Spectra. 105

3-8 Electron Diffraction. 106

3-9 TEM Imaging Conditions. 106

3-10 *Operando* Pellet. 107

3-11 Grid vs Pellet Images. 108

Figure Page

3-12 Gas Homogeneity Test. 109

3-13 Gas Homogeneity Calculation. 109

3-14 High *In-Situ* Conversion. 110

3-15 MFC Calibration Curves. 111

3-16 RGA Setup Tecnai. 112

3-17 Low-loss EELS Fitting. 113

3-18 EELS Energy Shift- MATLAB. 113

3-19 EELS LL Background Matching. 114

3-20 Core-loss EELS Fitting. 114

3-21 Comparison Experiment. 115

3-22 RGA Non-Linearity. 115

3-23 RGA-EELS Additional Comparison. 116

3-24 Image Series Acquisition. 116

4-1 Ru Nanoparticle Models. 133

4-2 JEMS Faceted Particle Creation. 133

4-3 Particle Image Simulations. 134

4-4 MATLAB Image Registration.. 135

4-5 FFT Measurement Error. 135

4-6 MATLAB Fourier Filtering. 135

4-7 Image Indexing and Filtering Code. 136

4-8 FFT Composite. 136

4-9 Diffractogram Processing. 137

Figure Page

4-10 Digital Micrograph Real-Space Lattice Measurement. 138

4-11 Ellipse Fitting of Experimental Particles. 139

4-12 Manual Method for Particle Orientation Determination. 140

4-13 Automated Method for Particle Orientation Determination. 141

5-1 *Operando* EELS Summary. 160

5-2 Pre-Oxidized *Operando* Experiment. 160

5-3 Pre-Oxidized Conversion vs Temperature. 161

5-4 Pre-Oxidized *Operando* Images. 161

5-5 Pre-Reduced *Operando* Experiment. 162

5-6 Pre-Reduced Conversion vs Temperature. 162

5-7 Pre-Reduced *Operando* Images. 163

5-8 Ru Wulff Shape. 165

5-9 RuO_2 Wulff Shapes. 165

5-10 Pre-Reduced *Operando* Hysteresis Experiment. 166

5-11 Pre-Reduced Hysteresis Conversion vs Temperature. 166

5-12 Pre-Reduced *Operando* Hysteresis with Images. 167

5-13 *Operando* Orientation Matching Results. 167

5-14 *In-Situ—Operando* Comparison. 168

5-15 *In-Situ* CO Orientation Matching Results. 168

5-16 *In-Situ* CO_2 Orientation Matching Results. 169

5-17 *In-Situ* O_2 Orientation Matching Results. 169

5-18 *In-Situ* Image Comparison. 170

Figure Page

5-19 Shape Matching Cross Correlation Results Summary. 172

5-20 Facet Area Distributions. 172

5-21 Individual Particle Facet Distributions. 173

6-1 Moiré Fringe Analysis. 189

6-2 Ru and RuO_2 in H_2 and H_2-O_2. 190

6-3 RuO_2 Layer During *Operando* CO Oxidation. 191

6-4 Image Simulation of RuO_2 Surface Layer. 192

6-5 Clean Ru Particle. 193

6-6 Titan *Operando* Experiment Summary. 193

6-7 Titan *Operando* Experiment Stimuli. 194

6-8 Clean Ru Particle. 194

6-9 Ru Particle With Uncertain Surface. 195

6-10 Image Acquisition Conditions. 195

6-11 Initial 200°C Image. 196

6-12 Titan *Operando* Catalyst Performance. 196

6-13 Disordered Surface Layers. 197

A 1 Temperature Difference. 238

A 2 RIG 150 Reactor Tube. 239

A 3 GC Method Export Dialog. 242

A 4 GC Data Background Fitting. 246

A 5 Fit Backgrounds. 246

A 6 Background Subtracted Chromatographs. 247

Figure Page

A 7 Background Noise. 247

A 8 Peak Areas Graph. 248

A 9 Gas Handling System Diagram- Basic. 260

A 10 Gas Handling System Diagram- Full. 261

A 11 Titan Gas Handling System. 262

A 12 LL EELS MATLAB Code 1. 267

A 13 LL EELS MATLAB Code 2. 268

A 14 Simulated Noisy Spectrum. 269

A 15 LL EELS Code Precision. 270

A 16 EELS 2D Integration Limits. 286

A 17 EELS Core-Loss Code Figure 1. 287

A 18 EELS Core-Loss Code Figure 2. 288

A 19 Montages of Registered Frames. 304

A 20 Aligned, Averaged Image. 305

A 21 Diffractogram ROI Artifact. 306

A 22 Measured Diffractogram. 307

A 23 Fourier Filtering. 308

A 24 Processed Diffractogram. 309

A 25 Ellipse Fit Error. 333

A 26 Shape Signature Production. 345

A 27 Shape Signatures. 345

A 28 Particle Image Montage. 346

Figure Page

A 29 Orientation Matching Figure. 347

A 30 Violin Plot. 348

LIST OF TABLES

Table Page

2-1 *Ex-Situ* Activation Energies Below 400°C. 64

2-2 *Ex-Situ* Activation Energies Above 400°C. 64

2-3 CSTR Equation Symbols. 64

4-1 Ru and RuO_2 Lattice Parameters. 132

4-2 Selected Ru and RuO_2 Plane Spacings. 132

5-1 Ru Wulff Data. 163

5-2 RuO_2 Wulff Data. 164

5-3 Tammann Temperatures. 170

5-4 Surface Energy Anisotropy. 171

5-5 Adsorption Energies. 171

6-1 Analyzed Images. 198

6-2 Analyzed Image Conditions. 198

1. Introduction

1.1. Motivation: The Value of CO Oxidation Catalysis

1.1.1. Renewable Energy, Fuel Cells

Catalysis is vital for the improvement of current energy technology, as well as the development of future energy technologies (Li and Somorjai, 2010). This motivates a significant scientific effort (Astruc et al., 2005; Blaser et al., 2003; Hashmi and Hutchings, 2006) to develop new and better catalysts and to understand the fundamental processes that occur, so that innovation can be accelerated (Nørskov et al., 2009).

This research is motivated in part by fuel cells, which are one of the important applications for catalysis of CO oxidation. Fuel cells still provide a very small proportion of the world's energy, but are becoming an increasingly important part of renewable energy portfolios. In the past, many of the industrial catalysts used for energy were used to process fossil fuels and their products (Armor, 2011). However, today use of renewable energy is rapidly increasing (EIA, 2015), often requiring catalysts (Bell et al., 2008; Thomas and Thomas, 2015). In 2007, excluding hydroelectric and nuclear energy, 1090 TWh of renewable energy were consumed in the US. In 2014, this number had increased to 1881 TWh, an increase of about 70% in just 7 years (EIA, 2015). Fuel cells currently play a very small part in this increase, but their use is also increasing significantly. According to the DOE 2013 Fuel Cell Technologies Market Report (Curtin and Gangi, 2014), the new capacity installed in 2013 was 173 MW. While this is still less than half of one percent of

the photovoltaic capacity installed in 2013 (Masson et al., 2014), it nevertheless indicates that fuel cell technology is gaining market share.

Fuel cells require several catalysts to function (Wieckowski, 2009; Zhang, 2008). Specifically, catalysts are required to split the fuel molecules on the fuel cell anode, as well as in the renewable production of fuels. In a hydrogen fuel cell, catalysts are also needed to remove CO impurities in the fuel gas, because concentrations greater than 10 ppm of CO will poison traditional anode catalysts, leading to significantly decreased performance (Cheng et al., 2007; Dhar, 1987; Park et al., 2009). CO is often present in the fuel gas, since H_2 is usually created from hydrocarbons through steam reforming, which also produces CO (Gandía et al., 2013). While the majority of the impurity CO can be oxidized through the water-gas shift reaction ($CO + H_2O \rightarrow CO_2 + H_2$) (Smith R J et al., 2010), around 1% may remain, and this CO must be removed by another method (Park et al., 2009). This residual CO concentration can be converted to CO2 by a simple oxidation reaction:

$2CO + O_2 \rightarrow 2CO_2$

1.1.2. CO Oxidation as a Model Reaction

While engineers may be interested in catalyzing CO oxidation only if it enables known useful technologies, many scientists see in the reaction another benefit. Due to its relative simplicity, CO oxidation is a model reaction ideal for studying the fundamentals of heterogeneous catalysis (Freund et al., 2011). CO oxidation is explicitly called a “model reaction” in several of the papers later covered in a review of CO oxidation over Ru (Aßmann et al., 2003; Böttcher and Niehus, 1999; Chen et al., 2007). Only 2 types of atoms, and 3 types of molecules are present in the basic reaction, and if water is involved (Freund

et al., 2011; Fujitani et al., 2014; Saavedra et al., 2014; Sheu and Chang, 2014), this adds only hydrogen, albeit with significantly increased complexity.

The sheer volume of work published on fundamental processes during CO oxidation attest to its importance as a scientific paradigm. A search for "CO oxidation" OR "carbon monoxide oxidation" on Thomson Reuters Web of Science yields over 12 thousand results, of which 1152 papers were published in 2015 alone, and the oldest result was published in 1923 (Benton, 1923), though this is certainly not the earliest publication on the subject, as this article references previous works on the topic. The intense study of CO oxidation is unlikely to abate in the near future, as many mechanistic details still remain unresolved, and new techniques (like the o*perando* TEM this dissertation is focused on) are often applied to simple systems.

1.2. *In-Situ* and *Operando* Determination of Structure-Property Relationships

Catalyst materials have been studied scientifically for centuries since their identification by Berzelius (Armor, 2011; Berzelius, 1836; Rideal and Taylor, 1919). More recently, the majority of the applied characterization tools observed the catalyst either before or after catalytic reaction (Haw, 2002). While catalysts should never be consumed during reaction, they are often modified (Thomas and Thomas, 2015). Furthermore, in some cases, this modification is only present during reaction, making post-reaction studies inadequate for the determination of the effect of structure on the reaction mechanism (Haw, 2002; Rodríguez et al., 2013). Nevertheless, individual *in-situ* characterization techniques should not be used in isolation; complimentary, well developed *ex-situ* techniques should

always be applied both to guide complex *in-situ* experiments and to confirm results. This was done in the current work, and is described in Chapter 2.

1.2.1. *In-Situ* Characterization of Catalysts

Many characterization techniques have been adapted to allow *in-situ* measurements. Indeed, though modifications to the techniques are often required, and limitations on the ambient conditions are usually present, nearly every characterization technique ever devised can be performed as an *in-situ* technique. Techniques which have recently been used to study catalysts include: Raman Spectroscopy (Bañares et al., 2000; Vuurman and Wachs, 1992), scanning tunneling microscopy (STM) (Hendriksen and Frenken, 2002; Kolmakov and Goodman, 2002), Fourier transform infrared spectroscopy (FTIR) (Burcham et al., 2000; Hug and Sulzberger, 1994), UV-visible spectroscopy (UV-Vis) (Bañares et al., 2000; Burcham et al., 2000), x-ray absorption spectroscopy to obtain x-ray absorption fine structure (XAFS) (Irie et al., 2009; Moen et al., 1997), nuclear magnetic resonance (NMR) (Gladden et al., 2006; Hunger and Wang, 2006), x-ray diffraction (XRD) (Rossignol et al., 2003; Shaw et al., 1991), and x-ray photoelectron spectroscopy (XPS) (Salmeron and Schlogl, 2008; Yamamoto et al., 2008). Extensive coverage of *in-situ* characterization of catalysts is available in several books, including one focused on spectroscopy by Haw (Haw, 2002), as well as a more recent book by Rodriguez, Hanson, and Chupas (Rodríguez et al., 2013), and will not be attempted here.

1.2.2. *In-Situ* TEM of Catalysts

An exhaustive review of *in-situ* characterization of catalysts would be a daunting task; similarly, an exhaustive review of all *in-situ* TEM/STEM work would be prohibitively long. Indeed, even a thorough review of the literature describing the smaller field of environmental TEM would be lengthy, and will not be attempted here, though several reviews on the subject are listed in the book chapter covering ETEM history in (Hansen and Wagner, 2015). However, a description of much of the work published on catalysts studied using environmental TEM is not beyond the scope of this work, as until recently it has been carried out almost exclusively under the direction of a small number of researchers. Indeed, a description of the work of Gai & Boyes, Crozier & Sharma, Helveg, Hansen & Wagner, Stach, and Takeda & Yoshida nearly exhausts the literature on the subject, though some early work by Baker (Baker et al., 1973, 1972; Baker and Chludzinski, 1980) who studied the growth of carbon filaments using Ni and Fe catalysts, and by Parkinson (Parkinson, 1989), who obtained images of lattice fringes in CeO_2 under 20 Torr of N_2 using an early windowed cell in a side-entry holder, should not be discounted. This is undoubtedly due to the small number of electron microscopes which have been modified to allow gasses and liquids into contact with the sample during observation. With the recent proliferation of windowed-cell holders capable of maintaining a fluid environment within the TEM (Allard et al., 2012; Creemer et al., 2008; de Jonge et al., 2010; Yaguchi et al., 2011; Yokosawa et al., 2012), this is sure to change in the future. The following review will therefore be organized around these few influential researchers.

Edward Boyes and *Pratibha Gai* were pioneers of some of the earliest work on differentially-pumped environmental TEM and STEM of catalysts, first at DuPont and later, the University of York. In 1997, they authored an early description of the modern differentially-pumped ETEM and some potential applications, including the study of catalysts (Boyes and Gai, 1997). In 2002, another similar paper was published (Gai, 2002a), along with an account of ETEM experiments with a liquid-environment holder, which injected a liquid onto the sample in the ETEM; polymerization was observed *in-situ* (Gai, 2002b). This work was followed by a study of hydrogenation of nitriles in liquid phase; the formation of the expected product was confirmed, but not quantified, using mass spectrometry (Gai et al., 2005). A few years later a review was published on the use of environmental TEM and STEM for studying gas-liquid-solid interfaces, where the solid was typically a catalyst for producing nanotubes/nanorods (Gai et al., 2008).

Beginning in 2012, the use and usefulness of aberration corrected TEM and STEM (AC-(S)TEM) for environmental TEM work was a major focus. AC TEM/STEM was used to determine the bonding strength between CeO_2 and Au (López-Haro et al., 2012). A 2014 paper elucidated further the benefits of aberration corrected ETEM and ESTEM, including the ability to observe single atoms of Pt on a carbon support. Additionally, they showed that delocalization of the image contrast was significantly reduced, and the contrast transfer function significantly extended, allowing direct interpretation of images (Boyes and Gai, 2014). This work was followed up by additional description of the observation of single atoms in an ESTEM (Boyes and Gai, 2015).

Considerable research on environmental TEM of catalysts has been performed at Arizona State University, of which this dissertation is a part. *Peter Crozier* is still at ASU,

while *Renu Sharma*, who was also instrumental in this work, is now working at the US National Institute for Standards and Technology (NIST).

Much of the work done at ASU has been centered around Ni catalysts. In 2005, *in-situ* reduction of a Ni precursor to Ni on TiO_2 was studied; no difference between the anatase and rutile forms of TiO_2 was observed (Li et al., 2005). Continuation of this work showed that Ni is non-wetting on anatase TiO_2, but wetting on rutile TiO_2, due to the lower interfacial energy of Ni-rutile. Partial TiO_2 layers were observed to form over the Ni (P. Li et al., 2006). Addition of Cu, in an attempt to form Ni-Cu bimetallic particles *in-situ* on TiO_2 was successful; it was found that most particles were uniform, but 15% were Ni enriched on the surface (Li et al., 2009). In 2011, Ni supported on SiO_2 was studied *in-situ* under conditions mimicking partial oxidation of methane. The catalyst was oxidized, forming core-shell structures above 300°C, but reduced again at high temperatures leading to a rapid increase in the activity of the catalyst (Chenna et al., 2011); additional details were published the following year (Chenna and Crozier, 2012a). The processes used to form the original SiO_2 supported catalyst were also studied *in-situ,* elucidating the ideal conditions for producing well-dispersed Ni catalysts (Banerjee and Crozier, 2012). Finally, hydrogen spillover on a Pr-doped-CeO_2 supported Ni catalyst was directly observed (Sharma et al., 2012).

Several other catalysts were studied at ASU as well. SiO_2 supported Pd was observed during oxidation and reduction in one of the early works on differentially-pumped ETEM (Crozier et al., 1998). Al_2O_3 supported Co and Ru-Co catalysts were synthesized *in-situ* where it was observed that the Ru increased the reducibility of the Co and also formed bimetallic particles (P Li et al., 2006). This was the first environmental STEM study of a

catalyst. CeO_2 was shown to undergo a phase transformation at high temperature due to ordering of O vacancies (Crozier et al., 2008; Wang et al., 2009). There was also a surface reconstruction from (111) nanofacets to a larger smooth (110) facet. Carbon nanotube growth was also studied, and it was found that the Fe catalyst particles used to grow the nanotubes could also gasify the tubes at the growth temperature if the precursor gas was removed (Feng et al., 2011). In the same year, work was published on a Fischer Tropsch catalyst; it was found that hematite reduced, forming Fe carbide, in a CO atmosphere at elevated temperatures (Janbroers et al., 2011). In 2012, the shape of Au supported on CeO_2 was observed to change in oxidizing and reducing atmospheres (Ta et al., 2012).

Recently, progress has been made toward *Operando* TEM using electron energy-loss spectroscopy (EELS) to monitor the gas composition inside the environmental cell of a differentially-pumped ETEM. In 2011, the first quantification of gas composition inside the TEM using EELS was demonstrated (Crozier and Chenna, 2011). The following year an initial attempt at *operando* TEM was reported (Chenna and Crozier, 2012b). Two years later, as part of the work described in this dissertation, more detail was given on quantification of gas composition during *operando* TEM using both residual gas analysis (RGA) and EELS (Miller and Crozier, 2014). Finally, the unique sample preparation used to achieved high conversions inside a differentially-pumped system was described in 2015 (Miller et al., 2015). Two additional papers are currently being prepared in which *operando* TEM is applied to the specific catalyst system of CO oxidation over Ru (Miller and Crozier, 2016a, 2016b).

Several reviews and general descriptions of environmental (S)TEM applied to catalysis have also been published by the researchers at ASU. In 2005, a paper describing the then-

current state of the art for ETEM, as well as a few applications was published (Sharma, 2005). A book chapter entitled Environmental Transmission Electron Microscopy in Nanotechnology, was also published (Sharma and Crozier, 2005). In 2011, a book chapter was written focused on heterogeneous catalysis studied using both *ex-situ* techniques and *in-situ* STEM (Crozier, 2011). The following year a tutorial for setting up *in-situ* ETEM experiments, describing some of the potential pitfalls associated with such work was published (Sharma, 2012). In 2015, Peter Crozier and Thomas Hansen collaborated on a review article describing recent *in-situ* studies of catalytic materials (Crozier and Hansen, 2015). Finally, that same year, Peter Crozier and Ben Miller wrote a chapter on spectroscopy in the ETEM for the book by Hansen and Wagner (Hansen and Wagner, 2015), which covered quantification of EELS spectra of gases and its application to *operando* TEM, as well as other spectroscopic investigations of catalysts.

Haldor Topsoe, a Danish catalyst company founded by Haldor Topsøe, has also been at the forefront of ETEM development and its application to the study of catalysis. *Stig Helveg* has played a central role in this work (Helveg, 2015), and is an author on a number of highly cited papers.

One early focus was on supported Cu as a catalyst for methanol synthesis. In 2002, a paper published in Science reported on the dynamic shape changes observed in Cu nanoparticles supported on ZnO (P. L. Hansen et al., 2002). The shapes observed in TEM images were interpreted so that the 3D shape was suggested (and found to be different) for H_2, H_2+H_2O, and H_2+CO. This is a very important result, as it means that the shape of nanoparticles can change due to changes in reaction conditions; an important question for this work is therefore: Do Ru particles change shape? The following year, additional *in-*

situ EELS and TEM of the Cu on ZnO catalyst showed that the Cu was reduced and strained when exposed to a reducing gas atmosphere (Wagner et al., 2003). In 2015, Holse, et al showed that in a Cu-ZnO catalyst the location of ZnO and Cu changed dramatically when the catalyst was reduced. Specifically, ZnO migrated to the surface of a Cu metal particle and was slightly reduced at the Cu-ZnO interface (Holse et al., 2015).

Other research focused on the growth of carbon nanotubes. In 2004, the growth of nanotubes using a Ni catalyst was observed *in-situ* (Helveg et al., 2004). This work, published in Nature, showed that growth occurred at dynamic Ni step edges which changed with time. In 2012, graphene layers were grown on MgO-supported Pt. Particles smaller than 6 nm formed nanotubes or sheets which grew away from the particles; larger particles were encapsulated (Peng et al., 2012).

In 2008, another paper was published focused on steam reforming of methane over several catalysts supported on ZrO_2 (Jones et al., 2008), of which Ru and Rh showed the highest performance. In 2010 and 2011 Pt nanoparticles were observed on Al_2O_3 and SiO_2 in an O_2 environment (Simonsen et al., 2011, 2010). Pt was found to sinter via an Ostwald ripening mechanism on both supports, but individual particles deviated from the expected mean field behavior due to local configuration of particles; this could only be observed because of the unique spatial resolution of *in-situ* ETEM. This study observed hundreds of particles, and required only basic low resolution information. For the present work, where subtle changes must be observed at high magnification, it is unclear whether it will be possible to detect deviations from the average catalyst behavior.

Several papers co-authored by Helveg have been focused on newly developed technologies and methods which have advanced the technique of environmental TEM. In

2008, a collaboration with Delft University of Technology resulted in development of a windowed-cell heating holder (Creemer et al., 2008) which was used to observe a Cu on ZnO catalyst. This was the first work demonstrating an *in-situ* pressure above one atmosphere in the TEM while maintaining good imaging resolution. More details of this heating holder design were given in 2010 (Creemer et al., 2010). In 2013, Vendelbo, et al. measured the local temperature of a windowed cell reactor using EELS to measure the local gas density which can then be related back to temperature (Vendelbo et al., 2013). In 2012, (Jinschek and Helveg, 2012) the resolution within an ETEM was reported to be dependent on both gas pressure and electron dose rate. This is a puzzling result, and one that, while not yet fully understood is likely of great importance to the ETEM community. It emphasizes the need to operate at dose rates as low as possible. In fact, a paper published in 2015 showed how focal series reconstruction could be applied to observe a Co_3O_4 catalyst for Fischer-Tropsch in CO using very low dose rates of 30-300 $e^-/Å^2/s$ (6-60 times lower than (Kuwauchi et al., 2012) described later in this section) and at 80kV (Helveg et al., 2015). Most of the aberration corrected images shown in the following chapters of this dissertation were acquired under low dose rate conditions, but focal series reconstructions were not attempted. Truly *operando* TEM (defined in section 1.2.3) was demonstrated by the group led by Helveg when they showed oscillations in the faceting of a Pt nanoparticle could be correlated with the conversion of CO to CO_2 within a windowed-cell holder (Vendelbo et al., 2014a). This raises a question regarding causation; does the variation in gas composition cause the observed change in facet distribution, or does the modified facet distribution change the gas composition? This results also suggests the simpler question: Does the faceting of Ru particles also change under different gas conditions?

Also from Denmark, *Thomas Hansen* published several papers as a researcher at Haldor Topsoe, before moving to the Technical University of Denmark (DTU), which works closely with researchers from Haldor Topsoe. *Jakob Wagner*, also currently at DTU, has been a frequent co-author.

In 2001, some of the earliest work using differentially-pumped ETEM was published in Science, and studied Ba-promoted Ru which was supported on BN and used for ammonia synthesis. The catalyst was imaged in both H_2 and N_2 (Hansen, 2001). The following year, Ba-promoted Ru supported on Si_3N_4, $MgAl_2O_4$, and graphitized C was studied. Ba was found to promote the reaction electronically, not structurally, as no difference in the Ru structure was observed (T. W. Hansen et al., 2002).

Significant attention was given to Ni catalysts and their behavior when exposed to various gases. In 2011, Ni nanoparticles supported on $MgAl_2O_4$ were sintered during exposure to H_2 and H_2O. Ripening of individual particles was used to predict long-term behavior of the ensemble (Challa et al., 2011). A few years later more data on this system was published (DeLaRiva et al., 2013) showing that Ostwald ripening occurs first, with migration and coalescence also occurring later in the sintering process. Sintering processes were also reviewed broadly in a paper which states that Ostwald ripening nearly always occurs during sintering, but that it dominates during the initial significant decrease in dispersion, after which both Ostwald ripening and migration/coalescence occur (Hansen et al., 2013). In the same year, the reduction of NiO particles exposed to H_2 was investigated in detail (Jeangros et al., 2013).

In 2012, a description of an aberration corrected ETEM, equipped with a light illumination holder was given (Wagner et al., 2012). This paper also described the mean

free path of electrons in several gases at 80, 200, and 300 kV. Hansen and Wagner have also published several reviews of ETEM and catalysis, including a 2014 paper (Hansen and Wagner, 2014) and a book chapter entitled "The Structure of Catalysts Studied Using Environmental Transmission Electron Microscopy" which is a part of the book they also edited, Controlled Atmosphere Transmission Electron Microscopy Principles and Practice (Hansen and Wagner, 2015).

Recently, *Eric Stach*, working at Brookhaven National Laboratory, has begun to publish work using an aberration corrected environmental TEM. In 2012, work on reduction of Co-CoO particles studied *in-situ* was published (Xin et al., 2012). In 2014, the dynamics of Pt-Co bimetallic particles were studied using AC TEM and STEM, showing that oxidation causes a migration of Co to the surface, where it first forms a CoO film, and then islands; reduction forms a Pt monolayer on the surface (Xin et al., 2014). The following year *operando* ETEM work was performed on a SiO_2-supported Pt catalyst using a windowed-cell reactor. However, to quantitatively measure gas products of the reaction, more catalyst powder was located downstream in a Clausen cell, allowing higher conversions to be obtained, but straining the definition of *operando* given in section 1.2.3 (Li et al., 2015).

Hideto Yoshida and *Seiji Takeda*, from Osaka University in Japan, have published several important papers covering catalysis studied using ETEM. In 2011, they introduced a "morphology parameter" (described in more detail in section 4.2.4) which made the description of catalyst shape more quantitative (Uchiyama et al., 2011). This was used to study the shape dynamics of Pt supported on CeO_2. At room temperature the Pt shape was more rounded, while at high temperatures the particles became more faceted (Yoshida et

al., 2011). In 2012, they published several papers, studying Au on TiO_2 (Kuwauchi et al., 2012) and CeO_2 (H. Yoshida et al., 2012). The structure of Au on TiO_2 was shown to be dependent on the dose and dose rate applied, and the authors emphasized the importance of tracking these parameters and limiting them to the extent possible. The Au on CeO_2 study, published in Science, presented an important but controversial result, as the authors claimed that CO adsorbates could be seen on the surface of the Au particles. Since the publication of this result, the validity of the interpretation has been questioned. Since the same CO oxidation reaction will be covered in this work, it will be interesting to investigate whether a similar structure is observed on Ru catalyst surfaces. Furthermore, given the oxidized Ru structures currently proposed to be active for CO oxidation over Ru, (covered in detail in section 1.3.2), could the researchers have been observing an oxide layer? The claim that CO adsorbates had been imaged was defended in 2013 (Takeda and Yoshida, 2013) when the authors summarized the work published in 2011-2012.

In 2012 a catalyst for carbon nanotube production, $Fe_{21}Mo_2C_6$, was observed. Image simulations were used to confirm the crystal structure and show that the structure and/or orientation fluctuate during nanotube growth (Hideto Yoshida et al., 2012). The following year a nanorod catalyst for the water-gas shift reaction was studied. The Co_3O_4 nanorods were converted to CoO under reaction conditions (Zhang et al., 2013a, 2013b). In the same year, CeO_2 supported Au for CO oxidation was again investigated (Kuwauchi et al., 2013), demonstrating that Au particles move stepwise and reversibly across a CeO_2 surface at room temperature under reaction conditions. In 2015, the authors published a review (Takeda et al., 2015), covering much of their prior work, and additionally discussing the

effect of gas pressure and spherical aberration correction on the achievable resolution in a differentially-pumped ETEM.

Several questions, which have been prompted by the past *in-situ* TEM studies of catalysts just reviewed, will be addressed in this dissertation.

Dose rate is clearly important. A high dose rate may modify the catalyst in ways that are not fully understood, and these modifications could be mistaken for an effect of the reaction environment. Therefore the dose rate must be maintained as low as possible, as mentioned in 3.2.4 and 7.2.3. The dose rate used should likely be as low as practicable, since ideally, observation of the catalyst should have no effect on the sample. Helveg et al suggest the use of focal series reconstruction to minimize the dose rate used (Helveg et al., 2015). This will be a subject discussed in section 7.2.3. If the resolution of the ETEM is dependent on dose rate, as suggested by Jinschek and Helveg (Jinschek and Helveg, 2012), then this provides another motivation to maintain the lowest possible dose rate.

The shape of nanoparticles can be modified by changes in reaction conditions as demonstrated by several of the works just reviewed. Shape changes, by definition mean a different set of crystal facets/edges/etc. will be exposed. Determining whether Ru particles change shape under reaction conditions is thus one of the primary objectives of this work. This will be the subject of Chapter 5 of this dissertation. The question of whether the gas composition causes changes in facet distribution, or if the changes in facet distribution modify the gas composition is one which is unlikely to be answered in a single PhD. This "chicken and egg" question is unlikely to have a simple answer, and it is not yet clear what ETEM experiment could be devised to address this.

The images of Takeda and Yoshida which have been interpreted as observations of adsorbed CO molecules on a nanoparticle surface are intriguing (H. Yoshida et al., 2012). However, skeptics will likely continue to reject this interpretation. Will similar structures be observed on the Ru catalyst for CO oxidation studied here? Section 6.2 includes an image (Figure 6-4) of a Ru particle which contains a qualitatively similar feature on the surface, but this is interpreted to be a RuO_2 layer. This suggests that the skeptics are correct in this case.

Transmission electron microscopy has the unique capability to observe the structure of a single catalyst nanoparticle, and environmental TEM allows observation of the particle under reaction conditions. This provides an opportunity to observe structures which deviate from the norm. This opportunity could also prove to be a limitation. Any one observed nanoparticle may not be representative of the catalyst, and the only way to determine whether it is representative or not is to also observe a large number of other particles. Observation of a statistically relevant number of nanoparticles at atomic resolution is currently time consuming, though a technique for finding good particles is introduced in section 3.3.7. One of the goals of this work, presented in Chapter 5, was to begin to treat observations of nanoparticles statistically, though the number of particles analyzed is still small. A goal for future work discussed in section 7.2.3 is to automate the acquisition of large numbers of particle images to facilitate higher-quality statistics.

1.2.3. *Operando*: an Extension of *In-Situ* Techniques

While *in-situ* measurements of catalysts can provide a wealth of information about the state of the catalyst under controlled conditions, the effect of these conditions on the

catalytic activity may not be well-known. Thus, it would be preferable, whenever possible to additionally measure the activity of the catalyst during the *in-situ* measurement, and this is known as *operando*. This term was first coined in 2000 at the 220th ACS National Meeting (Weckhuysen, 2002). It is now used extensively in the catalysis community, and a search for "*operando cataly*"* using Web of Science yields 694 results, with 118 of these from 2015 alone. Several reviews have also been published on the topic (Bañares, 2005; Tinnemans et al., 2006; Weckhuysen, 2003). Within the catalysis community, *operando* has been strictly defined to be the acquisition of "*in-situ* spectra under true catalytic operation as determined by simultaneous online activity/selectivity measurements" (Bañares, 2005).

Despite this strict definition, it seems reasonable that, just as the term *in-situ* is not limited to the study of catalysis, *operando* might be properly applied to other subjects of scientific research. A broader definition could therefore be: the simultaneous characterization of the structure and performance of a material during application of one or more stimuli. This broader application is shown schematically for the case of structural characterization performed using TEM/STEM in Figure 1-1. For thermal heterogeneous catalysis, the performance of the material is quantified by defining the activity and selectivity of the catalyst, as determined by measurement of gas compositions, and the stimuli include the reactant gases and the temperature. To date, several researchers have published initial *operando* TEM results (Chenna and Crozier, 2012b; Li et al., 2015; Vendelbo et al., 2014a). Further development of *operando* TEM for a differentially-pumped ETEM was one of the primary objectives of this work, and will be covered in detail in Chapter 3.

1.2.4. Operando ETEM of CO Oxidation over a Ru catalyst

Operando TEM investigation of a Ru catalyst for CO oxidation was the primary focus of this research. The choice of Ru was based on both the high activity of this catalyst, and the remaining uncertainty surrounding the mechanism. Ru nanoparticles have shown particularly high CO oxidation in hydrogen-rich gas streams (Chin et al., 2005; Kim et al., 2012; Oh and Sinkevitch, 1993). It has been known for some time that Ru behaves differently from other transition metals (Böttcher et al., 1997; Kim et al., 2000; Stampfl and Scheffler, 1997). Today this is thought to be related to the ease with which the Ru can be mildly oxidized when compared to other transition metals, like Pt, Rh, and Pd (Chen et al., 2007). Nevertheless, the exact structures present during active CO oxidation and their influence on the catalyst activity are still debated, as explained in section 1.3.2.

An objection could be raised to the use of Ru for an industrial process because Ru is rare in earth's crust, with a concentration of about 0.01 ppm. This is more abundant than Pt but slightly less abundant than gold (Krebs, 2006), making it likely to be an unsustainable long-term solution. However, application of advanced characterization leading to identification of the structures and properties which lead to the surprising activity of Ru may result in the rational design of earth abundant catalysts which mimic its behavior. Without a detailed knowledge of the fundamental processes and structures involved, there is little hope that the high activity of Ru can be replicated in an Earth-abundant material. Currently, as discussed in section 1.3.2 the active structures of Ru for CO oxidation are still debated, and the work described in this dissertation aims to contribute to this debate.

Indeed, several *in-situ* techniques have already been used to explore Ru as a CO oxidation catalyst, but the application of *operando* imaging to directly observe structures of supported Ru catalysts has not been investigated prior to this research. Achieving *operando* TEM is not trivial because, as described in detail in section 3.3.1, a typical TEM sample is small, so that little product is generated inside the TEM. Successful quantification of CO2 produced by a Ru catalyst in the ETEM is described in Chapter 3. A second challenge is to acquire high quality images of catalyst particles, extracting useful information from these (Chapter 4), and determining the morphology (Chapter 5) and surface structures (Chapter 6) present.

1.3. Introduction to CO Oxidation

1.3.1. CO Oxidation over Transition Metals

CO oxidation is an important reaction both technologically, and scientifically, as discussed in section 1.1. Many potential catalysts have been studied, but significant effort has been focused on Pt group metals (Pt, Rh, Ru, Pd, Ir) and, recently, on gold nanoparticles (Cant et al., 1978; Park et al., 2009; Santra and Goodman, 2002).

The activity of platinum has been studied in detail for decades. In 1972, Bonzel and Ku (Bonzel and Ku, 1972) studied the behavior of Pt (110) single crystals under UHV conditions and found that when exposed sequentially to the 2 reactants, the order in which the surface was exposed to CO and O_2 made a significant difference to the reaction rate, and to the proposed mechanism. If exposed to CO first, the mechanism was Langmuir-Hinshelwood, in which both CO and O must be adsorbed on the Pt surface, but if exposed

to O_2 first, a Eley-Rideal mechanism, in which only the O species is adsorbed, was proposed. This is consistent with the fact that on Pt CO adsorbs much more strongly, making it difficult for O_2 to dissociate and co-adsorb onto the CO covered surface. Bourane meticulously lays out the kinetics and proposed reaction mechanisms for CO oxidation over Pt supported on alumina (Bourane, 2004, 2003; Bourane and Bianchi, 2002a, 2002b, 2001). Two mechanisms are proposed, with the less active, but more prevalent mechanism involving a CO covered Pt surface, where O_2 occasionally dissociates and immediately reacts on the surface. The more active mechanism occurs only if the Pt is exposed to excess O_2 at high temperatures. Under these conditions, all the CO on the Pt surface can be oxidized, leading to a surface covered by strongly bound O species, which can rapidly react with any CO impinging on the surface. This is remarkably similar to the mechanism on Ru, described in section 1.3.2

The activity of Pt on alumina for preferential oxidation of CO in a H_2 rich flow (PROX) has been more recently studied (Kahlich et al., 1997). It was found that at temperatures between 150 and 200°C the Pt was completely covered in CO, leading to low conversion rates, but high selectivity. At higher temperatures above 250°C, or with low enough CO concentrations, the surface coverage of CO decreased, leading to a loss in selectivity since H_2 then obtained access to the surface. Other work (Manasilp and Gulari, 2002) showed that the presence of H_2O increased the activity of an alumina supported Pt catalyst, likely due to participation of hydroxyl groups; CO_2 inhibited the activity, however.

More recently, it has been suggested that atomically dispersed Pt on some supports may be more active on a per-atom basis than nanoparticles of Pt (Qiao et al., 2011; Yang et al., 2013). This is a promising result, since Pt and other precious metals are expensive, and any

method to reduce the amount needed to synthesize a working catalyst is therefore highly valuable.

Interest in Au as a CO oxidation catalyst began in 1987 when Haruta reported that nanoparticles of Au supported on Fe_2O_3 were active at temperatures down to -70°C, much lower than any other supported metal catalyst then known (Haruta et al., 1989, 1987, p. 87). Further study showed that the size of the gold particles was of primary importance, and that the support had a large effect on the catalysis, leading to the conclusion that the high activity was likely localized to the metal-oxide perimeter (Haruta, 1997). Schubert used a temporal analysis of products (TAP) reactor setup with isotopic O_2 to study the mechanism for CO oxidation over Au supported on multiple supports (Schubert et al., 2001). The mechanism proposed was that molecular and mobile O_2 species adsorbed on the oxide support. These then reacted with CO adsorbed on the Au particles, explaining the dependence on the metal-support interface. Fe_2O_3, TiO_2, and NiO_x were all found to be active. Other researchers found Au supported on alumina (Comotti et al., 2006) and CeO_2 (López-Haro et al., 2012; Ta et al., 2012; H. Yoshida et al., 2012) were also active. It was shown by Ta using ETEM that Au supported on CeO_2 were quite stable against sintering, under alternating reducing and oxidizing conditions (Ta et al., 2012).

More recently, evidence that water plays an important role in promoting CO oxidation over supported Au catalysts has been found by several groups (Fujitani et al., 2014; Saavedra et al., 2014). Saavedra used density functional theory and *in-situ* infrared spectroscopy to arrive at a proposed mechanism for the CO oxidation on supported gold in which an Au-OOH species reacts with Au-CO to form Au-COOH which then loses its H to nearby O or OH species, yielding CO_2. Fujitani suggested that, in fact, the effect of H_2O

is complex, depending on the particular support chemistry and synthesis conditions. The role of water was classified into 4 categories: creation of cationic gold active sites, direct involvement in CO_2 formation, activation of O_2 molecules, and transformation and decomposition of carbonate species, which tend to deactivate the supported Au over time.

While not garnering as much attention as Ru, Rhodium has also been studied as a potential catalyst for CO oxidation. Like Ru, Rh has also been found to form a thin oxide trilayer structure (Gustafson et al., 2004). Another study (Grass et al., 2008) showed that Rh nanoparticles were oxidized during CO oxidation, and smaller, particles with thicker oxide shells are more active. A recent paper (Kim et al., 2013) reported on Rh oxide layers on Rh particles 6 and 2 nm in diameter studied using XPS. The measured turnover frequency was highest for 2nm particles after moderate oxidation, while further oxidation decreased the activity.

Several researchers have performed comparison studies in which Ru and other noble or transition metals are compared. The earliest of these is the study by Cant, et al. (Cant et al., 1978) who studied SiO_2 supported Pt, Pd, Ir, Rh, and Ru. Most of the early papers on CO oxidation over Ru cite this work, in which the authors mention that Ru is unusual; the reaction rate changed for several hours after the initiation of pressure and temperature changes. They also report that the activation energy of Pt was lowest, then Ru, and finally Rh, Pd, and Ir. The authors predict that Ru may have a partially inactive oxide layer. While the article was not focused on Ru, this conclusion turned out to be quite accurate, and a good simple summary of the complex behavior of Ru. Chen et al. also found that Ru is different in important ways from Pd, Rh, and Pt (Chen et al., 2007). They explain that in all cases, a “hyperactive” state is reached when the catalyst surface becomes saturated with

oxygen. However, for Ru, this occurs under very different conditions (close to a stoichiometric mixture of O_2 and CO) than the other metals, which become saturated with oxygen only at very large O_2 to CO ratios. This is an extraordinary fact, and one which largely explains the interest in Ru, which is covered in detail below. It also hints at the reason Ru is so useful as a catalyst for preferential oxidation (PROX) of CO in H_2 rich streams, as shown by Oh and Sinkevitch (Oh and Sinkevitch, 1993) who reported on CO oxidation in H_2 rich fuel streams over Al_2O_3-supported metals: Pt, Pd, Rh, Ru, Co/Cu, Ni/Co/Fe, Ag, Cr, Fe; The Ru catalyst had the best performance, with Rh a close second. Cu/Co was the best of the base-metal catalysts tested. More recently, Park, et al. (Park et al., 2009) compiled a detailed review of PROX studies, with tables of CO conversions, from over 180 references; Liu, et al. (Liu et al., 2012) also wrote a review on PROX over Pt, Ru, Ir, Rh, Au, and Cu. Finally, Martynova, et al. studied (Martynova et al., 2013) CO oxidation on thin oxide films over metals (RuO_2 /Ru, RuO_2/Pt, etc.), and found higher initial reaction rates on surfaces with weakly bound oxygen species; of all the combinations tried, RuO_2 over Ru was the most active.

1.3.2. CO Oxidation over Ru

Significant experimental and theoretical effort has been expended in attempts to fully elucidate the mechanism behind the extraordinary activity of Ru based catalysts for CO oxidation.

Possibly the earliest published mention of the activity of Ru for CO oxidation is in the 1975 paper by Madey, et al. (Madey et al., 1975). The authors were inconclusive regarding the mechanism on the (0001) surface, but emphasize that Ru is different from Pt and Pd. A

few years later, Reed, et al. (Reed et al., 1977) published work mentioning CO oxidation over Ru (101), stating a clear difference between Ru and Pt or Pd, namely, that CO desorption is not the rate limiting step on Ru. In 1980, a paper was published (Lee, 1980) which foreshadowed the long debate over mechanisms, giving evidence that several forms of oxygen may be present at the surface, and that heating of the O species to 650 K "anneals" the surface oxygen so that it becomes less reactive.

A landmark paper was published in 1984 (Kiss and Gonzalez, 1984) , which investigated CO oxidation over SiO_2-supported Ru particles. A hysteresis was observed, in which the conversions decreased after going to high temperatures/conversions. This hysteresis was most pronounced for O_2 rich conditions, a fact that would shape much of the future debate over the most active structure. In fact, exposing the catalyst to an oxidizing ratio (0.25) of CO/O_2 overnight led to significant deactivation, not recovered by going back to stoichiometry. The high activity could be recovered by reducing the catalyst. This suggested that RuO_2 was not active for CO oxidation, a conclusion that would later be challenged, but never fully abandoned by the entire community. Deactivation in an O_2 rich stream was found to lead to CO species that reacted only at higher temperature, probably with subsurface oxygen. Buildup of this subsurface oxygen was hypothesized to be likely responsible for deactivation, a conclusion that would be abandoned as more evidence showed subsurface O species were actually quite important to the activity of Ru at high temperatures. Oscillations in activity were also observed in a stoichiometric gas mixture and attributed to alternating oxidation and reduction of the surface. Such oscillations would later be studied in some detail (Rosenthal et al., 2011, 2009).

A second landmark paper was published by Peden and Goodman in 1986 (Peden and Goodman, 1986). CO Oxidation over Ru (0001) was studied, using Auger electron spectroscopy performed post-reaction. It was found that in UHV, Ru is least active among the metals Pd, Pt, Rh, Ir, Ru, while at high pressures it is most active. This was attributed to the lack of O_2 on the Ru surface under UHV conditions. Nevertheless, the activity of Ru in both supported catalysts and single crystals is quite similar. Optimum CO conversion was found to result in 1:1 coverage of O on the Ru surface, while lower O coverage gave lower activity, possibly because the O at low coverages is a less active species. Very little deactivation was found to occur under O_2 rich conditions, in contrast to the results of Kiss and Gonzalez (Kiss and Gonzalez, 1984) for supported particles. This was hypothesized to be due to difficulty in oxidizing the single crystal vs nanoparticles. A few years later Hoffmann et al. (Hoffmann et al., 1990) studied CO oxidation over Ru (0001) using *in-situ* FTIR. They found that the residence time for CO on the Ru surface was very short (10^{-12} s). From this they concluded that an Eley-Rideal mechanism, in which only O adsorbed on the Ru surface, was responsible for the CO oxidation, though this was later questioned (Stampfl and Scheffler, 1999, 1997). The short residence time was attributed to a reduction in the adsorption energy of CO due to the pre-adsorbed oxygen covering the surface.

Beginning in 1996, a flurry of work on CO oxidation over Ru began, with at least 33 papers published directly discussing the topic between 1996 and 2009, as at least 3 competing structures were proposed to be the most active structure for CO oxidation over Ru. The structures that eventually emerged as possible candidates during this time (and the publication they first appeared in) were:

Ru metal (0001) with a (1x1)O layer on this surface, and possibly some oxygen present in the subsurface (Stampfl et al., 1996).

RuO_2, specifically the (101) surface, which can be readily grown on a Ru (0001) (Over et al., 2000).

A surface oxide, RuO_x $(2 < x < 4)$, sometimes assumed to have an O-Ru-O trilayer structure (Reuter et al., 2002).

The Ru metal, RuO_2, and trilayer structures are shown in Figure 1-2. Sometimes-heated debates and highly biased reporting of results were engendered by the deep divide in opinion between different authors, with the most avid defenders of the first two structures above being W. Goodman, and H. Over respectively.

Stampfl and Scheffler were authors of a series of 3 papers ((Stampfl et al., 1996; Stampfl and Scheffler, 1999, 1997), which applied mainly theoretical techniques to the then-supposed active structure of Ru with a (1x1)O layer. They found that O-O interactions in this layer were repulsive, so that islands of the O layer would not form, and instead a uniformly increasing coverage of the surface should occur. It was also predicted that the surface layer of O increases the Ru (0001) layer spacing at the top layer by 3%. A significant energy barrier (1.1 eV) was found to exist for the Eley-Rideal mechanism, and the authors concluded that the activity of Ru catalysts is thus likely due to CO adsorption at O vacancies, where the barrier would be smaller. They also concluded that a Langmuir-Hinshelwood mechanism was also unlikely due to an even higher energy barrier of 1.5 eV. Much later, other groups would conclude that activity is in fact due to reactions, not at vacancies, but at steps, or other defect sites (Kim et al., 2007; Rosenthal et al., 2009).

Böttcher and Niehus were authors on another series of papers (Böttcher et al., 2000, 1999, 1997; Böttcher and Niehus, 1999) attempting to elucidate the active structure of Ru catalysts using experimental techniques. They concluded that the presence of subsurface O below the (1x1)O layer on Ru(0001) was vital for high activity. Specifically, O content greater than the equivalent of 3 ML O gives the highest activity. They note that the subsurface O is mobile above about 225°C, and specifically stress that the subsurface O is not RuO_2, as this would not be formed under the conditions used. In fact, RuO_2 can be formed, by exposing the same amount of O_2 at 725°C, but this structure is much less active at moderate temperatures, only showing high activity above 725°C as the oxide decomposes. Furthermore, they found that the amount of highly reactive O adsorbed on the surface is dependent on the amount of O contained in the subsurface region. This levels off at around 10 ML in the subsurface. The conversion probability for this highly active O was found to be 0.18, which they note was the "highest found for this reaction."

Perhaps one of the best papers on the subject of CO oxidation over Ru is (Böttcher et al., 1999). Continuing their study of CO oxidation on Ru, Ru(0001) pre-exposed to O_2 was studied by transient experiments, where the CO_2 production was monitored over the course of 10 min while exposing the O-rich surface to a CO beam. Two distinct reaction channels were found in this work. The first occurs when reactive O species on the surface (about .3ML of O) react rapidly (within 20 s). The second involves the diffusion of O from the subsurface and only occurred when the sample temperature was above 225°C. The rate of O diffusion was increased at higher temperatures, but the CO residence time was decreased, leading to a small temperature dependence (and therefore a small apparent activation energy around 0.3 eV). At temperatures too low for O diffusion, the CO conversion rate

initially rose rapidly, and then slowed to 0, as the surface O was consumed. However, subsequently annealing the sample (which still contained O below the surface) at 375 °C restored the high initial activity of the catalyst. This is very important because it proved that subsurface oxygen could diffuse up to the surface and react with CO at catalytically relevant temperatures. The mobility of oxygen in the surface structure may thus be very important for high activity.

Ertl, winner of a Nobel Prize, and one of the great researchers in the field of catalysis was an author on another series of papers (Fan et al., 2001; Kim et al., 2000; Over et al., 2000; Wang et al., 2002, 2001) which began to turn the attention of the community away from Ru with a layer of O on the surface, toward RuO_2. Over et al. first claimed that RuO_2 (101) might be the active structure for CO oxidation (Over et al., 2000), after it was found that an active O rich Ru (0001) surface was composed of both 1x1 O monolayer regions and RuO_2 (110) regions. Exposure to CO formed small pits in the oxide, as observed using STM. It was claimed that the RuO_2 regions must be the active region. Kim et al. continued down this path, (Kim et al., 2000), again claiming that RuO_2 regions were the active region. Minimal catalytic data were given to support this. The fact that CO should adsorb more strongly on RuO_2 (110) than on 1x1 O surface was instead given as strong evidence for this hypothesis. Other evidence included the unsurprising reduction of an RuO_2 (101) surface by CO at 225°. Detailed study of the precise mechanism for CO oxidation over RuO_2 (101) was attempted in (Fan et al., 2001). Two oxidation channels were observed. If O at coordinatively unsaturated sites (cus) is available, this was proposed to react with CO first. If most O-cus had reacted, then O-bridge should react according to the authors. This study was continued in (Wang et al., 2001), where below room temperature, CO molecules

can adsorb on Ru-cus sites, but above this temperature, the bridge site O is reacted off, and CO adsorbs on the bridge sites. The following year another article was published (Wang et al., 2002). A detailed discussion of adsorbate locations and reaction pathways on RuO_2 (110) single crystal surfaces was given. The previous observation of a pressure gap (Peden and Goodman, 1986) was attributed to the high pressure required to produce an oxide structure.

At this point, Ru seemed to have been completely abandoned in favor of RuO_2 being the active surface, and several subsequent papers seem to stretch the facts to remain within this new understanding. However, in 2002 (Reuter et al., 2002), another possible active structure was introduced, namely the O-Ru-O trilayer structure, as a theoretical treatment of the transition from Ru with chemisorbed O to RuO_2 was attempted. The authors note that trilayer structures have also been proposed for the oxidation of other metal surfaces, notably Rh(111) (Gustafson et al., 2004). Scheffler, who was involved with earlier work on CO oxidation over Ru, went on to publish several more theory-based papers, in which the thermodynamics of a RuO_2 surface are considered. Specifically, in 2003, (Reuter and Scheffler, 2003) a surface phase diagram was produced using DFT. The phase diagram indicated that the highest activity for CO oxidation should be found in regions where there is no dominant stable phase at the surface (the phase boundaries). This is, in fact, where experimental studies have found high activity. In 2006, (Reuter and Scheffler, 2006), Monte Carlo simulations were used to predict the rate of CO oxidation over a RuO_2 (110) surface. The authors claimed that the reaction pathway with the lowest energy barrier has little to do with the CO_2 production at high activity, which is instead dominated by the surface coverages and dynamics. This entire approach for simulation of the CO oxidation

reaction was criticized 6 years later by Hess, et al. (Hess et al., 2012). This paper showed that kinetic Monte Carlo simulations of turnover frequency (TOF) are somewhat insensitive to the input parameters used to perform the calculations. Additionally, it concluded that the kinetic Monte Carlo calculations fail to accurately match experimental data other than reported TOFs. The usefulness of this technique was thus called into question.

Muhler was an author on a series of papers beginning in 2003, which argued that the pressure gap had been closed for CO oxidation over Ru, and that thin layers of oxide on Ru were the most active structure. The first of these papers, (Aßmann et al., 2003), studied Ru nanoparticles supported on SiO_2 and MgO The authors claimed that an RuO_2 surface layer formed by oxidation of the Ru particles is partially reduced during CO oxidation, and this is the active surface. However, very little evidence was presented to show that an oxide phase was ever formed on their material, and the article seems to be quite biased. The same year, a review of the literature related to CO oxidation over RuO_2 was published (Over and Muhler, 2003). It was clearly biased toward RuO_2 being the active structure. The authors suggested that deactivation of supported ruthenium catalysts (Kiss and Gonzalez, 1984) may have been due to growth of RuO_2(100) domains, rather than (110). They do admit that at temperatures above 225°C, this picture becomes complicated, since RuO_2 (110) is no longer stable in a stoichiometric mixture of CO and O_2 but high activity is still observed under these conditions.

In 2004, a continuation of the supported-Ru work was published (Aßmann et al., 2004). Much experimental reactor data is shown, in contrast to much of the previous work on RuO_2. The maximum conversion achieved in the reactor decreased with increasing O_2

concentration. A reduction in H_2 could restore the activity of the deactivated catalyst. No significant oxidation of Ru was observed under net-reducing conditions. The authors nevertheless claimed that even in reducing conditions the Ru particles were covered by an RuO_2 surface layer; this was not substantiated with evidence. The inactivity of fully oxidized particles was attributed to the formation of a c(2x2) phase on the RuO_2 (100) surfaces, despite there being no evidence for this besides the low activity of the catalyst. The following year, micron sized particles of RuO_2 were studied in a reactor and using temperature programmed reduction (TPR) (Narkhede et al., 2005). TPR of a Ru catalyst after stoichiometric CO oxidation (in which high activity was observed) yielded no observable reduction. The authors claim that this was because the RuO_2 layer present on the particles was below the detection limit of the measurement, and insisted that a layer of RuO_2 was present, despite the lack of evidence. A final paper by this author on the subject reviewed much of the literature up to 2008 (Aßmann et al., 2008).

Stampfl, who had published several of the early papers, previously covered, on CO oxidation over Ru (Reuter et al., 2002; Stampfl et al., 1996; Stampfl and Scheffler, 1999, 1997), published a theory-based monograph on oxidation of metals including Ru (Stampfl, 2005). Density functional theory (DFT) and Monte Carlo techniques were applied and showed that increasing O coverage leads to decreasing adsorption energy, but a full monolayer of O will form before subsurface O does. This monolayer of O should be stable. According to Stampfl, subsurface oxygen likely forms a modified O-Ru-O trilayer structure. She notes that this is rather similar to RuO_4 molecules. While RuO_2 is considered by others to be the active phase, this may not be the case.

In 2005, He, et al. (He et al., 2005) published a paper in which *in-situ* surface XRD was used to study the oxidation of Ru (0001) in both pure O_2, and a mixture of O_2 and CO. The presence of stoichiometric CO in the gas significantly inhibits the formation of RuO_2 and an induction period was observed. Though the authors do not state this, it seems likely that this induction period corresponds to the time required for the CO and O_2 in the batch reactor to react on the surface, eventually leaving a small amount of residual O_2 with no CO (Campbell, 2006), which then quickly oxidized the sample.

From 2004 to 2006, Blume, et al. published a series of 3 papers on the oxidation of a Ru (0001) surface, the nature of the oxide layer, and the activity of the oxidized surface. In the first paper, (Blume et al., 2004), an oxygenated Ru (0001) surface was studied using LEED and ultraviolet photoelectron spectroscopy (UPS). Under the low temperature oxidation conditions used, no evidence of crystalline RuO_2 formation was seen, but CO oxidation activity similar to that observed on RuO_2 was obtained from the oxidized surfaces. A continuation of this work, (Blume et al., 2005) studied the incorporation of O into the subsurface region using spatially resolved XPS, and concluded that below 225°C RuO_2 is not formed. Instead, depending on O exposure and temperature, several O species are found in the thermal desorption spectra. A phase diagram of oxidized Ru structure is presented based on these data. The third paper, published in 2006 (Blume et al., 2006), reported very interesting results. It used *in-situ* XPS to determine the exact oxidation state of Ru during CO oxidation. After oxidation of Ru (0001) at 175°C a "surface oxide" formed with 1.5-2.0 ML O; this was not RuO_2. This was reduced using CO/O_2 with a partial pressure ratio of 4, as the temperature was increased by 2°C per minute. The surface was reduced, until only 0.7 ML O remained. After oxidation at a higher temperature of 395°C,

a RuO_2 film at least 15 Å thick was formed. This was also reduced with CO/O_2 and the RuO_2 directly reduced, (it did not convert first to a "surface oxide"), leaving 0.7 ML. The temperature required for CO oxidation was slightly higher in this case. A 3rd experiment was conducted, in which a Ru surface was heated in CO/O_2 with a ratio of 1. At temperatures below 125°C, CO was visible on the surface. At higher temperatures, O was incorporated into the subsurface, while little O, and no CO, was present at the surface; any CO was likely being converted to CO_2. Increasing the temperature led to more subsurface O until, at around 225°C, the surface oxide began to transform into RuO_2. This RuO_2 formed patches so that both surface oxide and RuO_2 coexisted. At 315°C about 80% of the surface was covered in RuO_2 and the activity began to decline. Meanwhile, the activity increased steadily between 150°C and 275°C even though RuO_2 and surface oxide coexisted only above 225°C. The conclusion the authors gave was that there is no distinct difference between the activity of RuO_2 and the "surface oxide" phase. This may be an understatement, as RuO_2 may be largely inactive, with the surface oxide accounting for most of the observed CO oxidation activity of oxidized Ru.

The following year, Goodman, et al. stated clearly that RuO_2 is not the active phase during CO oxidation in a review (Goodman et al., 2007a) of the literature, including the early works on supported catalysts. This article prompted a strong defense of RuO_2 as the active phase from Over, et al. (Over et al., 2007). The authors used calculations based on a L-H mechanism to prove that Goodman's claim cannot be correct. This does not seem to be a convincing proof, since no one, including Over who is an author on many of the papers reviewed here (Aßmann et al., 2008, 2004; Böttcher et al., 1999, 1997; Hess et al., 2012; He et al., 2005; Kim et al., 2000; Over et al., 2009, 2000; Over and Muhler, 2003; Stampfl

et al., 1996), has yet succeeded in a full theoretical description of the high activity of Ru catalysts for CO oxidation. They also present several bits of evidence from the literature, but several of these are highly questionable, and a few have been already stated above to be unsupported by the evidence. In response to this defense of RuO_2, Goodman, et al. (Goodman et al., 2007b) refute several of the points in (Over et al., 2007) that were particularly poor. The authors also make several important observations, including that the TAP reactor measurements showing that RuO_2 is highly active were reporting transient rates, not steady state rates; this blatantly ignores the early observations that RuO_2 catalysts suffer significant deactivation (Kiss and Gonzalez, 1984). Additionally, the temperature ranges used in all studies that had showed the high activity of RuO_2 were quite low. An extrapolation not justified by the available data would be required to compare the rate to that found on Ru metal catalysts.

Goodman continued to publish papers arguing that RuO_2 does not account for the observed high activity of Ru. In 2009, a lengthy paper (Gao et al., 2009) estimated that the number of active sites on Ru (1x1)O is between 0.01 and 10^{-5} ML. If this is accurate, then the reactivity on a per-site basis would be very large compared to RuO_2, which has many more active sites, but was found to be only 4 times as active under oxidizing conditions. Under stoichiometric conditions over an RuO_2 catalyst, significant reduction occurred, but the evolution of the reactivity with time and temperature was quite complicated. Reduction of the oxide led to a reduced but inhomogeneous surface that was more active than an atomically flat Ru (0001) surface. Under oxidizing conditions, however, the activity was found to drop as the temperature was increased from 125°C to 200°C. This is unusual behavior, and was hypothesized to be due to the presence, at low temperatures, of a very

reactive form of O on the RuO_2 surface, which was not present at higher temperatures. Under oxidizing conditions at temperatures between 50°C and 175°C significant deactivation occurred. Another paper in 2012 (Gao and Goodman, 2012) was mainly a review of work done in the past, with a bit of new *in-situ* work. As before, the authors stressed that the active phase cannot be just RuO_2. They concluded that activity on a 1ML O covered Ru (0001) surface can be accounted for by conversion at step sites. This is consistent with the findings of Kim, et al. who compared reactivity on the Ru(109) surface with that on the (001) surface (Kim et al., 2007). Both Ru surfaces were exposed to a small amount of O, giving 0.5 ML on (001) and 0.65 ML on (109). No CO_2 production was observed on the (001) while some CO_2 was produced on the (109), likely due to the excess O present at the many steps on the (109) surface.

A valuable contribution to the body of knowledge regarding the oxidation of Ru to RuO_2 was made by Flege et al. in 2008 (Flege et al., 2008). A portion of the surface oxide formed during oxidation at 520°C is characterized as a "disordered trilayer-like structure" with less O than a perfect trilayer. This surface oxide and RuO_2 coexist on the surface, as clearly seen with low energy electron microscopy (LEEM). Surprisingly, the disordered trilayerlike structure sometimes consumed small regions of the RuO_2 already formed on the surface, while the RuO_2 never consumed the disordered layer. This clearly showed that the trilayer-like structure is not merely a metastable precursor to RuO_2! Interestingly, during reduction of the oxidized surface with CO, reduction (to a (2x1)O structure) of the (1x1)O phase still remaining was initiated near the boundaries of the surface oxide domains, but not near the RuO_2 domain boundaries. Later, reoxidation of the (2x1)O to the

(1x1)O phase also began at the surface oxide domain boundaries. This is intriguing behavior, and not fully understood.

Also in 2009, Over, et al. published an *in-situ* surface XRD study (Over et al., 2009) focused on oxidized Ru(0001). A batch reactor setup was used. Oxidation of the catalyst seemed to result in an increase in the activity. However, in all experiments, this activity was also reduced after some time; this is presumably due to the consumption of most of one reactant. Thus, any deactivation of the catalyst cannot be discerned. In a chamber with 85 mbar CO and 32 mbar O_2, the activity rapidly increased around a temperature of 420°C. An RuO_2 peak in the SXRD appeared just before this ignition. A series of 2 batch reactions with slightly oxidizing conditions showed that RuO_2 formed, but also indicated that the thickness of the RuO_2 film increased from 4.2 to 5 nm while the average domain size decreased from 6 to 5 nm. This is interesting, since grain sizes generally increase when heated. In light of the results of Flege et al. (Flege et al., 2008) just discussed, this suggests that there could have been another phase growing on the surface at the expense of the RuO_2 under reaction conditions.

A powder RuO_2 sample was explored by Rosenthal et al. (Rosenthal et al., 2011, 2009), who observed oscillatory behavior. An important conclusion at which the authors arrived is that the catalyst surface during reaction is heterogeneous, (very rarely ever pure RuO_2) and this will complicate any attempt at interpretation of catalytic data. They also suggest that TOF may not be a useful way to compare catalysts if the number of active sites is not known because of structural heterogeneity. They emphasize that defects, and temporal fluctuations may also be important. The authors also suggest that the "healing" of defects in RuO_2 at high temperatures may be the reason that RuO_2 deactivates.

Recently, several papers have been published on more well-defined nanoparticles of Ru than the early works on supported catalysts. Joo, et al. (Joo et al., 2010) studied 2-6 nm particles synthesized by a colloidal method. They found that larger particles have higher activity, and noted that some larger particles may be FCC. Qadir, et al. (Qadir et al., 2012) synthesized particles supposedly 2.8 and 6 nm in diameter. These were observed using ambient pressure XPS during reduction, oxidation, and CO oxidation in an oxidizing mixture of CO and O_2. It was found that the smaller particles were more heavily oxidized than the larger particles. Specifically, bulk RuO_2 was formed in the small particles and this led to lower catalytic activity. Unfortunately, the degree of the difference in catalytic activity was not specified. Kusada et al (Kusada et al., 2013) also studied nanoparticles of Ru, reporting that FCC Ru nanoparticles were produced. These were claimed to be more active for CO oxidation than hcp nanoparticles. The activity of the FCC particles appeared to increase with increasing size. The authors report the opposite trend for hcp particles, contradicting the results of Qadir (Qadir et al., 2012). This could be due to a different gas composition, but this cannot be determined, since Kusada neglected to specify the composition of the gas mixture used for the activity measurements.

More recently, several papers have been published which focus on the oxidation of thin films. In 2012, Martynova, et al. (Martynova et al., 2012) produced oxidized films of varying thickness on Ru (0001). Thicker films yielded slightly higher activity, while disordered films were more active than ordered ones. This is interesting, and fits with the conclusion of Rosenthal, et al. (Rosenthal et al., 2009) that the healing of defects may be responsible for deactivation in RuO_2 catalysts. The next year another paper was published by Qadir, et al. (Qadir et al., 2013), this time on a thin film. A 45 nm film of Ru was

observed using ambient pressure XPS during reduction, oxidation, and CO oxidation in an oxidizing gas mixture. The results showed significant deactivation of the film, likely due to oxidation to RuO_2. The deactivated film could be partially regenerated by reducing the catalyst in H_2. Coloma Ribera, et al. also studied the growth of RuO_2 on a polycrystalline Ru film using several methods (Coloma Ribera et al., 2015, 2014). They found that both a low density surface oxide and a normal density oxide just beneath the surface oxide formed at 400°C. Additionally, distinctive RuO_2 columns also grew, with (110) facets on the sides. This is very different from the behavior observed for single crystal Ru (0001). It may be that these are the result of Ru grains aligned just right for the growth mechanism. While the authors suggest that Ru may have diffused up through the oxide, this seems unlikely, and it is more likely that the RuO_2 was pushed up by growth of the oxide at its base, fed by diffusion of Ru through the underlying Ru film.

The preceding detailed critical review of the literature regarding CO oxidation over Ru catalysts has led to the conclusion that the most active structure for CO oxidation is likely a disordered layer of oxidized Ru.

There is ample evidence to exclude a bulk RuO_2 structure as the most active structure. This includes the deactivation of supported catalysts under oxidizing conditions which could be reversed by a reduction step (Aßmann et al., 2004; Kiss and Gonzalez, 1984; Qadir et al., 2013, 2012). This has been explained away as a re-structuring of the RuO_2 surface, exposing inactive facets (Aßmann et al., 2004; Over and Muhler, 2003), but this seems to be unfounded. Also, under stoichiometric gas mixtures above 225°C RuO_2 is not stable, but high activity for CO oxidation is still observed (Over and Muhler, 2003). Indeed,

several studies noted a lack of RuO_2 during active CO conversion (Blume et al., 2006; Böttcher et al., 2000, 1997; Narkhede et al., 2005).

While bulk RuO_2 is not the most active structure for CO oxidation, it is clear that the active structure is an oxidized layer. Subsurface O was implicated by several groups (Böttcher et al., 2000, 1999, 1997; Böttcher and Niehus, 1999) and the ability of subsurface O to diffuse to the surface and react with CO was unequivocally proven in the 1999 paper by Böttcher, et al., in which transient experiments showed that above 225°C this diffusion occurred, while at lower temperatures it did not. Other researchers suggested a trilayer-like structure (Reuter et al., 2002), with (Flege et al., 2008) describing a "disordered trilayer-like structure." This surface structure was found to coexist with RuO_2, and was observed to sometimes consume RuO_2, while RuO_2 did not consume the trilayer under the conditions observed. This is clear evidence that the trilayer is not merely a meta-stable precursor to RuO_2. Stampfl (Stampfl, 2005) mentioned that the trilayer structure is remarkably similar to RuO_4, a molecule which, in its pure form, is a liquid which is a strong oxidizing agent. Other groups have contended that while bulk RuO_2 is not active, thin layers of RuO_2 are active (Aßmann et al., 2008, 2004, 2003; Martynova et al., 2013; Over et al., 2009; Qadir et al., 2012; Rosenthal et al., 2009).

Several groups have emphasized the heterogeneity of the catalyst surface, even for single crystal Ru (Blume et al., 2006; Flege et al., 2008; Over et al., 2000; Rosenthal et al., 2011, 2009). Others have stressed the importance of defects (Kim et al., 2007; Rosenthal et al., 2009) or disorder (Flege et al., 2008; Martynova et al., 2012).

Indeed, disorder may be the defining feature of active structures for CO oxidation over Ru. RuO_2 is a highly ordered material, and has been shown to have low activity compared

to other oxidized structures. Studies claiming that thin RuO_2 is active while thicker RuO_2 is not also support the conclusion that disorder is important, since very thin films of oxide will inevitably be disordered. The trilayer-like structures, sometimes explicitly labeled "disordered", and also likened to RuO_4 molecules, which are a liquid in pure form, and thus naturally prone to disorder, have been suggested by several groups to be highly active. If subsurface oxygen plays an important role in CO oxidation, then a disordered structure would also facilitate diffusion of O to the surface. Finally, disordered structures are more difficult to characterize experimentally than crystals, and even more challenging to model, which may help explain the elusiveness of a satisfying conclusion to the debate which surrounds this material. This critical review of the literature thus leads to the conclusion that heterogeneity and disorder may be essential elements for a full description of the mechanisms which cause Ru to be one of the most active materials for CO oxidation.

This has important consequences for this work. Disordered structures are more difficult to characterize in the TEM compared to perfect crystals. The RuO_2 layers expected to be active will be very thin, and thus challenging to image. Nevertheless, one of the objectives of this work, covered in Chapter 6, is to image these structures.

1.4. Summary

CO oxidation is an important catalytic reaction, both because of its technological applications and its scientific value as a model reaction. *In-situ* studies of catalysts are valuable since the structures relevant to catalysis may only be present under reaction conditions. TEM is just one of many characterization tools in which *in-situ* experiments may be performed. Within the TEM community, almost all *in-situ* studies of catalysts have

been conducted at just a few laboratories around the world, with a few pioneering researchers involved. While *in-situ* TEM allows catalyst structures to be observed under reaction conditions, *operando* TEM goes further, measuring the activity of the catalyst simultaneously. This dissertation is focused on *operando* TEM studies of Ru catalysts for CO oxidation. Ru is one of several metals extensively studied for CO oxidation, but is the best at catalyzing the reaction in a H_2 rich flow. The literature on CO oxidation over Ru catalysts is somewhat polarized, with several surface structures argued to be the most active. There is consensus however, that an oxygenated surface of some kind is responsible for the high activity of Ru.

1.5. Research Objectives and Outline

The primary scientific goal of this research is to determine structure-activity relationships for Ru, a CO oxidation catalyst. To achieve this goal several objectives have been established.

First, the catalytic activity of the Ru catalyst must be characterized. Second, a technique should be developed which allows catalyst activity to be measured within a TEM so that the structure can be observed simultaneously. This is known as *operando* TEM. Third, images acquired during *operando* experiments should be analyzed to determine whether the morphology of the catalyst changed as the activity of the catalyst was measured under various conditions. Finally, the surface structure of Ru nanoparticles should be closely examined to determine whether the surface structure of the catalyst correlates with the measured activity.

These objectives have been achieved, and the results are described in Chapters 2-6 of this dissertation. Chapter 2 describes the synthesis of the catalyst and the characterization of its activity in an *ex-situ* reactor. Chapter 3 describes the details of the *operando* technique including the unique sample preparation and the quantification of EELS of gases used to quantitatively determine conversions within the ETEM. Chapter 4 describes methods used for image analysis. Chapter 5 presents the results of early *operando* experiments, and the morphology of the catalyst observed under various conditions. Chapter 6 describes the surface structures observed in the aberration corrected Titan ETEM and their correlation with catalytic activity. Chapter 7 concludes with a summary of this work, as well as proposed extensions of the research which might yield further results

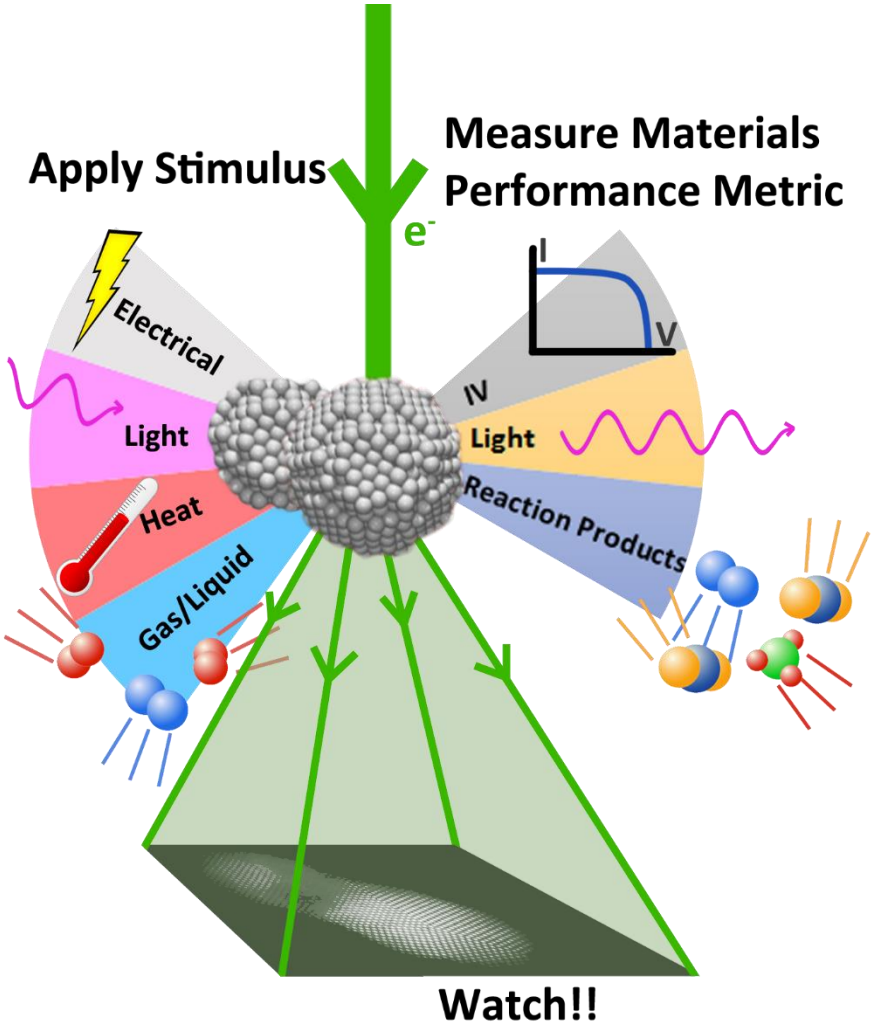

Figure 1-1 *Operando* TEM. Diagram produced to graphically define *operando* TEM. *Operando* TEM involves observation of the material structure using TEM, while simultaneously applying stimuli and measuring a performance metric of the material. The list of stimuli and performance metrics displayed is not intended to be comprehensive.

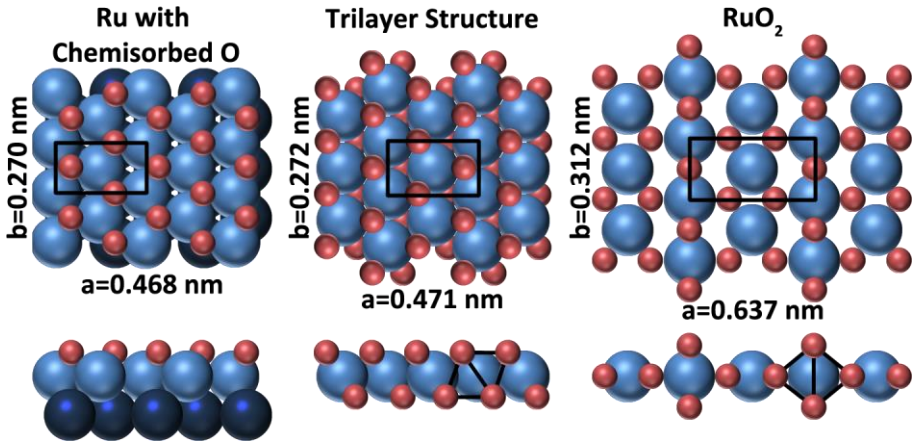

Figure 1-2 Proposed Active Structures. Three structures proposed in the literature as the most active structure for CO oxidation over a ruthenium catalyst. The orientation of oxygen octahedra are given in the profile views of the trilayer and RuO_2 structures. These models were produced based on the models in the article which first elucidated the trilayer structure (Reuter et al., 2002).

2. Catalyst Synthesis and *Ex-Situ* Experiments

2.1. Catalyst Synthesis

The catalyst used in all *in-situ* and *ex-situ* experiments was produced in a single batch using the method described below, in which the amorphous silica spheres were first synthesized, and then impregnated with a Ru salt.

2.1.1. Production of SiO_2 Spheres

Amorphous silica spheres were produced using the Stöber method (Stöber et al., 1968). 30 ml of nanopure water, 150 ml ethanol, and 18 ml of 29% ammonia were mixed in a flask. 12 ml of tetraethyl orthosilicate (TEOS) were added to the solution, which was then magnetically stirred and heated to 58°C for 2 hours. The solution was then evaporated at 100°C, until no liquid remained. The resulting powder of spheres was then calcined for 2 hours at 500°C. An image of the spheres without any catalyst is seen in Figure 2-1.

2.1.2. Production of Ru Particles on Spheres

Ru particles were formed on the SiO_2 spheres using a wet-impregnation procedure. This is commonly used to produce supported catalysts (Regalbuto, 2007). A solution of ruthenium(III) chloride hydrate in H_2O was produced at a concentration of 0.174 g/ml. The pore volume of the silica sphere powder was assumed to be 45% of the powder total volume, based on results for randomly packed spheres (Onoda and Liniger, 1990; Song et al., 2008). A volume of solution equal to the pore volume for the spheres being impregnated was added to the powder and mixed thoroughly for 10 min in a small mortar and pestle

(Banerjee and Crozier, 2012). This was done inside a glove box saturated with water vapor so that the liquid from solution would not evaporate rapidly. It was observed that for a correct volume of solution, the powder formed rigid clumps, and after further stirring became a viscous fluid, before finally drying into a powder again.

This powder was dried at 100°C in air for 1 hour. It was then heated to 500°C in flowing Ar-5%H_2 for 4 hours to convert the salt to Ru metal. A conventional calcination step was skipped as recommended by Chenna (Chenna, 2011). The resulting loading was 2.5 weight percent. The supported Ru catalyst is seen in Figure 2-2.

2.1.3. Preparation of the Catalyst for Reactor Studies

To prepare the catalyst for reactor experiments, the silica supported Ru catalyst was diluted with sand to homogeneously distribute a small amount of catalyst over the entire cross section of the reactor tube (Aßmann et al., 2004). This also allows the amount of catalyst to be precisely varied, even when the amount of catalyst is less than can be weighed easily in the lab. By mixing an easily measurable mass of catalyst in a much larger mass of sand, reserving one half of the mixture, and then diluting the mixture with additional pure sand, in an iterative process, an entire series of samples can be rapidly produced. Each sample will then contain half the catalyst concentration as the previous sample. Small amounts of catalyst are beneficial for several reasons. First, since the CO oxidation reaction is highly exothermic, a concentrated catalyst bed would heat up significantly, compromising the validity of non-local temperature measurements (Aßmann et al., 2004; Rosenthal et al., 2009). Secondly, the Ru catalyst is highly active, but low conversions are

needed to perform accurate kinetic measurements from a reactor at steady state with a plug-flow geometry (Fogler, 2006), so a small amount of catalyst must be used.

2.2. Ex-Situ Experiments

2.2.1. Equipment

Ex-situ catalytic reactions were performed in a reactor acquired from In-Situ Research Instruments (ISRI) called the RIG-150 microreactor (Chenna, 2011). This instrument is equipped with mass flow controllers (MFCs) which allow precise computer control of the gas flow through the reactor. Up to three reactant gases and one carrier gas may be flowed simultaneously. A precise calibration of the mass flow controllers must be obtained for each gas used, by measuring the gas flow using a bubble flow meter, and determining the linear relationship between this flow and the applied voltage in the MFC. Most calibration values had been previously obtained, but those for CO were determined for this work.

The reactor vessel used in this instrument was a quartz tube with an internal diameter of about 3/8 in and a length of 12 in. The tube has a frit about 4 inches from the bottom to keep the catalyst at a good position in the vertical tube furnace of the RIG-150. A model of this tube is given in Figure A 2 of Appendix I. This furnace is capable of operating at temperatures up to 900 °C, and is controlled using a thermocouple inserted down into the quartz tube, but separated from the gases of the reactor by a quartz sheath. The location of the thermocouple relative to the catalyst is of primary importance, since a temperature gradient exists within the reactor. This was characterized, and more detail can be found in Appendix I.

Gases flowing from the RIG-150 reactor were analyzed using gas chromatography. Basically, a gas chromatograph works by flowing a small sample of a gas mixture through a long, thin tube, called the column (Grob and Barry, 2004). After the sample is injected, a carrier gas is used to push the sample gases through the column. Different gas species will require more or less time than others to pass through the tube, and so they are separated. One or more detectors can then be used to measure the amount of each gas species as it exits the column. After the last sample gas species has passed through the column, (usually within 4-10 minutes) another sample of the gas mixture may be taken.

The GC used for this work was a Varian 3900 GC equipped with a 10 m long Varian PLOT column (MolSieve5A) with a 0.32 mm diameter, designed to separate permanent gases like H_2, CO, O_2, and N_2. The column is unable to separate CO_2, but this is acceptable, since the CO oxidation reaction is sufficiently simple that the amount of CO converted under stoichiometric conditions can be assumed to have all converted to CO_2. Helium was used as the carrier gas in our experiments. The detector installed on the 3900 GC is a thermal conductivity detector (TCD). This functions by measuring the difference in thermal conductivities between a reference gas flow (pure helium carrier) and the carrier/sample gas flow from the column (Grob and Barry, 2004). This difference is measured using a Wheatstone bridge type circuit, which produces a voltage that is proportional to the concentration of sample gases in the carrier gas flowing from the column.

A plot of the voltage from the TCD over time should be a flat baseline punctuated with peaks corresponding to each gas component in the gas sample admitted into the GC. Such a raw spectrum, known as a chromatogram, is shown in Figure 2-3. The time it takes for a

given gas to reach the end of the column, known as the elution time, is dependent on several factors. These are all controlled by setting up a method for the GC. The 3900 GC is computer-controlled using a Varian software package known as Galaxie. This software allows convenient entry of all the parameters associated with a method, and can record data in both a proprietary Galaxie data format, as well as ASCII-based text files or Excel files, as specified in the method. The basic GC method used for the analysis of CO oxidation reactions is given in Appendix II. This method is unique to the column used, and should be modified if the column model is changed. The software can also be used to set up automated sampling of gases. After each chromatogram has been recorded, a pneumatically-powered sampling valve admits another sample of gas into the column, and the process is repeated. Typically, the same method is used for every sample in a given experiment, but the method can be different for each sample if desired. A typical reactor experiment takes several hours, allowing many chromatographs to be acquired, and can be run overnight.

The data acquired during an experiment must be analyzed and this analysis was automated using a MATLAB code specifically written for this purpose. Details of the code are available in Appendix III, but the basic functions are as follows. The code first allows the user to open any number of text or excel files with data from the Galaxie software. The data is then checked for consistency, and a basic background subtraction is performed. The code then proceeds with a detailed background subtraction procedure designed to accurately subtract a background that has no functional dependence, varies from one chromatogram to the next, and is several orders of magnitude smaller than the signal peaks. This was achieved using an iterative procedure, which was conceived after a careful

analysis of this unique problem. After successful implementation of the procedure, (included in Appendix III), a search was made to determine whether a similar procedure for background subtraction had been previously published. A similar procedure was found (Galloway et al., 2009), precluding publication of this method. After background subtraction, the user selects which peaks should be integrated, and the integrated intensity of each peak (proportional to the concentration of that gas species) over the set of chromatograms is plotted.

2.2.2. Experiments

To determine the activity of the Ru catalyst, a couple of *ex-situ* reactor experiments were performed using initially identical mixtures of 1 mg of the SiO_2-supported Ru in 1.3 g of silica sand. The Ru catalyst was tested after two distinct pre-treatments, intended to force the catalyst into two well-defined initial conditions. Either the catalyst was reduced in Ar-5%H_2 or the catalyst was oxidized (forming RuO_2) in pure O_2 by flowing 40 sccm (standard cubic centimeters per minute) of the gas for 3 hours at 500°C in the RIG-150. This step was programmed at the beginning of each *ex-situ* experiment measuring catalyst activity.

To test the reduced Ru metal catalyst, immediately after the catalyst was reduced and the temperature returned to room temperature, the gas flow was switched to 4 sccm CO and 2 sccm O_2 with 36 sccm He, a stoichiometric mixture of CO and O_2. The temperature was ramped from room temperature to 250°C at a rate of 1°C per minute, this maximum temperature was held for 20 minutes, and then reduced back down to room temperature. The ramp up and then down was repeated twice, to check the reproducibility of the result.

Results from this experiment are shown in Figure 2-4, where it is seen that at the maximum conversion reached, the reaction rate was 12.6 mmol m^{-2} s^{-1}.

From the plot, it is clear that the conversion displays a hysteresis, being higher on the ramp down than on the ramp up. However, when the ramp up was repeated, the conversion was back to the level of the first ramp-up indicating that any change to the catalyst's activity was transient, and any structural modification was reversible. On a closer inspection (see inset in Figure 2-4), the second ramp up actually shows slightly lower conversion than the first, further emphasizing that the increase in catalyst activity on ramp-down was transient. It is unlikely that the observed hysteresis is simply due to some mass or heat transport limitation within the reactor, since the time separating the measurements marked with purple squares in Figure 2-4 was 40 minutes. This seems longer than it would take for the catalyst to cool or for the product gas produced at higher temperatures to be flushed out of the system, considering that the volume of gas filling the lines connecting the reactor and GC is replaced every 2 minutes. However, it is still possible that complex ignition/extinction phenomena may be involved, complicating the interpretation of this hysteresis as indicated in (Aßmann et al., 2004).

A nearly identical experiment was performed for the catalyst that had been oxidized as described above, this oxidized catalyst displayed markedly lower activity, with conversions less than 1% for temperatures up to 250°C. The amount of catalyst, gas flow rates, and temperature ramp rates were identical; the only experimental difference, other than the oxidation state of the catalyst, was that the maximum temperature explored was higher. Even at 450°C, the maximum conversion observed was less than 10%, corresponding to 11.0 mmol m^{-2} s^{-1}. as seen in Figure 2-5. A clear trend is seen in the conversions observed

for the oxidized catalyst around 300°C. On the initial ramp up, the conversion is very low, but on the first ramp down, and the second ramps up and down, the conversion is much higher. This is likely due to a reduction of some part of the catalyst (possibly very small particles, as these would be reduced most quickly) during the conversion at temperatures above 350°C.

The figures in this chapter present the performance of the catalyst in terms of conversion and reaction rate in mmol m^{-2} s^{-1}. These two are related by a scalar factor for the 2 experiments presented, which used identical flow rates and amounts of catalyst (which were assumed to have the same surface area). However, this relationship between conversion and reaction rate is only valid at low conversions in the plug-flow reactor geometry used! Thus, for conversions above 50%, the reaction rate cannot be accurately calculated using this simple method due to mass transport limitations. This has been emphasized in the figures by discontinuing the right axis above 50% conversion. The reaction rate expressed in mmol m^{-2} s^{-1} can also be related to a turnover frequency (TOF) if assumptions about the number of active sites on the catalyst are made. For the reduced catalyst, the areal densities of surface atoms were determined for each facet in the Wulff shape, (described in section 5.2, and shown in Figure 5-8) and the weighted average obtained based on the area of facets present; this areal density was determined to be 17 atoms/nm^2. If every surface atom is assumed to be a reaction site, then the turnover frequency in molecules of CO_2 per surface site per second can be calculated. This is related to the reaction rate by a scalar factor, so that the TOF is just 2.2 times the reaction rate if this is given in units of mmol m^{-2} s^{-1}. Turnover frequencies are given on the right axis of Figure 2-6 which includes a subset of the data given in Figure 2-4 and Figure 2-5. It must

be stressed that assuming every surface Ru atom to be an active site is probably incorrect, so the best way to express the activity of the catalyst in this case is in terms of mmol m^{-2} s^{-1} rather than turnover frequency as discussed in section 3.3.6.

The catalytic data shown in Figure 2-4 and Figure 2-5 can be more rigorously analyzed by fitting the conversion data with a function to extract descriptive parameters like activation energies. The first step is to plot the data in an Arrhenius plot, as shown in Figure 2-7. If a single rate-limiting step governed the catalytic activity, then at low conversions, perfectly acquired data would be linear. There are several reasons why the data shown in Figure 2-7 is not perfectly linear. CO conversions over the pre-reduced catalyst went up to nearly 100%, and at such high conversions in a plug-flow geometry, the data cannot be analyzed in this way. Data at the highest conversions should therefore be ignored. At conversions below 1%, the data becomes noisy and unreliable. This data should also be rejected. Finally, over wide temperature ranges, several mechanisms, and thus more than one rate-limiting step, may be represented. For example, at temperatures below 225°C subsurface oxygen becomes mobile in oxidized Ru (Böttcher et al., 1999). This may explain the lack of activity in the oxidized catalyst below this temperature. The changes in slope around 330°C and again around 400°C, have not been interpreted, but help to define the regions over which the slope has been measured. Data within the area shaded dark grey in Figure 2-7 were thus used to calculate the activation energies given in Table 2-1. These are effective activation energies, representing the rate-determining step for the CO oxidation reaction, over a limited temperature and conversion range. For the pre-oxidized catalyst, which was heated to 450°C, another set of activation energies was calculated from the region shaded light gray in Figure 2-7, and these are given in Table 2-2. While these

activation energies can be used to describe the overall reaction rate, it is not clear whether these energies can be ascribed to any single physical process on the catalyst surface. This is directly addressed by Reuter and Scheffler, who performed advanced Monte Carlo modelling using statistical mechanics and DFT to derive turnover frequencies from a large number of physical processes occurring simultaneously on a RuO_2 surface (Reuter and Scheffler, 2006). The authors concluded that "…TOFs in the core region of highest catalytic activity [are] quite insensitive to modest errors in the rates [of elementary physical processes]."

The data show that the effective activation energies are generally lower for the oxidized catalyst compared to the reduced one. Nevertheless, the reaction clearly proceeds much faster for the reduced catalyst, since the reaction rate is significantly higher. This initially seems counterintuitive, but is possible, because the reaction rate depends on more than just the thermally activated rate-determining step, and several necessary processes are temperature dependent. This is directly addressed by Böttcher et al., who state that a low effective activation energy can be a result of competing processes: O diffusion from subsurface layers increases with increasing temperature, but the concentration of CO on the surface decreases with temperature (Böttcher et al., 1999). Another possibility is that the number of highly active sites on the RuO_2 surface may be orders of magnitude lower than on the reduced catalyst. This would lower the activity, even if the activation energy for those sites was smaller than for the reduced catalyst. A combination of these two mechanisms are most likely responsible for the low activation energy but low activity of the oxidized catalyst.

2.3. Estimating ETEM Conversions

The data gathered from the plug-flow reactor and presented in this chapter serves two purposes. Such data is useful for characterizing the catalyst, and ensuring that it is as active as expected based on previous work by others studying Ru. Quantifying the catalyst activity is also useful for determining whether the *operando* TEM technique which is the main focus of this work will be effective when applied to this material. If the highest reaction rate achieved by a catalyst was 3 orders of magnitude less than the Ru studied here, this would fall below the detection limit of the *operando* technique as currently described. Thus, determination of the reaction rate is important for screening which catalysts can be usefully examined using *operando* TEM in a differentially-pumped ETEM. While the detection limit of the *operando* EELS quantification technique is less than 1% (see Figure A 15 of Appendix V), this would not allow accurate quantification of the change in activity over the course of an experiment; to obtain a reasonable range of rate data, a minimum of 10% conversion should be sufficient.

Using the reaction rate from the plug-flow *ex-situ* reactor to estimate conversions in the differentially-pumped ETEM, which does not have a plug-flow geometry, is not trivial and a derivation of this is therefore provided here (all symbols used are listed with their units in Table 2-3). The ETEM cell can be modelled as a continuous stirred-tank reactor (CSTR) as discussed in section 3.3.1. The conversion estimate begins with the equation for conversion in a CSTR, given in equation 2-1 below. This assumes a constant volumetric flow and a 1^{st} order reaction. Neither of these assumptions are strictly true for CO oxidation, but since this derivation seeks to provide a means for the calculation of

conversions in other reactions, not just CO oxidation, the simple case of a first order reaction with constant volumetric flow will be instructive without introducing unnecessary complication. The basic equation for conversion, χ, is (Compton et al., 1985),

2-1 $$\chi = \frac{k\tau}{1+k\tau}$$

where $1/k$ is the average time required for a CO molecule to be converted and τ, the residence time, is the average time spent by a CO molecule in the reactor, (in this case, the ETEM cell). In this derivation, τ is calculated using properties of the ETEM cell, while k is calculated using both properties of the cell, and kinetic parameters obtained from analysis of the *ex-situ* reactor data.

The residence time τ is easily calculated by dividing the volume of the cell, V_{cell}, by the total volumetric flow rate into the cell, F_{tot}. F_{tot} , (in units of cm^3/s) can be calculated from the standard flow rate into the cell F_{tot}^s in standard cubic centimeters per minute (sccm) by the following equation:

2-2 $$F_{tot} = \frac{F_{tot}^s}{60}\frac{P^s}{P_{cell}}$$

In this equation, P_{cell} is the cell pressure, P^s is the standard-state pressure (1 ATM = 760 Torr), and the factor of 60 converts from minutes to seconds. The residence time is thus:

2-3 $$\tau = \frac{60P_{cell}V_{cell}}{F_{tot}^s P^s}$$

As mentioned above $1/k$ is the average time (in seconds) for a CO molecule to be converted; thus k is an effective turnover frequency (in s^{-1}) for CO. This is a thermally activated process and can be written in terms of an Arrhenius equation as:

2-4 $$k = A_A e^{\frac{-E_a}{RT}}$$

where R is the gas constant (in eV/K), T is the temperature in K, E_a is the activation energy (in eV), and A_A is an attempt frequency describing how often a CO molecule reaches a catalytically active site. This attempt frequency requires some careful consideration. In an archetypal CSTR, the reactants spontaneously react together, or the reaction is catalyzed using a homogeneous catalyst. This is not the case here; in the ETEM cell, only a very small region of the cell contains the catalyst. Gas molecules in all locations outside the pellet have an incredibly small probability of reacting. Thus, the attempt frequency cannot be the same attempt frequency observed in the plug-flow geometry. Instead a "time-averaged" attempt frequency A_A is used, which is related to the attempt frequency, A, within the pellet by the volume fraction of the pellet within the cell, V_f. This is because the average time a gas molecule spends within the pellet (during which it has a reasonable chance to be converted) is simply the residence time in the cell divided by the volume of the cell, and multiplied by the volume of the pellet, V_{OP}. Thus, the time-averaged attempt frequency A_A is simply:

2-5 $$A_A = A * V_f = A * \frac{V_{OP}}{V_{cell}}$$

The attempt frequency within the pellet itself is not identical to that within the plug-flow reactor, since the density of catalyst particles is different within the plug-flow bed and within the pellet. This should be taken into account. It should also be noted that the attempt frequency is itself a function of temperature, with a $\sqrt{T}$ dependence which arises from the velocity distribution predicted by the kinetic theory of gases. Thus, denoting the attempt

frequency derived from fitting the data from a plug-flow reactor as A_0, the attempt frequency in the pellet is:

2-6 $$A = A_0\sqrt{T}\frac{\rho_{OP}}{\rho_{PFB}} = A_0\sqrt{T}\frac{M_{OP}V_{PFB}}{M_{PFB}V_{OP}}$$

where ρ_{OP} and ρ_{PFB} are the densities of catalyst in the *operando* pellet and plug-flow bed respectively; M_{OP}, M_{PFB} and V_{OP}, V_{PFB} are the masses of catalyst powder in the *operando* pellet and plug flow bed, and their volumes.

Combining equations 2-2 to 2-6 yields:

2-7 $$k\tau = A_0\sqrt{T}\frac{M_{OP}V_{PFB}}{M_{PFB}V_{OP}} * \frac{V_{OP}}{V_{cell}}e^{\frac{-E_a}{RT}} * \frac{60P_{cell}V_{cell}}{F_{tot}^{S}P^{S}}$$

V_{cell} and V_{OP} cancel out in this equation, and we are left with:

2-8 $$k\tau = A_0\sqrt{T}\frac{M_{OP}V_{PFB}}{M_{PFB}}e^{\frac{-E_a}{RT}} * \frac{60P_{cell}}{F_{tot}^{S}P^{S}}$$

This can be input into equation 2-1 to yield the conversion in terms of known values. The attempt frequency in the plug-flow reactor A_0 and the activation energy E_a can be obtained by fitting turnover frequency data from a plug-flow reactor experiment using the functional form:

2-9 $$\sqrt{T}A_0e^{\frac{-E_a}{RT}}$$

It should be noted that the $\sqrt{T}$ dependence has not been accounted for in Figure 2-7, where the standard Arrhenius form has been used. The activation energies given in Table 2-1 and Table 2-2 are also calculated without the $\sqrt{T}$ factor.

All other parameters in equation 2-8 are known, measurable quantities. Values for these known quantities at 200 °C and under the conditions of the *operando* experiment summarized in Figure 6-6 are given in Table 2-3. The ETEM conversion obtained using

these values at 200°C is 35% and at 300°C is 98%. The *ex-situ* data used to calculate these numbers is the Pre-Reduced Up 2 data in Figure 2-4.

2.4. Summary

For this work a Ru catalyst supported on amorphous silica spheres was produced from simple reagents. The catalyst was studied in an *ex-situ* reactor using gas chromatography to quantify CO conversion; the high activity of the catalyst was confirmed, and a hysteresis in the conversion observed when the sample was reduced. The reduced sample was much more active than the same material oxidized prior to reaction. Kinetic parameters were derived from these experiments, and used to estimate the conversion expected in the differentially-pumped environmental TEM.

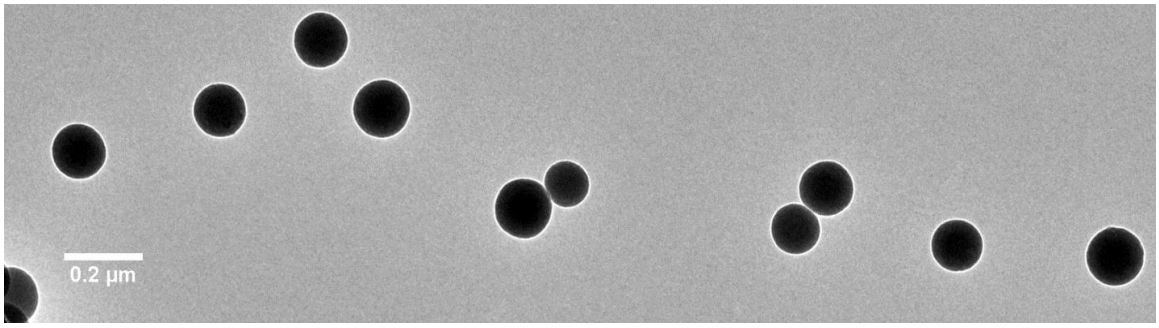

Figure 2-1 SiO_2 Spheres. A low magnification image of silica spheres on a continuous carbon film. The spheres are all round and the size distribution is narrow.

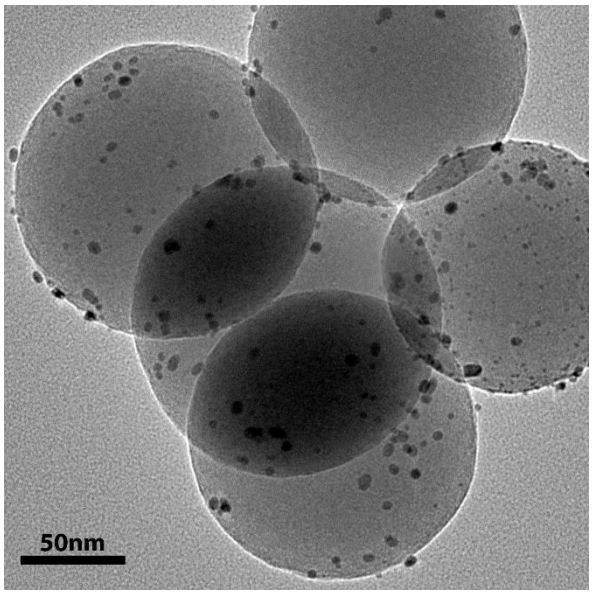

Figure 2-2 Ru-SiO_2. Low magnification image of the amorphous silica sphere supported Ru catalyst, showing the good dispersion of the Ru particles.

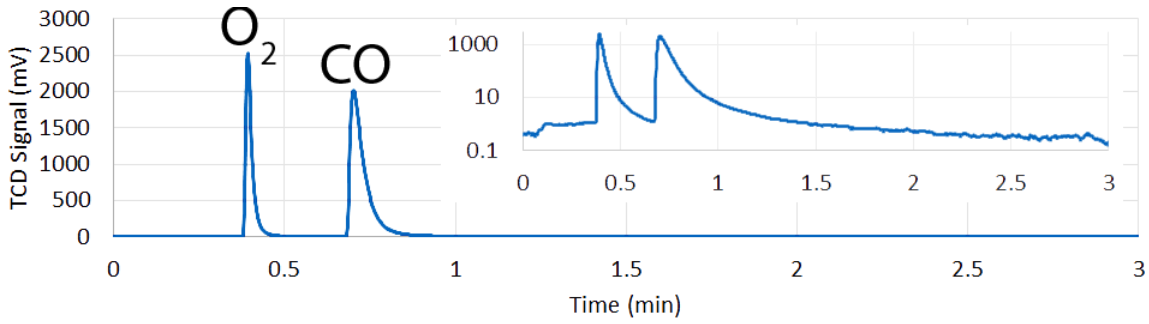

Figure 2-3 GC Raw Data. Raw data from the gas chromatograph used in the *ex-situ* experiments, showing a peak from CO and from O_2. The inset shows the same spectrum on a log scale, so that the background signal is visible.

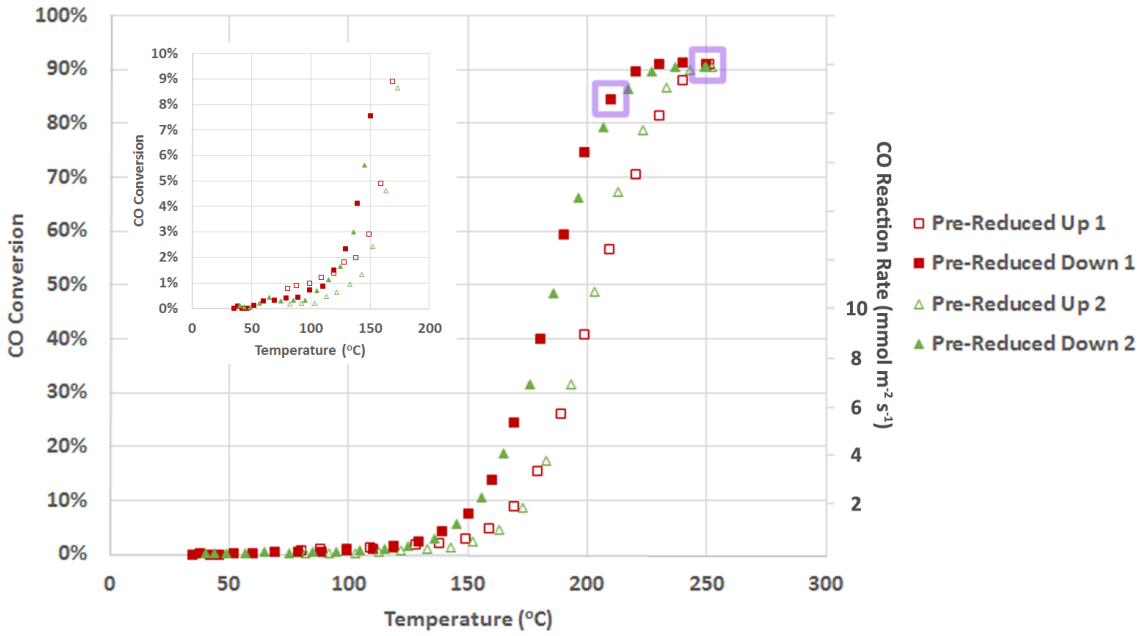

Figure 2-4 *Ex-Situ* Conversion. Reduced Catalyst. Results from the *ex-situ* experiment in which the Ru catalyst was heated to 250°C and then cooled to room temperature before repeating the ramp up and down again. The inset shows the conversions less than 10% at a different scale for clarity. The left axis gives the CO conversion, while the right axis gives the reaction rate up to only 50% conversion (see text). The data points boxed in purple were taken 40 min apart.

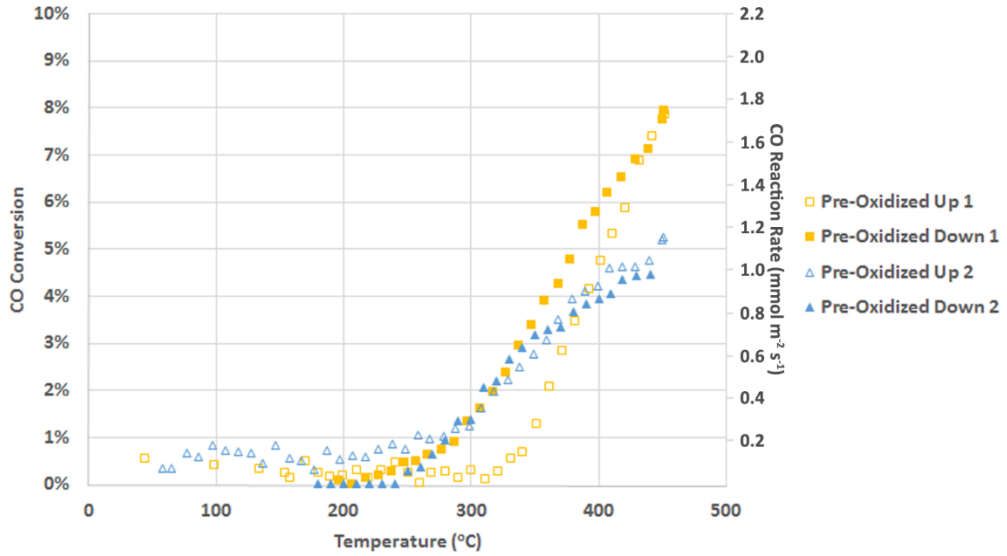

Figure 2-5 *Ex-Situ* Conversion. Oxidized Catalyst Results from the *ex-situ* experiment in which the Ru catalyst was heated to 450°C and then cooled to room temperature before repeating the ramp up and down again. The right axis gives the reaction rate, while the left axis gives the CO conversion. Note that the conversion scale has a maximum of 10%.

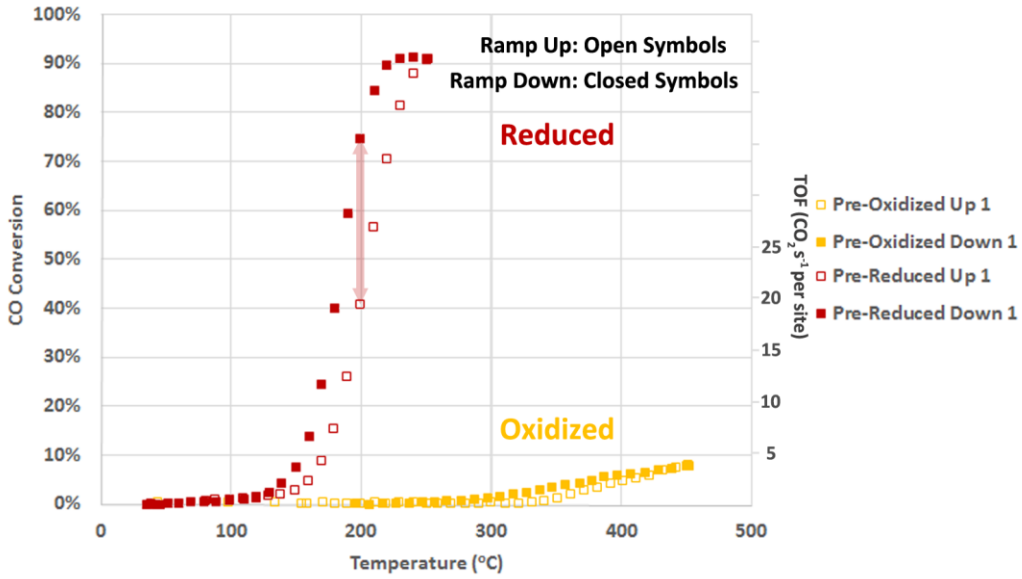

Figure 2-6 *Ex-Situ* Conversion Data. The first ramp up and down for both the reduced (Figure 2-4) and oxidized (Figure 2-5) samples are compared, showing clearly the superior activity of the reduced sample. The right axis gives the turnover frequency (TOF) in terms of CO_2 molecules produced per second per surface Ru atom up to only 50% conversion (see text).

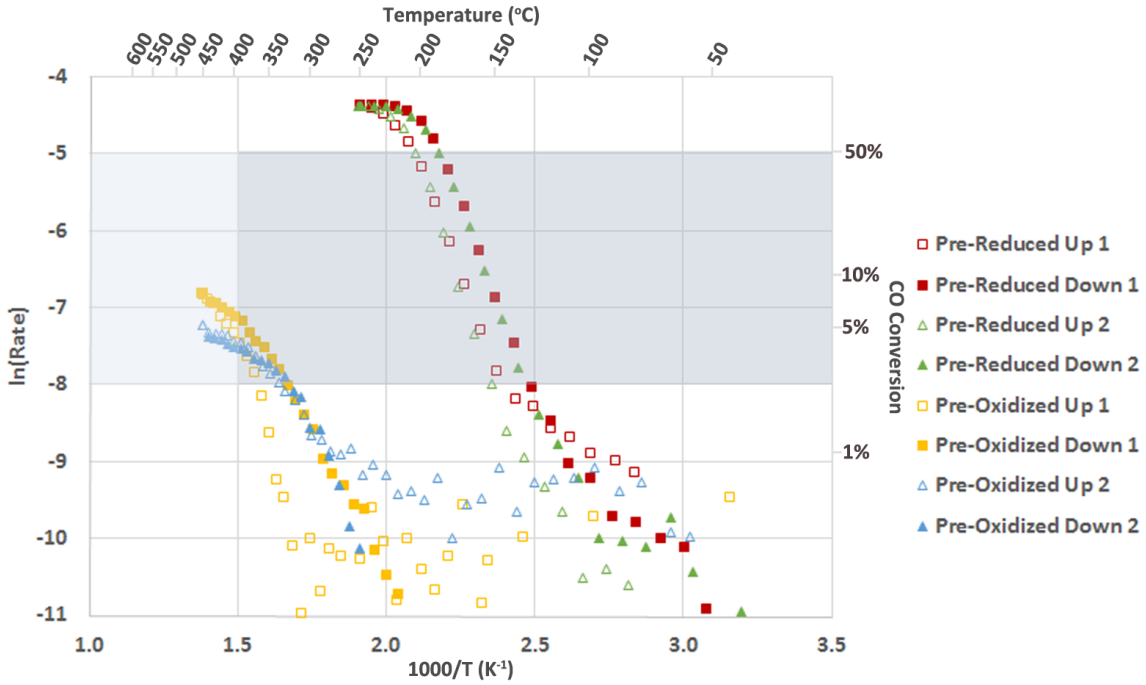

Figure 2-7 *Ex-Situ* Arrhenius Plot. The reactor data given in Figure 2-4 and Figure 2-5, in an Arrhenius plot. Data within the dark gray region were used to obtain the activation energies given in Table 2-1, while data within the light grey region were used for the activation energies given in Table 2-2. The rate here is in mol m^{-2} s^{-1} The right axis gives the CO conversion on a log scale.

Table 2-1 *Ex-Situ* Activation Energies Below 400°C.

	Pre-Reduced (Up)	**Pre-Reduced (Down)**	**Pre-Oxidized (Up)**	**Pre-Oxidized (Down)**
Ramp 1	0.92 eV	0.91 eV	0.66 eV	0.40 eV
Ramp 2	1.05 eV	0.88 eV	0.33 eV	0.19 eV

Table 2-2 *Ex-Situ* Activation Energies Above 400°C.

	Pre-Oxidized (Up)	**Pre-Oxidized (Down)**
Ramp 1	0.43 eV	0.23 eV
Ramp 2	0.14 eV	0.14 eV

Table 2-3 CSTR Equation Symbols. Symbols used in the derivation of equation 2-8, with their units; numerical values are also supplied for all quantities appearing in the final equation, 2-8. The *ex-situ* data used to calculate the plug flow (PF) numbers is the Pre-Reduced Up 2 data in Figure 2-4.

Symbols	**Units**	**Plug Flow/ETEM**	**Values (200°C)**
$\boldsymbol{A, A_A}$	s^{-1}	PF,ETEM,ETEM	$6.5 * 10^{10}$,-,-
$\boldsymbol{A_0}$	$s^{-1}K^{-1/2}$		
T	K	ETEM	473
$\boldsymbol{M_{OP}, M_{PFB}}$	mg	ETEM,PF	0.2, 1
$\boldsymbol{V_{OP}, V_{PFB}, V_{cell}}$	cm^3	ETEM,PF,ETEM	-,1.1,-
$\boldsymbol{E_a}$	eV	PF	1.02
$\boldsymbol{P_{cell}, P^s}$	Torr	ETEM	2.7,760
$\boldsymbol{F^s_{tot}}$	sccm	ETEM	1.43
$\boldsymbol{F_{tot}}$	cm^3/s	ETEM	-
$\boldsymbol{V_f}$	-	ETEM	-
$\boldsymbol{k}$	s^{-1}	ETEM	-
$\boldsymbol{\tau}$	s	ETEM	-
$\boldsymbol{\chi}$	-	ETEM	-

3. *Operando* Experimental Technique

3.1. The *Operando* Challenge: Quantifying Product Gases in the ETEM

Linking catalyst structure to catalytic performance is a primary objective to advance the science of heterogeneous catalysis (Rodríguez et al., 2013; Thomas and Thomas, 2015). To accomplish this, one must know the structure of a working catalyst when it is catalyzing a reaction. *In-situ* TEM techniques attempt to solve this problem by imaging the sample while subjecting it to conditions that simulate a reactor (Crozier and Hansen, 2015; Hansen and Wagner, 2014; Parkinson, 1989; Su et al., 2015). During *in-situ* experiments, the conditions within the microscope may be different from conditions present in *ex-situ* reactors. Additionally, the temperature and gas composition inside the ETEM cell are sometimes not accurately known (Crozier and Chenna, 2011; Vendelbo et al., 2013). If the conditions are not precisely known or controlled, a catalyst which may be assumed to be active may actually be inactive and the link between catalyst structure and performance will be ambiguous. To address this problem it is necessary to measure the catalyst relative activity throughout the *in-situ* experiment. This is the goal of *operando* TEM. In an *operando* experiment, the gas composition within the microscope is measured (Chenna and Crozier, 2012b; Miller and Crozier, 2014). This decreases the uncertainty regarding the gas composition around the sample. More importantly, it makes it possible to follow the course of the reaction, monitoring the changes in catalyst activity and structure simultaneously. Now the ensemble of structures observed in the TEM is unambiguously active for the reaction being studied whenever the expected gaseous products are observed. The

correlation between the relative catalyst activity and the catalyst structure will now be much tighter.

A typical 3 mm TEM grid used for observing powder TEM samples has a very low surface area over which to disperse a catalyst powder, and the minute amount of catalyst inside the microscope will yield a correspondingly small number of product gas molecules (Chenna and Crozier, 2012b). In a windowed cell setup, it may be possible to detect this small number of product gas molecules in the outlet flow from the holder, since the total volume of gas is quite small, and nearly all the gas contacts the catalyst sample (Vendelbo et al., 2014a). In a differentially-pumped environmental TEM (ETEM) (Crozier and Chenna, 2011) however, the reactant-gas flow is much larger, so the partial pressures of product gases will be smaller for the same amount of catalyst. If these partial pressures are near the detection limit of the equipment used to measure the gas composition, it will be difficult to accurately measure the catalyst's changing activity. A simple solution to this problem is to increase the amount of catalyst present in the TEM, so that an easily quantifiable amount of product gas is produced. This can be accomplished by dramatically modifying the sample preparation procedure (Miller et al., 2015). With significantly higher partial pressures of product gases, both mass spectrometry and electron energy-loss spectroscopy may be used to measure the gas composition in the ETEM cell. This will be explained in detail below.

3.2. Existing Methods

Some of the experimental framework necessary to perform *operando* TEM already existed at Arizona State University prior to the beginning of the present work. This will be

recounted here. Section 3.3 will go on to describe the additional developments which were accomplished as a part of this work to achieve fully functional *operando* experiments. It should be noted that the development of *operando* TEM at ASU was begun on the Tecnai ETEM, used for years at ASU for *in-situ* experiments, but modified as part of this work to facilitate *operando* TEM. However, one and a half years into this project, a new aberration-corrected Titan ETEM was delivered to ASU, which necessitated many changes to the experimental methods and some additional instrumentation setup. This chapter will not describe experimental results; descriptions of the experiments themselves, the analysis methods used on the TEM data, and the conclusions obtained from the results will be given in Chapters 4, 5, and 6.

3.2.1. Existing Control and Monitoring of ETEM Conditions

In a successful *operando* experiment, several conditions must be precisely controlled, including the temperature, gas pressure, and inlet gas composition. Methods for controlling all these conditions on the Tecnai ETEM were already in place when the work was begun.

The temperature in the Tecnai was controlled using a Gatan furnace-style heating holder. The furnace body is covered in Ta, which does not catalyze the CO oxidation reaction, and can withstand high temperatures if the gas environment is not oxidizing. The sample is held in place with an externally-threaded hex ring, which screws into the internally-threaded body of the furnace. An image of the holder taken from the Gatan website is shown in Figure 3-1. A cutaway diagram of the holder furnace is seen in Figure 3-2. A similar holder with an Inconel furnace body is also available from Gatan, but the Inconel alloy contains nickel which can form Ni carbonyls when exposed to CO, especially

at the moderate temperatures around 200°C used in the CO oxidation experiments (Brynestad, 1976). This is a serious issue, as described in more detail in section 3.3.2. MEMS (micro-electro-mechanical-systems) based holders were not used, despite their decreased thermal drift (Allard et al., 2012, 2009; Creemer et al., 2010, 2008), because the amount of sample material that can be heated using these holders is small. This would undermine our unique sample preparation method, described in section 3.3.1, and would thus make *operando* TEM in the differentially-pumped Titan difficult,. The same Ta heating holder was used for both the Tecnai and Titan experiments.

The pressure in the Tecnai experiments was measured using two Edwards Baratron© capacitance manometers, which are designed to handle two different pressure ranges relevant to ETEM work. The pressure was controlled using a leak valve which allowed a controlled amount of gas to flow from part of the vacuum system held at high pressure (~0.5 bar) to the sample chamber, which was thus maintained at a much lower pressure, usually around 2 Torr. The problem with this system for controlling the pressure is that the high pressure was not maintained at a constant value, but rather decreased over time. Any change in the pressure on one side of the leak valve affected the pressure on the other side, so the pressure in the ETEM cell was not constant during lengthy experiments. Since the thermal conductivity and heat capacity of a gas are pressure dependent, the decreasing pressure led to a slow increase in the temperature of the holder and specimen, causing constant thermal drift over the course of each ETEM experiment. The problem of decreasing pressure could have been overcome by simply keeping the mixing tank pressure linked to atmospheric pressure. If the mixing tank was instead a “mixing bag” in which the volume of the tank was variable, but the pressure always 1 bar, this would have eliminated

the consistent pressure drop over the course of a long experiment. This solution was not attempted, since all work was instead switched to the Titan, for which a new gas handling system was designed (see section 3.3.2).

The gas composition in the Tecnai experiments was controlled in a simple and inexpensive way, which introduced several problems. The heart of the mixing system on the Tecnai was a steel mixing tank, with a volume of approximately 1 liter. This tank was connected via flexible bellows to 5 different gas tanks. Two gases could be mixed by simply filling the tank to a desired pressure using one gas, and then adding a second gas until the appropriate pressure was achieved for the desired mixture. By the same method, up to 5 different gases could be mixed. While an accurate initial mixture could be obtained by carefully following this method, over time the leak valve separating the high pressure mixed gas from the ETEM chamber would allow one gas through more quickly than the rest (Johnsen and Chatterjee, 2011); this gas species became depleted in the tank mixture over time. Thus, the gas composition flowing into the environmental cell of the TEM changed gradually over time. This problem is inherent to the flow of a gas mixture through a small orifice, and cannot be overcome without a complete redesign of the system (this was done for the Titan; see section 3.3.2).

3.2.2. Existing Measurement of Products using Mass Spectrometry

The Titan ETEM was delivered with a built-in RGA (residual gas analyzer), with modern software for computer controlled acquisition. The RGA is capable of collecting gas from two different locations in the Titan vacuum as seen in Figure 3-3. In this figure, it can be seen that opening Vrga1 samples gas from near the gas inlets to the ETEM, while

opening Vrga2 samples gas directly from the ETEM cell, close to the sample. A “sniffer tube” is used, so that the gas can be sampled very close to the sample holder inside the ETEM cell. The exact location of this tube can be seen in the first figure of (Mortensen et al., 2015). Regardless of the source for the RGA, the gas must first pass through a leak valve, which allows the vacuum surrounding the RGA to be maintained, by dedicated pumps, at a lower pressure than the source from which the gas is drawn. This is essential, since the RGA must be operated at low pressures (O’Hanlon, 2003).

The RGA software, Quadera, used in the Titan allows continuous monitoring of a large number of mass to charge ratios. In this work, integer ratios from 1 to 50 were monitored. Each ratio was measured approximately once every 10 seconds, and can be measured continuously for many hours. Only a few of these mass to charge ratios were usually analyzed in detail, as seen in Figure 3-4. CO conversions can be estimated from RGA data by first subtracting a background, (the RGA signal before gas is admitted to the reaction cell, or prior to reaction) and then simply taking the ratio of the signals from CO and CO_2, divided by known standard ionization cross sections (O’Hanlon, 2003).

For a 50-50 mixture of CO and CO_2, this method was quite effective, as seen in Figure 3-21 reproduced from (Miller and Crozier, 2014) and described in detail later. However, this apparently satisfactory result may have been somewhat fortuitous because the mass spectrometry technique using the RGA is one that introduces significant complications to quantification. Though it is extremely sensitive to small quantities of gas molecules, if a molecule of oxygen were to be doubly ionized, or split into two oxygen ion fragments, with one charge each, the resulting species would be seen at a mass of 16 amu. This is the same mass as a methane molecule, and this example underscores one of the primary deficiencies

of this technique, namely that the signals from different gas species sometimes overlap completely. Most notably for our experiments, CO and N_2 have an identical mass of 28, and are thus difficult to distinguish, leading to an overestimate of the CO concentration. The simple method employed here is to subtract constant background values, obtained when no gases are admitted to the ETEM, from each of the experimental peaks. A more thorough treatment of this peak overlap issue would require reference spectra to be taken for all the gases present in the system, so that a linear combination fit to the experimental data could be obtained (O'Hanlon, 2003). This was never attempted. Additional issues affecting the accuracy of the RGA technique will be discussed in section 3.3.5 where the experimental details behind Figure 3-21 will be explained in detail. The sensitivity of the RGA hardware is quite high, as can be seen in the raw spectrum of Figure 3-5, where peak intensities 3 orders of magnitude smaller than the largest peak can be clearly seen. This sensitivity can be further increased for the Titan RGA, since it is equipped with a secondary electron multiplier detector (O'Hanlon, 2003). However, this instrumental sensitivity is not equivalent to the sensitivity to any particular gas, since most peaks result from a combination of several different gas species, and the problems arising from this overlap become more pronounced for quantification of gases present in very small quantities.

3.2.3. Existing Measurement of Products using EELS

In addition to measuring the gas composition using mass spectrometry with an RGA, the gas composition can also be measured using electron energy-loss spectroscopy (EELS). The basics of the technique for this quantification was already described in (Crozier and Chenna, 2011) before this work began. Inside the TEM, electrons can scatter off a deeply

bound inner-shell level or more loosely bound valence-shell electrons of both the TEM sample and any gas present in the cell. The energy lost by the fast electron will be determined by the type of excitation taking place. By collecting and analyzing the energy spectrum of the transmitted electrons using a suitable spectrometer, (see Figure 3-6) detailed information about the composition and bonding in the sample or gas can be obtained. A detailed description of general EELS theory and instrumentation will not be given here, as this has recently been covered in a chapter on spectroscopy by Crozier and Miller published in a 2015 Springer book on environmental TEM (Hansen and Wagner, 2015). Even more detail on electron scattering theory, energy loss spectroscopy instrumentation and data analysis can be found in the references therein (Egerton, 2007, 1978; García de Abajo and Aizpurua, 1997; Howie and Walsh, 1991; Inokuti, 1971; Johnson and Spence, 1974; Leapman et al., 1980; Raether, 1967), and in the comprehensive book by Egerton (Egerton, 2011).

The basic physics of the interactions of a fast electron with atoms in a solid and with atoms in a gas are similar, but there are several practical differences relevant to the conditions in the ETEM.

First, at the (low to atmospheric) pressures used in ETEM, individual gas molecules have negligible electronic interaction with each other, and can be assumed to be independent entities. This means that the signal obtained from a single gas molecule in a gas mixture will be indistinguishable from that obtained from the single gas molecule in isolation. This contrasts sharply with the behavior seen for atoms or molecules in solids or liquids, whose electronic interactions cause changes in the fine-structure of the core-loss

EELS edges, as well as the long-range interactions which are probed in the plasmon peaks of the valence-loss region of the spectrum.

Second, for a differentially-pumped environmental TEM, electrons undergoing identical inelastic scattering processes at the top and bottom of the gas cell several millimeters apart may follow very different trajectories through the objective lens and the lower section of the TEM column. This will give rise to a difference between the fraction of inelastically scattered electrons entering the spectrometer (Crozier and Chenna, 2011). For example, if the C and O core-loss edges from CO gas are observed, a larger fraction of the C than of the O signal is collected resulting in a systematic error in the relative collection efficiencies of the two edges. The effect is likely to be largest for larger angle scattering events and the magnitude of this effect should be smaller when smaller collection angles are employed. Acquisition of core-loss spectra of gases should therefore be performed with small collection angles. If small collection semiangles are employed (a few mrad), gas compositions can be determined using standard atomic cross sections to within 5-10% (Crozier and Chenna, 2011). If reference spectra of single gases are acquired, and these are used to determine empirical cross section ratios, the results may be more accurate. This may not be an issue for holder-based ETEM cells, in which the gas is confined to a thin layer near the eucentric height of the microscope.

Electron energy-loss spectra of gases may be acquired and quantified from both the core-loss and valence-loss (low-loss) regions (Crozier and Chenna, 2011; Miller and Crozier, 2014).

In the valence-loss region, every gas molecule has its own distinctive signature from 5 to 25 eV loss. A series of low-loss spectra from a few different permanent gases from (Crozier

and Chenna, 2011) is shown in Figure 3-7. These spectra show significant differences both in the number and location of the peaks present and quantification is straightforward for these gases. These signals overlap, but since the component gases present in the gas mixture are usually known, it is simple to determine the molar concentrations. The valence-loss spectrum from the gas mixture can be expressed as a linear combination of the individual component gas valence-loss reference spectra. Since reference spectra are used to quantify an experimental spectrum, it is essential that the experimental data be acquired under electron-optical conditions identical to those of the reference spectra. For suitably normalized spectra, the weighting coefficients in the linear combination can be directly related to the molar concentrations of the components by the following equation for two gases, which is derived in (Crozier and Chenna, 2011).

3-1
$$\frac{a}{b} = \frac{\alpha\left(\frac{\lambda}{t}\right)_A P_A}{\beta\left(\frac{\lambda}{t}\right)_B P_B}$$

This approach is easily extended to mixtures of several gases. The equation is valid for two gases provided the scattering parameters are small and plural scattering is similar in all the spectra employed for the analysis. To achieve these requirements for low-loss spectra, the gun lens of the Tecnai was set to 5 and the extraction voltage to 3500. The spot size was set to 1 with the usual condenser aperture. Low-loss spectra were acquired with the microscope in image mode. The illumination convergence was set so that at 8700x magnification the beam spot was the size of the small circle on the viewing screen. The entrance aperture of the EELS spectrometer was set to 2 mm and the dispersion to 0.05 eV. The acquisition time used was 4 s. With such a long exposure time, the zero loss peak must be shifted off the detector to prevent saturation. The collection angle is limited to 50 mrad

by the lower differential pumping aperture of the environmental cell. These conditions were only slightly modified from those used for the original published article on EELS of gases in the ETEM (Crozier and Chenna, 2011).

In the core-loss region of the EELS spectrum from a gas, individual edges corresponding to the elemental components of the gas are observed, and these can be quantified in a similar manner to that usually employed for core-loss EELS of solids. However, it must be emphasized that, as mentioned above, the large difference in position between a gas molecule at the top and at the bottom of a differentially-pumped cell can cause significant problems with quantification unless a sufficiently small collection angle is used (Crozier and Chenna, 2011). Additionally, more intensity is needed for the core-loss EELS than the low-loss, so the TEM was set to diffraction mode in order to get as many electrons as possible through the EELS entrance aperture. The conditions used for the Tecnai were only slightly adapted from those used in prior work. The gun lens was 5 with an extraction voltage of 4100. The spot size was 1 with the usual condenser aperture. An entrance aperture of 2 mm was used with a dispersion of 0.05 eV and an acquisition time of 4s. The convergence and collection semiangles were 2.4 and 2 mrad respectively.

The low-loss and core-loss EELS techniques used to quantify gas mixtures each have advantages and disadvantages, depending on the gases being analyzed. In the application of this technique to CO oxidation experiments, the core-loss spectra are easily quantified, since the π^* peak of the C K-edge from CO and CO_2 are close together, but not overlapped; thus, this technique was used for all the *operando* CO oxidation experiments. The low-loss technique is quite versatile however, since any mixture of gases can be analyzed over the same small energy range. Additionally, for quantification of mixtures containing hydrogen

gas, the low-loss region must be used since that is the region of the spectrum containing the H_2 edge.

3.2.4. Observation of Catalyst Structure

The structure of the supported Ru catalyst was observed using conventional phase contrast TEM. Techniques like STEM and electron diffraction were not used much, due to the nature of the sample and the experiments. STEM was not used because the catalyst particles observed in TEM were found to be dynamic, constantly changing orientation and position due to the weak interaction with their support (amorphous SiO_2). This weak interaction was ideal for elucidating the catalytic properties of Ru/RuO_2, however, since the support had little effect on the catalytic properties. Since the particles would move significantly during a STEM image acquisition, this would have resulted in significant artifacts at high magnifications. Additionally, both the Tecnai and Titan ETEMs were optimized for TEM imaging, and the STEM resolution of both microscopes is worse than the TEM resolution.

The SiO_2 support also made electron diffraction more difficult. Since electron diffraction averages over 3D space, it was less useful for samples like the silica-supported Ru which are predominately SiO_2. The silica accounts for 99.55% of the solid volume of the supported catalyst powder. Because of this, powder electron diffraction patterns of the material were dominated by a diffuse background from the amorphous support, as seen in Figure 3-8a. However, after subtracting a background from the patterns, and suitably combining the patterns from many individual frames (see section 4.2.2), a useful powder pattern can emerge, as seen in Figure 3-8c.

The majority of the structural data obtained from both the Tecnai and Titan ETEMs were conventional phase contrast images. The conditions used on the two microscopes were quite different (see Figure 3-9).

For the Titan experiments accelerating voltages of both 300 and 80 kV were used. When 80 kV was used, the monochromator was also used, because without this, the image resolution would be significantly reduced, since the temporal coherence is the limiting envelope function determining the maximum resolution of the microscope as seen in Figure 3-9b for the 80 kV condition. When an accelerating voltage of 300 kV was used, the monochromator is not needed to achieve high spatial resolution, as seen in Figure 3-9a. In fact, the spatial resolution is better at 300 kV than at 80 kV with the monochromator. The aberration corrector was always used on the Titan, and for all experiments described here, the spherical aberration was set to be slightly negative (between -10 and -30 μm), unless otherwise noted in the text.

The dose rate was carefully controlled during experiments on the Titan. This is essential for obtaining reliable results since the electron beam itself can change the catalyst, and observation of subtle changes to the catalyst during catalytic reactions is the goal of this work. The Titan microscope control software has a feature to calculate the beam dose rate (in $e/Å^2/s$) by exposing the small viewing screen to uniform illumination. This makes it easy to control the dose rate under any imaging condition and an effort was made to maintain the dose rate below 300 $e/Å^2/s$ ($0.5A/cm^2/s$) for all experiments. The dose rate used was sometimes lower than this. Additionally, to keep specimen charging by secondary electrons to a minimum, the total beam current passing through the ETEM cell was kept

low either by using the monochromator slit at 80 kV or by reducing the spot size using the first condenser lens at 300 kV.

For the Tecnai, the accelerating voltage was always 200 kV but the beam dose rate was not always well-controlled. It is clear from the weak phase-object approximation images in Figure 3-9c why the images from the Tecnai are inferior to those obtained on the Titan. Both the temporal coherence due to the energy spread of the electron beam and the spatial coherence mainly due to the spherical aberration of the objective lens are substantially worse than on the Titan ETEM, which is image corrected.

3.3. New Developments

3.3.1. Sample Preparation- Increasing the Amount of Catalyst in the TEM

The fundamental difficultly with *operando* TEM is that the amount of catalyst inside the ETEM is typically very small. This has been overcome through the development of a unique sample preparation procedure, which was described in some detail in a paper published recently (Miller et al., 2015).

The early paper by Chenna and Crozier (Chenna and Crozier, 2012b) on *operando* TEM of CO oxidation showed the way forward to overcome the limitation of a small amount of catalyst present in a traditional TEM grid sample. In this paper, the authors describe a method for sintering glass wool and then cutting out a small disk with a hole in the center to place in the TEM sample holder. While this was sufficient for a few proof-of-concept experiments, the danger of loose glass fibers falling inside the ETEM was serious, and there was no way to measure the amount of catalyst present in the sample, so that a

calculation of reaction rate was impossible; only catalyst conversions and relative reaction rates could be determined, which could not be compared to other experiments. Finally, these TEM samples did not include a conductive mesh grid, essential for high resolution imaging as explained below, and thus no high resolution images could be obtained.

The TEM sample developed for operando TEM as part of this work is a combination of two distinct samples, simultaneously loaded into a single TEM holder, as depicted in Figure 3-2. The first part of the sample is a metal mesh grid over which catalyst is dispersed. In the experiments described in this document the mesh was Ta unless otherwise noted. The second half of the sample is an inert porous *operando* sample pellet, made from Pyrex glass fibers, which is also covered with the same catalyst (CO conversion on the Pyrex and mesh was shown to be negligible). Both the grid and pellet must fit into the Gatan heating holder furnace described in section 3.2.1, which is only 0.75 mm deep.

To produce the Ta mesh part of the TEM sample, 3 mm round sections are punched out of a 100-mesh woven Ta mesh using a $1/8^{th}$ inch hole punch intended for paper crafts. This works well, though a few stray wires must sometimes be cut off after punching. To increase the electrical contact with the Ta holder, the Ta wire mesh grids are lightly ground using a 30 μm lapping film, removing some of the surface oxidation just prior to loading the grid with catalyst. The grid is loaded by crushing a bit of catalyst powder between 2 glass microscope slides and then rubbing the grid through the powder.

To produce the *operando* sample pellet, Pyrex fibers (about 80 microns in diameter) are first crushed in a small mortar and pestle so that the length of each fiber is on the order of a millimeter. This prevents self-alignment of fiber bundles, which was found to occur with long, uncrushed fibers. The crushed fibers are then packed into a 3 cm long quartz

tube whose inner diameter is 3 mm. The packed tube is then fired at 700°C for 3 hours, to initiate sintering of the fibers into a network. After cooling to room temperature, the resulting porous cylinder of networked fibers is pushed out of the quartz tube, and sliced into sections approximately 1-2 mm thick with a razor blade. One side of each section is ground flat with sandpaper before placing the section into a small jig designed for finishing the pellets. The jig, depicted in Figure 3-10a, consists of two steel parts with a 0.8 mm hole through the centers. One of the parts has a counter bore that is 0.6 mm deep to accommodate the pellet. The pellet is placed, flat surface down, inside this counter bore, and the rough surface is ground to the level of the steel with sand paper, leaving a 0.6 mm thick pellet. The steel pieces are then put together, and a 0.8 mm drill bit bores a hole through the pellet, guided by the steel parts to the exact center. The finished pellet is rinsed on a filter paper with nano-pure water to flush out any residual loose fibers. Loading catalyst onto the porous pellet is accomplished by impregnation using a suspension of the catalyst in water (see Figure 3-10b). Single drops of this catalyst suspension are impregnated into the pellet and allowed to dry before the next drop is added. The pellets are kept at about 80°C during this process to decrease the drying time between drops. The loading can be varied as needed, but for the present work was on the order of 20 µg of supported catalyst per pellet.

An *operando* pellet produced by the method just described is seen in Figure 3-10c. The pellets are approximately 3 mm in diameter and 0.6 mm thick, and weigh approximately 3 mg each, though there is some variation from one pellet to the next. The hole in the pellet is large enough that it does not place any additional restrictions on the maximum tilt angle achievable using the holder which is 35°. A typical Pyrex pellet has a porosity of about

70%, and thus good gas permeability. A typical Pyrex pellet also has a large surface area, which can be calculated by considering that the pellet is composed of cylindrical fibers of known density. The surface area of a cylinder SA (neglecting the end caps) is $2\pi rL$, while the mass m of the cylinder is $\pi r^2 L\rho$. Combining these two equations yields the surface area in terms of the mass m, fiber radius r, and density ρ.

3-2 $$SA = \frac{2m}{r\rho}$$

This approach gives a surface area of approximately 7 cm^2 (0.2 m^2/g) for the pellet which is composed of long, thin fibers (8 μm in diameter). This is about 50 times the surface area of a normal 200 mesh 3 mm TEM grid.

For *operando* experiments involving temperatures above 500°C, Pyrex glass fibers should not be used, but should be replaced by quartz fibers. Fabrication of a quartz pellet is similar to that of the Pyrex pellets, except that the quartz tube packed with crushed fibers should be fired at 1100°C for 2 hours, and the fibers must be crushed more finely than the Pyrex. Quartz pellets are also suitable for studying photocatalysts due to their superior UV light transmission.

While the pellet half of the sample is essential for increasing the amount of catalyst produced inside the TEM, the grid half of the sample is also vital to achieve atomic resolution imaging. This is because silica-supported catalyst particles, which were dispersed on the *operando* pellet, were challenging to image in the TEM, since the pellet fibers are insulating and charge under the electron beam. Even at room temperature in vacuum, the disruption to the optics was so severe that no lattice fringes could be seen within particles that were in contact with the fiber pellet. A "good" image of a silica-sphere-

supported particle on a fiber at room temperature is shown in Figure 3-11a. While the basic shape of the catalyst particle can be seen, no detail is discernable. Images are therefore acquired from supported catalyst particles dispersed on a metal mesh, rather than those on the fiber pellet. An image obtained from a mesh-supported particle in the Titan ETEM, at 480°C in 0.75 Torr H_2, is shown in Figure 3-11b. Imaging on the metal mesh significantly improves the image quality, and lattice fringes are visible, allowing for identification of the phase of the particle, which in this image is Ru.

We have introduced the *operando* pellet to increase the conversion inside the microscope, and this is effective, yet the silica-sphere-supported particles dispersed over a metallic mesh are the ones actually imaged. This setup necessitates that the conditions be nearly identical for both the supported catalyst dispersed over the mesh and over the pellet. The temperature difference between the fiber pellet, and the metal mesh should be relatively small since they are both inside the furnace of the Gatan heating stage which controls the temperature, and is known to produce a uniform region (Mortensen et al., 2015). The gas composition should also be virtually identical, because the gases within the TEM sample chamber appear to be well mixed.

Experimental evidence for a well-mixed composition was obtained by a simple experiment, summarized in Figure 3-12, using a pellet ground flat on 2 sides. Core-loss EELS was used to measure the gas composition at the center of the hole in a pellet during CO oxidation. The stage was then moved so that the gas composition was measured outside the pellet, beyond one of the ground edges. The gas composition measured with EELS was found to be identical in these two locations. This is an unlikely result unless the gas composition is approximately homogeneous around the sample. A hand-waving argument

could be made that since the EELS signal originates from the entire 5 mm gap between the pole pieces, that any lateral inhomogeneity in the gas composition close to the sample will be washed out by the gas near the pole pieces. This is incorrect. A simple calculation can show that if inhomogeneities did exist, they would not be washed out by integrating over the 5 mm pole-piece gap along the beam direction. MATLAB was used to numerically integrate a concentration gradient which could plausibly be formed as the result of catalysis occurring on pellet-shaped object as shown in Figure 3-13a. For simplicity, the composition at any point in space was assumed to have a $1/d^2$ dependence on the distance d from the nearest toroid surface (assuming a 1/d dependence instead did not affect the conclusion). For the positions marked in Figure 3-13b the integrated intensity is 5 times higher at point A than point B. Thus, if such a concentration gradient was actually present in the ETEM, this would be easily distinguished in the EELS spectra. Since the measured spectra are instead identical, the composition must not have a strong gradient, and the gas is well mixed within the cell. This allows the ETEM cell to be modelled as a continuous stirred-tank reactor, since gas continuously flows into and out of the ETEM cell and the composition is well mixed.

Several difficulties with the sample preparation arose which were never fully resolved. The first is that the reproducibility of the pellet production process was poor. The synthesis steps which were most likely responsible for this poor reproducibility are crushing the fibers and packing the quartz tubes with the crushed fibers. Ideally, all the fibers would be crushed to the same length, but this is never achieved, and sifting the fibers to decrease the range of lengths was not attempted. Packing the fibers into the quartz tubes is also somewhat subjective, and the packing density of the fibers depends on both the force with

which they are compacted in the tube, as well as the length of the crushed fibers being packed.

The second major problem with the pellets is that it was difficult to precisely measure the amount of catalyst loaded onto individual pellets. The mass of catalyst on a typical pellet was on the order of 0.2 mg. This was near the detection limit for the mass balance in our lab, which has a readability of 0.1 mg. Additionally, glass fibers sometimes fell off the pellet during the catalyst loading procedure, leading to underestimation of the mass of catalyst present on the pellet. The likelihood of this occurring was successfully reduced by washing the pellets prior to loading. This uncertainty in the mass of catalyst in each pellet led to a corresponding uncertainty in the catalyst activity during *operando* experiments. Importantly, this does not affect the accuracy with which relative activity over the course of a single experiment can be measured.

Despite these difficulties, the *operando* pellet sample successfully achieved its primary purpose, which was to increase the conversion inside the differentially-pumped ETEM enough so that this could be measured accurately with electron energy-loss spectroscopy. An early experiment demonstrating this is summarized in Figure 3-14. It is clear from a simple inspection of the data that significant conversion of CO to CO_2 took place as the temperature was increased from 150°C to 340°C. This data was analyzed using the linear combination method, and the results of this quantification are given in the inset of Figure 3-14, where up to 80% conversion is seen. This maximum conversion observed in the *operando* experiment was surprisingly high considering that the reactor geometry of the ETEM cell is complex, with a large volume of gas, and a small TEM sample, so that at any given moment, only a small amount of the gas is in contact with the catalyst.

Early in this work, it was concluded that the small size of the *operando* pellet relative to the entire ETEM cell made it unlikely that all the gas entering the cell would interact with the pellet. This has been found to be false. A thought experiment involving a simple probability can be used to show this. If a single molecule enters the ETEM cell, it can either hit the pellet at some point before exiting the cell, or it can first "hit" the orifice of one of the differential pumping apertures, at which point it has already exited the cell and cannot hit the pellet. The probability of the molecule hitting any surface in the cell is approximately proportional to the area of that surface, and the probabilities of the two options stated above must sum to 1, since there is no 3rd possibility. Therefore the probability of the molecule exiting the cell prior to striking the pellet, thus bypassing the catalyst is:

3-3 $$P_{Bypass} = \frac{A_{DPA}}{A_{DPA}+A_{Pellet}}$$

where A_{Pellet} is the exposed surface area of the pellet, which is approximately equal to the two flat (circular) sides of the pellet, which has a diameter of 3 mm. A_{DPA} is the area of the two differential pumping apertures which are 200 μm in diameter. This gives a P_{Bypass} of 0.4%, so over 99% of the gas entering the ETEM cell will contact the catalyst pellet.

The purpose of the unique *operando* sample preparation was to increase the catalyst surface area inside the ETEM, so that significant conversion would take place. This was clearly effective. While the pellet solution was effective, other groups around the world have attempted other methods to measure the gas composition, and thus the relative catalytic activity, inside an ETEM. Currently, the most popular method is to use mass spectrometry with windowed cell holders (Vendelbo et al., 2014a). The windowed cell

holder approach can be successful because the flow rate of gas into the cell is very small. Even with a small amount of catalyst, high conversions can thus be achieved using this method. However, both EELS spectra and TEM images will contain a background signal from the window material, making analysis of both more difficult. Another approach (Li et al., 2015) is to flow the gas exiting a windowed cell holder through an additional catalyst bed, maintained under identical experimental conditions as the sample inside the windowed cell holder. This bed can contain substantially more catalyst, so that the total conversion is dramatically increased. It remains to be seen whether one of these approaches, or the approach used in this work will become standard practice for *operando* TEM.

3.3.2. Advances in Control and Monitoring of ETEM Conditions

Prior to this work, the temperature and pressure were measured continuously during experiments on the Tecnai, but this data was not continuously recorded. Measurements were noted by hand, and detailed data was not available. Interfacing the old measurement devices to a computer would not have been a simple task, so after a brief unsuccessful attempt, a different approach was taken. A webcam was used to record the temperature and pressure inside the cell. Image frames were recorded at set intervals, (usually every minute) with embedded timestamps. If an experiment was successful, these images were collected, and the temperature over time was manually input into Excel, for correlation with RGA and EELS data. The same procedure was followed on the Titan for recording the temperature, while the pressure was logged electronically.

Switching to the Titan ETEM provided an opportunity to overhaul the design of the gas mixing system. The microscope includes 3 gas inlets, each with its own leak valve.

However, the inlets are not designed for mixing gases, and in fact, the 2 so-called reactant gas inlets cannot be simultaneously opened to mix two reactants. This means that any precise mixing must be done first, before flowing gas into the TEM. A gas handling system was therefore designed, with some input from Jimmy Liu and Peter Crozier, and built with help from other graduate students. The system design is described in detail in Appendix IV. Briefly, the system consists of 2 mass flow controllers (MFCs), which are each attached to 3 gas cylinders. The MFCs flow gas into a small mixing chamber, which is then connected to all 3 gas inlets on the ETEM (a single inlet is used for any given experiment).

The pressure within the Titan was controlled by maintaining a constant flow of gas into the microscope using the MFCs. The flow rate required to maintain 1 Torr of pressure in the environmental cell was different for each gas species. Thus, a calibration of each species is required. This has been completed for several gases, as shown in Figure 3-15. Additional gases can be calibrated by flowing a set flow rate, waiting ~20 min for the pressure to reach equilibrium, recording the pressure achieved and repeating the procedure with a higher flow rate until enough data is gathered to produce an accurate parabolic fit as seen in the inset of Figure 3-15.

The gas composition within the ETEM cell of the Titan was also controlled using the MFCs. The desired partial pressures inside the cell were converted into flow rates using the calibrations previously obtained, and the MFCs were set to these flow rates. Once an equilibrium pressure was reached, the composition and pressure in the cell should be constant for as long as necessary, unlike in the Tecnai system where both the pressure and composition varied over time. More detail about the MFCs can be found in Appendix IV.

An additional concern for both the Tecnai and the Titan gas systems was carbonyl contaminants in the CO gas. When Ni or Fe are exposed to CO gas it is possible to form Ni or Fe carbonyls (Brynestad, 1976). These molecules are composed of a single metal atom bonded to several CO, and are a gas at room temperature. At elevated temperatures, like those found at the catalyst, the carbonyls can decompose, depositing the metal atom, and eventually growing particles. This impurity must therefore be removed from the gas stream entering the ETEM. This was done with a series of two filters. First, a commercial activated carbon filter was used. After this, a custom filter was produced for this work, consisting of a ¼ inch quartz tube filled with a mixture of high surface area fumed silica and quartz wool. The wool was necessary to maintain a low density in the powder under vacuum with enough porosity so that gas could still flow. This tube was heated to 200°C (the ideal temperature for carbonyl decomposition (Brynestad, 1976)) to decompose residual carbonyls which passed through the carbon filter. A similar filter was kept at liquid nitrogen temperatures by Peden and Goodman (Peden and Goodman, 1986), though this would only trap, rather than decompose, the carbonyl molecules.

3.3.3. Advances in Measurement of Products with Mass Spectrometry

A residual gas analyzer (RGA) was used to perform mass spectrometry on the gases present in the Tecnai vacuum system during the *operando* experiments. Prior to the start of this work, an RGA was sitting in the room, but was inoperable, and some modification to the Tecnai vacuum system was required. The RGA was a Pfeiffer Prisma QMA 200, a quadrupole mass spectrometer, which uses an electron beam to ionize gas molecules passing through it, and then accelerates the resulting charged species through a set of

quadrupoles. The ions are separated according to their mass-to-charge ratio (m/z) and the ion currents are measured using a Faraday cup.

The modified vacuum setup created for the RGA is shown in Figure 3-16. This required the addition of a small turbo pump dedicated to the RGA. To maintain the high vacuum necessary for its operation, the RGA was placed behind a leak valve, and was pumped by the dedicated turbo-pump to a vacuum less than 10^{-4} Torr. A bellows, weighted down with sand bags was placed between the microscope and the RGA to damp out vibrations arising from the fan which cools the RGA electronics. The dedicated turbo pump was placed in an adjacent room to minimize its impact on the microscope resolution. This setup allowed the RGA to be operated close to a pressure of 10^{-4} Torr which is near the upper pressure limit for the instrument by adjusting the leak valve appropriately for each experiment, yielding a high signal-to-noise ratio in the data.

The RGA on the Tecnai was computer controlled using its original windows software, which, unlike the Titan RGA software, was quite old and not user-friendly. Due to software constraints, analog data, like that shown in Figure 3-5 could not be continuously recorded and saved. Instead, the RGA was set to measure the amplitude of 15 different mass-to-charge ratio peaks approximately every 10 seconds, rejecting the rest of the mass spectrum. This was generally sufficient for this work. The methods for analyzing the data from the Tecnai RGA were similar to those used for the Titan RGA data and previously described in section 3.2.

3.3.4. Advances in Measurement of Products with EELS

While the acquisition conditions and basic quantification procedure for EELS of gases had been determined prior to this work, quantification was still being done in Excel using rudimentary methods for determining the goodness of fit. A more robust and automated procedure for quantification of spectra was therefore developed and tested.

Previously, spectra were acquired one at a time in Digital Micrograph, though several spectra were usually acquired manually for each condition probed. For this work, a code was sought to automate this process. The digital micrograph scripting database hosted by Graz University of Technology (Grogger, n.d.) was found to contain a script explicitly written to automatically acquire multiple EELS spectra (Mitchell and Schaffer, 2005). This script records a series of 2D images of the detector, rather than a series of integrated, 1D spectra. This is ideal, since more information is retained, and custom processing routines can be developed, taking advantage of the 2D information, as described in Appendix VI. Most EELS data presented in this document was acquired in this format.

A typical low-loss spectrum from a nominally 50-50 mixture of CO and CO_2 is shown in Figure 3-17 along with the reference spectra for CO and CO_2 which have been used to fit the spectrum from the gas mixture. A MATLAB code was written (see Appendix V) which automated the process of finding the ideal linear combination by a constrained weighted least squares method (Miller and Crozier, 2014). This code can perform this operation on a single spectrum, multiple spectra, on a STEM-EELS data cube, or on the data cube generated by the multiple EELS acquisition code referenced previously (Mitchell and Schaffer, 2005). In addition to performing the least squares fit, the MATLAB code

automatically shifts the energy scale and accounts for the background. To do this, the code first normalizes the reference spectra so their integrated intensities are all unity over the energy range of 4 to 44 eV. Cross correlation of the mixture spectrum with the reference spectra is used to perform a rough energy calibration in case the mixture spectrum has an incorrect energy calibration. Next, the linear combination of selected gases that best fits the spectrum from the gas mixture in the TEM is computed by a weighted least squares method, where the peaks in the mixture spectrum are given a higher weighting, by setting the weights equal to the square of the intensity. This least squares fit is repeated many times, while shifting the mixture spectrum slightly relative to the (precisely calibrated) reference spectra to get a precise, automatic energy calibration of the mixture spectrum, as shown in Figure 3-18, where an optimal fit is given in green and the poorest fits in red.

After the ideal fit is found (Figure 3-19a), it is seen that the residuals often show a clear functional dependence, as seen in Figure 3-19b. This is due to the zero loss tails of the reference and mixture spectra being slightly different. No background removal was performed on either the reference or mixture spectra to attempt to completely remove the zero loss tails; instead the backgrounds of the reference and mixture spectra were matched. This is done in practice by fitting the residuals using an inverse power law, and this fit is subtracted from the measured spectrum. This procedure, shown in Figure 3-19, is equivalent to performing a background subtraction on both the mixture and reference spectra, to remove the zero loss tails, but is more robust in this case, where only a small window prior to the peak onset is available, making a more traditional background subtraction difficult. After the residual fit has been subtracted, the background-matched spectrum is then taken through the steps of fitting and shifting again to determine a new

optimized fit. This process of matching the background is repeated as necessary until no clear power law dependence of the residuals is found Figure 3-19d. No procedure for deconvolution of plural scattering was applied, since plural scattering is minimal at the gas pressures used, where the electron mean free path is much larger than the pole piece gap. Once the linear combination coefficients have been determined, information about the reference spectra is used to compute the gas partial pressures, as detailed in (Crozier and Chenna, 2011). The full MATLAB code and additional detailed explanation of its function are found in Appendix V. Application of this quantification method to the mixture spectrum in Figure 3-17 yields a result of 49.2% CO_2, 50.8% CO, with a standard deviation of 0.7% as discussed in section 3.3.5 below.

Core-loss quantification was similar to the low-loss method, and used a linear combination of reference spectra to fit the spectrum from a gas mixture (see Appendix VI). For all the core-loss spectra, including the reference spectra, the backgrounds were fit with the usual inverse power law. Since the spectra were usually only acquired over a 50eV range, the pre-edge window was usually less than 25 eV. This background was extrapolated across the entire spectrum and subtracted prior to beginning the analysis. (This is in contrast to the low-loss method, where the backgrounds of the reference and mixture spectra are matched rather than subtracted.) After background subtraction, a non-negative non-linear least squares approach was used to find the linear combination of reference spectra from CO and CO_2 which best fit the mixture spectrum. This is shown in Figure 3-20 for a nominally 50/50 mixture of CO and CO_2. The spectra were fit over the entire acquisition range of about 50 eV, and the result obtained was a composition of 51.0% CO_2 49.0% CO,

with a standard deviation of 0.4%. This is quite close to the nominal composition, and in good agreement with the low-loss EELS result.

3.3.5. Comparing EELS LL, EELS CL, and RGA results

All the techniques used to measure the gas composition inside the TEM should ideally yield identical results if correctly implemented and quantified. To determine whether this was the case, a simple comparison experiment was performed on the Tecnai ETEM, in which a 50-50 mixture of CO and CO_2 was flowed through the ETEM cell at a pressure of 1.5 Torr, and the composition measured over 70 minutes. For the first 20 minutes, the low-loss EELS method was used, and for the final 20 minutes core-loss spectra were taken. During the entire experiment, data from the RGA was collected simultaneously. Results from this experiment are summarized in Figure 3-21.

Using the data from the comparison experiment, the precision of each EELS technique can be evaluated independently of its accuracy because EELS spectra were taken from a gas of constant composition automatically every 20 seconds using a script for digital micrograph (Mitchell & Schaffer, 2005). 60 spectra were taken in the low-loss region of the spectrum, giving a mean value of 49.6% CO_2 and 60 from the core-loss region, giving a mean of 50.7% CO_2. It is clear from a visual inspection of the plot in Figure 3-21 that the variance for both quantification methods is small. The standard deviation of the results shown in Figure 3-21 for the low-loss and core-loss techniques are 0.7% and 0.4% respectively, and the standard errors of the means are 0.10% and 0.05%. The difference between the mean value obtained using the low-loss and core-loss techniques is 1.1%, with the mean of the low-loss just below the nominal composition of 50%, and that of the core-

loss just above. The pressures in the microscope during the EELS reference spectra acquisition were controlled to be within 2% of 1 Torr for both CO and CO_2. Even this small error is much larger than the variation in gas composition computed from the 60 individual core-loss or low-loss spectra shown in Figure 3-21, so the greatest uncertainty in the calculation of gas partial pressures using either region of the spectrum comes from the uncertainty in the reference gas pressures, rather than the quantification procedures, which are quite precise.

The ratio of CO_2 to the total $CO+CO_2$ obtained using the RGA as a function of time for the comparison experiment is shown in Figure 3-21. This result was obtained by first subtracting a background, the RGA signal before gas is admitted to the reaction cell, and then simply taking the ratio of the currents from CO and CO_2, divided by known standard ionization cross sections (O'Hanlon, 2003). This yields a value that ranges from 48.5% CO_2 to 50.3% CO_2.

The RGA data shown in Figure 3-21 exhibits a sharp dip and broad peak around 30 minutes into the experiment; 28 minutes after beginning the gas flow, the flow was suddenly slowed, so that the pressure in the cell dropped about 20%. This pressure change does not significantly affect the molar concentration ratio in the reaction cell but it caused the RGA peak ratio to drop by about 5%, and thus changed the computed CO to CO_2 composition. When the pressure was restored to the original value the signal ratio did *not* return to the exact same value. Indeed the steady drop with time that can be seen in Figure 3-21 is primarily due to a gradual pressure drop in the mixing tank leading to a corresponding pressure drop in the cell. This demonstrates that the signal from the RGA as a function of pressure is not linear, making it difficult to directly relate a measured

current in the RGA to a partial pressure of gas in the vacuum system. Additional evidence of the non-linearity of the RGA is shown in Figure 3-22.

Furthermore, the placement of the RGA in the Tecnai vacuum system (near the turbo pump which provides the first level of differential pumping as shown in Figure 3-16) far from the catalyst sample along with the RGA's differential pumping system, may result in the gas composition in the RGA being different from that in the reaction cell due to differential diffusion in the vacuum system. The initial rise in the RGA data in Figure 3-21 demonstrates that gas reaches the RGA within about one minute of its introduction to the ETEM, but about 5 min are required for the composition to reach equilibrium. These limitations combine to make the RGA data quantification uncertain, though as the results given in Figure 3-21 show, simple data quantification still seems to be reasonably accurate in this case.

Even with the limitations of the RGA previously described, mass spectrometry is a useful technique for monitoring the gas composition within the ETEM. The main benefit of the technique is its independence from the operation of the microscope. The RGA can collect data during imaging, EELS acquisition, or even with the electron beam blanked. Thus, data can be acquired continuously over the course of an entire experiment. Furthermore, the data can be easily visualized live while the user is operating the microscope, allowing any changes in gas composition to be identified immediately.

The EELS and RGA techniques have advantages and disadvantages. The EELS techniques are quantitative, and probe the gas in the environmental cell directly. In either EELS technique, a disadvantage for *operando* studies is that the beam cannot be used for high resolution imaging while it is employed to detect the gases via EELS. This is in

contrast to the mass spectrometry technique using the RGA, which can gather data continuously during the course of the experiment. The RGA is however, a less reliable technique for accurate quantification of gas compositions, and probes the gas in the vacuum system far from the ETEM reaction cell. The RGA and EELS techniques are thus complimentary, and ideally suited to *simultaneous* use.

While it is ideal to use both the EELS and RGA techniques during every experiment, broken and missing equipment resulted in most of the *operando* experiments attempted being performed with either RGA or EELS, not both. There were however a few *operando* experiments where both were used and this allowed additional comparison of the results from the two techniques. An example is given in Figure 3-23. A clear trend is observed in this data, where at compositions where the CO and CO_2 pressures are equal (O_2 was also present, unlike the data in Figure 3-21) the two techniques give different results, while at high or low concentrations of CO_2 the techniques are in closer agreement. It seems most likely that the RGA is in error, and the EELS technique correct, due to the multiple issues with quantification of RGA data already discussed. By this interpretation, the RGA is either overestimating the amount of CO or underestimating the amount of CO_2. It is not clear why either of these effects would be increased for a 50-50 mixture of CO and CO_2 with O_2 and this remains unresolved.

3.3.6. Quantification of Catalyst Activity- From Conversion to TOF

While relative measurements of catalytic activity can be obtained by simply measuring the gas composition inside the ETEM cell, more rigorous quantification of catalyst activity during *in-situ* experiments requires additional parameters to be accurately known. This

quantification was not possible in the previous work by Crozier and Chenna (Chenna and Crozier, 2012b), who did not know how much catalyst was present in the ETEM during their experiments. Many reports of catalytic activity in the literature give values for turnover frequency (TOF) (Aßmann et al., 2004; Gao et al., 2009; Joo et al., 2010; Martynova et al., 2012; Peden and Goodman, 1986). This necessitates an assumption about the density of active sites on the catalyst surface, which may be accurately made for single crystal surfaces, but is more tenuous for supported nanoparticle catalysts. It is safer to report activity in units of number of product molecules (or mols) per unit surface area per second if the specific surface area has been well-characterized, as done in section 2.2.2. If the specific surface area is not known, then activity should be given in units of product molecules per unit mass (Thomas and Thomas, 2015). The uncertainty in the calculation of reaction rates or turnover frequencies is large for the *operando* experiments described in this dissertation because of the imprecision in the measurement of the mass of catalyst loaded onto each pellet, as discussed previously in section 3.3.1. Nevertheless, the reaction rates observed in the TEM can be estimated, with an uncertainty equal to about half the measured rates.

3.3.7. New Methods for Observation of Catalyst Structure

While there is little novelty in the use of conventional phase contrast imaging, one aspect of the image acquisition process used in this work was not standard. Rather than acquiring single images using the TEM cameras, a series of 5 images was typically taken automatically using a Digital Micrograph script written by Vincent Hou found on the DM scripting database (Grogger, n.d.). The individual frames were generally acquired with an

exposure time of 0.5 s without any set gap between frames, though due to the time required for image processing, the frames are typically acquired around 1 s apart as shown in Figure 3-24. These images are all contained within a single .DM3 format file as 5 frames called slices. These can be opened by Digital Micrograph as well as by the MATLAB codes which were written as part of this work, and described in section 4.2. Several benefits arise from this method of acquisition. First, individual frames can be registered and suitably averaged to yield a single image with a better signal-to-noise ratio. This increase in signal-to-noise cannot be achieved by simply taking longer exposures with the camera, since the specimen often drifts and moves during acquisition, and the effect of this during a longer exposure would be an increasingly blurred image. Secondly, by comparing individual frames visually, the images give more information about the dynamic changes taking place in the sample being observed over time scales on the order of the total acquisition time.

It might be assumed that recording a video from the camera, rather than a series of only 5 frames would provide the above benefits in even greater abundance. Unfortunately, the software available at ASU to record video is rudimentary, and while a series of images of what appears on the screen can be recorded as video, all of the metadata usually acquired and stored in image files saved in the Gatan Digital Micrograph format are lost. By using the script to acquire a series of images, this metadata is retained. Series larger than 5 could be acquired using the script, but series of 5 were found to be adequate and practical.

Tomography was also not attempted in this work. Acquiring tomographic series requires that the sample remain unchanged, and reasonably stable, during the acquisition of all frames, and this condition is not always satisfied in the ETEM, where dynamic

changes are often occurring. More discussion of the value of tomography for this work will be given in section 7.2.3.

Possibly one of the most important practical challenges faced in this project was that of finding Ru particles which were oriented in a favorable (close to zone-axis) orientation. The Ta heating holder used in this work (see section 3.2.1 and Figure 3-1) is only capable of tilting along one rotation axis, making it impossible to accurately tilt the sample. Additionally, amorphous SiO_2 supported particles routinely shift orientation slightly during observation at elevated temperatures in gas, making tilting tedious and unproductive even if a holder designed for accurate tilting is used.

In a well-loaded TEM sample, thousands of nanoparticles were visible within a single grid square, so statistically, it should be possible to find particles in suitable orientations. The probability for finding particles close enough to particular zone axis orientations so 2 sets of fringes are visible was quantified by Fraundorf, et al. (Fraundorf et al., 2005) and for a 4 nm Ru particle, imaged at 80kV, the probability of finding a particle close to the [101] zone axis is about 0.01. If we assume that to locate and check a single particle at high enough magnification to determine the visibility of fringes requires about 30 seconds, then with constant searching, a particle in the [101] zone axis will be found on average once every 50 minutes! This does not include time spent acquiring image data or EELS spectra. Since many particles must be observed during a single experiment, this is obviously not practical, and a faster method for finding particles must be used.

It was found that particles in zone axis orientations could be more rapidly located by using the objective lens current wobbler intended for doing “rotation center” alignment on the FEI TEMs. By wobbling the objective lens current, electrons which are diffracted out

to high angles by lattice planes are focused to varying positions in the image, and the visual effect is bright contrast that moves out some distance from the particle and then returns, in a cyclic pattern. This contrast can be seen even at magnifications far too low to actually resolve the fringes. Particles with no visible fringes at high magnification will not display this behavior. For particles on a zone axis where multiple fringes are visible, multiple bright contrast regions will move parallel to their respective plane normals as the lens current is wobbled, enabling identification at low magnification.

3.4. Summary

In this chapter, the *operando* experimental technique developed to quantify product gases inside the differentially-pumped ETEM was summarized including methods used by previous researchers, and new developments from this work. The methods used to control gas pressure and composition were described, including the gas handling system built for the Titan, (described in more detail in Appendix IV) as well as methods for removing carbonyls from the gas stream. The basic principles previously developed for acquiring and quantifying EELS of gases were described, and the new methods for automated analysis and quantification were briefly explained (further detail is given in Appendix V and Appendix VI). The installation and use of a residual gas analyzer was described along with the basic method used to obtain semi-quantitative gas compositions from the data. These two techniques for measuring gas composition were directly compared and the benefit of using both explained. The conventional TEM imaging method was described, including the acquisition of multiple frames at low electron dose rates, and the technique used to locate ideally oriented particles. The novel sample preparation which enabled this work by

dramatically increasing the amount of catalyst in the TEM was also described and its success noted.

Figure 3-1 Ta Heating Holder. The Gatan Ta heating holder used for all *operando* experiments. This image was taken from the Gatan website.

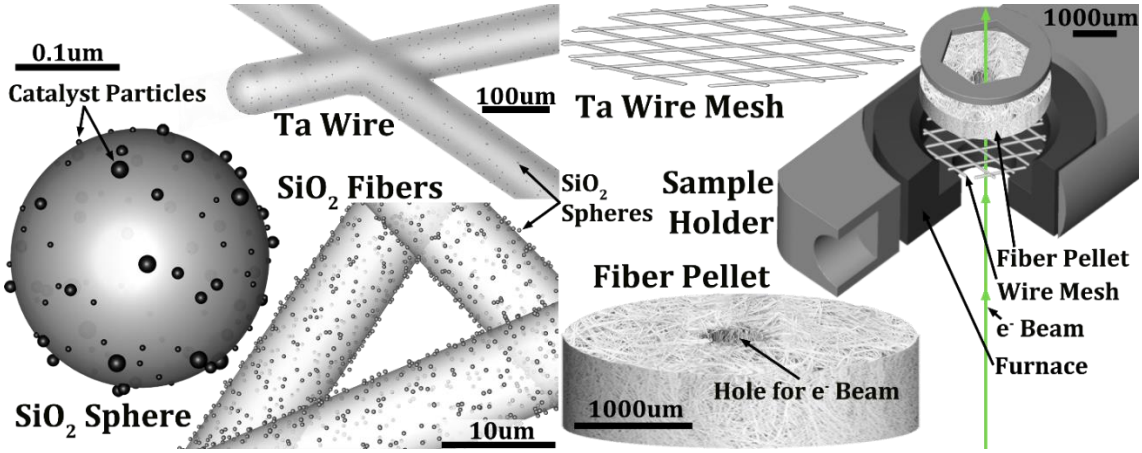

Figure 3-2 *Operando* Sample Prep. An overview of the sample configuration used in the *operando* experiments. Both a Ta wire mesh and a SiO_2 fiber pellet are covered with silica-sphere-supported Ru catalyst particles, and placed inside the holder, with the wire mesh closer to the eucentric plane in the Ta heating holder.

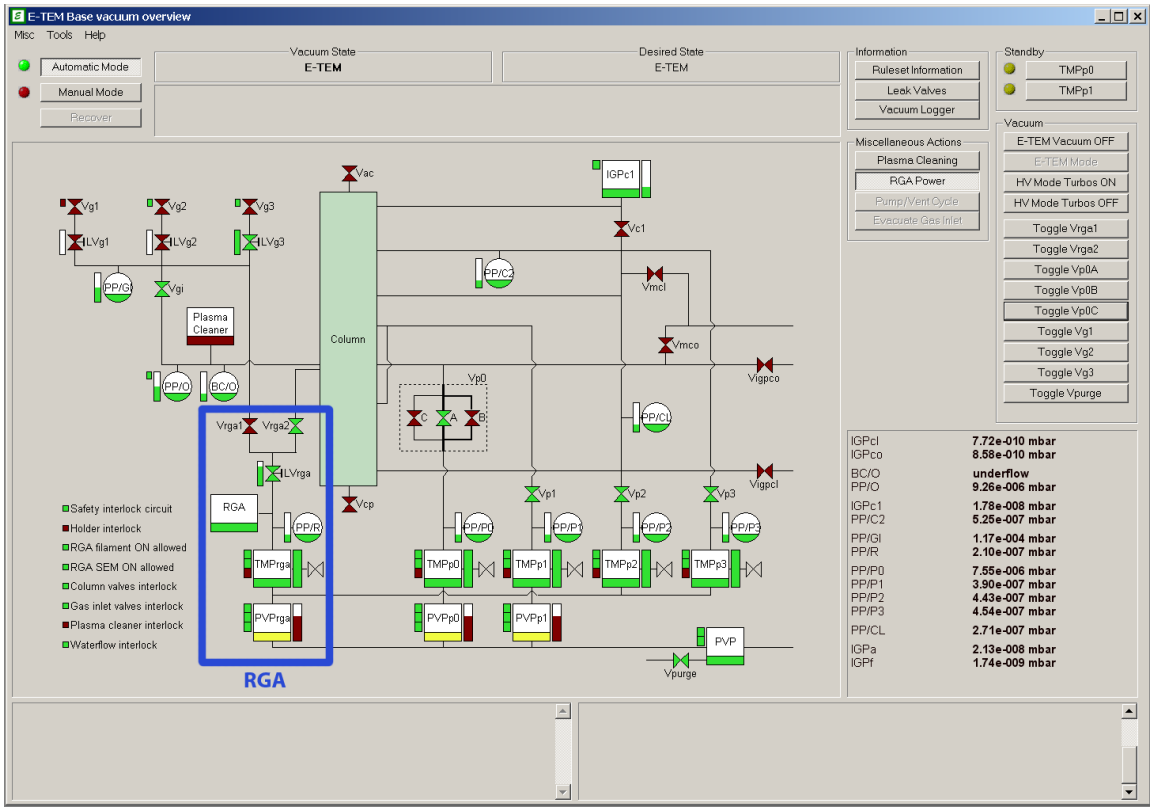

Figure 3-3 Titan ETEM Window. The primary ETEM control window on the FEI Titan computer. The RGA (residual gas analyzer) system includes 2 pumps and a leak valve to maintain the low pressure needed. The RGA can sample gases either from the gas inlets, or from the ETEM column (the currently selected configuration in this image.)

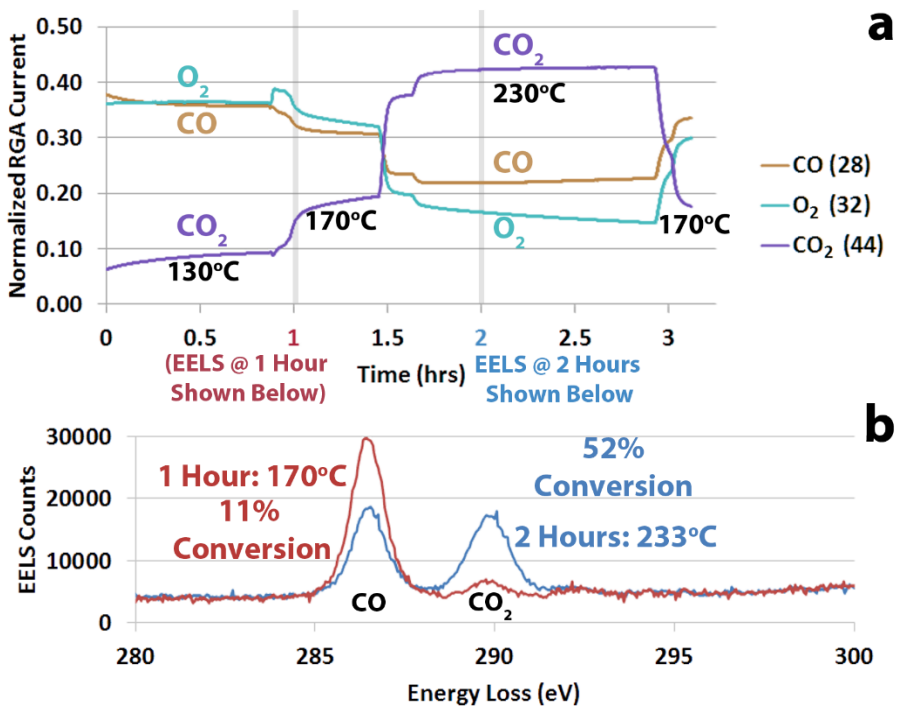

Figure 3-4 RGA-EELS *Operando* Data. a) RGA data over several hours from masses 28, 32, and 44 amu, showing the clear increase in CO_2, and corresponding decrease in CO and O_2, within the ETEM cell as the temperature is increased from 130°C to 230°C. b) EELS spectra were also acquired at several points during the experiment, including the two shown and quantified here.

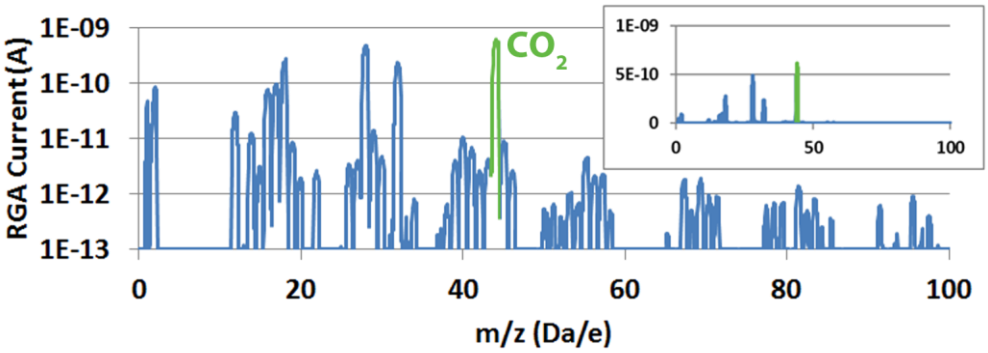

Figure 3-5 Raw RGA Data. A raw analog spectrum from a gas mixture including CO_2, O_2 and CO is shown. Many small peaks are visible due to the high sensitivity of the RGA. The inset shows the same data plotted on a linear scale.

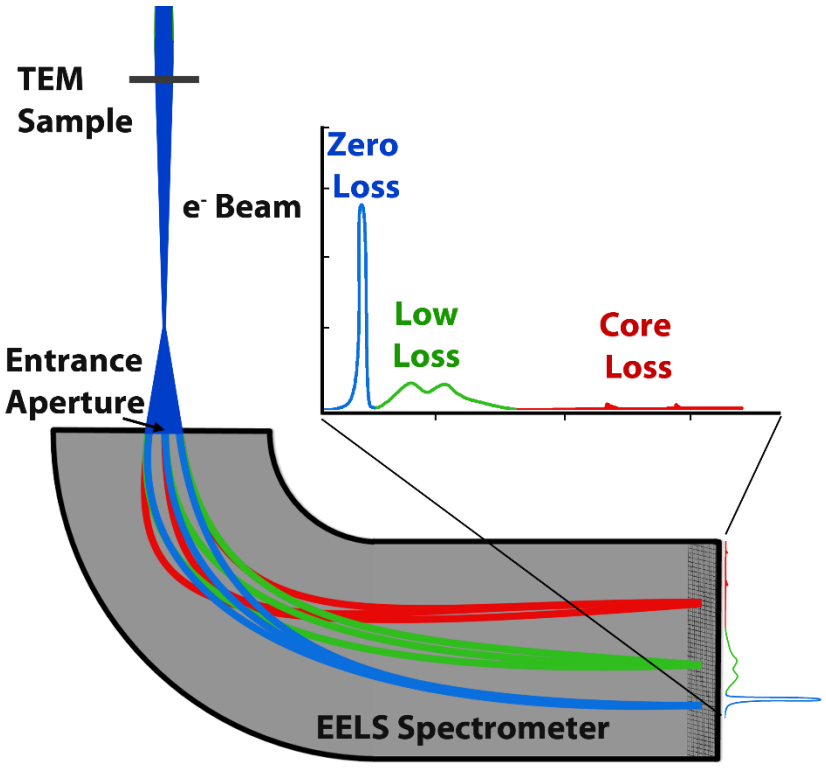

Figure 3-6 EELS Basics. Schematic illustration of magnetic prism spectrometer. Electrons of different energy take different paths through the spectrometer. These electrons can be focused onto a camera to record spectra, which may include the zero loss peak the low-loss region, and/or the core-loss region.

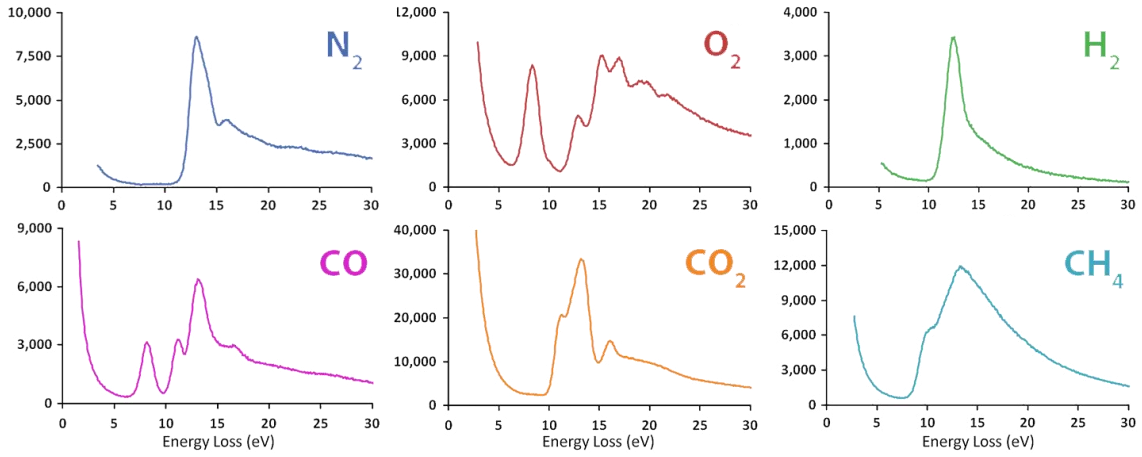

Figure 3-7 EELS Low-Loss Spectra. Different gas molecules result in distinctive low-loss spectra in EELS. These can be measured easily in the ETEM, and used to quantify mixtures of gases. Modified from (Crozier and Chenna, 2011).

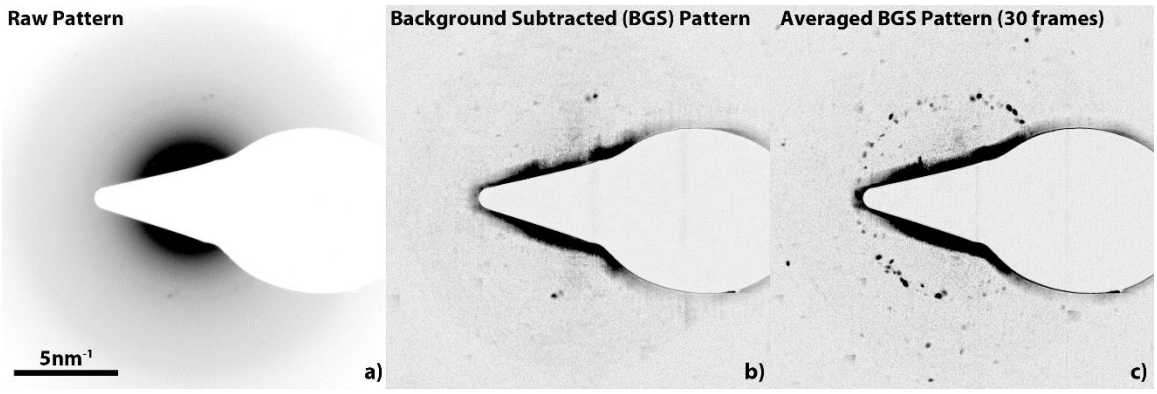

Figure 3-8 Electron Diffraction. a) A single 2 s acquisition of a powder electron diffraction pattern from the silica supported Ru catalyst. b) "Rolling ball" background subtraction performed using ImageJ emphasizes the few spots visible in the pattern. c) 30 frames from 6 distinct areas are combined by taking the maximum intensity (from the stack of 30 frames) at each pixel.

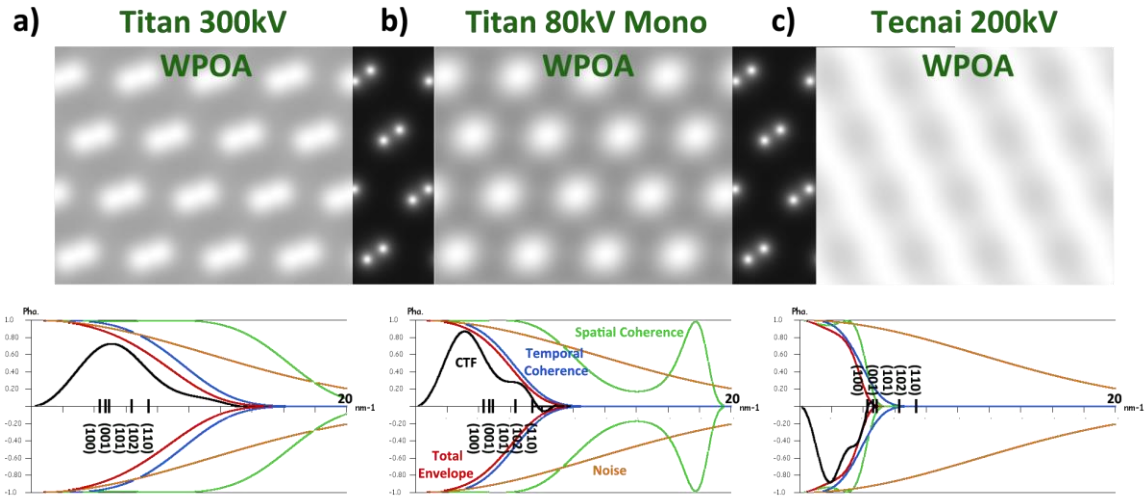

Figure 3-9 TEM Imaging Conditions. TEM imaging conditions, with WPOA (weak phase object approximation) images and CTFs (contrast transfer functions) calculated using JEMS. a) Titan at 300kV showing superior image resolution. b) Titan at 80kV with the monochromator in use, showing the significant worsening of the temporal coherence at 80kV. c) Tecnai at 200kV, showing the dramatically worse spatial coherence and image quality due primarily to the spherical aberration of the objective lens, which is not corrected.

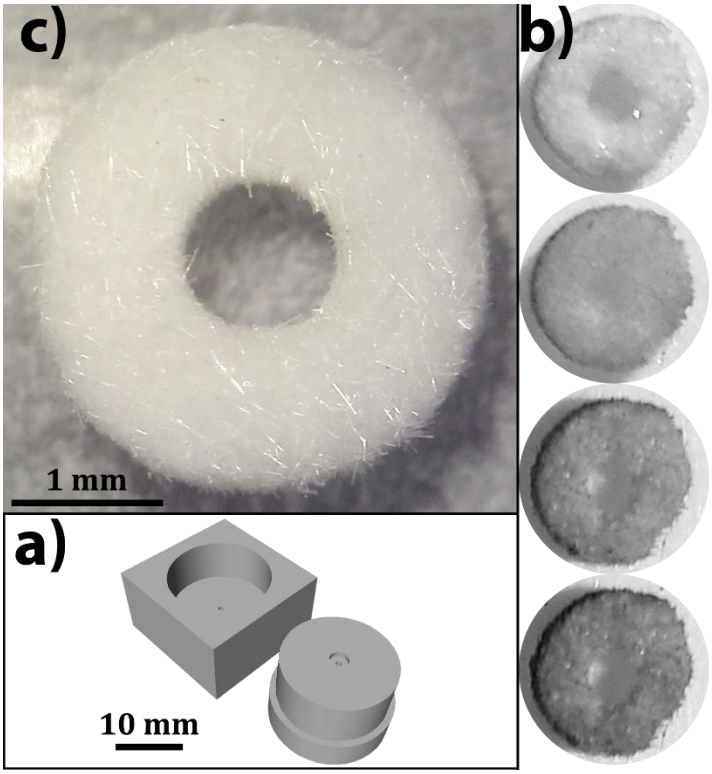

Figure 3-10 *Operando* Pellet. a) The jig designed to finish the pellets, showing the small counter bore, in which the pellet sits, in the right half. b) Series of images of an *operando* pellet after successive drops of a catalyst suspension have dried. c) Optical image of the *operando* pellet, showing the texture and size. The hole in the center allows the electron beam to pass, and the wire mesh grid to be observed in the TEM.

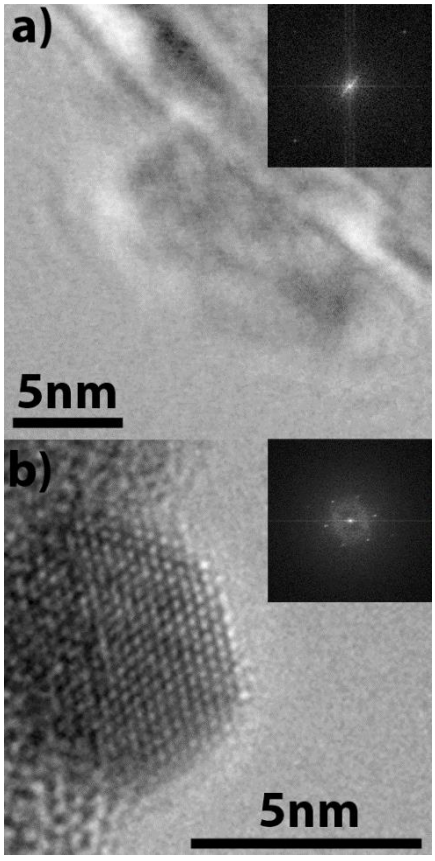

Figure 3-11 Grid vs Pellet Images. a) An image of a Ru particle supported on a silica sphere that is in contact with the insulating fiber pellet, showing the dramatic effect of charged fibers on the image resolution, even without gas and at room temperature. b) An image taken at 480°C in 0.75 Torr H_2, from a particle supported on a silica sphere that is in contact with the Ta wire mesh, showing several lattice fringes clearly resolved.

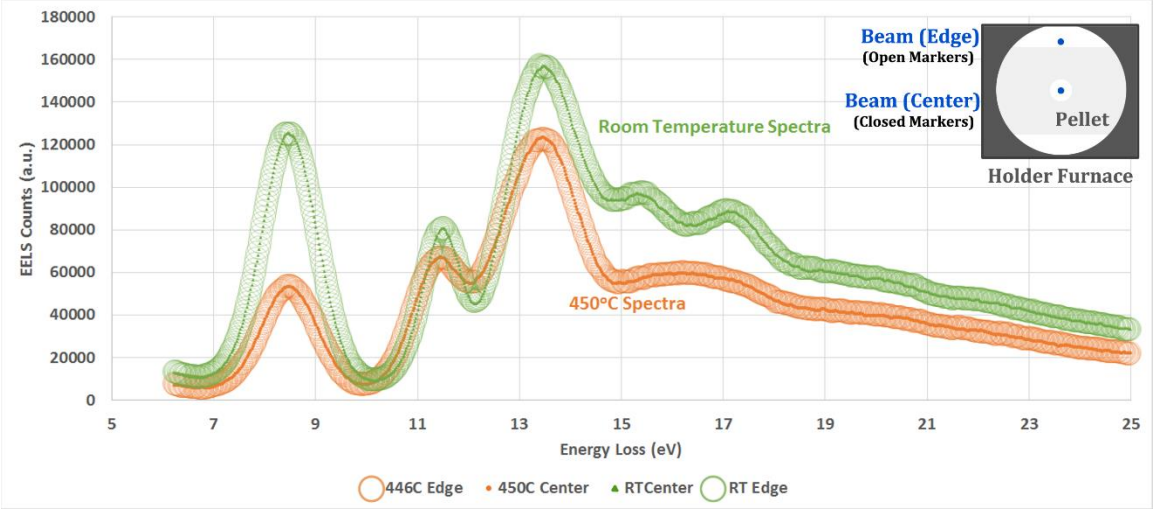

Figure 3-12 Gas Homogeneity Test. Four low-loss EELS spectra, showing that the gas composition at the outer edge of the fiber pellet is identical to the composition in the center of the pellet at both 450°C and room temperature, though the spectra at these two temperatures is significantly different due to high conversion at 450°C. At each temperature, the large open symbols are the spectrum from the outside edge, while the small filled symbols are the spectrum from the center of the pellet. The inset shows the location of the measurements.

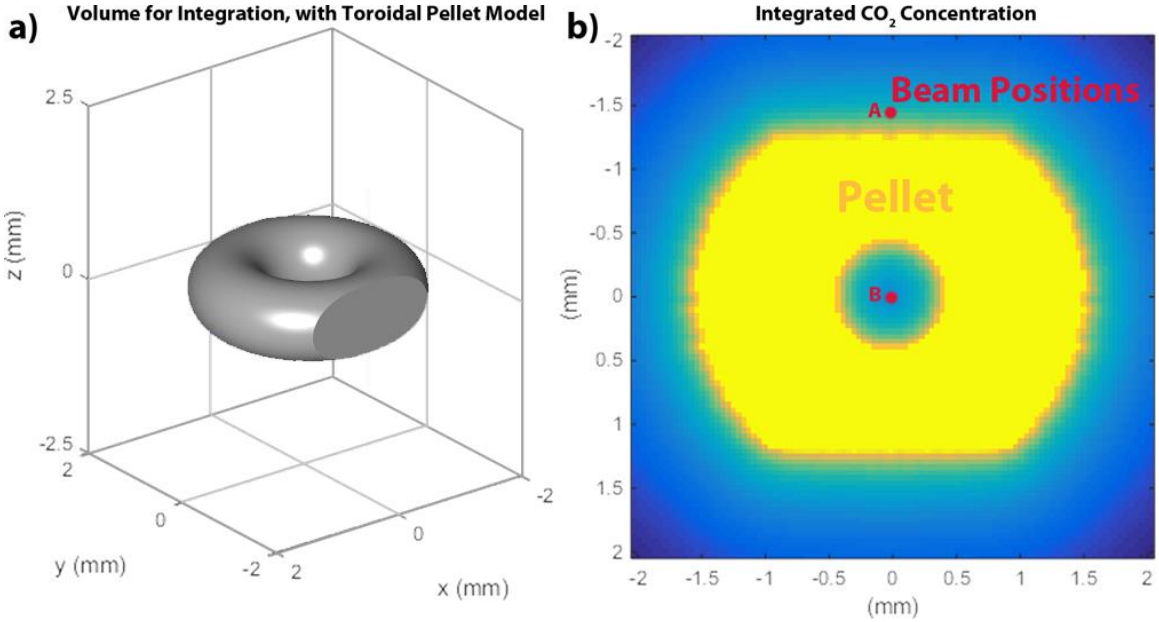

Figure 3-13 Gas Homogeneity Calculation. a) the 3D toroidal pellet model with 2 sides cut flat. This model was created and used in MATLAB to calculate a simple model for the composition at every point within the 3D plot volume. b) a 2D plot of the composition

integrated along the beam (z) direction from -2.5 to 2.5. The intensity at position A is 5 times higher than at B.

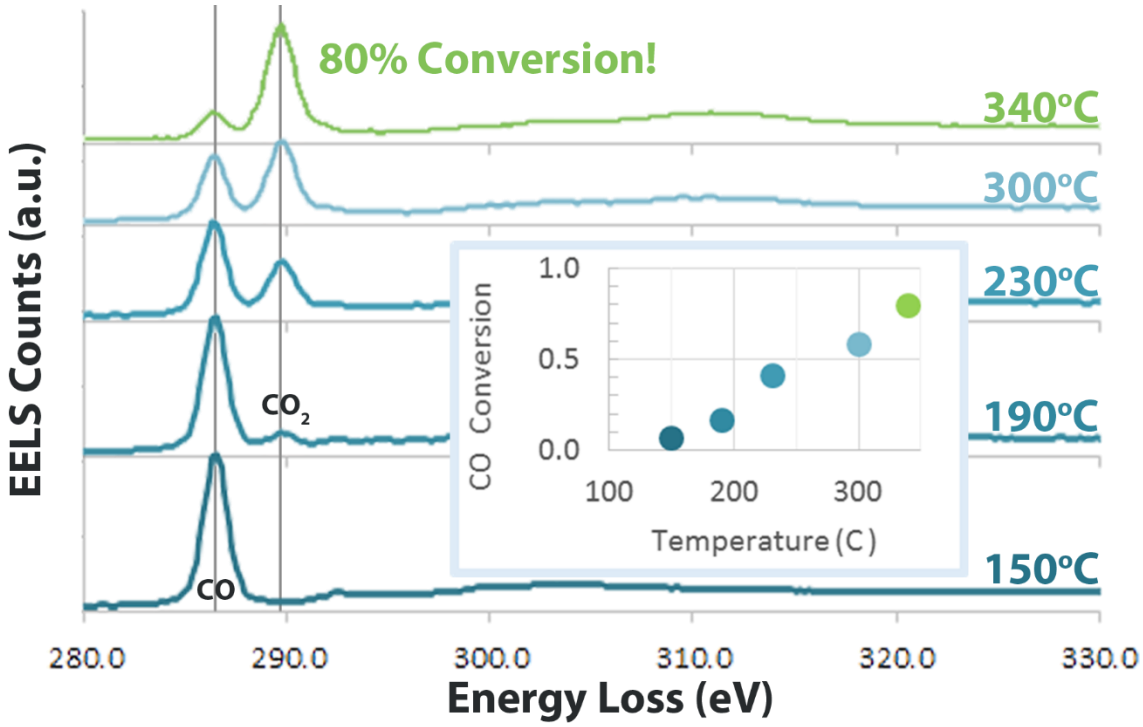

Figure 3-14 High *In-Situ* Conversion. Core-loss spectra showing the carbon K-edge recorded as a function of temperature from a CO oxidation experiment with a Pyrex-fiber pellet. The inlet gas was a stoichiometric ratio of CO and O_2 at 2.6 mbar. The spectra were quantified by fitting a linear combination of reference spectra and the calculated conversions are shown in the inset.

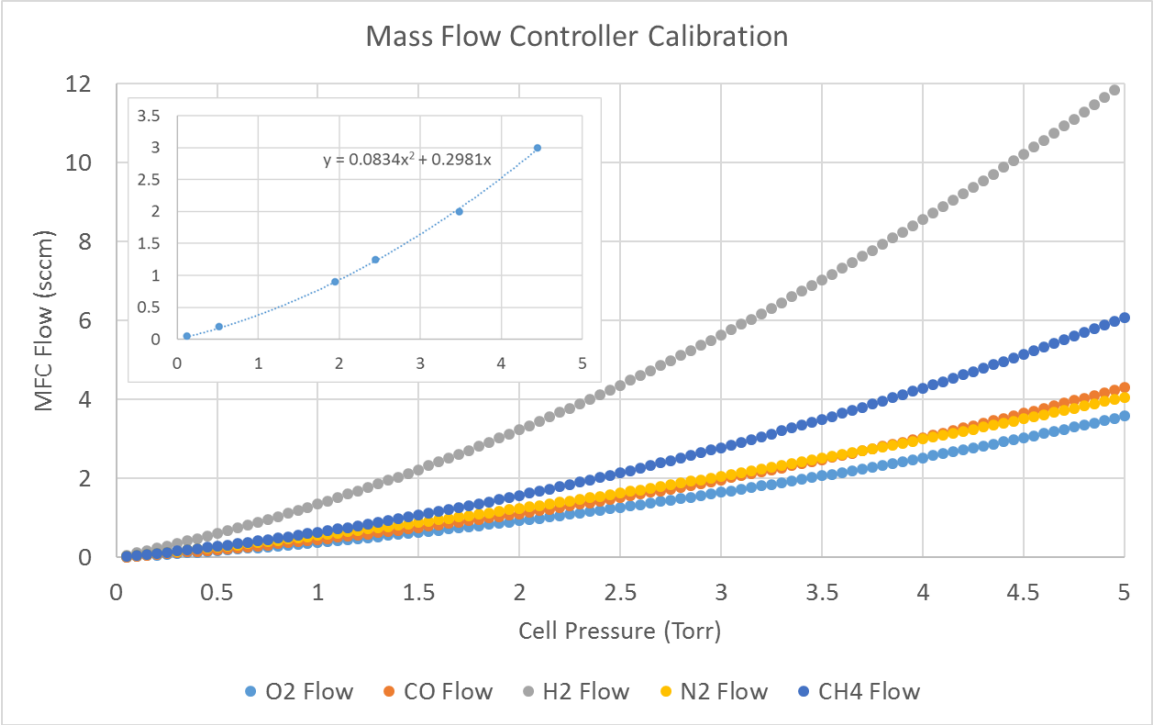

Figure 3-15 MFC Calibration Curves. The curves shown are parabolic fits to experimentally measured data for each gas flowed through the Titan mass flow controllers (MFCs). The experimental data and associated fit for O_2 are shown in the inset.

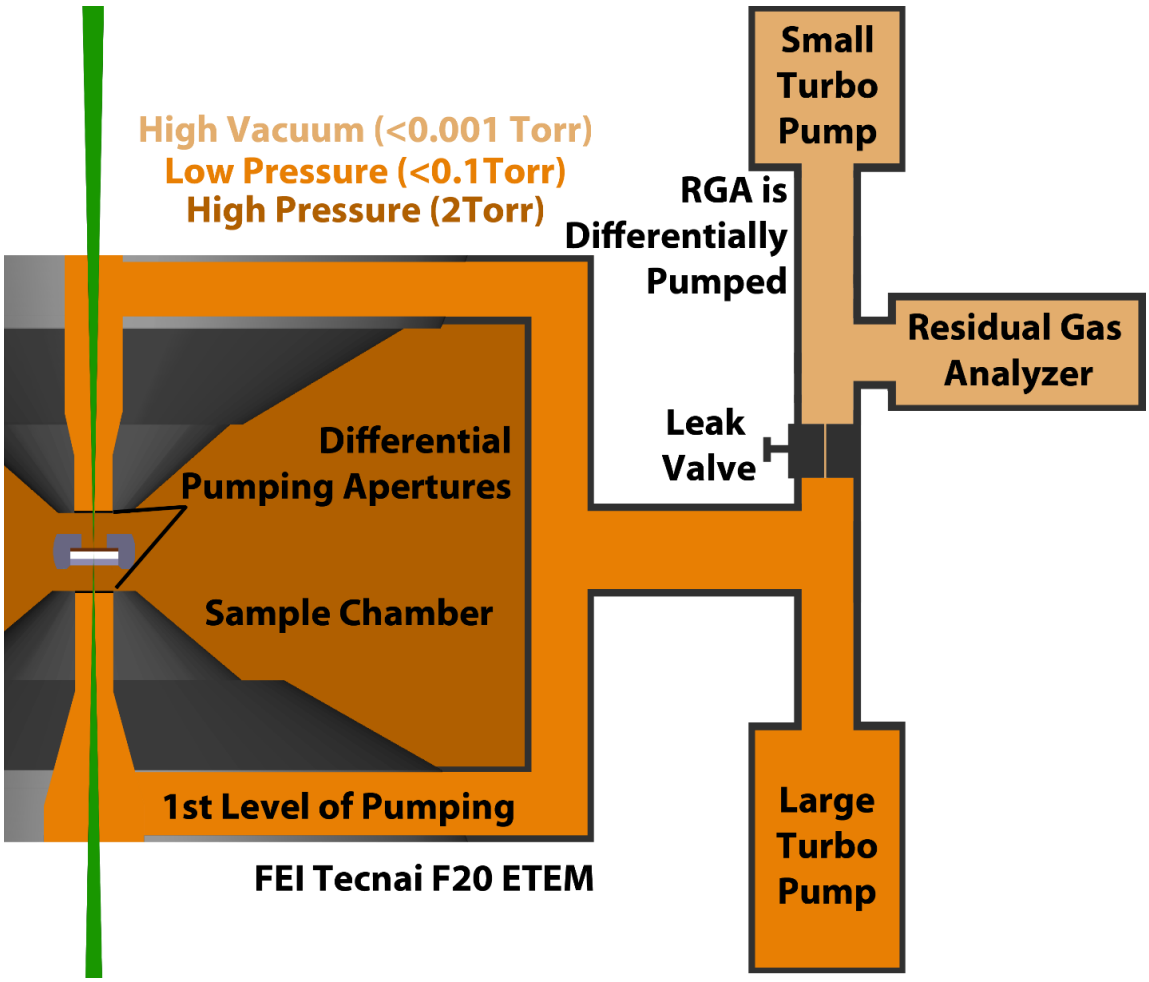

Figure 3-16 RGA Setup Tecnai. A schematic diagram showing how the RGA is interfaced to the reaction cell of the ETEM (which is located between the upper and lower pole pieces of the objective lens). A leak valve and 2nd small turbo pump work together to control the pressure at the RGA.

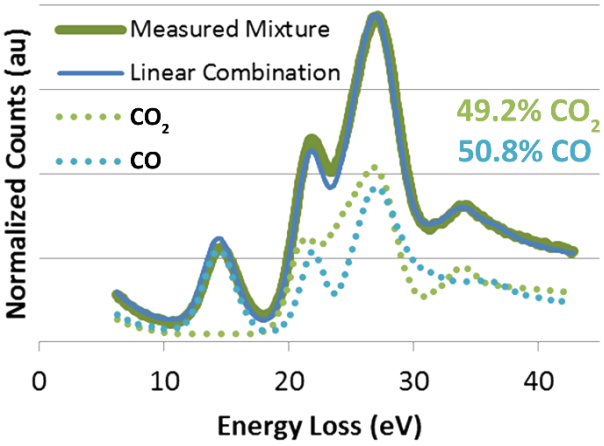

Figure 3-17 Low-loss EELS Fitting. Illustration of the linear combination method for low-loss EELS of gases quantification for a 50/50 mixture of CO and CO2. The spectra from multiple individual gases (dotted lines) were suitably combined to yield a spectrum (blue) closely fitting the spectrum obtained from a mixture of those gases (green).

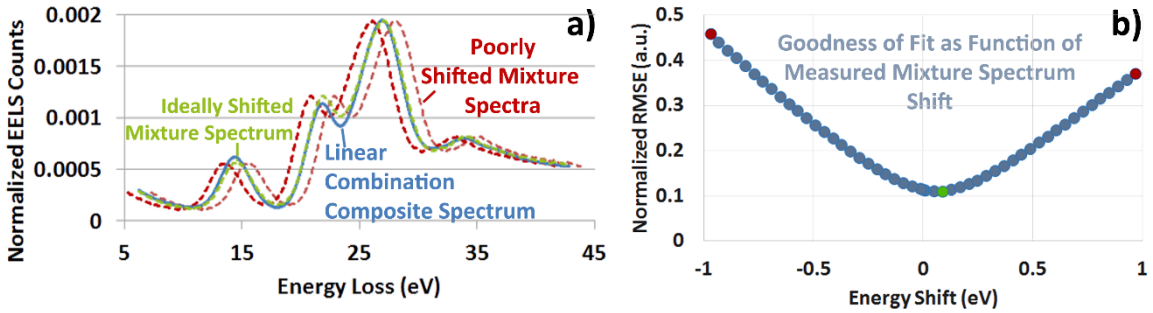

Figure 3-18 EELS Energy Shift- MATLAB. The energy calibration method used for the low-loss EELS analysis automation. To automatically and precisely calibrate the energy-loss axis of spectra measured from gas mixtures, the mixture spectrum is systematically shifted through a range of a few eV, while the reference spectra used to compute the fit (blue) remain fixed. a) Examples of good (green) and poor (red) energy shifts. b) The root-mean-square-error (RMSE) of the linear combination fit plotted as a function of energy shift showing a single minimum when the spectrum is correctly calibrated.

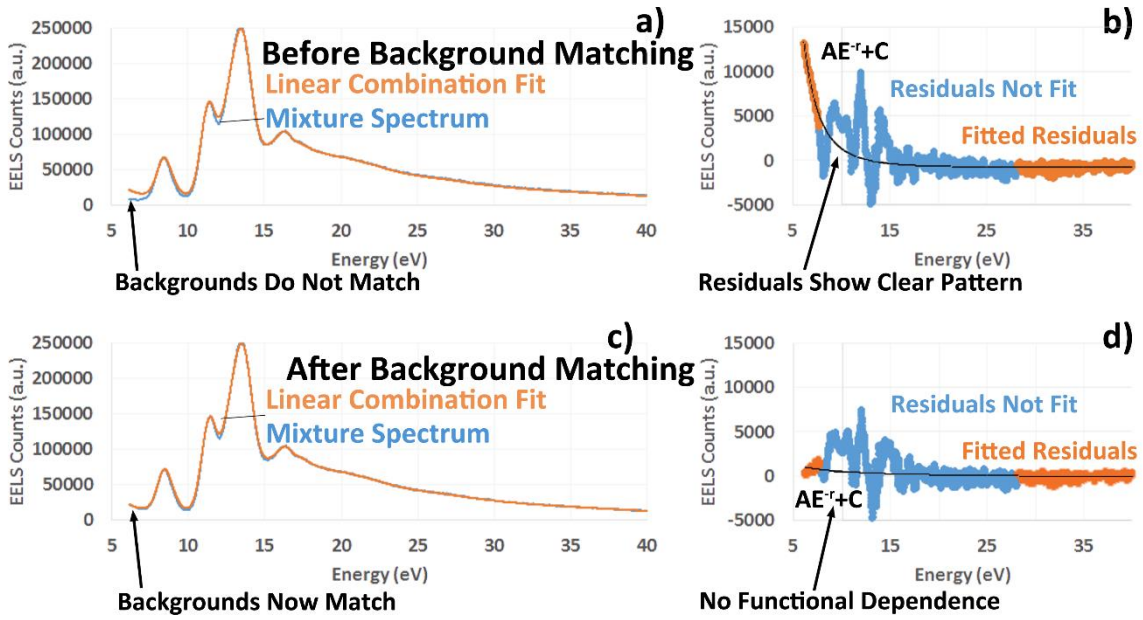

Figure 3-19 EELS LL Background Matching. The background matching method used for the low-loss EELS analysis automation. a) After fitting a linear combination of experimentally obtained spectra of individual gases (orange) to a spectrum from a gas mixture (blue), the background of the composite spectrum and mixture spectrum do not match. b) The residuals from the fit show a clear pattern. This pattern can be fit quite well with a power law function (black). c) Subtracting this fitted function yields a mixture spectrum with a background that more closely matches that of the individual reference spectra so that no clear functional dependence is seen in the residuals (d).

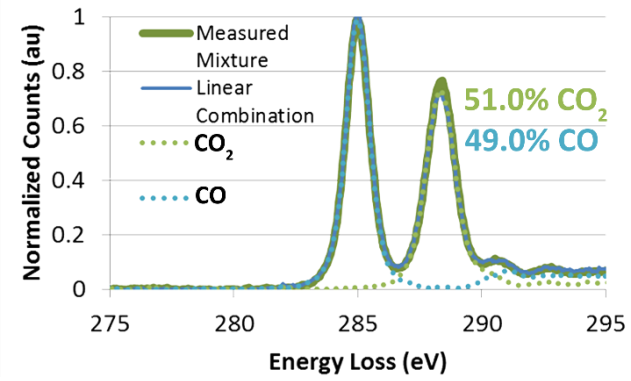

Figure 3-20 Core-loss EELS Fitting. Illustration of the linear combination method for core-loss EELS of gases quantification for a 50/50 mixture of CO and CO_2. The spectra from multiple individual gases (dotted lines) were suitably combined to yield a spectrum (blue) closely fitting the spectrum obtained from a mixture of those gases (green).

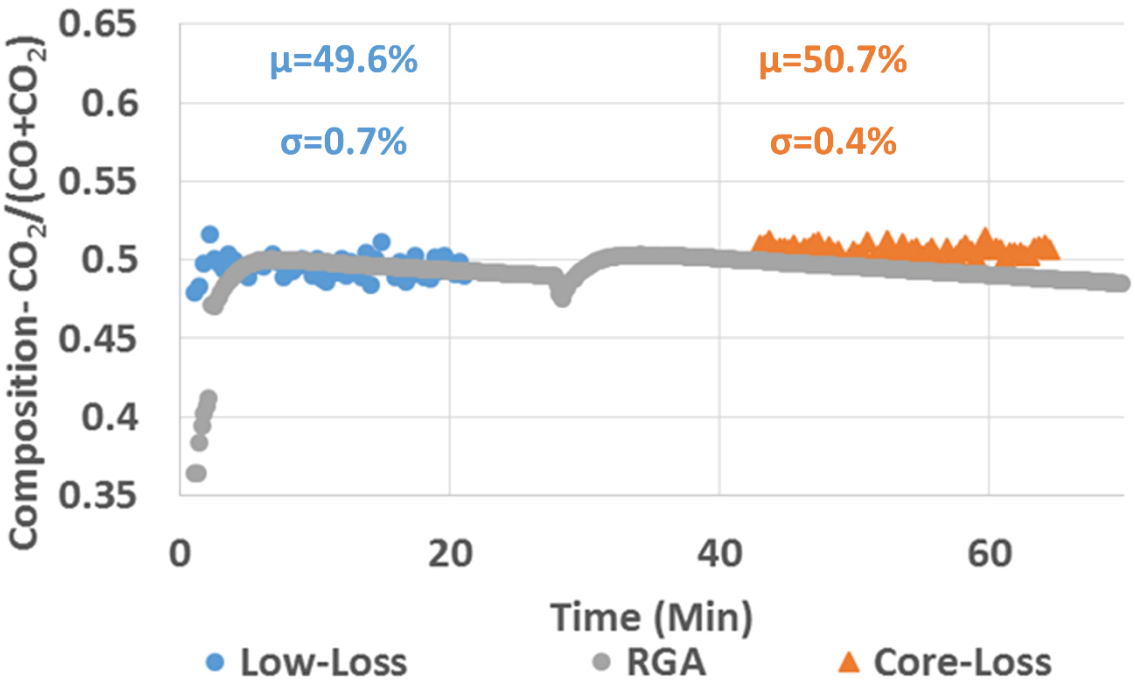

Figure 3-21 Comparison Experiment. The composition determined from quantification of EELS spectra series from both the low-loss (blue) and core-loss (orange) regions are compared to the signal from the RGA (grey). Energy loss spectra were taken every 20 seconds in two 20 min blocks. Peaks in the mass spectrum were monitored every 10 seconds. The time between the two blocks of EELS spectra was used to adjust the spectral acquisition parameters.

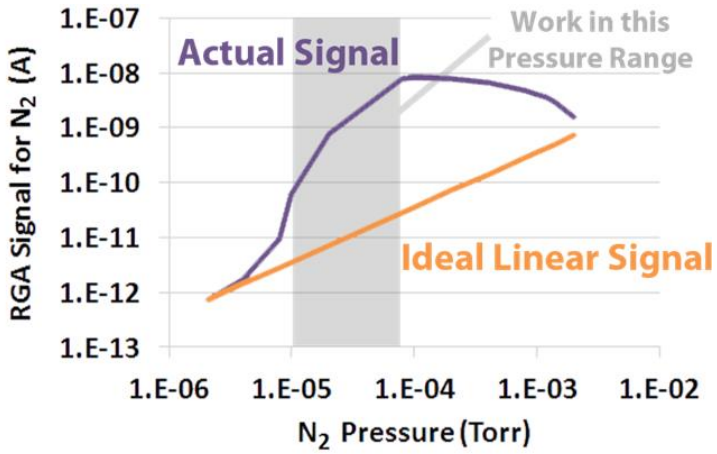

Figure 3-22 RGA Non-Linearity. The RGA signal at 28 amu is given as a function of the pressure at the RGA during N_2 flow (measured using an inverted magnetron vacuum

gauge) on a log-log plot. The RGA signal was found to be highly non-linear, even within the ideal pressure range for the instrument.

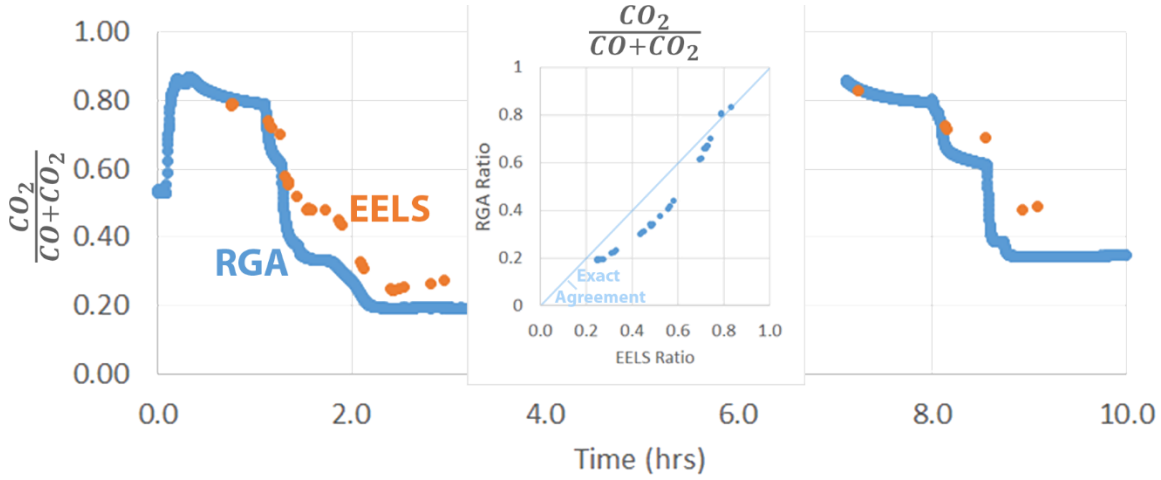

Figure 3-23 RGA-EELS Additional Comparison. Data obtained over the course of several hours during an *operando* experiment from both RGA and EELS shows a disparity between the calculated compositions. The inset plots the RGA composition ratio as a function of the EELS composition ratio, revealing a clear trend.

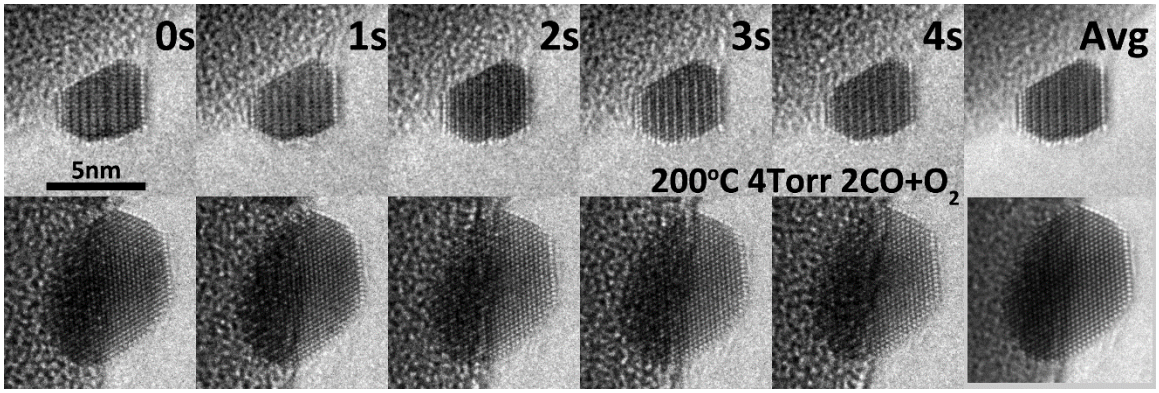

Figure 3-24 Image Series Acquisition. Series of 5 frames acquired for 2 particles in the Titan ETEM using a Digital Micrograph script (Grogger, n.d.). The 6th image in each series is an average of the 5 frames.

4. Image Analysis Methods for Structure Determination

Software for many types of image analysis already exist, and several software packages, including ImageJ and Digital Micrograph (basic version) are freely available. The capabilities of these software packages are limited however, and especially when performing repetitive complicated analyses requiring a mixture of human input and computer automation, a full scripting language is often preferable. The scripting language chosen for this work was MATLAB, which has a large array of functions and tools for working with image data, which can be represented using matrices, which MATLAB was originally designed to manipulate. Some detail regarding the individual MATLAB codes will be given in this chapter, with more detail, and the codes themselves, given in Appendices VII-X. In addition to image processing techniques, image simulation is also often essential for analysis of phase contrast TEM images. This will be covered in Section 4.1. Section 4.2 will cover image registration, fringe spacing measurement and image filtering, real-space measurements of fringe spacings, and several methods for determination and quantification of particle shape. All of the topics in section 4.2 will include a MATLAB implementation.

4.1. Existing Methods

4.1.1. Image Simulations

Comparison of experimental images with image simulations are often necessary for the proper interpretation of phase contrast images, which are often complex (Bernal et al., 1998; Malm and O'Keefe, 1997; OKeefe, 1994). In this research, the software used to

simulate images was Java electron microscopy software (JEMS) v 4.3 (Stadelmann, 2016) which is a development of the EMS software (Stadelmann, 1987) by its original author, Pierre Stadelmann. Some models were built directly in JEMS, while others were built using CrystalMaker®. Visual comparisons of the experimental and simulated images were performed using Adobe Photoshop®.

The first and most important step in image simulation is building of the crystal model. A unit cell model was constructed for Ru using space group $P6_3/mcc$ based on the lattice parameters found in the database of the International Centre for Diffraction Data; a RuO_2 unit cell was also produced based on lattice parameters from the same source. Table 4-1 gives these lattice parameters. Table 4-2 additionally lists the largest 8 plane spacings for both Ru and RuO_2. The Ru unit cell was created in CrystalMaker, saved as a CIF, and imported into JEMS. Two nanoparticle models, approximately 5 and 10 nm in diameter, were also produced in CrystalMaker, based on the Wulff shape of Ru (Gavnholt, 2009), discussed in detail in Section 5.2. These are shown in Figure 4-1.

The models shown in Figure 4-1 were produced painstakingly in CrystalMaker by increasing the number of unit cells displayed, then cutting the model with different planes, corresponding to the desired facets. Each facet was cut individually. The model was then oriented on the screen in the orientation for which a simulation was desired. The whole model was converted to a "molecule" and then converted back into a "crystal" with orthorhombic symmetry. This yields a supercell, which can be exported as a CIF and then imported into JEMS. This process is quite tedious, since all steps must be repeated for every different size particle, and the orientation, conversion, and export steps must be repeated for every desired orientation of the particle.

An alternative method is now available in JEMS. This is a recent development of the software, in which now faceted particles can be produced rapidly in JEMS itself. Under the miscellany tab in JEMS there is a “to particle” menu item. The number of unit cells desired in each direction is first specified. Then a 3D model of the resulting sphere of atoms can be viewed. Facets can then be cut into the spherical particle by specifying the distance to the surface in various crystallographic orientations, as seen in Figure 4-2. Common orientations are suggested, but any orientation can be entered and used to cut the particle. The cut settings can be saved and reloaded. The faceted particle can then be oriented in the desired crystallographic orientation, and then cut into slices which can be opened in JEMS and used directly in a multislice image simulation. The resulting saved model can also be opened in JEMS and then exported as a CIF file for modification in CrystalMaker or another software.

Image simulations performed in this work using JEMS were based on the multislice algorithm (Goodman and Moodie, 1974; Kirkland, 1998), originally proposed by Cowley and Moodie (Cowley and Moodie, 1957). This method for simulating electron microscopy images begins by dividing up the crystal to be imaged into thin slices; the potential within each slice is projected along the beam direction to the entrance plane of the slice. After the projected potentials have been calculated, scattering functions are generated, which interact with the wave function of the incoming electrons. The wave function is scattered by the scattering function of the first slice, then propagated to the position of the next slice using a propagation function. The resulting wave function is scattered by the 2^{nd} slice, and again propagated to the following slice. This continues until the last slice in the crystal is reached, at which point the wave function is called the exit-surface wave function. This wave

function could be used to generate a “perfect” image of the crystal. However, such images could not be directly compared to experimental data since all experimental images must be generated using imperfect microscopes. Thus, additional calculations can be performed to convert the exit function into a realistic image by including the effects of the microscope’s contrast transfer function as well as the effect of the modulation transfer function of the camera. This is all done seamlessly in JEMS, but requires that the microscope parameters are set correctly, including the various aberrations, accelerating voltage, and stability parameters like the energy spread of the electron beam. A full description of the steps involved will not be included here.

Examples of two image simulations of nanoparticles are shown in Figure 4-3. A multiply twinned RuO_2 particle was simulated, using CrystalMaker to create the twinned particle, and then JEMS to perform the image simulation. A Ru particle not in a zone axis orientation was also successfully simulated. In this image, several features are replicated in the simulation. These include the primary lattice fringes, as well as more complex “curved” fringing effects in the center of the particle resulting from the shape and orientation. Additionally, bright and dark regions present in the image are also replicated in the simulation, giving a high degree of confidence that the orientation of this particle was correctly inferred from the single high resolution TEM image.

Comparison of experimental TEM images with simulated ones was not quantitative, but qualitative matching was performed by overlaying the simulated and experimental images in Photoshop, so that minor discrepancies could be observed. No simulated image ever matched the experimental images exactly, for a number of reasons. First, the Wulff-shaped models used were too simple to exactly match experimental data obtained from real

particles with defects and slight deviations from the Wulff shape. Additionally, no attempt was made to create Winterbottom-shaped models for any of the image simulations, as this would add little to our understanding and require significant effort. Secondly, while some particles were observed to be quite close to a known zone axis, the exact tilt of the particles was never known, since randomly oriented particles were observed and not tilted exactly, as described in 3.3.7. Finally, while some information was available on the aberrations present in the TEM during observation, a complete knowledge of the unique set of aberrations contributing to each image is not available, so these parameters could not be precisely set in the image simulation software. Since this work was focused primarily on the development of *operando* technique, not image simulation, the match between experiment and simulation was deemed adequate.

4.2. Methods Created or Enhanced for this Work

4.2.1. Image Registration

Image registration is a valuable technique for the analysis of TEM images when more than one image frame is acquired. Since nearly all images acquired as part of this project were acquired in sets of 5, as seen in Figure 3-24, image registration can be used to produce an average image from the 5 frames, increasing the signal to noise, and providing a baseline for comparing the 5 individual frames. Early in this work, ImageJ was used for image registration, (see image averages in Figure 3-24) but recently a MATLAB code was written to allow more control and automation (see Figure 4-4).

ImageJ does not include image registration in the basic software download, but installation of two plugins, “TurboReg” and “StackReg” provides this functionality. Specifically, StackReg can align a stack of images automatically (by iteratively calling TurboReg). If a single averaged frame is desired, and many individual frames are available, additional accuracy can be obtained by first running the registration, and then averaging every 2 (or 3) consecutive frames, and then performing another round of registration on the new image stack, which will have fewer frames, each with improved signal to noise. However, this method does not always produce higher quality images, since including a few blurred frames will result in a less sharp final result.

The MATLAB code which was written utilizes functions from MATLAB’s image processing toolbox, specifically intended to allow image registration. These functions have several options, however, and two distinct metrics are available for the registration, of which the mutual-information metric was selected. The alignment is performed in 2 passes, to allow more precise alignment of a small area selected after the first pass. For an initial rough alignment the code also takes advantage of a Fourier-space technique called phase correlation (Zitová and Flusser, 2003), not included as a pre-defined function. For more information on the structure of the MATLAB code, see Appendix VII.

4.2.2. Fringe Spacings Measurement and Fourier Filtering

The MATLAB code written for image registration was integrated into a larger code for performing Fourier filtering and measurement of image spacings with sub-pixel accuracy. Measuring fringe spacings in TEM images is an important task, and one which should be done with the greatest possible precision. This can be achieved by locating peaks in a

diffractogram with sub-pixel accuracy. A method for this was developed by de Ruijter, who was able to measure fringe spacings with a precision of less than 0.001 Å under favorable conditions (de Ruijter et al., 1995). This method was coded in MATLAB and used to determine the peak positions of fringes in an FFT with sub-pixel accuracy. This is essential, as shown in Figure 4-5, where it is clear that a single pixel error in a fringe measurement could lead to an incorrect spacing identification. In addition to measuring the spacings, the MATLAB code produces filtered images allowing the user to immediately see the spatial distribution of measured fringe spacings (Figure 4-6), and also saves all measured spacings in a data file, along with other valuable information generated by the code. An additional code can subsequently be run which is capable of importing CIF files of crystal structures, calculating possible lattice spacings from those structures, and finding the 3 lattice spacings from one or several structures that most closely match the measured fringe spacing. This is seen in Figure 4-7, and described in more detail in Appendix VII.

When hundreds of images are acquired over the course of an experiment rapidly summarizing this data is valuable. To this end, a method using ImageJ was developed for compositing many FFTs into a single visual representation. FFT patterns were first background subtracted using the "rolling ball" background subtraction (Sternberg, 1983) built into ImageJ. The patterns were then combined by finding (at each position in the image) the maximum pixel value from the set of FFTs to be combined. This is far superior to averaging, which would reduce the intensity of a spot found only in a single frame to a negligible value if hundreds of frames were combined. A composite FFT produced in this way from the data acquired in the experiment summarized in Figure 6-6 is shown in Figure 4-8. This method can be further enhanced for this data, since images were always acquired

in series of 5; prior to combining all the frames, all sets of 5 FFT frames were averaged, and the resulting average FFT patterns were background subtracted again. This can be rapidly accomplished using ImageJ which has a built-in function for such periodic averaging. A similar method can be used for diffraction patterns (Figure 3-8), as long as the center of all the patterns can be accurately identified, and the patterns aligned before they are combined.

The diffractograms shown in chapter 6 figures have been heavily processed to remove the background associated with non-periodic image features, including the amorphous SiO_2 support. This background subtraction is described in some detail in Appendix VII. This processing improves the appearance of the diffractograms, allowing bright spots to be discerned easily both close to the center of the pattern (where the background dominates the signal) and far from the center, where the signal is often low. It also results in the highest intensity in the diffractogram being located at a fringe spot rather than the center of the pattern, which can cause the intensities in the rest of the image to appear washed out, as seen in Figure 4-9. This figure also shows that this processing does not negatively impact the important information in the diffractogram, or introduce significant artifacts.

4.2.3. Real-Space Measurements

Often, measurement of fringe spacings can be made most accurately through the use of a Fourier transform (de Ruijter et al., 1995), though observed fringe spacings do not always match actual lattice spacings precisely (Malm and O'Keefe, 1997; Tsen et al., 2003). This information is, however, representative of the entire area from which the transform was generated, and spacings at the surface of nanoparticles cannot be measured relative to the

‘bulk’ spacing from the entire particle using a single diffractogram. Instead, real-space measurement methods should be used to directly measure fringe spacings.

Several principles should be applied to real-space measurements. First, measure the largest possible number of consecutive fringes, and divide the measured distance by the number of fringes. It must be noted, however, that this largest possible number may be quite small for surface spacings. Second, average the image perpendicular to the measured distance before attempting to measure it. The average should be performed over as large a distance as possible such that the averaged area is uniform. Again, this may be limited for nanoparticle surfaces. Third, ensure that the measured distance is exactly parallel to the fringe spacing measured. The first two principles listed here can be easily applied in Digital Micrograph, which includes a tool for this purpose (the profile tool).

Another method that can be used to increase the precision of fringe spacings measured in Digital Micrograph is to enlarge the image itself using bi-linear interpolation. This is beneficial, since there is sometimes significant uncertainty introduced into the measurement by the large width of a single channel in the profile generated by the profile tool. In Figure 4-10a this width is 0.26 Å (nearly 13% of the fringe spacing). Enlarging the image by 2x decreases the width of a single channel to 0.13 Å, allowing more precise measurements of spacings in the image. A detailed optimization of this procedure, or analysis of the effect of interpolation on the accuracy of the measurement was not attempted.

The third principle described above is not as easily applied in Digital Micrograph. Indeed, the majority of the difference between the profile obtained in a and b of Figure 4-10 arises from the slight mis-orientation of the profile tool lines in the two image

windows. Partly to resolve this issue, a MATLAB code was written for real-space measurement of fringe spacings by an undergraduate student working on this part of the work. Basically, a Fourier-space method was used to determine the orientation of fringes, which were then actually measured in real-space.

It should be emphasized that the *fringe* spacings measured in an image may not always accurately represent the *plane* spacings present in the observed crystal. It has been shown using image simulations, that fringe spacings may differ by several percent from the plane spacings from which they arise (Crozier, 1999; Malm and O'Keefe, 1997).

4.2.4. Morphology index and ellipse fitting

Statistical descriptions of catalyst particle size are commonly determined using (S)TEM techniques (Datye et al., 2006; Granqvist and Buhrman, 1976; Su et al., 2015). The shape of individual catalyst particles has also often been determined using electron microscopy (Chang et al., 2010; Chen et al., 2009; P. L. Hansen et al., 2002; Yankovich et al., 2014). However, any statistical description of the shape of a large ensemble of particles is much more difficult to obtain experimentally though this is an important goal (Barnard, 2014).

An attempt to provide such a statistical description was recently made by the group of Takeda (Takeda and Yoshida, 2013; Uchiyama et al., 2011). They introduced a "morphology index" from which they produced a morphology diagram, similar to a phase diagram. This morphology index is a number that quantifies the degree of faceting of a particle. The number is obtained by fitting an ellipse to the outline of the particle. A faceted particle will not be fit precisely by an ellipse, and the mean-squared-error of the fit is used

to calculate the morphology index; a larger error, and thus larger index, indicates a more faceted particle. This method was applied to the data obtained in this work, (as seen in Figure 4-11) using the code described in the following section. The method was found to be unsatisfactory, as visual analysis of the fitted particles showed that some particles which were clearly faceted were fit more accurately than other particles which had a distinctly rounded morphology.

4.2.5. Determining Particle Orientation and Shape

TEM images are 2D projections of the 3D sample structures in the microscope. The exact 3D structure can never be deduced from a single image; this is sometimes called the projection problem (Frank, 2014; Herman and Lewitt, 1979). This can be largely overcome by obtaining a series of images of the same structure from different perspectives, and then mathematically reconstructing the 3D object (Crowther et al., 1970; Frank, 2014; Lewitt and Bates, 1978). This is known as tomography. This might seem to be a natural technique to be applied for this work, where a goal is to determine the shape of nanoparticles. Tomography utilizing many images at different tilts could, in principle, determine the exact shape of single particles unambiguously. However, no tomography was performed in this work. There are several reasons this was not attempted, including the temporal resolution and beam dose required; This is discussed further in section 7.2.3, where an alternative is also suggested for future use.

Two methods for determining particle orientation and shape were developed and employed as part of this work. Both methods begin by assuming a shape (the Wulff shape, discussed in section 5.2), and proceed to determine whether the assumed shape matches

the experimental image. The first method was manual, and required that at least one set of lattice fringes be visible in the image of the nanoparticle. The second method was automated, but still required some human input. This method was less accurate, but made it possible to analyze larger ensembles of particles, even if those particles did not display lattice fringes. Perhaps most importantly, the automated method produces a quantitative measure of how well the model matches the experimental image, while the manual method is merely qualitative.

The manual method, shown schematically in Figure 4-12, begins by indexing the observed lattice fringes in the experimental image. If a single set of fringes is observed, the corresponding lattice plane is found in the 3D Wulff shaped model, using CrystalMaker and the model is rotated so that the orientation of the plane is identical to the orientation of this set of fringes in the image. Finally, the model is rotated around an axis normal to this lattice plane, such that the boundary contour of the model is made most similar to the contour of the experimentally imaged particle. This similarity is subjectively (but quite accurately) determined by the person rotating the model. If several sets of lattice fringes are visible, as in the particle shown in Figure 4-6, then the zone axis can be uniquely determined, and the model is simply viewed from the same zone axis direction, with an allowance for small off-axis tilts (Fraundorf et al., 2005). This manual method of orientation determination is dependent on the visibility of lattice fringes in the experimental image, and is furthermore subjective in the case of only a single set of fringes. The quality of the match to the model is also subjective, being simply the impression of the human observer, and is not quantified.

The automated method for orientation determination was implemented in MATLAB, and did not depend on human input for determining the orientation, or on the visibility of fringes. It instead relied entirely on the observed particle boundary contour, in a process known to the computer vision community as pose estimation (Reibacher, 2014; Rosenhahn and Sommer, 2005).

The observed particle boundary contour was determined using human input, but this input was semi-automated through the use of the same MATLAB code originally written to fit each particle outline by an ellipse (see Appendix VIII). This code allows the user to zoom in on a particle of interest in an image, and outline the area of the particle not obscured by the supporting sphere by clicking on points in the image, beginning at the sphere boundary and right-clicking on the final point, also on the boundary of the sphere. An ellipse is then fit to this outline, ignoring the straight line along the sphere boundary, as seen in Figure 4-11. The outline, the ellipse fit coefficients, and other important parameters are then saved in a data file, which can be subsequently read by other MATLAB codes.

The automated fitting of experimental outlines to determine particle orientation was achieved by first using MATLAB to rotate a Wulff-shaped model, similar to that seen in Figure 5-8, to 400 different quasi-random orientations, extracting the silhouette outline of the model in this orientation and then producing a 1D shape signature (based on the distance to the centroid) from the 2D outline (Costa et al., 2001). Similar 1D shape signatures were produced from the experimental particle outline traces already produced and saved by the ellipse fitting code. The shape signature of each experimental particle was then compared by cross correlation to the 400 shape signatures from the model, to

determine the most likely orientation of the particle. Because part of the Ru particle is always cut off by the SiO_2 support, 9 different cut fractions are also considered for each of the 400 orientations, as shown in Figure 4-13. The maximum cross correlation coefficient thus obtained for each particle (circled in red in Figure 4-13) was used as a metric for how well the Wulff model fit the particle image. (More details on this procedure and the MATLAB code may be found in Appendix IX.) The statistical distribution of this metric over an entire data set, has been used as a quantitative measure of how well the Wulff shape fit the experimental data under different environments. Specifically, a cross correlation coefficient above 0.85 was considered a good match. (See Appendix IX for details on how this number was obtained.) The similarity of Ru particles to the Wulff shape under different gas environments can thus be evaluated quantitatively.

4.3. Summary

This chapter revealed the methods used for image analysis and structure determination in this work. The creation of models for image simulations was described as along with a brief mention of the software used to perform multislice simulations. The two methods implemented for registering images acquired in sets of 5 were described (more detail in Appendix VII). The code written to perform fringe spacing measurement with sub-pixel accuracy was briefly explained, with more detail also given in Appendix VII. Principles which should be applied when performing real-space measurement of fringes were discussed. Finally two methods for determining the orientation of a nanoparticle, by first assuming them to be Wulff-shaped, were elucidated. The automated method, using cross-

correlation of shape signatures to rapidly determine the orientation of particles based solely on (manually traced) silhouettes was emphasized and more detail is given in Appendix IX.

Table 4-1 Ru and RuO_2 Lattice Parameters.

Crystal	System	Space Group	a	b	c
Ru	Hexagonal	$P6_3/mcc$	0.2704	0.2704	0.4282
RuO_2	Tetragonal	$P4_2/mnm$	0.4496	0.4496	0.3106

Table 4-2 Selected Ru and RuO_2 Plane Spacings.

	RuO_2 Plane	Spacing (nm^{-1})	Spacing (nm)
	(110)	3.15	0.318
	(011)	3.91	0.255
	(200)	4.45	0.225
	(111)	4.50	0.222
	$(\bar{2}10)$	4.98	0.201
	$(\bar{1}21)$	5.93	0.169
	$(\bar{2}20)$	6.30	0.159
	(002)	6.44	0.155
Ru Plane	**Ru Plane**	**Spacing (nm^{-1})**	**Spacing (nm)**
$(\mathbf{10\bar{1}0})$	(100)	4.27	0.234
(0002)	(002)	4.67	0.214
$(10\bar{1}1)$	(101)	4.87	0.206
$(10\bar{1}2)$	(102)	6.33	0.158
$(11\bar{2}0)$	(110)	7.39	0.135
$(\bar{1}2\bar{1}1)$	$(\bar{1}21)$	7.75	0.129
$(0\bar{1}13)$	$(0\bar{1}3)$	8.20	0.122
$(20\bar{2}0)$	(200)	8.53	0.117

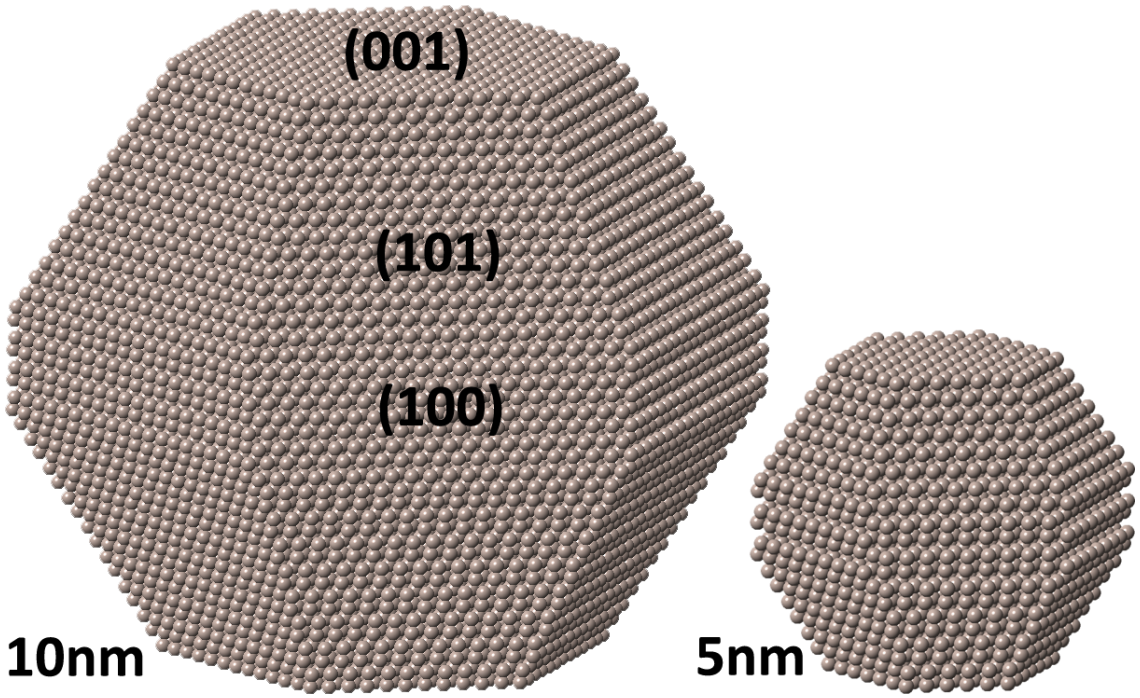

Figure 4-1 Ru Nanoparticle Models. Two Wulff-shaped Ru nanoparticle models, used in image simulations. Only the 3 largest surface facets have been retained.

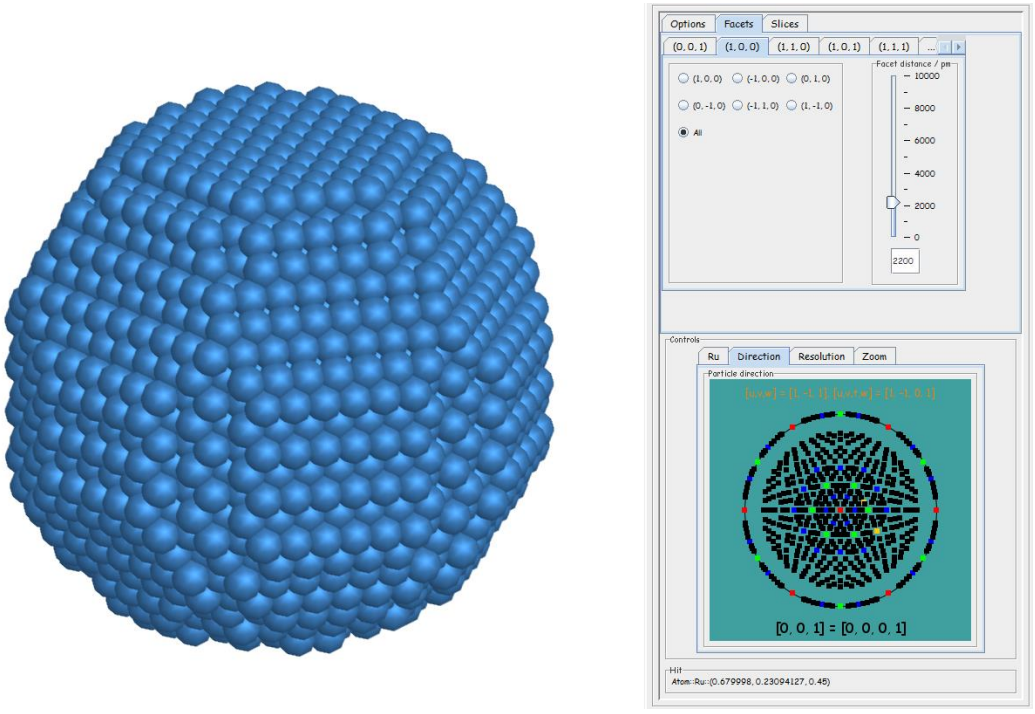

Figure 4-2 JEMS Faceted Particle Creation. Approximately 4.5nm diameter particle. At the right are options for cutting facets using specified planes in the hexagonal system, as well as a stereographic projection for selecting the orientation of the particle.

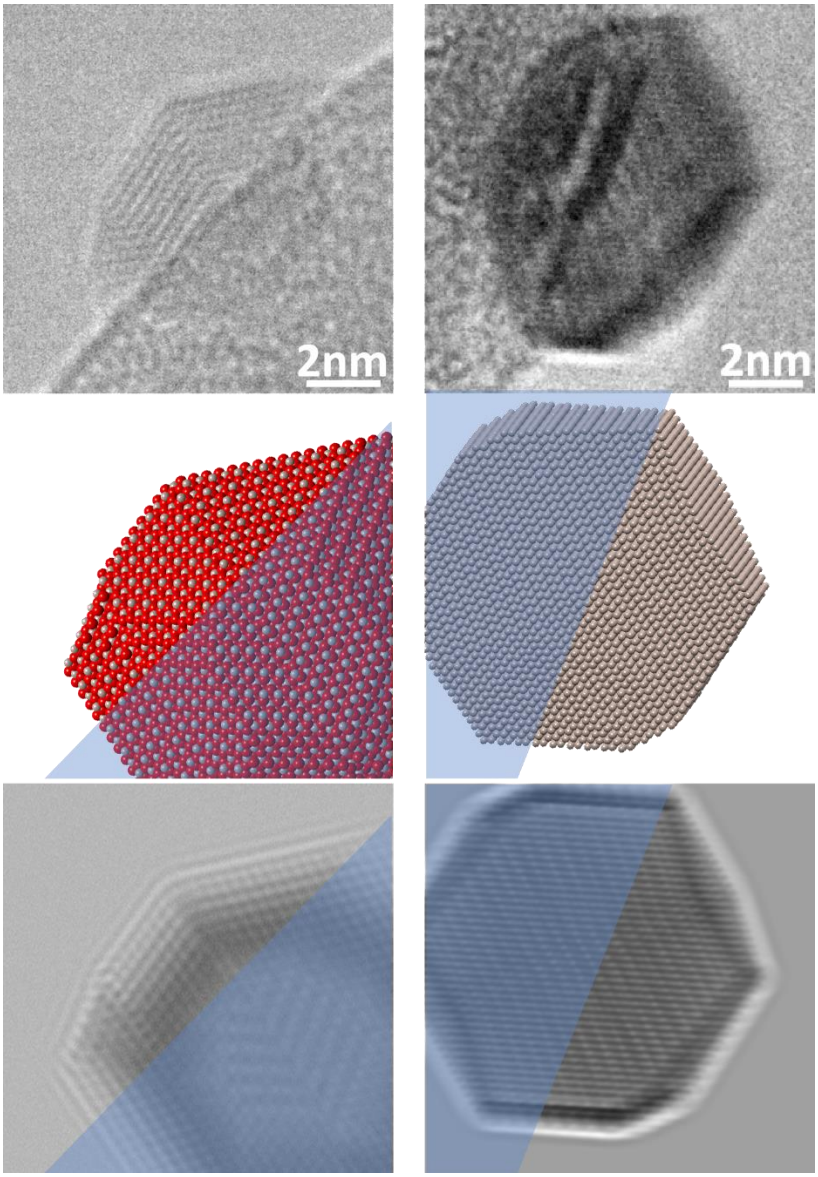

Figure 4-3 Particle Image Simulations. Left: A RuO_2 particle with multiple twin boundaries. Right: A Ru Particle not in a zone-axis orientation, which was nonetheless simulated successfully using JEMS.

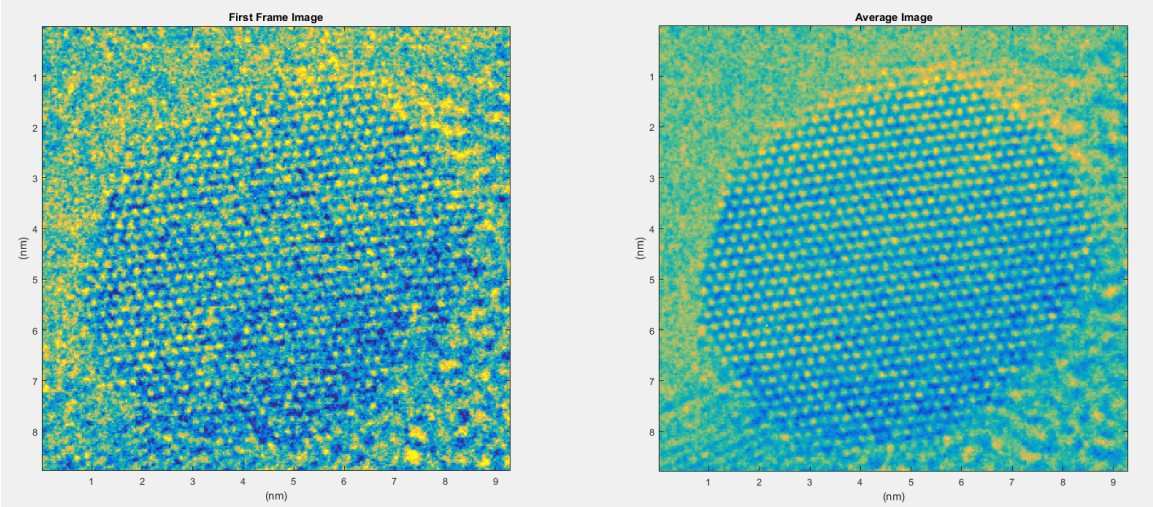

Figure 4-4 MATLAB Image Registration. Left: First of 5 image frames. Right: Average of 5 image frames, showing greatly enhanced signal to noise.

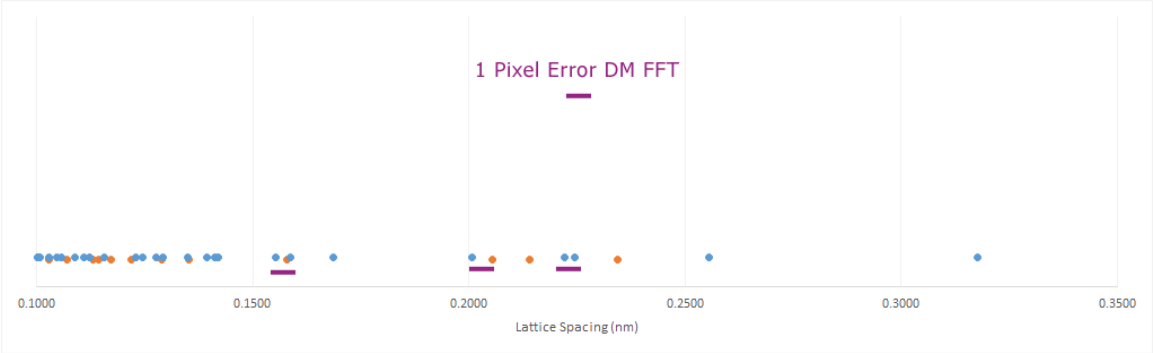

Figure 4-5 FFT Measurement Error. Ru (orange) and RuO_2 (blue) spacings are compared to the error (0.06 Å) which is introduced by mis-measuring a lattice fringe by a single pixel in an FFT of a 512x512 region (measuring an approximately 0.2 nm spacing at an actual image magnification of approximately 13000x.)

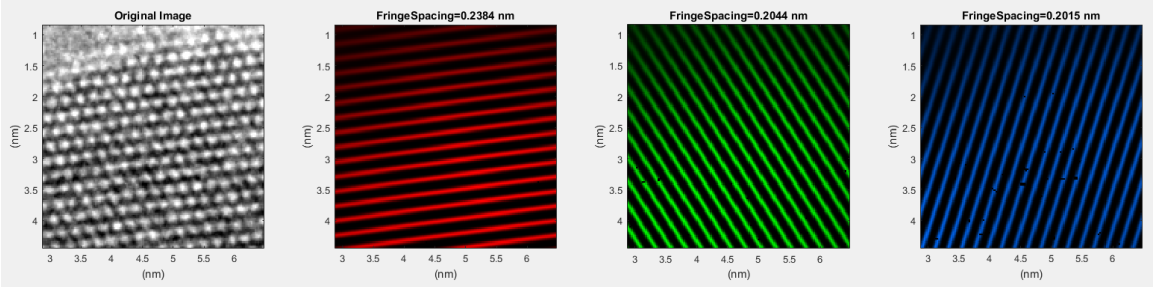

Figure 4-6 MATLAB Fourier Filtering. MATLAB figure, showing three filtered images, as well as the original unfiltered image. The 4 frames are linked, so that the area seen in all 4 is always identical.

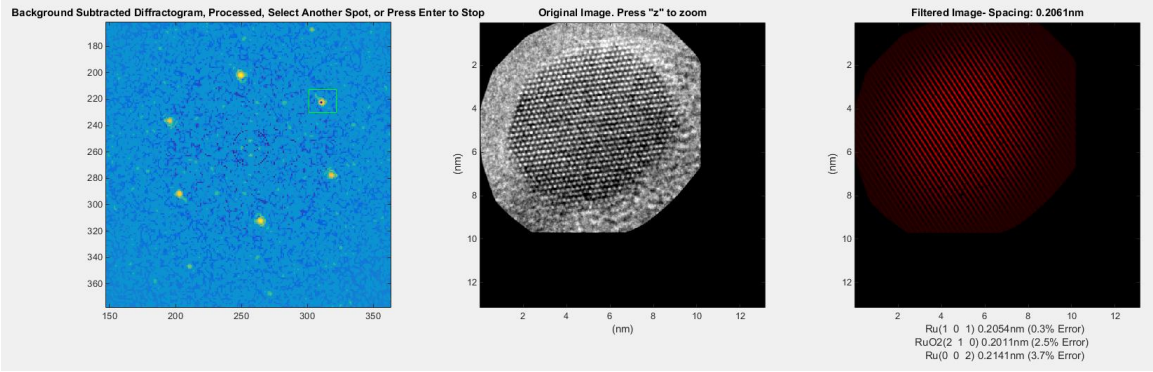

Figure 4-7 Image Indexing and Filtering Code. Left: A background-subtracted diffractogram, with the selected spot measured with sub-pixel accuracy. Center: the original image. Right: A filtered image, based on the lattice spacing selected in the diffractogram, with the measured spacing above, and 3 best-matching Ru or RuO_2 spacings below.

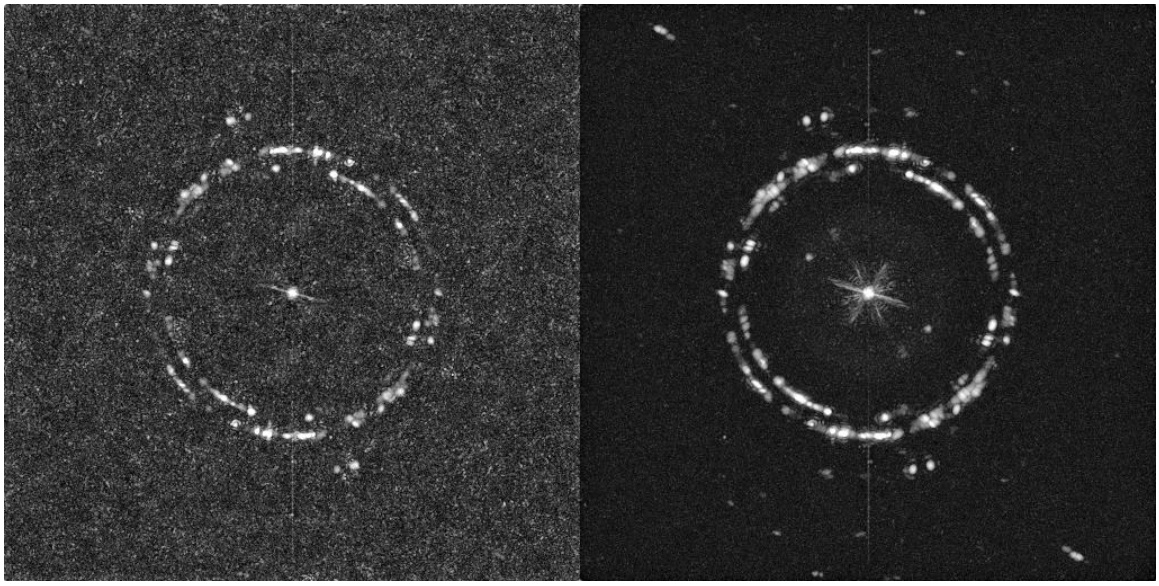

Figure 4-8 FFT Composite. Left: A composite of 2440 FFTs of images from the experiment summarized in Figure 6-6. Right: A composite of the same data with an additional averaging step, described in the text.

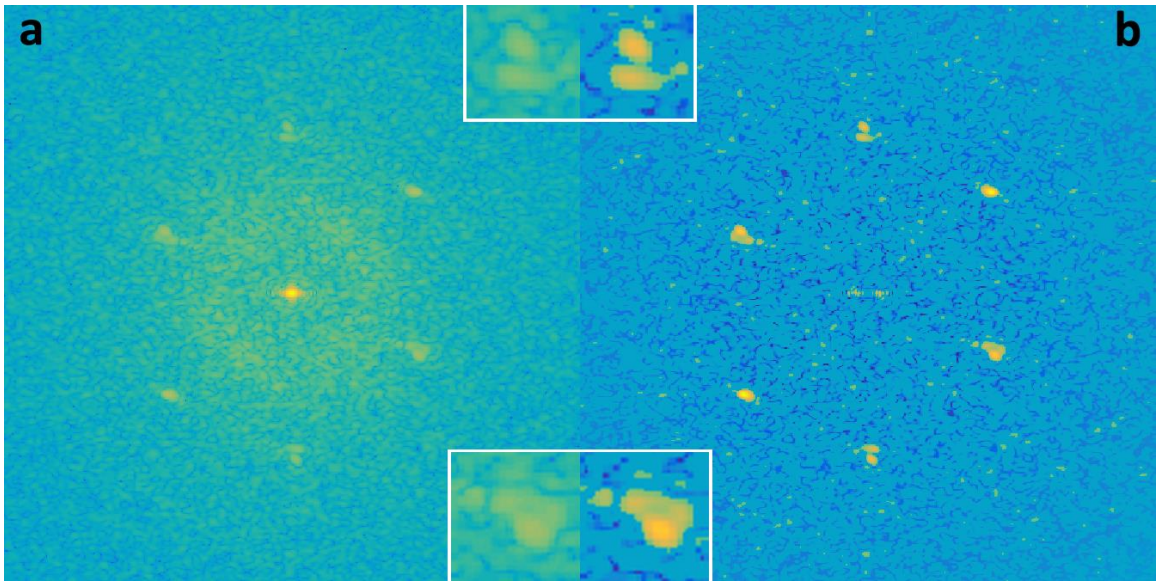

Figure 4-9 Diffractogram Processing. A diffractogram (from the image shown in Figure 6-3) before (a) and after (b) processing to remove the background intensity resulting from non-periodic image features such as the amorphous SiO_2 spheres. The processing does not alter the shape and size of spots, as shown in the insets which enlarge 2 spots from the diffractograms Details of the processing are given in Appendix VII.

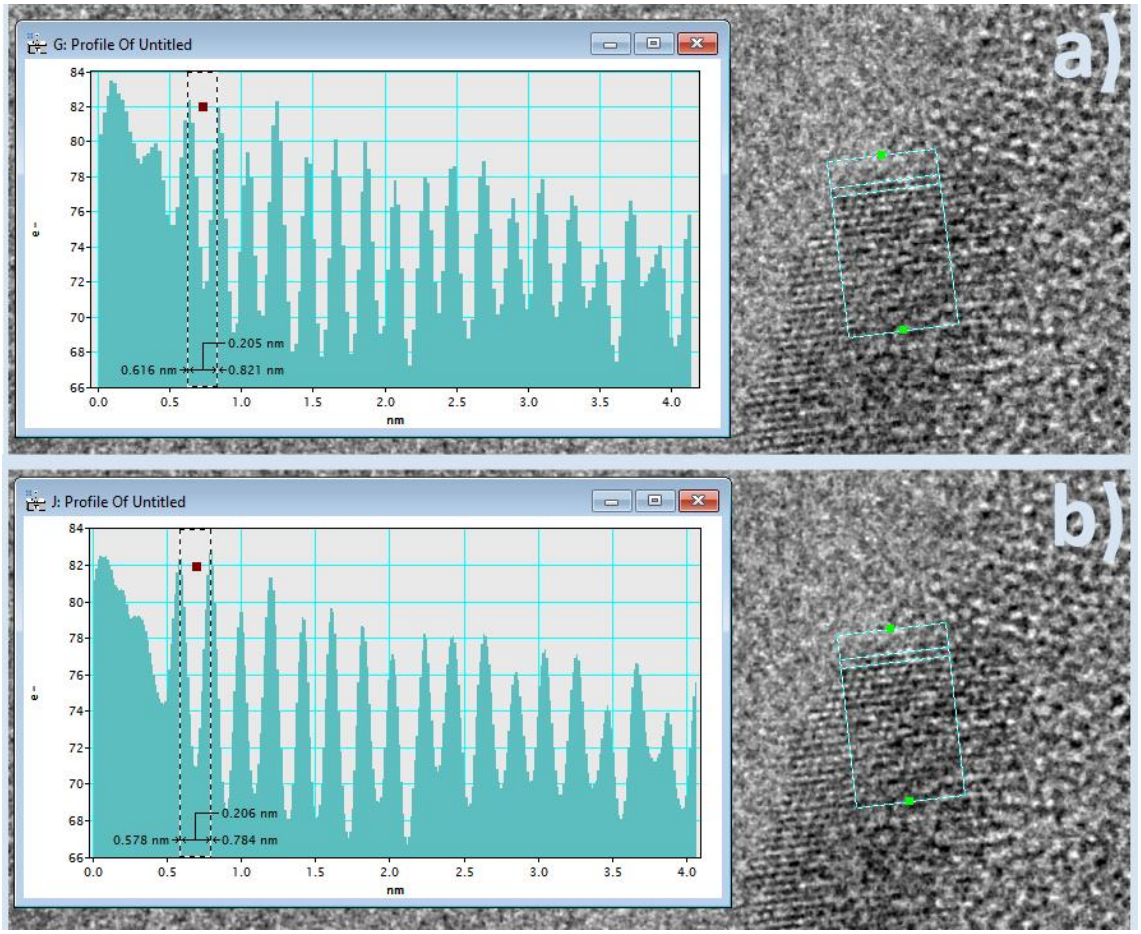

Figure 4-10 Digital Micrograph Real-Space Lattice Measurement. The profile tool is used to measure the spacing at the surface of a nanoparticle. Only the top fringe is measured. a) the measurement performed on the original image. b) the same measurement performed on an image that has been scaled up using bi-linear interpolation in Digital Micrograph, making the fringe measurement slightly more precise.

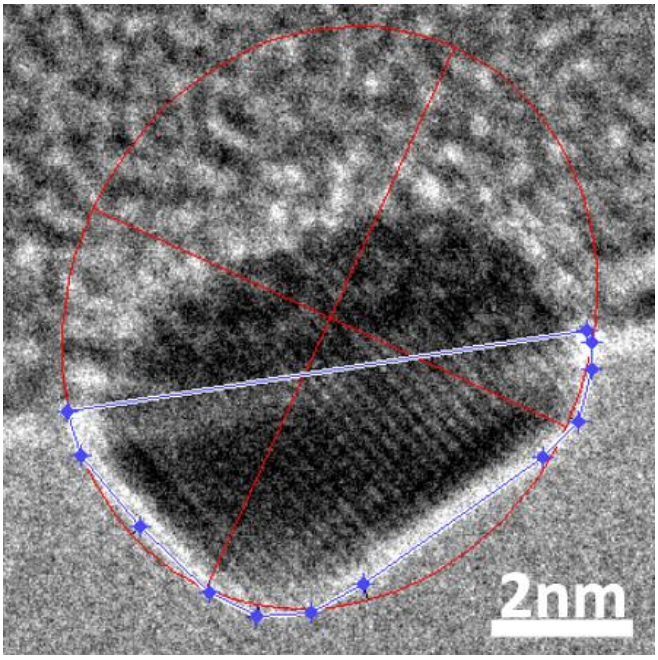

Figure 4-11 Ellipse Fitting of Experimental Particles. An image of a small Ru particle has been traced manually in MATLAB, and the trace was fit with an ellipse. The ellipse does not fit well, consistent with the particle's faceted shape.

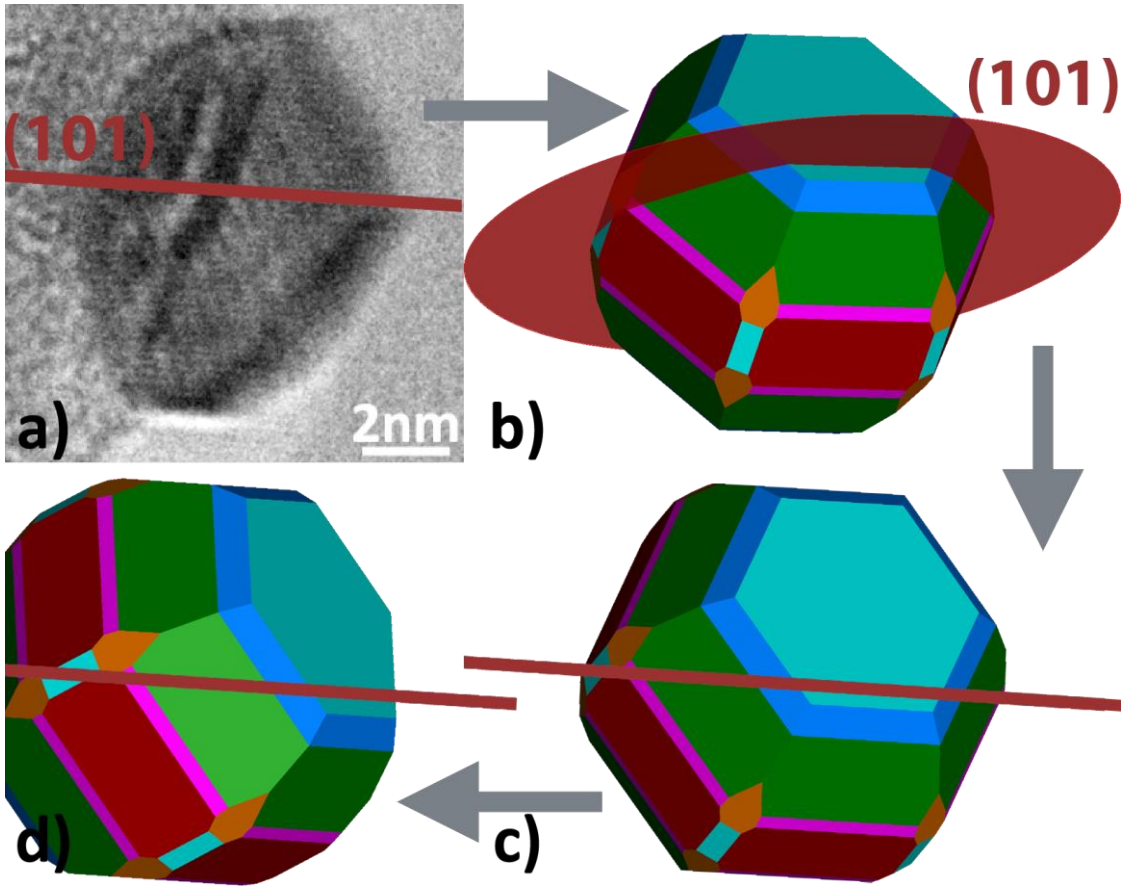

Figure 4-12 Manual Method for Particle Orientation Determination. a) The observed lattice fringe is indexed. b) The corresponding plane is found in the Wulff-shaped model. c) The orientation of this plane is set to the observed orientation. d) The model is rotated around an axis normal to this plane, such that the boundary contour is made most similar to the contour of the experimentally imaged particle.

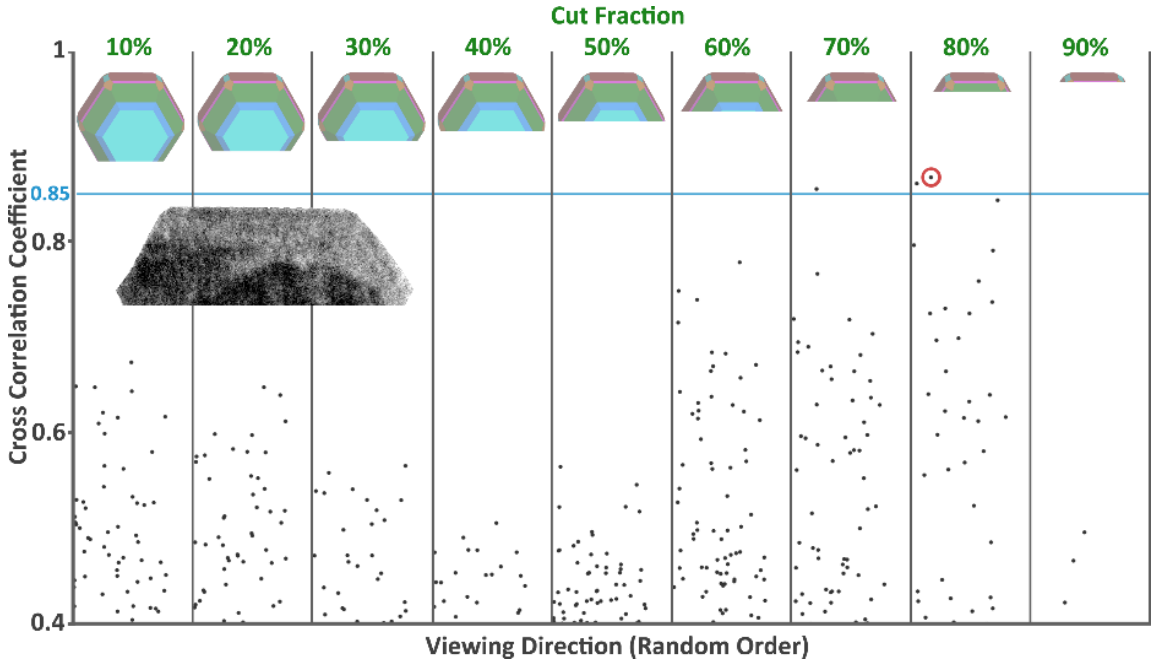

Figure 4-13 Automated Method for Particle Orientation Determination. The quantitative orientation matching of a single experimental particle shown, cut out of its image, in the top-left. The cross-correlation coefficients obtained for many different orientations of the Wulff-shaped model are plotted for 9 different model cut fractions (shown for a single orientation at the top of the plot). The data point circled in red is the coefficient from the orientation and cut that most closely matches the experimental image.

5. CO Oxidation over Ru/RuO_2: Catalytic Activity and Particle Shape

5.1. Confirmation of *Ex-Situ* Results

Several *operando* experiments were performed with stoichiometric mixtures of CO and O_2 to confirm the results found from *ex-situ* experiments (described in section 2.2.2). The EELS data from these experiments are summarized in Figure 5-1. Two results were specifically confirmed: the superior activity of a reduced catalyst and the CO conversion hysteresis observed for the reduced catalyst. Using the RIG-150, reduction and oxidation procedures identical to those used for the *ex-situ* experiments were used prior to *operando* experiments, with additional *in-situ* reduction performed for the reduced catalyst, since some oxidation is inevitable during transfer to the ETEM from the reactor. Moiré

5.1.1. Pre-Oxidized *Operando*

One of the first *operando* experiments successfully completed explored the behavior of the Ru catalyst after it was oxidized fully to RuO_2. The gas composition was fixed at a stoichiometric mixture of O_2 and CO with a total pressure of 2 Torr. In this experiment the temperature was increased from room temperature up to a maximum around 450°C, then the temperature was decreased back to room temperature. At each temperature, the catalyst was imaged to determine the morphology.

The CO conversion data obtained using EELS is summarized in Figure 5-2, where the CO conversion obtained using EELS is plotted along with the temperature recorded at the time each spectra was acquired. The catalyst displayed relatively low conversion compared to the catalyst reduced prior to CO conversion, as seen in Figure 5-1. It is also clear from

Figure 5-3 that no real hysteresis was observed in the CO conversion, in agreement with the *ex-situ* data given in Figure 2-6. This contrasts sharply with the data gathered for Ru reduced prior to CO oxidation, which displays a distinctive hysteresis, as seen in Figure 2-6 and Figure 5-1.

Images of the supported Ru catalyst were obtained at points indicated by grey circles in Figure 5-2. The structure of the catalyst throughout the experiment was observed to be primarily RuO_2 particles, or Ru core RuO_2 shell particles. A few examples are shown in Figure 5-4. Prolonged exposure to the electron beam resulted in further reduction of some particles to Ru metal.

5.1.2. Pre-Reduced *Operando* Experiment 1

A similar *operando* experiment was performed using a reduced catalyst to confirm both the higher activity compared with the oxidized catalyst as well as the existence of the hysteresis observed in the *ex-situ* experiment on a reduced Ru catalyst (Figure 2-6). After an *in-situ* reduction in H_2 at 480°C for 2 hours to ensure any oxide formed during transfer to the ETEM was reduced, the temperature was lowered to room temperature. CO and O_2 were then flowed in a stoichiometric mixture at a total pressure of 1 Torr. This is time equals zero in Figure 5-5. Images were acquired at room temperature, and then the temperature was increased to 200°C, and more images and spectra were taken. The temperature was then reduced back to room temperature and the catalyst left in the CO and O_2 flow overnight. This is indicated in Figure 5-5 by the jagged symbol at around 4 hours. The temperature was increased back to 200°C the following morning, and the experiment resumed. A maximum temperature of 330°C yielded a CO conversion of 22%. This is

significantly higher than the conversion at this temperature over the RuO_2 catalyst, which was less than 10%, in keeping with the *ex-situ* reactor results given in Figure 2-6. The reduced catalyst also displayed a hysteresis in the conversion, as seen in the *ex-situ* data. This hysteresis is visible in Figure 5-6. Because the temperature was not ramped smoothly as it was in the *ex-situ* experiment, the shape of the hysteresis is different, but the presence of the hysteresis is clear. The hysteresis is actual evidence of a change in the catalyst, and not just an apparent hysteresis due to a delay in the gas composition within the ETEM. The proof of this is most readily seen in Figure 5-5, which shows that temperature was dropped a bit too far originally, leading to conversions near 0, at around 22 hours; however, when the temperature was increased just slightly an hour and a half later, the activity increased dramatically, yielding conversions only reached at about 275°C before the catalyst was activated. This hour and a half gap proves that the change in conversion is due to a change in the activity of the catalyst, and is not a result of residual CO_2 gas from the high conversion condition.

Several images obtained in this experiment are shown in Figure 5-7. The first image was acquired at room temperature, and shows something with amorphous-like contrast on the top of the nanoparticle. It is unclear what this is, but it could be carbonaceous, or could even be an oxidized form of Ru (possibly not RuO_2) since no crystallinity is observable. Many of the images in this condition display similar material on the surfaces of the nanoparticles facing away from the sphere. The amorphous material seems clearly separated from the SiO_2 in most cases, making it unlikely that the material is SiO_2 from the support. The amorphous material observed at room temperature is much less prevalent at 200°C and not present after the catalyst was heated up to 330°C and cooled again to 200°C.

Apart from the elimination of the amorphous material, there was little observable change in the catalyst morphology, which matches the Wulff shape of Ru quite well.

The two experiments just described confirmed that the behavior observed in the *ex-situ* experiments could be duplicated during *operando* experiments in the Tecnai ETEM. Both the hysteresis of the reduced catalyst, and the significantly lower activity of the oxidized catalyst were replicated successfully. The pre-oxidized catalyst was confirmed to consist of oxide particles which were being slowly reduced *in-situ* as evidenced by the formation of Ru cores, while the reduced catalyst was confirmed to consist of Ru particles with no apparent oxide shells.

5.2. Nanoparticle Shape

Many of the fundamental studies of CO oxidation over Ru catalysts have been conducted using single crystal surfaces, however, industrial heterogeneous catalysts are usually supported nanoparticles. Knowledge of particle shape is important when working with nanoparticle catalysts (Roldan Cuenya, 2013; Roldan Cuenya and Behafarid, 2015). If the shape of a particle is known, then the distribution of surface facets is also known. Each facet presents a different atomic arrangement, and may have vastly different catalytic properties, especially for oxide particles (Narkhede et al., 2005; Over and Muhler, 2003; Roldan Cuenya and Behafarid, 2015). The distribution of edges and corners is also determined by the shape, and these may also have a significant impact on the catalytic activity.

Based on the surface energy of the various facets for a given metal, it is possible to calculate an equilibrium shape for a small particle. The thermodynamic equilibrium shape

of a single crystal nanoparticle in vacuum is known as the Wulff shape (Ringe, 2014; Wulff, 1901). A simple extension of this concept for a supported particle is the Winterbottom shape (Enterkin et al., 2011; Winterbottom, 1967; Zucker et al., 2012). Other modifications to this simple picture have also been made for crystals with twin planes, and factoring in kinetics (Marks and Peng, 2016; Ringe, 2014). Basically, the Wulff construction posits that the magnitude of a vector from a particle's center of mass to a surface facet, normal to that facet is proportional to the energy of that facet. A new software called Wulffmaker, distributed as a Wolfram Mathematica .cdf (computable document format) file was created recently (Zucker et al., 2012) to compute the Wulff shape of any particle from surface energy and crystallographic data, and is freely available online.

The Wulff construction assumes that all particle surfaces are in contact with only vacuum, which is rare. The Ru catalyst synthesized for this work is supported on amorphous silica, so a modification of the Wulff construction is needed to accurately describe the thermodynamic equilibrium shape of the particle in contact with another surface. In fact, rigorous proof (Winterbottom, 1967) shows that the modification (now known as the Winterbottom shape) is simply a truncation of the particle by the surface, but otherwise the particle retains the original Wulff shape. The degree of truncation depends on the relative energies of the particle surfaces in contact with vacuum and with the substrate, as well as the surface energy of the substrate in contact with vacuum. The Wulffmaker software also has the ability to produce Winterbottom shapes (Zucker et al., 2012).

There are at least 3 reasons why real particles would not conform to the Wulff or Winterbottom shape. These shapes are determined by thermodynamics alone, and

additional complication must be introduced to take kinetic limitations into consideration (Marks and Peng, 2016; Ringe, 2014). Also, at the atomic scale, sharp corners are high energy sites, and atoms may be missing from these high energy positions (Alpay et al., 2015). Finally, the Wulff and Winterbottom shapes are generally calculated based on surface energies for a particle in vacuum, rather than in a fluid, since surface energies for every crystal facet in a gaseous or liquid environment are not usually known.

The Wulff shape of a Ru nanoparticle, based on the 7 surface energies given in (Gavnholt, 2009), is shown in Figure 5-8 with a Winterbottom shape for Ru pictured as well. If the shape of an ensemble of supported Ru particles during catalysis was shown to match the Wulff/Winterbottom shape, this would allow the distribution of facets, edges, and corners to be calculated for that ensemble. The Ru catalyst synthesized for this work was supported on amorphous SiO_2 spheres, as described in section 2.1. This support does not have a strong metal-support interaction (Cornils et al., 2000), meaning that the Wulff/Winterbottom shape is more likely to be observed than if the support had a strong interaction with the metal particles (Kuwauchi et al., 2013; Ta et al., 2012).

5.3. The Shape of Nanoparticles in a High-Activity State

Wulff and Winterbottom shapes, like the ones shown in Figure 5-8 are generally calculated based on surface energies for a particle in vacuum, rather than in a fluid, since surface energies for every crystal facet in a gaseous or liquid environment are not usually known. While surface energies could hypothetically be measured under different gas conditions to determine the expected facet distributions, a more direct measurement can be made by acquiring images of nanoparticles in these environments. It is therefore interesting

to observe the shapes of Ru nanoparticles exposed to various gas mixtures relevant to CO oxidation, so that the distribution of surface facets actually present during reaction can be ascertained.

5.3.1. Pre-Reduced *Operando* Hysteresis

The pre-oxidized catalyst, being significantly less active, was largely ignored after the experiment described in section 5.1.1. The hysteresis of the reduced catalyst around 200°C, first encountered in Figure 2-4, and confirmed by the data in Figure 5-5, was an interesting behavior for further *in-situ* study. In this hysteresis, the catalyst displayed two distinctly different activities at the same temperature around 200°C (allowing the effect of simple thermal activation to be excluded), and this hysteresis was confirmed to be due to a change in the catalyst itself (and not a heat/gas flow artifact) by the experiment described in section 5.1.2. Thus, another *in-situ* experiment was attempted to further explore this behavior.

In the experiment summarized in Figure 5-10 the catalyst was imaged at around 200°C before and after increasing the temperature to 300°C in a stoichiometric mixture of CO and O_2 at 1 Torr. The CO conversion in the ETEM was monitored more closely during the minutes immediately following the temperature decrease back to 200°C by recording an EELS spectrum every 7 seconds for 3.5 minutes. This data is shown with the rest of the EELS acquired in Figure 5-11. In this figure, the hysteresis is again seen clearly. Again (as in the experiment shown in Figure 5-5) the temperature was decreased to a value too low for significant conversion to be observed in the ETEM once the temperature stabilized. Nevertheless, based on the *in-situ* data already presented which clearly established the

hysteresis behavior of the catalyst, it can be assumed that the catalyst remained in the higher activity state for some time after the temperature reached 200°C.

High resolution images could not be taken immediately after the temperature was decreased, since the sample drifts badly as the temperature reaches equilibrium. Images were thus taken approximately 1 hour after the temperature was decreased. A pair of images from before and after the temperature increase to 300°C are shown in Figure 5-12. Both of these images show particles which are clearly close to Winterbottom-shaped. Winterbottom-shaped atomic models are shown in the figure to the left of the images. Analysis of the Moiré fringes visible in the upper image is described in section 6.1.

More than 20 particles imaged at 200°C after the temperature was increased to 300°C were analyzed using the automatic orientation matching method described in section 4.2.5. The resulting models are shown in the left side of Figure 5-13, with the cropped experimental particle images on the right. The maximum cross correlations of the model shape signatures with the experimental shape signatures for this experiment are summarized in the distribution labeled "*Operando*" in Figure 5-19. The average value was 0.83. This is close to the value of 0.85, above which the match is considered to be very good. Particles imaged before heating to 300°C (not shown) were also analyzed, and yielded an average maximum-cross-correlation of 0.825. Thus, it appears that under stoichiometric gas conditions between 200-300°C, Ru particles are close to the Wulff/Winterbottom shape. Reasons for this behavior are discussed below in section 5.5.1.

5.4. The Shape of Nanoparticles in Single-Gas Environments

The shape of particles during active CO oxidation is close to matching the Wulff(Winterbottom) shape for Ru. A series of *in-situ* experiments were also performed in the Tecnai ETEM to determine whether the particle morphology would also be close to the Wulff shape under several single gas conditions. The particles under these conditions could thus be compared to particles observed during CO oxidation. This is summarized schematically in Figure 5-14. While only one particle from each gas environment is shown in Figure 5-14, at least 20 particles from each condition were analyzed using the automated shape matching procedure, to obtain information about the ensemble of particles responsible for catalytic activity. Details are given in the following sections.

5.4.1. CO *In-Situ*

Figure 5-15 shows the results from matching 25 particles imaged in 2 Torr pure CO at 200°C using the automated method for orientation matching described in section 4.2.5. The resulting models are shown in the left side of Figure 5-15, with the cropped experimental particle images on the right. The maximum cross correlations of the model shape signatures with the experimental shape signatures for this experiment are summarized in the distribution labeled CO in Figure 5-19. The average value was 0.78. This indicates that the particle ensemble matches the Wulff shape reasonably well, though there are some particles that are not fit well by the Wulff-shaped model, producing a tail in the CO distribution shown in Figure 5-19. This is not unexpected, since this sample seems to be close to the Wulff shape, and at 200°C it is unlikely that CO gas would alter the shape of the sample.

It is interesting to note that at this temperature in CO, little amorphous material is observed on top of the Ru particles.

5.4.2. CO_2 *In-Situ*

Figure 5-16 shows the results from matching 22 particles imaged in 2 Torr pure CO_2 at 200°C using the automated method for orientation matching described in section 4.2.5. The resulting models are shown in the left side of Figure 5-16, with the cropped experimental particle images on the right. The maximum cross correlations of the model shape signatures with the experimental shape signatures for this experiment are summarized in the distribution labeled CO_2 in Figure 5-19. The average value was 0.78; this demonstrates that the particles match the Wulff shape reasonably well, though there are a few particles that are not fit well by the Wulff-shaped model, and fall in the tail in the CO_2 distribution shown in Figure 5-19. Again, this is not unexpected, since at 200°C it is unlikely that CO_2 gas would significantly alter the shape of the sample.

5.4.3. O_2 *In-Situ*

Ru particles exposed to O_2 undergo significant oxidation, as seen in the 2 images of particles exposed to O_2 shown in Figure 5-14 and Figure 5-18. This oxidation was not complete however, and a core-shell structure was observed. Figure 5-17 shows the results from matching 23 particles imaged in 2 Torr pure O_2 at 200°C using the automated method for orientation matching described in section 4.2.5. The mean maximum-cross-correlation under this condition was found to be 0.77, which is still close to the values obtained for the other 3 conditions, and the facet distribution (based on an assumed Ru Wulff shape) is also

largely unaffected. This is reasonable, since the original Ru particle shape seems to be preserved underneath the 1 nm oxide layer which is formed. Ru particles maintaining their shape is consistent with an oxidation process in which the oxygen diffuses down to the Ru-RuO_2 interface (Coloma Ribera et al., 2015; Reuter et al., 2002). It is quite different from the behavior observed for Ni, Fe, Cu, and Al in which, for small nanoparticles, metal atoms diffuse up through the oxide, resulting in void structures (Chenna et al., 2011; Nakamura et al., 2007; Railsback et al., 2010; Wang et al., 2005).

5.4.4. Summary of *In-Situ* Data

The image data acquired from the *in-situ* experiments was valuable as a benchmark against which to compare the *operando* images of the Ru catalyst. A single representative image from each condition is shown in Figure 5-18. It is clear from these images that the Ru particles in CO_2 and CO appear to be fully reduced, and the particle in O_2 is oxidized with a core-shell structure. The match between the shapes of the experimental particles and the Ru Wulff shape is good, for all the *in-situ* conditions, though the particles exposed to O_2 had more particles which poorly matched the Wulff shape, as seen in the distributions given in Figure 5-19.

5.5. Shape Analysis Conclusions and Discussion

5.5.1. Shape of Ru Catalyst During CO Oxidation

Data from an *operando* experiment performed on the Tecnai ETEM are shown in Figure 5-12. As noted previously, the catalyst shape before and after high conversion is quite similar, with mean maximum-cross-correlations of 0.825 and 0.830 respectively. This

orientation matching as well as a simple visual inspection of the data indicate that the particle morphology is not significantly different before and after the reaction. Several hypotheses have been considered to explain this apparent lack of change in particle morphologies.

The first hypothesis is that Ru cannot change shape because it is a refractory metal and the temperatures at which the catalytic reactions take place are too low for significant diffusion to occur. Often the Tammann temperature ($0.5T_{melt}$) is used as a guide to determine whether bulk diffusion is likely. Above this temperature, significant shape changes would be expected to occur, since atoms could diffuse easily, while significantly below this temperature much less shape change is expected. This hypothesis works well to explain why shape changes have been observed in Cu nanoparticles in CO and O_2 using ETEM (P. L. Hansen et al., 2002); Cu has a Tammann temperature of 680 K, and the experiments were performed around 490 K, about 72% of the Tammann temperature. Ru has a Tammann temperature of 1300 K and the experiments on the reduced Ru catalyst described in this dissertation remain below 575 K, just 44% of the Tammann temperature. Additionally, the recent *operando* TEM work on Pt during CO oxidation supports this interpretation (Vendelbo et al., 2014b). In this work, obvious changes in the faceting of Pt particles was observed at 660 K. Pt has a Tammann temperature of 1020 K, so the changes were observed at 65% of the Tammann temperature. This hypothesis is challenged however by the work of Takeda in which Au nanoparticles were observed to change morphology at room temperature under different gas mixtures of CO and O_2 (Uchiyama et al., 2011). Au has a Tammann temperature of 670, so room temperature is only 44% of the Tammann temperature; this is exactly the same ratio as in our experiments. All these temperatures are

summarized in Table 5-3. This may be explained by the higher dose rate used to observe the Au nanoparticles; the lowest dose rate used in that work was still over 8 times higher than maintained in the Titan experiments reported here. While this will not raise the temperature of the particles significantly, as explained by the authors, direct excitation of individual atoms may lead to enhanced diffusion. It is also possible that this observation on gold nanoparticles is not affected significantly by the electron beam, and thus disproves the hypothesis that the temperatures used in this work are too low for significant shape changes to be observed, since the Tammann temperature ratios (see Table 5-3) are identical.

Another possible hypothesis which should be considered is whether the Ru surface energies are simply too uniform to drive significant changes in shape under different conditions. The surface energies (in $eV/Å^2$) of the 3 largest Ru facets given in Table 5-1 are 0.176, 0.197, and 0.199; these all vary from their mean by less than less than 8%. However, Cu, Pt, and Au also have relatively uniform surface energies (Yoo et al., 2016), as seen in Table 5-4, and vary from their means by less than 7%, 14%, and 12% respectively. Oxides typically vary by much more than this, with the variation in RuO_2 being 18% at the 200°C condition and 23% at the room temperature condition presented in Table 5-2. If the difference in surface energies for Ru were much higher, then this would provide a greater driving force for a shape change. However, Cu clearly undergoes shape changes despite its small surface energy anisotropy, so this hypothesis alone cannot explain the difference between Cu and Ru.

A third hypothesis that could specifically explain the difference between the lack of shape changes on Ru and clear shape changes on a gold catalyst at room temperature

involves the presence and identity of surface adsorbates. As mentioned in section 1.3.1, Ru is different from other CO oxidation catalysts like Au, Pt and Pd, because it preferentially adsorbs O rather than CO under stoichiometric conditions. In fact a simple calculation of CO and oxygen coverage based on adsorption energies from (Kalinkin and Savchenko, 1982; Pfnür and Menzel, 1983) (see Table 5-5) gives a difference of 17 orders of magnitude in the number of oxygen and CO species adsorbed under a stoichiometric ratio of CO and O_2 in the low pressure limit of the Langmuir isotherm. Using this simple approximation, even if the O_2 pressure is lowered to 10^{-6} Torr, with 2 Torr of CO, a difference of 11 orders of magnitude remains. While this approximation is rough, the abundance of oxygen on the surface under nearly all non-UHV conditions is well-attested in the literature on CO oxidation over Ru reviewed in section 1.3.2 and especially emphasized by (Chen et al., 2007). It is possible that oxygen on the surface might restrict the diffusion of Ru, which would make shape changes more difficult. A study of the rearrangement of Ru steps following oxygen adsorption concluded that "...an ordered oxygen layer obstructs the large scale diffusion of Ru atoms…" (Held et al., 1995). Additionally, if differences in the gas adsorbates on the nanoparticle surfaces are responsible for the morphology changes observed on Cu, Pt, and Au, as proposed, then a surface always dominated by adsorbed oxygen would preclude this driver of changes in shape.

The temperature dependent diffusion alone cannot explain the unique behavior of Ru, which lacks the shape changes observed in Au, Cu, and Pt. Surface energy anisotropy is also inadequate to fully explain the difference between Ru and these metals. The presence of O adsorbed on the surface under all conditions studied may restrict the movement of Ru on the surface, and may also indicate that there is no adsorbate-induced change in surface

energies, and thus no driving force for morphology changes. However, it is likely that all three of these play a role in the unique behavior of Ru, with the temperature dependent diffusion a dominant factor.

Whatever the reason that Ru particles maintain the same shape under a variety of gas environments, as shown in this chapter, the fact remains that Ru nevertheless displays marked changes in activity under different conditions. If these activity changes are not the result of changes in the particle morphology, it is likely that the surface structure/phase has been changed either by oxidation or reduction of the surface, and this is responsible for the observed activity changes. However, it is not possible to observe the structure of the surface directly using the Tecnai ETEM due to delocalization, which prevents the image at the surface from being directly interpretable (Otten and Coene, 1993).

Chapter 6 of this dissertation is focused on determination of the surface structures present during catalysis, mainly from aberration corrected TEM images obtained using the Titan ETEM. However, knowledge of the Ru particle shape is still valuable as surface structures are studied. Assumptions about the 3D shape of the catalyst particles simplifies the task of interpreting the structures observed, making it possible to produce simple models which can become the initial input for TEM image simulations. Without any assumptions about the particle shape, image simulations of these nanoparticles might not be possible, and would certainly require much more trial and error.

5.5.2. Extracting Catalytically Relevant Parameters

Knowledge of the shape of a catalyst particle is not intrinsically valuable. This shape information must be converted into catalytically relevant knowledge. This can be

accomplished by determining the distribution of surface facets present during catalysis. Each facet is different, presenting a different atomic geometry for the adsorption, surface migration, reaction, and desorption processes of which a catalytic conversion is composed. Much of the literature reviewed in section 1.3.2 was focused on single crystal surfaces, while industrial catalysts are typically supported particles.

After the best-matching model orientation has been determined for each experimentally observed particle, the distribution of surface facets for that Winterbottom shape can be known. Now, it is not only possible to calculate the facet area distribution for an ideal Wulff particle, but also the average facet area distributions from the ensembles of Winterbottom-shaped particles observed under different conditions. This was completed by counting the number of each family of facets on each best-matching 3D model.

The facet area distributions from the CO, CO_2, O_2, and *operando* environments are given in Figure 5-20. This data shows that the Winterbottom shapes of particles in the CO, CO_2 and *operando* environments expose the same surface facets as unsupported Ru Wulff particles would, with very little variation due to the gas environment. Data from all individual particles, given in Figure 5-21, show that individual particles display more variation, but the effect of the ensemble is that deviations become averaged out. This result is not surprising for Ru on amorphous silica, since this support was chosen to minimize the effect of the support on the particles, and was unlikely to foster a specific favorable orientation. A more strongly interacting support like CeO_2 would likely effect the orientation of the particles more strongly (Kuwauchi et al., 2013; Ta et al., 2012), and thus possibly skew the distribution of exposed facets.

While the shape information extracted by this analysis has not uncovered any dramatic effects of the gas environment, it is nonetheless useful information. Most of the research devoted to CO oxidation over Ru has been focused on the low-energy (001) surface of Ru (Böttcher et al., 1997; Gao and Goodman, 2012; Goodman et al., 2007a; He et al., 2005; Peden and Goodman, 1986), or the (101) surface of RuO_2 (Fan et al., 2001; Over, 2012; Over et al., 2000; Wang et al., 2002). Study of the (001) surface of Ru was justified by Peden and Goodman by arguing that the turnover frequencies they calculated on this surface were quite similar to turnover frequencies obtained from supported nanoparticle Ru catalysts (Peden and Goodman, 1986). However, from Figure 5-20 it is clear that the Ru(001) facet accounted for only 18% of the nanoparticle surface area in the *operando* environment in which CO was being actively oxidized. This suggests that the activity of a supported catalyst is unlikely to be determined by the activity of the (001) surface, and emphasizes the importance of other surfaces such as the {101} family of facets.

5.6. Summary

Operando experiments performed on the Tecnai ETEM confirmed the existence of a hysteresis in the CO conversion previously observed in an *ex-situ* reactor, as well as the much lower activity of RuO_2 particles. The thermodynamic equilibrium Wulff shape of Ru was defined and discussed. The shape of nanoparticles both during CO oxidation and under O_2, CO, and CO_2 gas environments was examined, and found to be close to the Wulff shape in all cases, though in O_2 a thick oxide shell was formed. Hypotheses explaining the stability of the Wulff shape in this system were discussed in the context of previous ETEM

work by other researchers who observed shape changes in nanoparticles of other metals. Finally, parameters important for catalysis were extracted from the Wulff-shaped model.

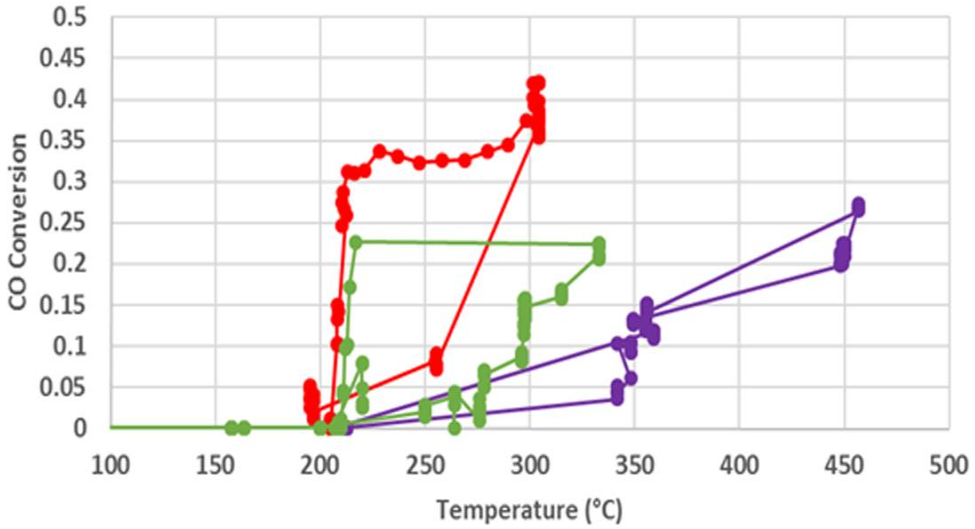

Figure 5-1 *Operando* EELS Summary. Quantified core-loss EELS data from 3 experiments (Figures 5-3, 5-6, and 5-9) confirm the results of *ex-situ* experiments (Figure 2-6). Green and red data are from a pre-reduced catalyst, displaying hysteresis and high activity relative to a pre-oxidized catalyst (purple) which also lacks the hysteresis. All three experiments were performed using stoichiometric mixtures of CO and O_2. In each case, the lowest conversions are observed on the temperature ramp up.

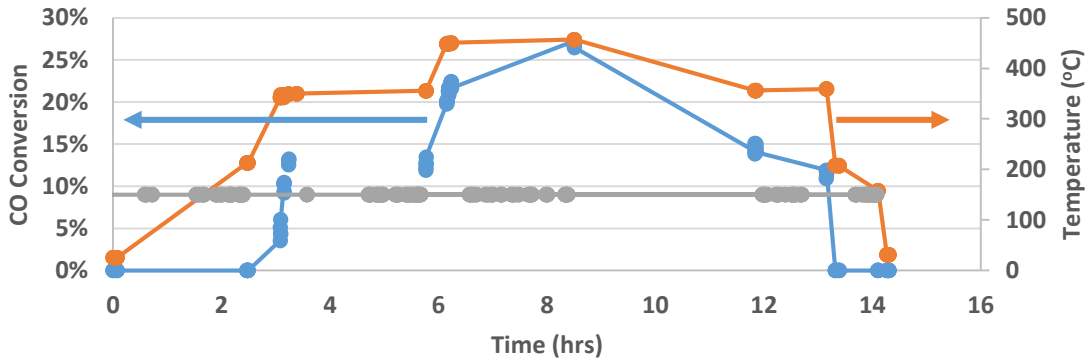

Figure 5-2 Pre-Oxidized *Operando* Experiment. A summary of the pre-oxidized catalyst *operando* experiment, showing the temperature on the right axis, and the CO conversion on the left plotted over time. Times when images were acquired are shown as grey circles.

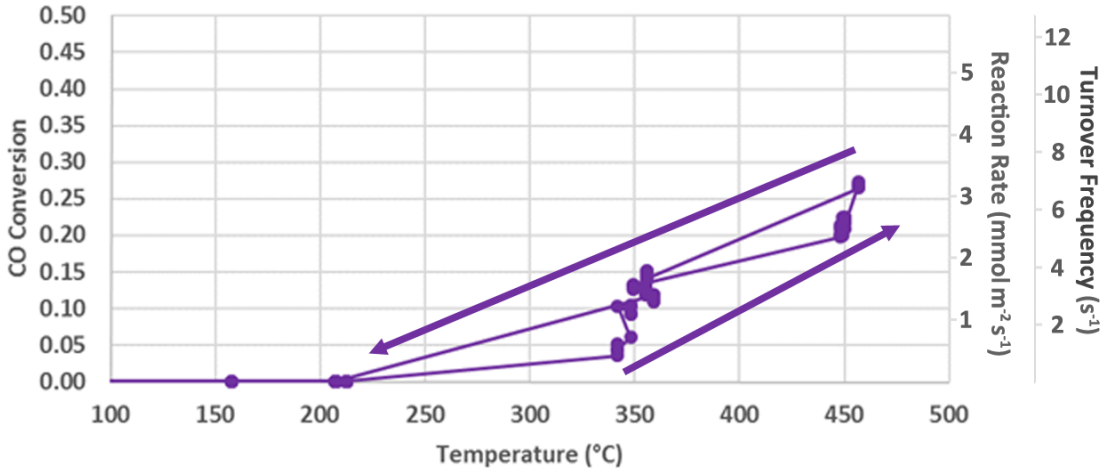

Figure 5-3 Pre-Oxidized Conversion vs Temperature. A plot of the data in Figure 5-2 with CO conversion plotted vs temperature. The data does not display a hysteresis, consistent with the *ex-situ* data shown in Figure 2-6.

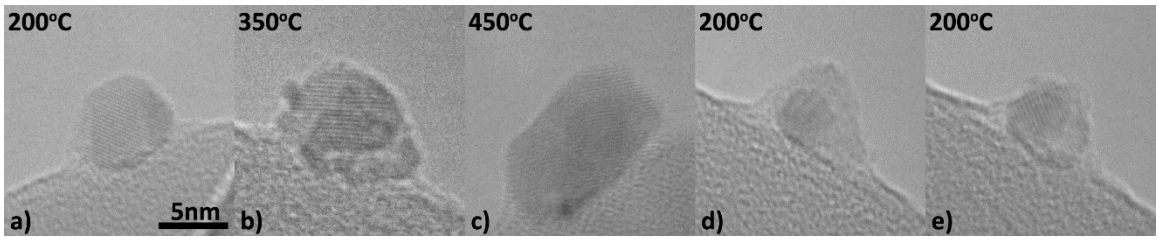

Figure 5-4 Pre-Oxidized *Operando* Images. A few selected images from the pre-oxidized *operando* experiment in a stoichiometric mixture of CO and O_2 a) RuO_2 particle. b) RuO_2 particle with small Ru particles forming. c) a core-shell Ru-RuO_2 particle. d) and e) a core shell particle where the RuO_2 was found to be reduced; this was likely accelerated by the electron beam.

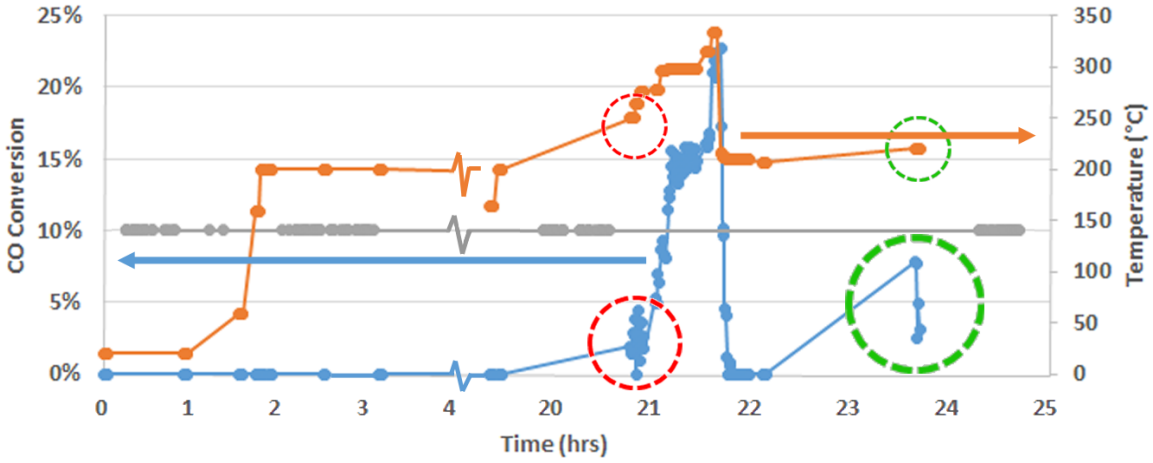

Figure 5-5 Pre-Reduced *Operando* Experiment. A summary of the first pre-reduced catalyst *operando* experiment, showing the temperature on the right axis, and the CO conversion on the left plotted over time. Times when images were acquired are shown as grey circles. If the activity of the catalyst was unchanged during the experiment, then the conversion data in green should be lower than that circled in red, since the temperature is lower. The circled data is thus proof that the hysteresis was observed. It must be a real, structural effect, and not merely an artifact since the data circled in green was acquired about an hour and a half after the conversion had been high.

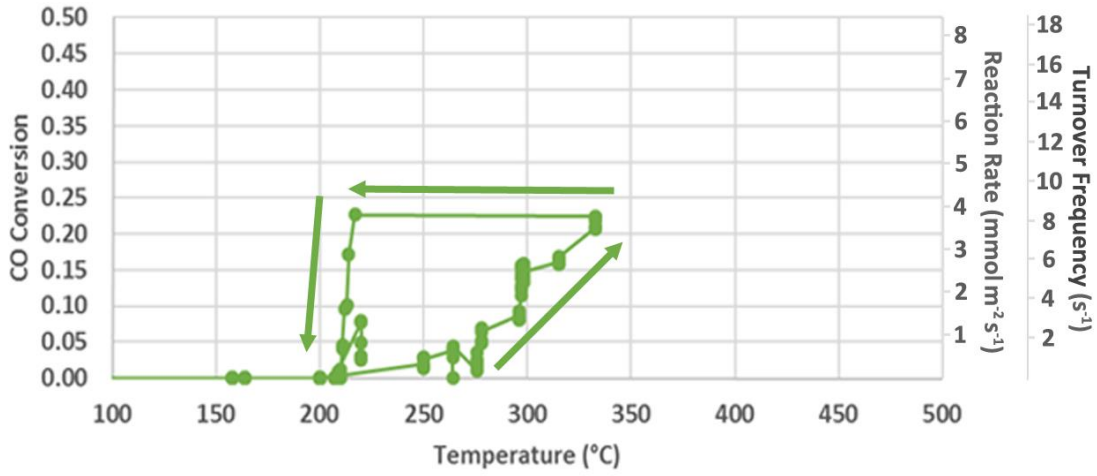

Figure 5-6 Pre-Reduced Conversion vs Temperature. A plot of the data in Figure 5-5 with CO conversion plotted vs temperature. The data shows a clear hysteresis, consistent with the data in Figure 2-6.

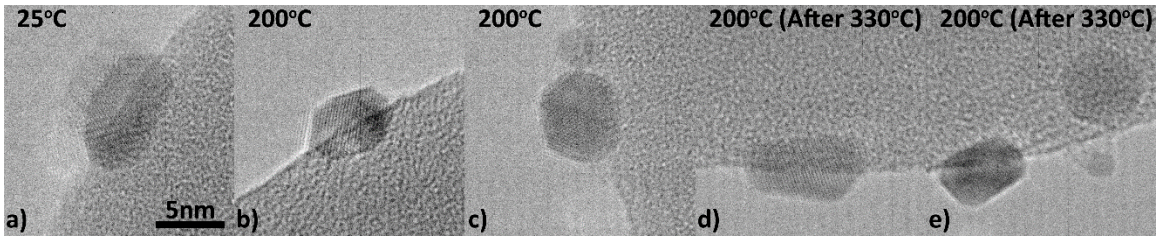

Figure 5-7 Pre-Reduced *Operando* Images. A few selected images from the first pre-reduced *operando* experiment in a stoichiometric mixture of CO and O_2. a) Ru particle at room temperature with some amorphous material on top. b) and c) Ru particles with clean surfaces at 200°C prior to heating to 300°C. d) and e) Ru particles at 200°C after heating to 300°C.

Table 5-1 Ru Wulff Data. Surface energies and areas for Ru Wulff shape(Gavnholt, 2009). The shape obtained from this data is shown in Figure 5-8.

Ru Facet	Surface Energy ($eV/Å^2$)	Percentage of Wulff Surface Area
(001)	0.176	17%
(100)	0.197	20%
(101)	0.199	40%
(201)	0.203	6%
(102)	0.210	11%
(110)	0.221	2%
(111)	0.221	4%

Table 5-2 RuO_2 Wulff Data. Surface energies and areas for RuO_2 Wulff shapes, under two different conditions (Wang et al., 2013). Top: 2 Torr O_2 at 200°C. Bottom: 10^{-6} Torr O_2 at 20°C. Corresponding Wulff shapes are shown in Figure 5-9.

RuO_2 Facet	Surface Energy ($eV/Å^2$)	Percentage of Wulff Surface Area
(111)	0.043	86%
(110)	0.054	14%
(101)	0.061	0%
(001)	0.068	0%
(100)	0.077	0%

RuO_2 Facet	Surface Energy ($eV/Å^2$)	Percentage of Wulff Surface Area
(111)	0.033	98%
(110)	0.046	2%
(101)	0.049	0%
(001)	0.053	0%
(100)	0.066	0%

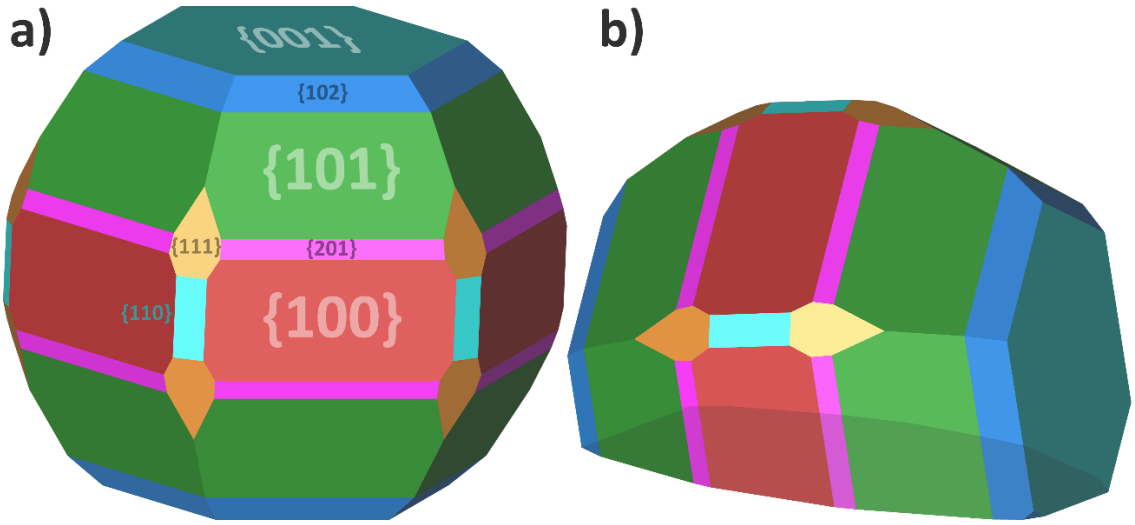

Figure 5-8 Ru Wulff Shape. Theoretical Wulff shape for Ru in vacuum based on the surface energies from (Gavnholt, 2009) given in Table 5-1. b) Winterbottom shape for a Ru particle in vacuum in contact with a non-interacting support, shown in the orientation observed experimentally in Figure 6-1.

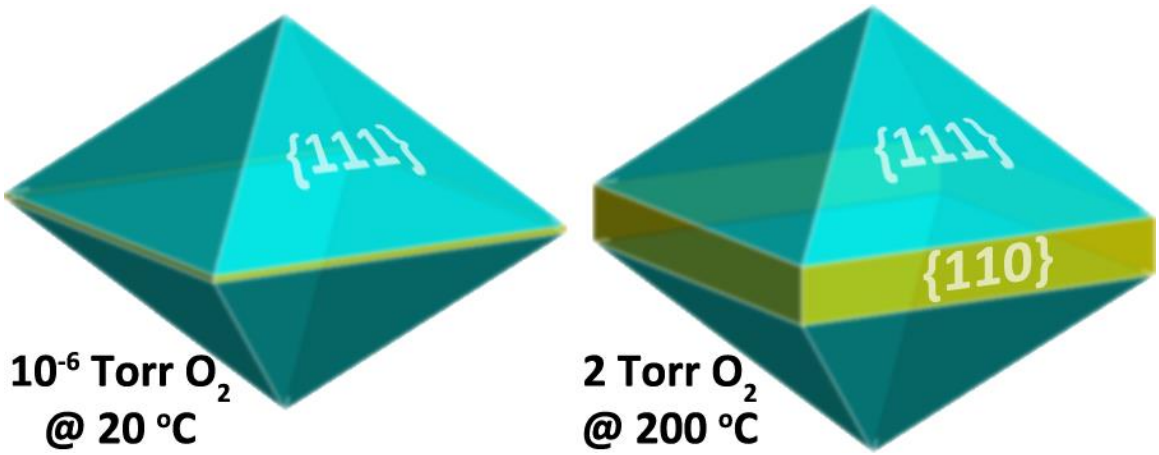

Figure 5-9 RuO_2 Wulff Shapes. Theoretical Wulff shape for RuO_2 under 2 different conditions based on the surface energies from (Wang et al., 2013) given in Table 5-2(Gavnholt, 2009)[233](Gavnholt, 2009)(Gavnholt 2009).

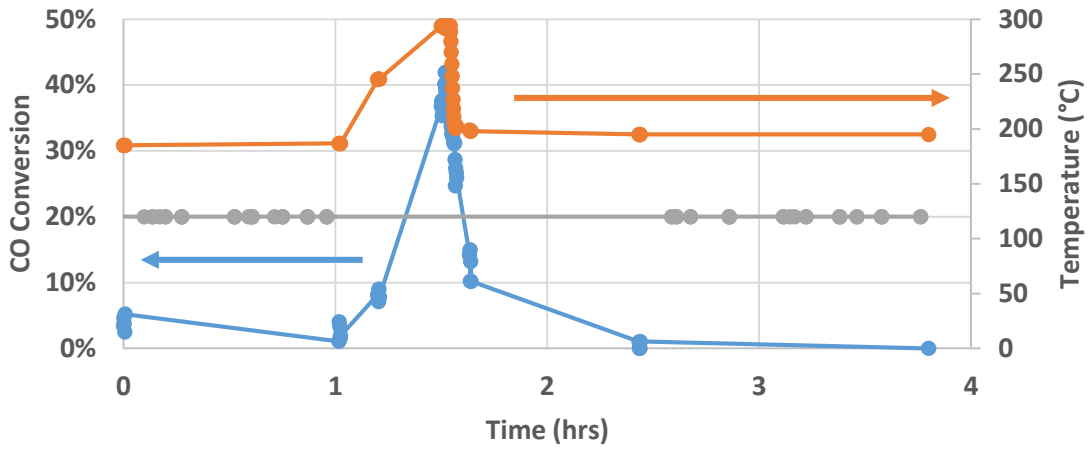

Figure 5-10 Pre-Reduced *Operando* Hysteresis Experiment. A summary of the pre-reduced catalyst hysteresis *operando* experiment, showing the temperature on the right axis, and the CO conversion on the left plotted over time. Times when images were acquired are shown as grey circles.

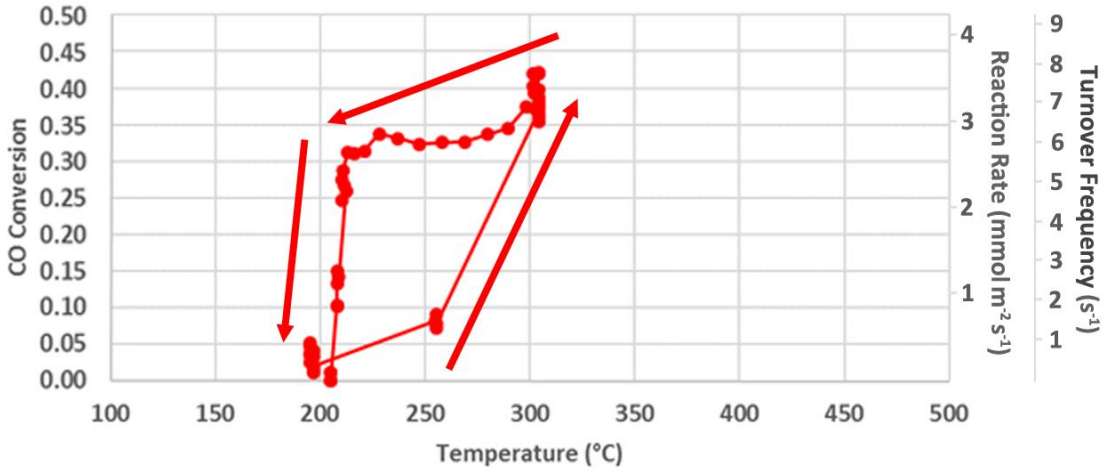

Figure 5-11 Pre-Reduced Hysteresis Conversion vs Temperature. A plot of the data in Figure 5-10 with CO conversion plotted vs temperature. Again the data show a clear hysteresis. In this experiment, the CO conversion was measured every 7 seconds for 3.5 minutes when the temperature was rapidly decreased back to 200°C.

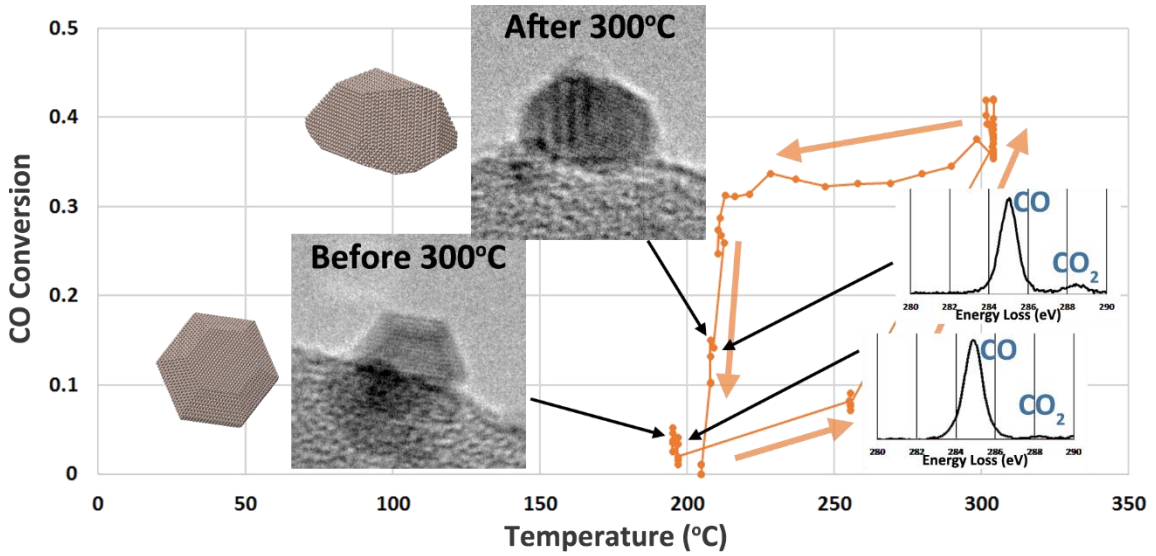

Figure 5-12 Pre-Reduced *Operando* Hysteresis with Images. *Operando* TEM data showing a hysteresis in the CO conversion similar to that observed in the reactor data displayed in Figure 2-6. Each point in the plot was obtained by quantifying an electron energy loss spectrum, two of which are displayed in the inset graphs. Two images are also shown, with one taken under low conversion conditions and the other taken during high conversion at nearly the same temperature. Models of the Ru particle shape, oriented using the manual method illustrated in Figure 4-12 are also shown.

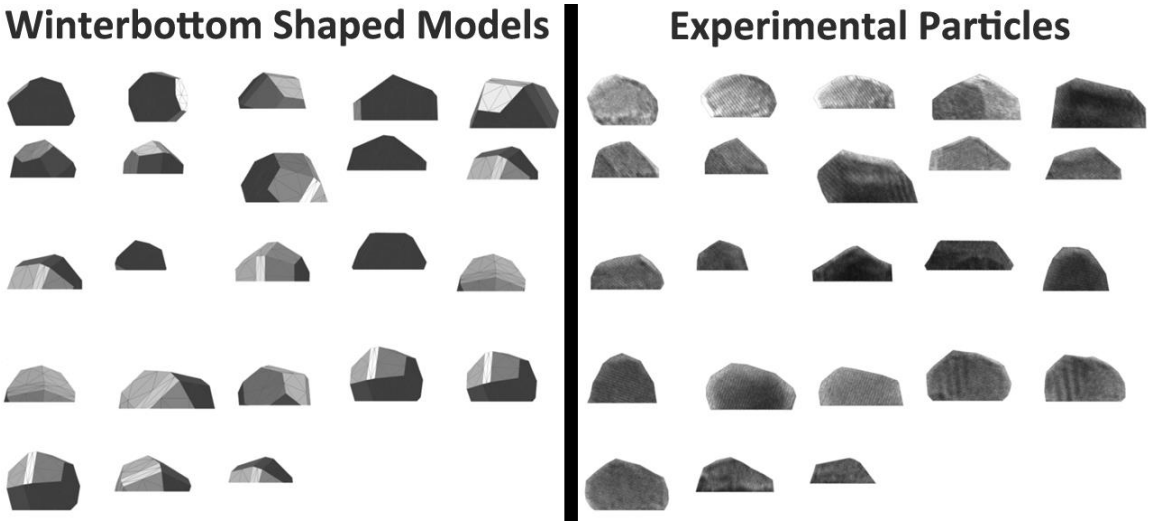

Figure 5-13 *Operando* Orientation Matching Results. A visual comparison of 23 experimental Ru particles from the pre-reduced hysteresis *operando* experiment with the best-fitting Winterbottom models found using the automated orientation matching technique described in section 4.2.5 and illustrated in Figure 4-13.

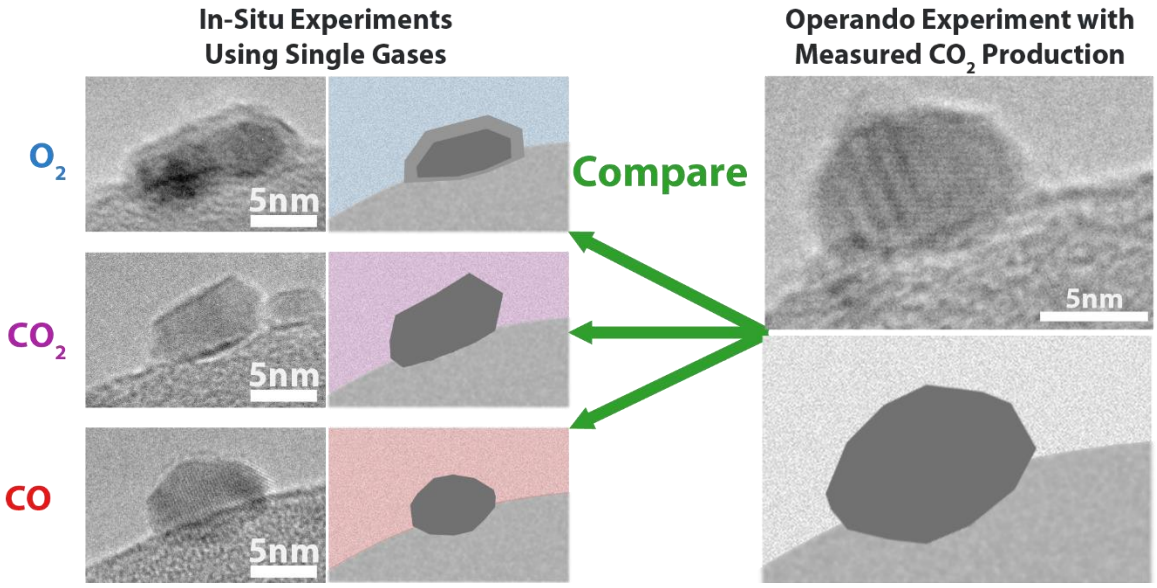

Figure 5-14 *In-Situ—Operando* Comparison. Images of Ru particles exposed to 3 different single gas environments inside the ETEM (left), as well as during CO oxidation (right). In the CO, CO_2, and *operando* conditions the shape is faceted and close to the Wulff shape, while exposure to O_2 produces a thick oxide shell around the particle.

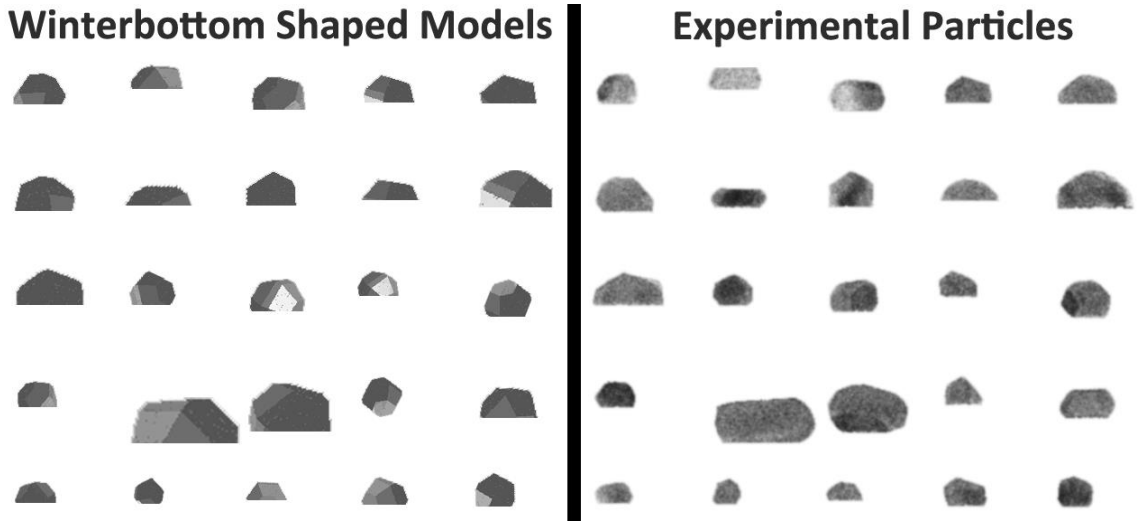

Figure 5-15 *In-Situ* CO Orientation Matching Results. A visual comparison of 23 experimental Ru particles from an *in-situ* CO experiment with the best-fitting Winterbottom models found using the automated orientation matching technique described in section 4.2.5 and illustrated in Figure 4-13.

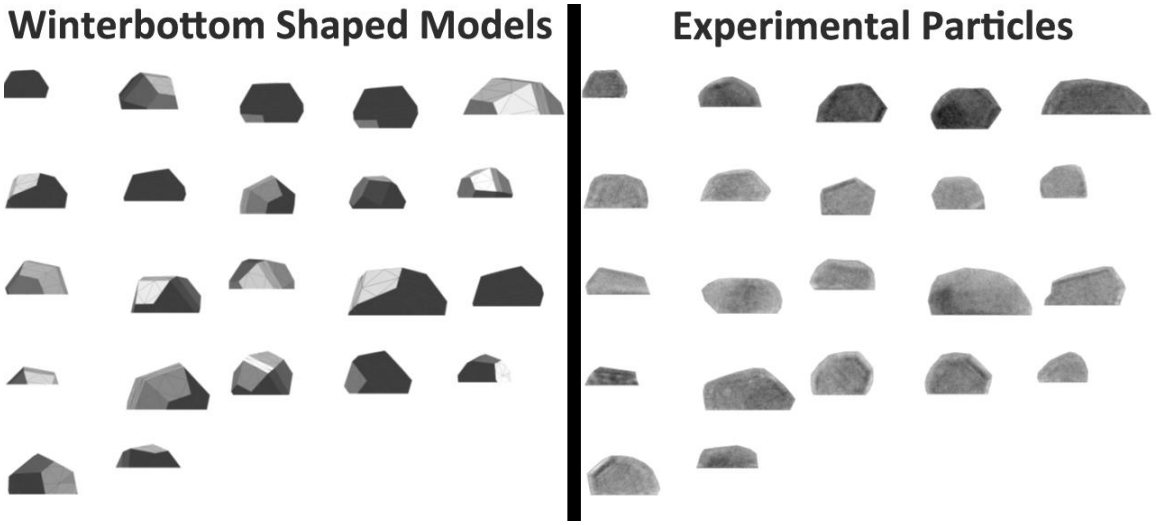

Figure 5-16 *In-Situ* CO_2 Orientation Matching Results. A visual comparison of 22 experimental Ru particles from an *in-situ* CO_2 experiment with the best-fitting Winterbottom models found using the automated orientation matching technique described in section 4.2.5 and illustrated in Figure 4-13.

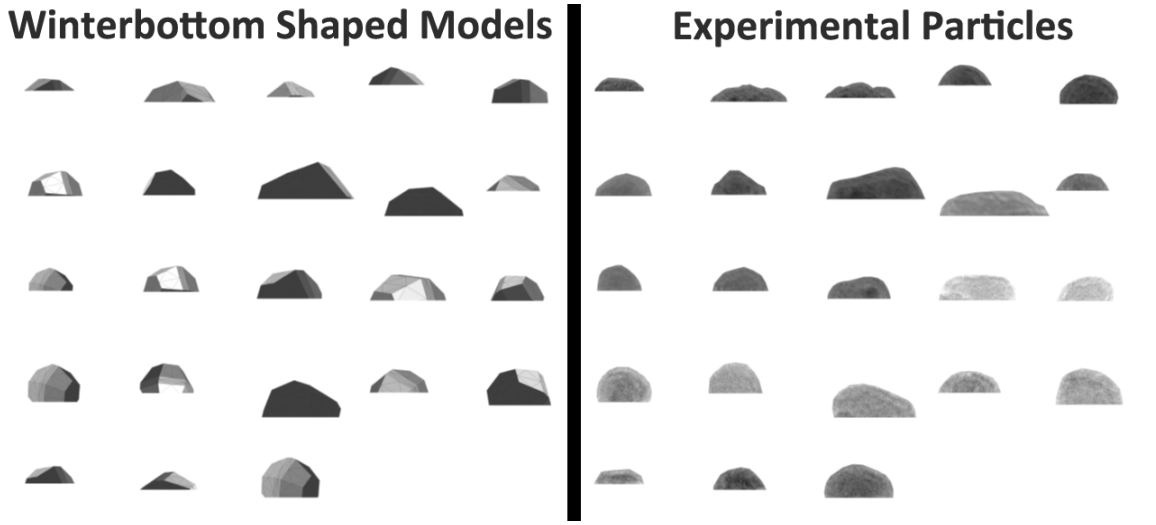

Figure 5-17 *In-Situ* O_2 Orientation Matching Results. A visual comparison of 23 experimental Ru particles from an *in-situ* O_2 experiment with the best-fitting Winterbottom models found using the automated orientation matching technique described in section 4.2.5 and illustrated in Figure 4-13.

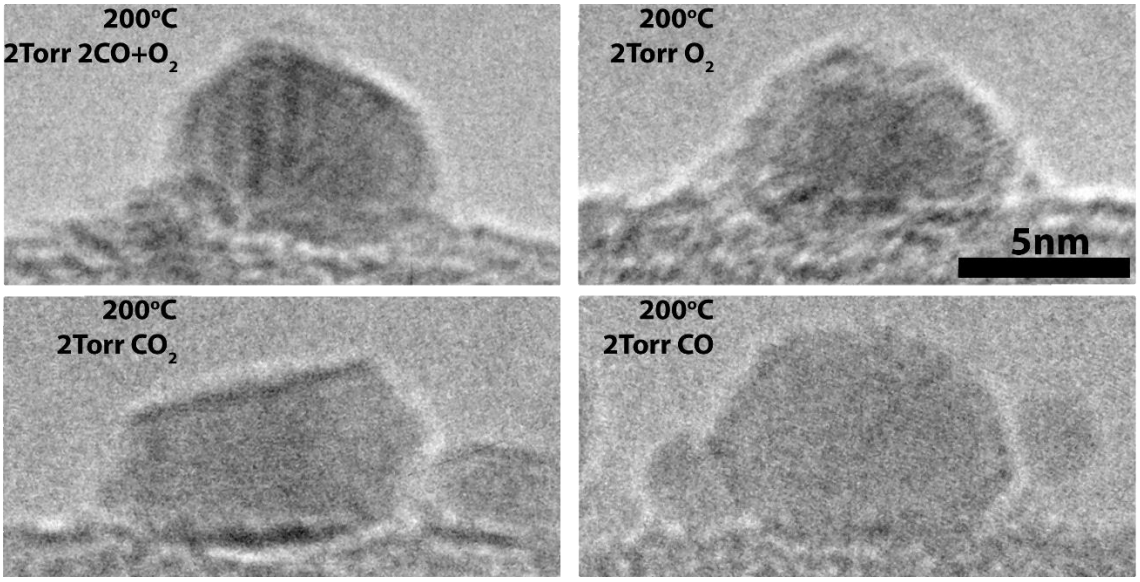

Figure 5-18 *In-Situ* Image Comparison. A comparison of 4 representative experimental images from the 3 *in-situ* conditions and the pre-reduced hysteresis *operando* experiment.

Table 5-3 Tammann Temperatures. Tammann temperatures for selected metals are compared to the temperatures at which nanoparticles were observed using ETEM.

	Au	**Cu**	**Pt**	**Ru**
Tammann Temperature (K)	670	680	1020	1300
Experimental Temperature (K)	300	490	660	575
Fraction of Tammann	44%	72%	65%	44%

Table 5-4 Surface Energy Anisotropy. Calculated surface energies for selected metals and RuO_2 showing the small surface energy anisotropy for metals.

Metal	(100)	(110)	(111)	Mean	Maximum Difference From Mean (%)	Ref.
Au	0.074	0.077	0.063	0.071	12%	(Yoo et al., 2016)
Cu	0.113	0.120	0.104	0.112	7%	(Yoo et al., 2016)
Pt	0.139	0.142	0.113	0.131	14%	(Yoo et al., 2016)
Ru	0.176	0.197	0.199	0.191	8%	(Gavnholt, 2009)
RuO_2	0.043	0.054	0.061	0.053	18%	(Wang et al., 2013)
RuO_2	0.033	0.046	0.049	0.043	23%	(Wang et al., 2013)

Table 5-5 Adsorption Energies. Selected adsorption energies in eV of CO and oxygen on Ru from several sources.

Ru Facet	CO	Oxygen	Reference
(0001)	1.8		(Pfnür and Menzel, 1983)
(0001)		3.5	(Kalinkin and Savchenko, 1982)
(0001)	1.3		(Hoffmann et al., 1990)
-	~1	~5	(Somorjai and Li, 2010)
(0001)	1.7	2.4-2.6	(Stampfl and Scheffler, 1997)

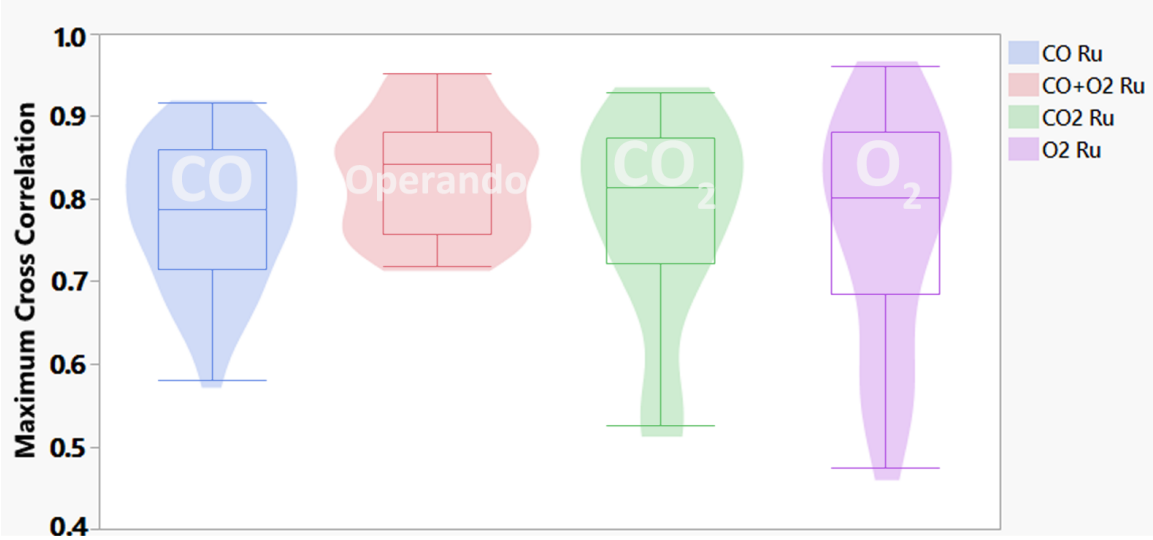

Figure 5-19 Shape Matching Cross Correlation Results Summary. Violin plot of the normalized cross-correlation with a more traditional box plot overlaid for each of the 3 *in-situ* conditions, as well as for the *operando* experiment. A cross correlation of 1 corresponds to a perfect match, which will never be achieved; >0.85 is considered a very good match, as discussed in Appendix IX.

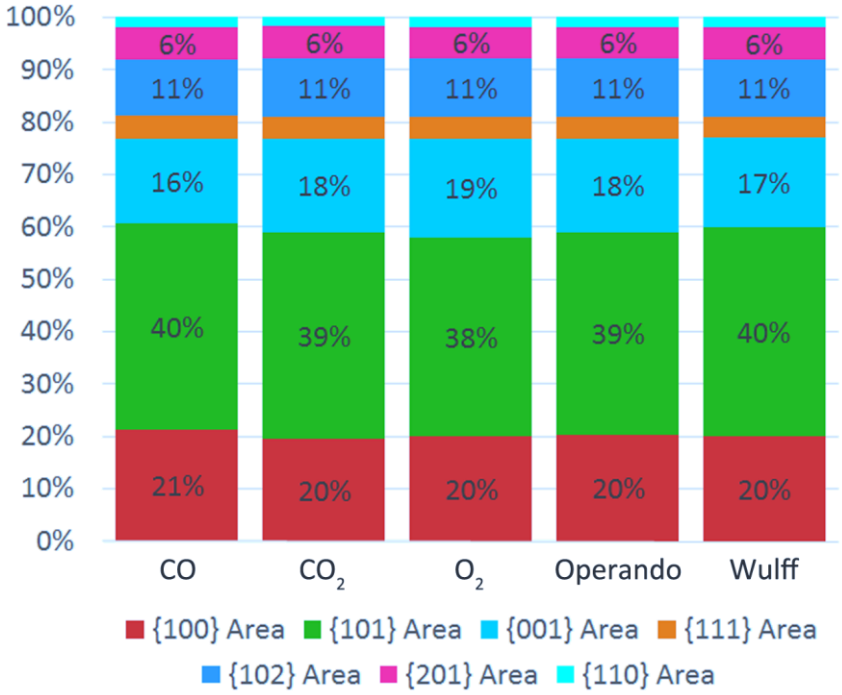

Figure 5-20 Facet Area Distributions. The relative area of the 7 facets considered changes little for ensembles of Winterbottom-shaped particles in different conditions. The distributions are also similar to the distribution found for the Wulff shape.

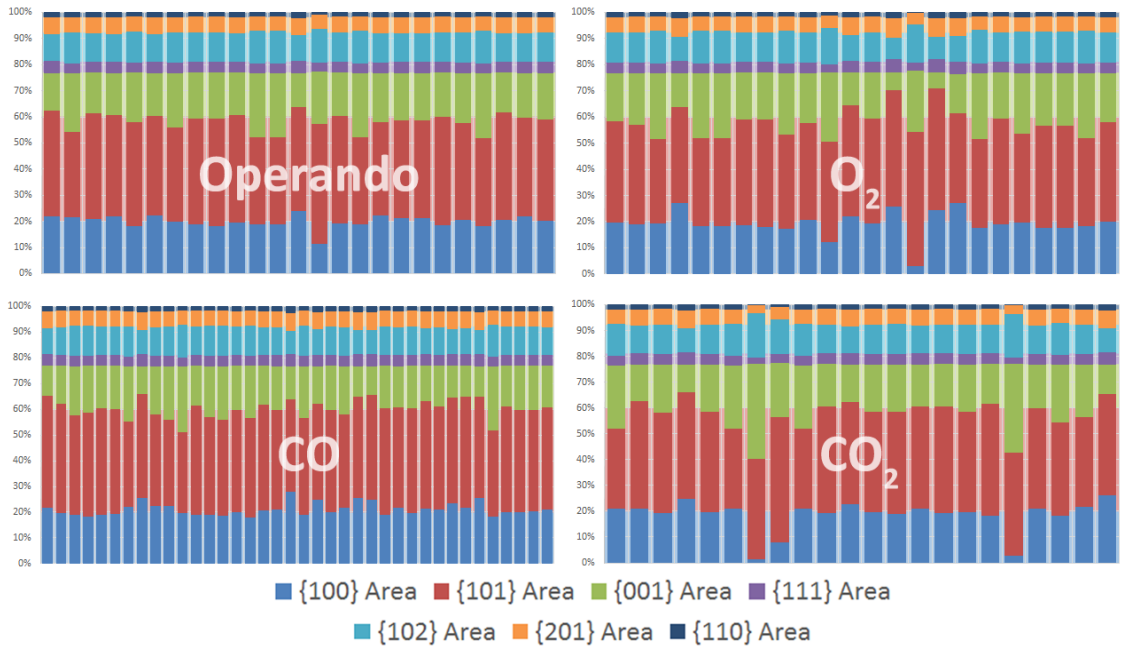

Figure 5-21 Individual Particle Facet Distributions. Distribution of facets area in each of the best-matching models determined for the experimental particles from 4 different environmental conditions. (The average distributions for each of the 4 conditions are given in Figure 5-20.) The background of each plot is colored with the original Wulff shape facet distribution in lighter tones.

6. CO Oxidation over Ru/RuO_2: Catalytic Activity and Particle Surface Structures

6.1. Early Evidence for RuO_2 Surface Layers

In Chapter 5, the presence of a hysteresis in the activity of a reduced Ru catalyst (first observed in the *ex-situ* data presented in section 2.2.2) was confirmed *in-situ*. Briefly, when the catalyst was exposed to a stoichiometric mixture of CO and O_2 at around 200°C the activity was low, but after increasing the temperature to 300°C and reducing it back to 200°C, the activity was much higher for at least an hour. Furthermore, it was shown that the difference in activity was not attributable to a difference in the shape of the catalyst, as the catalyst shape was close to the Wulff shape of Ru both before and after the hysteresis, as shown in sections 5.3.1 and 5.5.1. This suggests that the change in activity could instead be due to a change in the surface structures present on the catalyst nanoparticle surfaces.

The particle from Figure 5-12 imaged at 200°C after the temperature was increased to 300°C displays a clear set of Moiré fringes in addition to the usual Ru lattice fringes. Analysis of this Moiré spacing, given in Figure 6-1. In this image, a Ru spacing of 0.229 nm, matching a (100) plane, is clearly visible, but the other lattice spacing needed to produce the Moiré pattern is not visible in the image and does not appear in the diffractogram. It is nevertheless possible to deduce the lattice spacing required to produce the observed Moiré fringes. The reciprocal space vector $g_{Moiré}$ for the Moiré fringe produced by 2 spacings A and B should be simply $g_A - g_B$ (Williams and Carter, 2008). This is shown graphically in Figure 6-1, where the Moiré vector $g_{Moiré}$ is labeled in magenta both in its observed location in the diffractogram, and with its origin at the observed Ru spacing. Since the diffractogram has inversion symmetry, there are two Moiré

fringe spots and two possible locations for the invisible lattice fringe. One of these possibilities falls directly on a (101) RuO_2 spacing. This suggests that the Moiré is the result of a surface oxide layer formed on the Ru nanoparticle. While the identity of the surface material has thus been determined, the details of this layer are not accessible, since the poor resolution and delocalization inherent to the Tecnai microscope obscure the surface. This initial observation of an apparent RuO_2 layer on the surface of a Ru particle during a period of high activity for CO oxidation prompted a search for RuO_2 layers in the new aberration corrected Titan ETEM.

6.2. Thin RuO_2 Observed During CO Oxidation

The FEI Titan ETEM is equipped with image correcting optics, which allow optical aberrations to be reduced significantly, giving an information limit of 1.0 Å while the FEI Tecnai ETEM is an older microscope, without aberration correction, and has an information limit of 1.4 Å (Takeda et al., 2015). Most importantly for this work, the delocalization of image contrast which plagued the Tecnai images is significantly reduced in the Titan, making it possible to observe the structure at the surface of nanoparticles.

An aberration corrected FEI Titan microscope was used to capture the images given in Figure 6-2 in which more detailed structural information about the surface layer can be observed. To provide an unambiguous observation of RuO_2 layers growing on Ru nanoparticles, the catalyst was exposed, first to pure H_2, and then to a mixture of H_2 with a small amount of O_2. In 2 Torr of H_2 at 200°C the particle appears fully metallic, with Ru lattice fringes appearing continuous up to the surface (Figure 6-2a), though the diffractogram shows evidence of possible RuO_2 layers even in pure H_2. Adding just 0.01

Torr of O_2 to the H_2 gas inside the ETEM had a dramatic effect on the surface of the nanoparticle. Different fringe spacings are now visible at the particle surface in the image shown in Figure 6-2b. The spacings 0.228 nm and 0.255 nm were found to be consistent with RuO_2 (111) 0.2221 nm and RuO_2 (101) 0.2555 nm, differing by just 2.7% and 0.2% respectively. In addition to the reasonably close match between the measured fringe spacings and the RuO_2 lattice spacings, the orientation of the observed RuO_2 (111) spacing matches what would be expected on the Ru (100) surface. Kim, et al. published work on single crystal Ru (100) surfaces, which revealed that RuO_2 (100) films could be grown on the Ru (100) surface, with only a 4.5% compression of the RuO_2 along the [010] direction (Kim et al., 2001). The fringes observed here are in relative orientations consistent with this epitaxial oxide film structure. Finally, the angle between the two RuO_2 surface layers (in the image plane) matches the RuO_2 Wulff shape, when the RuO_2 Wulff model is set to the experimentally observed zone axis, suggesting that the RuO_2 surface layer may be a single continuous crystal; this is shown in the inset of Figure 6-2b, where the RuO_2 Wulff shape is overlaid in red on the region of the image containing the RuO_2 surface layers.

The oxidation of a Ru nanoparticle exposed to only 0.01 Torr of O_2 with 2 Torr of H_2, a strong reducing gas, is consistent with the high catalytic activity of Ru in a H_2 rich gas stream and its highly selective oxidation of CO over H_2 (Chin et al., 2005; Kim et al., 2012). If the catalyst is able to oxidize virtually all of 1% CO in a gas stream with 50% H_2 and only 1% O_2, then the competing oxidation of H_2 is clearly not being catalyzed. Thus, it is not surprising that the H_2 gas flowed in this experiment was not sufficient to reduce the RuO_2 layer formed on the catalyst. Indeed, this observation suggests that CO oxidation

in a H_2 rich stream may be catalyzed by RuO_x surface layers which are stable despite the H_2 rich gas environment.

Once it was confirmed that epitaxial RuO_2 layers grown *in-situ* within the FEI Titan ETEM could be observed, *operando* experiments similar to the experiments performed earlier on the Tecnai were conducted to determine whether such layers were present during CO oxidation. During one experiment, the catalyst was held in the ETEM for 12 hours at room temperature with CO at a pressure of about 2 Torr, to reduce the catalyst nanoparticles to Ru metal. The temperature was then increased to 200°C and, after a few minutes, about 0.7 Torr of O_2 gas was added to the ETEM cell. This caused a swift increase in the CO conversion to just under 50%, which in turn led to a temperature rise up to 225°C. Under these conditions, the catalyst was observed and the image shown in Figure 6-3 was captured. A visual inspection of the image reveals that the particle shape does match the Wulff shape reasonably well, though with an enlarged (110) plane, as the corner is truncated slightly (indicated by the arrows in Figure 6-3a and b). Inspection of a diffractogram obtained from the image shows that several of the lattice fringe spots appear to be split. Careful measurement of these split spots reveals that in each case the main spot most closely matches a Ru spacing, while the other spots match RuO_2. The Ru fringe spacings match the bulk Ru lattice spacings to within less than 2.5% while the RuO_2 spacings match to within 0.8%. The angles are also correct for both of the resulting Ru and RuO_2 patterns to within 5%. This is clear evidence that during CO oxidation a thin oxide layer can be formed on the Ru surface.

Analysis of the diffractogram shown in Figure 6-3 is concrete evidence for RuO_2 layers forming on the surface, but the surface layer is not clearly visible in the image, unlike the

layer observed in the H_2-O_2 mixture and shown in Figure 6-2b. During another *operando* experiment, however, a very similar structure to that seen in the H_2-O_2 mixture was observed. In this experiment, named in this dissertation the Titan O_2 o*perando* experiment, the catalyst was left for 12 hours at 215°C in 1.5 Torr of pure O_2. The CO pressure was then increased to 3 Torr, giving a stoichiometric mixture of CO and O_2. After 2.5 hours at this condition, during which the CO conversion was between 5 and 10%, the image shown in Figure 6-4 was acquired. The image shows a surface structure which appears similar to that seen on the Ru (100) surface of the particle in Figure 6-2b. The Ru particles are in the same zone axis, and a careful analysis reveals that the structures are also the same. As with the Ru particle exposed to H_2 and O_2, both the fringe spacings and the relative orientation of these spacings match the expected lattice spacings and orientation for a RuO_2 (100) film forming on a Ru (100) surface. In this case, the entire Ru particle is oriented even closer to an exact zone-axis orientation. This makes image simulation of the particle easier, and Figure 6-4c shows a simulation of the surface layer which matches reasonably well, and is based on a model of the entire particle, of which a part is shown in Figure 6-4b. Noise was added to the simulation by overlaying a semitransparent copy of a region in the image containing only faint amorphous contrast from the gas in the cell.

Not all particles imaged during CO oxidation display evidence of RuO_2 layers. Figure 6-5 shows a particle exposed to 2 Torr CO and 0.7 Torr O_2 at 300°C; at this condition the CO conversion was about 60%, but the Ru particle surface shown in Figure 6-5 appears to be fully metallic, with no RuO_2 layers formed. The particle is again close to the thermodynamic equilibrium shape. Several other images lacking RuO_2 layers will be discussed in the following sections.

6.3. Correlation Between Activity and Surface Layers

Several of the images shown in this chapter were acquired during a single, extended *operando* experiment performed on the Titan ETEM. This experiment is summarized in Figure 6-6. While this figure appears complicated, the experiment was composed of two simple parts. In the first part of the experiment, an attempt was made to reproduce the hysteresis observed in both the *ex-situ* and previous *operando* experiments. This was completed over the course of two days. In the second part of the experiment, the oxygen pressure was increased to a stoichiometric ratio and finally to several oxygen rich conditions, before returning to a slightly oxygen poor condition, as shown in Figure 6-7.

Ample evidence of RuO_2 layers was found during this experiment. Few particles were observed which displayed no evidence of RuO_2. The particle shown in Figure 6-5 is one of the few particles which appeared to be completely clean, without any oxide layers. Another clean particle is shown in Figure 6-8. Most of the other particles observed show some evidence of RuO_2 layers. In some cases, like in Figure 6-3 and Figure 6-4, the evidence is compelling, while in other cases, like the particle shown in Figure 6-9, the evidence is less clear, and the existence of a RuO_2 layer is uncertain. The evidence for RuO_2 layers is summarized in Table 6-1 and conditions for these images are given in Table 6-2.

Figure 6-10 shows the points in the Titan *operando* experiment at which the images given in this chapter were acquired. Under all conditions there are particles which may have RuO_2 layers, but under multiple conditions, particles are found which appear to be clean Ru, without any surface oxide.

An analysis of several images during the first part of this *operando* experiment seems to show that more clean particles are observed under the high activity conditions at 300°C, and immediately after the temperature is lowered back to 200 °C. An image from before the temperature was increased to 300°C is given in Figure 6-11 and shows clear evidence of a RuO_2 layer. However, Figure 6-5 and Figure 6-8 show clean Ru particles at 300°C and soon after the temperature was decreased back to 200°C. This is consistent with the following hypothesis: at higher conversions O_2 is partially depleted and thus it becomes more difficult for RuO_2 layers to form. RuO_2 layers already formed are reduced by reaction of CO with lattice O, leading to more clean Ru particles. This is reasonable, since the amount of O_2 present in the gas stream was a little less than for a stoichiometric composition. It is important to note however, that even at very small partial pressures of O_2 the surface will continue to have some adsorbed oxygen, as discussed in section 5.5.1 due to the large binding energy of O_2 on Ru (see Table 5-5). At least one particle (not shown) was observed to still have an RuO_2 layer even at 300°C, so some heterogeneity was still found. Averaged over the entire experiment, only half the catalyst surface is estimated to be covered by crystalline RuO_2 layers based on visual inspection of filtered images where RuO_2 spacings were isolated. Very few particles appear to be fully covered by RuO_2 layers.

The conversion data in this experiment is given in Figure 6-12. Both EELS and RGA were used to collect data. As explained in chapter 3, the EELS data can be quantified more reliably, but the RGA data is constantly acquired over the course of the entire experiment. A third curve is also shown in Figure 6-12 in blue; this is data calculated using equations 2-1 and 2-8 derived in section 2.3 for conversions in the ETEM. The activation energy and

attempt frequency used in the calculation were obtained from the reduced catalyst ramp up data shown in Figure 2-6 between 1% and 50% conversion (150°C-200°C). To more precisely fit the data in this experiment, the amount of catalyst in the pellet was used as a fit parameter. This yielded a mass of catalyst in the pellet of 0.28 mg, slightly higher than the 0.2 mg measured, but still within the measurement error, as discussed in section 3.3.1. It should also be noted that since the amount of O_2 was lower than for a stoichiometric mixture, it is not possible to achieve 100% conversion; based on the CO flow rate of 1.11 sccm and O_2 flow rate of 0.32 sccm, the maximum possible conversion is about 68%.

This calculated conversion data, plotted in Figure 6-12, assumes that the reaction rate can be characterized by a single activation energy and attempt frequency, and thus, a single mechanism, over the temperature and gas composition ranges explored. This does not produce a good fit to the data at several points. Insight into the dependence of structure on activity can be gained by analysis of these regions. One point where the calculation and experiment diverge is between 28 and 35 hours into the experiment, when the conversion was significantly higher than was calculated. This is consistent with the hysteresis described in chapters 2 and 5, since the conversion was higher at 200°C after the catalyst had been at 300°C. If, as discussed in section 1.3.2, crystalline RuO_2 is detrimental to CO oxidation, then the partial reduction of the catalyst at 300°C should result in less RuO_2 on the surface, and thus higher conversions after this reduction. Another point of contrast is more subtle, but at 300°C, the conversion was also slightly lower than expected; according to the calculation, the conversion should reach a maximum of 99% of the highest possible conversion under these conditions, or about 67%. Using EELS, a conversion of only up to 62% (91% of the maximum possible) was observed. This may indicate a reduction in the

number of active sites, or it may be caused by a change in the apparent activation energy as a result of a change in the reaction pathway on the surface, as discussed in section 2.2.2 for the *ex-situ* data.

Another obvious departure from the calculated conversion occurs when excess O_2 is flowed into the ETEM cell between 58.5 and 67.5 hours into the experiment. During this time, the measured CO conversion is decreased dramatically, while the calculated conversion remains high. This must be due to a change in the catalyst structure under reaction conditions, namely further oxidation of the catalyst, likely forming thicker crystalline oxide layers.

6.4. Surface Structure Discussion

6.4.1. The Surface Structures Present During CO Oxidation

The review of the literature on CO oxidation over Ru presented in section 1.3.2 highlighted several structures, 3 of which are shown in Figure 1-2, which have been proposed in the past to be the active structure for CO oxidation over Ru.

Bulk crystalline RuO_2 was once hypothesized by some to be the active structure for CO oxidation, but this was later rejected by the community who recognized that this could not be correct. The *ex-situ* experiments performed in this work clearly support this conclusion.

Another hypothesized active structure for CO oxidation which has received strong support is a thin crystalline layer of RuO_2 over Ru metal. Some past studies of both single crystals (Kim et al., 2000; Martynova et al., 2012; Over et al., 2009, 2000; Wang et al., 2002), as well as nanoparticle Ru catalysts (Aßmann et al., 2004, 2003; Qadir et al., 2012)

have suggested that such thin oxide layers are responsible for the high activity for CO oxidation. While much of this chapter has focused on observations of RuO_2 layers, and may appear to support this conclusion, the highest activity was observed under conditions where more particles have no observed crystalline RuO_2. This suggests that the RuO_2 is a spectator structure, present during CO oxidation, but not contributing significantly to the catalysis. Furthermore, not all particles show RuO_2 layers during CO oxidation, even under conditions where RuO_2 has been observed. In some cases this may be a result of RuO_2 domains that are not oriented close enough to any major zone axis, so that they are not visible in the TEM. In other cases, like that shown in Figure 6-5, it seems likely that the Ru particle surface simply is not covered by any crystalline RuO_2 film. Averaged over the entire Titan *operando* experiment, only about half the catalyst surface is estimated to be covered by crystalline RuO_2 layers. The data presented in this chapter therefore lead to the conclusion that the observed thin RuO_2 layers are spectator structures and do not cause the high activity of this catalyst.

The work of other researchers also indicates that crystalline RuO_2 could be a spectator structure (Blume et al., 2006; Rosenthal et al., 2009), as significant heterogeneity existed, and the activity of RuO_2 could not be accurately determined. Finally, there is no satisfactory explanation for why thin films of crystalline RuO_2 should be active while thicker films of the same phase are inactive. Perhaps the best explanation is that active thin films are somehow structurally distinct from bulk RuO_2, which is clearly inactive. However, if the structure is changed sufficiently, it may become necessary to describe it as something other than defective crystalline RuO_2. Indeed, if the structure is significantly changed, it may be more accurate to categorize the oxide layer as RuO_x. Thus, while

crystalline RuO_2 layers are observed in this work, and that of others, during CO oxidation, this is unlikely to be the active structure.

Clean Ru metal with only chemisorbed oxygen not incorporated into the structure was also at one time proposed to be the most active structure. This work cannot exclude the possibility that Ru with chemisorbed oxygen is the active structure based on the experimental data. The highest conversions shown in Figure 6-12 occurred when the catalyst was consuming nearly all the oxygen in the cell. However, considering the strong energetic driving force for oxidation of the Ru surface even at room temperature (313 kJ/mol or 3.244 eV (Jacob et al., 2004)), it seems unlikely that the catalyst would lose all but adsorbed oxygen even under these conditions.

Ru with only chemisorbed O_2 has been refuted strongly in the literature in the past. Over, et al. claimed that the high activity on observed on ruthenium catalysts could never be achieved by Ru with chemisorbed oxygen (Over et al., 2007). Basically, the amount of CO adsorbed on the oxygen-covered surface is far too low for a Langmuir Hinshelwood mechanism, and the activation barrier far too high for an Eley-Rideal mechanism (Over et al., 2007). This structure also does not explain the high activity of Ru relative to other transition metals (Chen et al., 2007). Thus, based on the work of other researchers, Ru is likely not the most active structure.

Another proposed active structure for CO oxidation is variously called a trilayer, a disordered trilayer-like structure, and a surface oxide. While these titles may not be referring to exactly identical structures, they are all referring to structures of RuO_x with x between 2 and 4 which have some degree of order, but display more short-range than long-range order. These have been shown to coexist with crystalline RuO_2, and importantly,

have even been observed to consume RuO_2 under some conditions (Flege et al., 2008). These structures have been shown to be active, and this should not be surprising when it is considered that the trilayer structure has been likened to RuO_4 molecules (Stampfl, 2005); RuO_4 is a highly oxidizing liquid at room temperature. If there are structures resembling RuO_4 on the surface of Ru during CO oxidation, these would be both highly reactive, and likely to form disordered structures.

A highly disordered structure is often more difficult to observe experimentally; this is certainly the case in high resolution TEM if the amorphous material is obscured by a larger crystalline structure. While disordered materials can be observed and characterized, if the material is very thin, it can become difficult to distinguish from background noise under low dose conditions. This is especially true in the ETEM, where the gas in the cell produces a background intensity distribution which appears amorphous, as seen in the vacuum Figure 6-4c. However, in Figure 6-4a the bottom-right facet of the particle appears to support amorphous material of some kind. It is reasonable to suppose that this could be disordered RuO_x with x between 2 and 4. Even more convincing evidence for disordered RuO_x layers is given in Figure 6-13 where there can be no doubt that disordered material is present on the surface under conditions of high O_2 flow (a). The amount appears to be slightly reduced after the O_2 flow was reduced (b). It seems unlikely that it is SiO_2 since the amount changes slightly, and this particle was observed previously in the experiment (not shown) where it did not display the disordered layers. It is also unlikely to be carbonaceous contamination, since this would be quickly oxidized by the catalyst at 225°C. While some images, like these show clear evidence of disordered layers, it is quite difficult to exclude the possible existence of thin disordered layers based on any of the images

acquired in this work. It is thus possible that thin disordered layers are present on all the particles. It has been proposed in the past that a disordered oxidized surface could be a highly active structure for CO oxidation (Blume et al., 2006; Flege et al., 2008; Martynova et al., 2012). This is consistent with the observations of this work.

Based on the evidence in the literature suggesting that disordered RuO_x, which may sometimes lack long-range order, making it difficult to detect experimentally, is active for CO oxidation, along with the observation that fully crystalline particles of RuO_2 are not active, and thin RuO_2 layers appear to be spectator structures, I propose that disordered RuO_x is the most active structure for CO oxidation. The existence of significant structural heterogeneity in which the more easily observed crystalline RuO_2 layers coexist with RuO_x also provides an explanation for the prolonged debate over this system, and for the difficulty of experimental studies to reach firm conclusions.

6.4.2. Structure-Reactivity Correlation

The complex reality of the Ru system appears to be that multiple structures are present on the surface during periods of high activity. In fact, several different structures may all be active simultaneously, as explicitly stated by several researchers (Blume et al., 2006; Flege et al., 2008; Reuter and Scheffler, 2003; Rosenthal et al., 2009). Often this was observed on single-crystal Ru; the heterogeneity of the surface of Ru is likely compounded for Ru particles, where multiple surface facets, and many different edge and corner configurations can exist.

The purpose of the *operando* TEM experiments described in this dissertation was to elucidate structure-activity relationships. Specifically, they were intended to observe the

most active structure during high activity. The results suggest that thin layers of crystalline RuO_2 are not the most active structure, since it is observed least often during periods of highest catalytic activity; the Ru system is complicated, however, and a few particles may still have RuO_2 layers under these conditions. Furthermore, the difficulty in observing disordered RuO_x which is hypothesized to be the most active structure, along with the heterogeneity of the catalyst means that even direct observation of the surface structures of the catalyst during high activity has not resulted in a definitive conclusion regarding the active structure. While this could be viewed as a disappointing failure, it follows the method of all scientific progress, by presenting hypotheses and disproving those that are not supported by the available evidence. This work can also help to point the way forward as further exploration of this system is conducted. This will be the subject of the final chapter.

6.5. Summary

Early evidence for RuO_2 layers on Ru nanoparticles under high-activity conditions in the Tecnai ETEM prompted a search for RuO_2 layers using the aberration-corrected Titan ETEM. This was successful, as RuO_2 layers were observed both in a mixture of O_2 and H_2, and later during CO oxidation. These layers were observed through analysis of diffractograms, as well as by real-space measurements in images which were confirmed using image simulation. The correlation between RuO_2 layers and high activity was found to be negative however. The structures proposed in the literature were evaluated in light of the data obtained from an extended *operando* experiment. The data suggest that RuO_2 is a

spectator structure, which is still observed due to the heterogeneity of the Ru surface. Disordered RuO_x, with x between 2 and 4, is proposed to be the active structure.

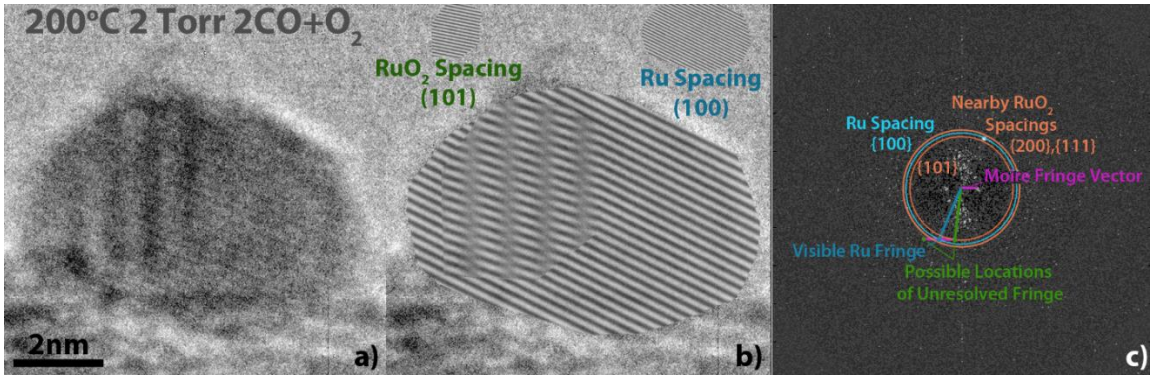

Figure 6-1 Moiré Fringe Analysis. a) Ru particle imaged at 200kV in 2:1 mixture of CO and O_2 at 2 Torr and 200°C. b) demonstration of the Moiré pattern produced by the two sets of fringes shown. c) graphical Moiré vector analysis, showing that the observed Moiré vector added to the visible Ru fringe vector yields a possible RuO_2 (101) lattice vector.

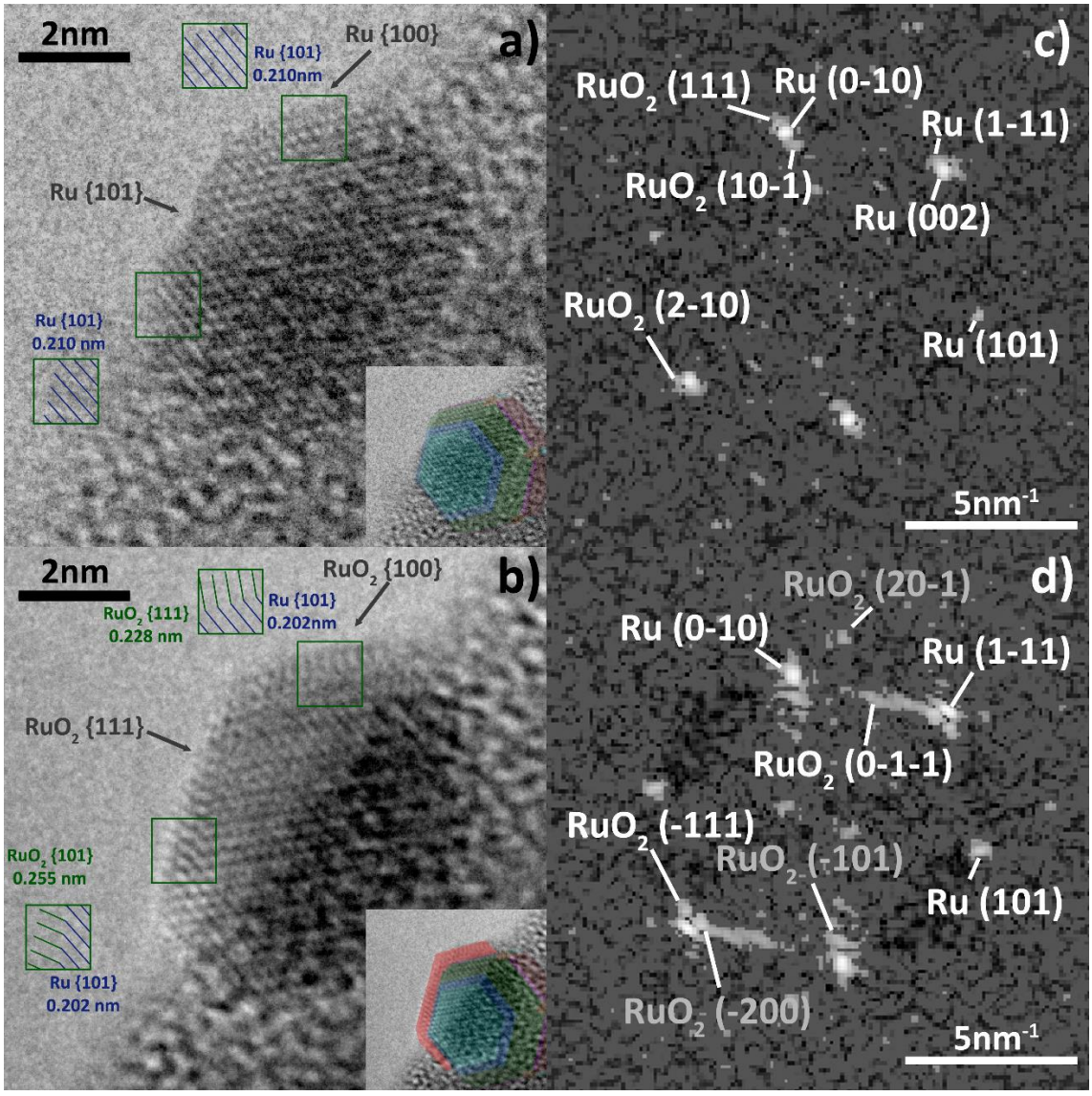

Figure 6-2 Ru and RuO_2 in H_2 and H_2-O_2. a) Ru particle imaged at 80KV in 2 Torr H_2 at 200°C, showing Ru metal fringes extending to the surface, with the Wulff shape overlaid in the inset. b) the same particle after addition of 0.01 Torr O_2 showing RuO_2 fringes at the surface. The inset shows that the underlying Ru Wulff shape is preserved, but angle between the RuO_2 surface layers now matches the RuO_2 Wulff shape (red). c) Diffractogram of image in a) with clear Ru fringes, and possible RuO_2 fringes labeled. d) Diffractogram of image in b) with Ru fringes, as well as several sets of RuO_2 fringes labeled. Three of the RuO_2 fringes (labeled in grey) are from a less visible oxide layer. Two other RuO_2 fringes form the more visible surface layers (labeled in white).

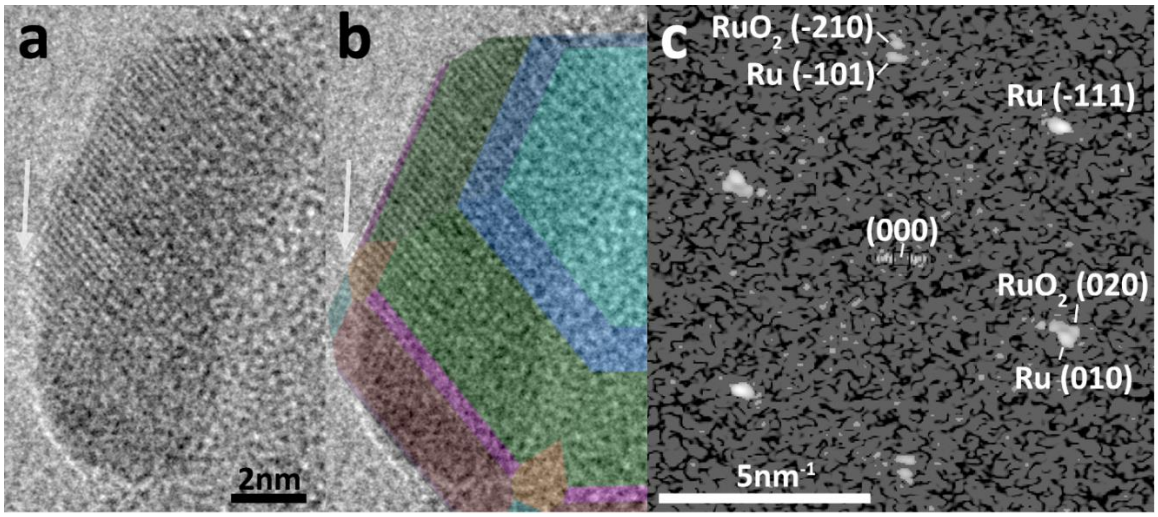

Figure 6-3 RuO_2 Layer During *Operando* CO Oxidation. a) Ru particle imaged at 300KV in 2 Torr CO and 0.7Torr O_2 at 225°C. b) overlaid Ru Wulff shape. c) Processed diffractogram showing both Ru and faint RuO_2 fringes.

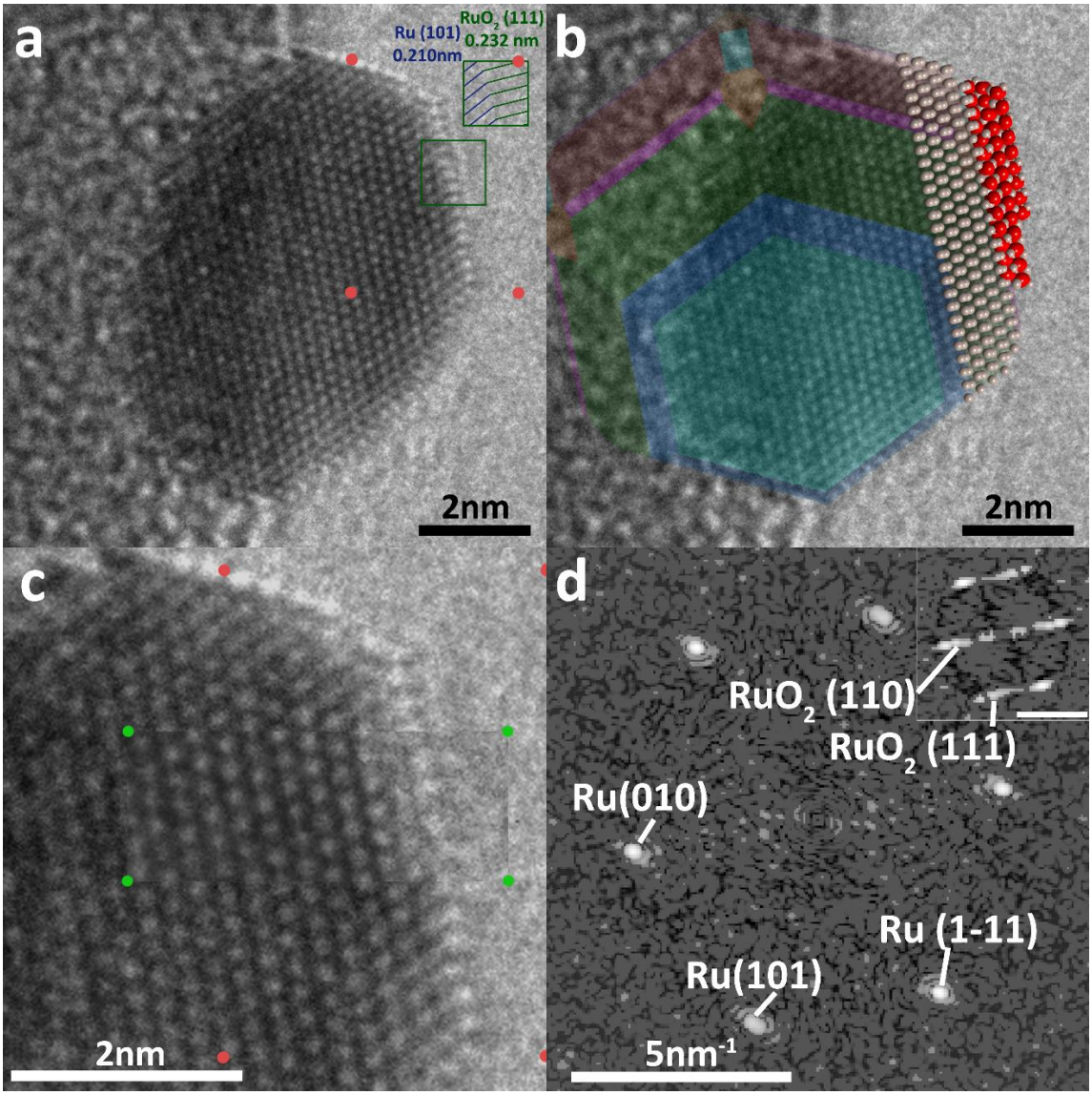

Figure 6-4 Image Simulation of RuO_2 Surface Layer. a) Ru particle imaged at 80 kV in 2:1 mixture of CO and O_2 at 3 Torr and 215°C , displaying fringes similar to those observed in Figure 6-2b. Disordered material of some kind is also barely visible in the bottom of the image. b) overlaid Ru Wulff shape, and part of the model used for the image simulation, shown in c), where green dots mark the extent of the simulated image. The red dots in both a) and c) indicate the region used to produce the diffractogram in the inset of d) which shows spots that do not appear in the diffractogram produced from the entire region displayed in a).

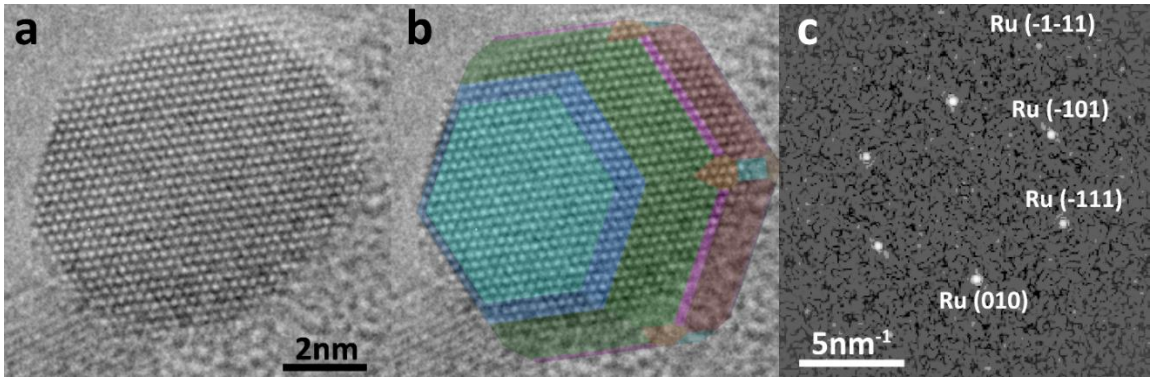

Figure 6-5 Clean Ru Particle. a) Ru particle imaged at 300kV in 2Torr CO and 0.7Torr O_2 at 300°C displaying a clean metallic surface. b) Overlaid Ru Wulff shape. c) Diffractogram showing an absence of RuO_2 fringes

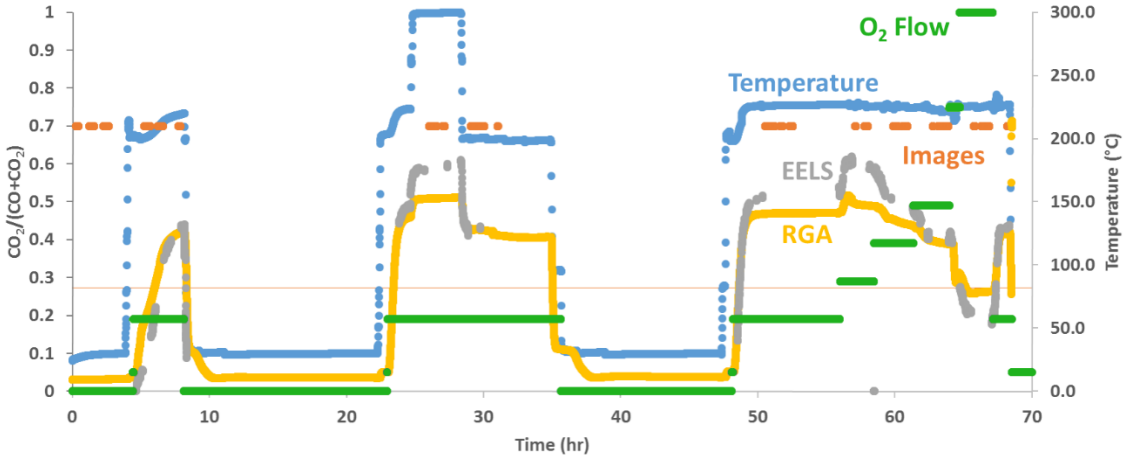

Figure 6-6 Titan *Operando* Experiment Summary. Plot showing the progression of the Titan *operando* experiment over time. Temperature is plotted on the right axis, and the CO_2 conversion quantified using both EELS (grey) and RGA (yellow) is on the left axis. The normalized O_2 flow is also plotted, with a horizontal line indicating a stoichiometric composition; finally, the points where images were acquired is indicated with orange markers. Between 10 and 22 hours, and between 36 and 48 hours, no one was present at the microscope.

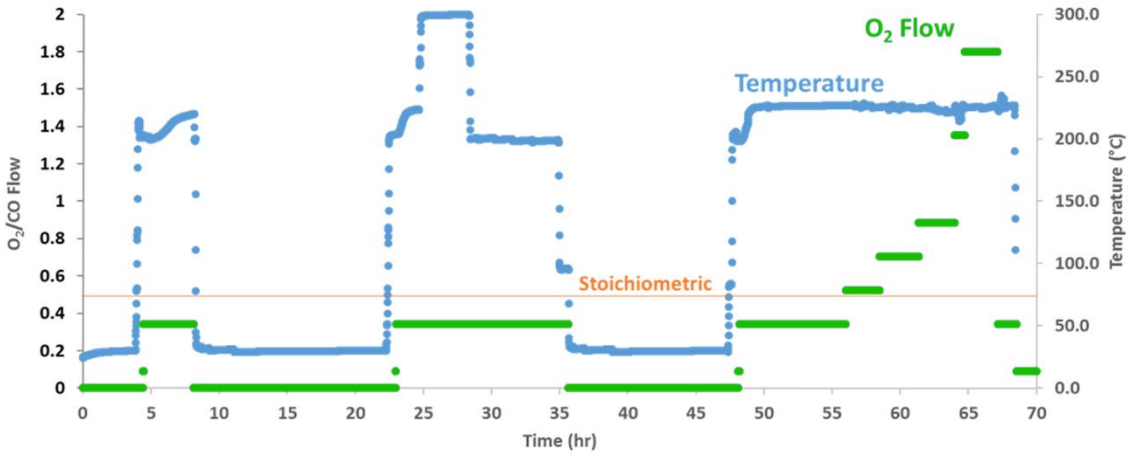

Figure 6-7 Titan *Operando* Experiment Stimuli. A subset of the data shown in Figure 6-6, with the O_2 flow ratio (not normalized) plotted on the left axis, and temperature again plotted on the right axis.

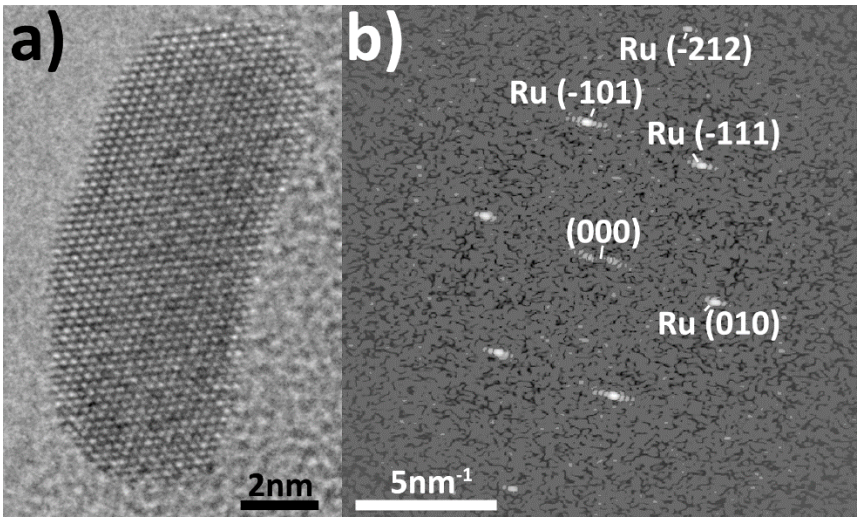

Figure 6-8 Clean Ru Particle. a) The same particle as shown in Figure 6-3, but imaged at 300kV in 2 Torr CO and 0.7 Torr O_2 at 200°C just after the temperature was decreased from 300°C. b) Diffractogram showing the presence of Ru spacings. The beating pattern around the fringes is a result of the abrupt termination of the fringes at the particle surface.

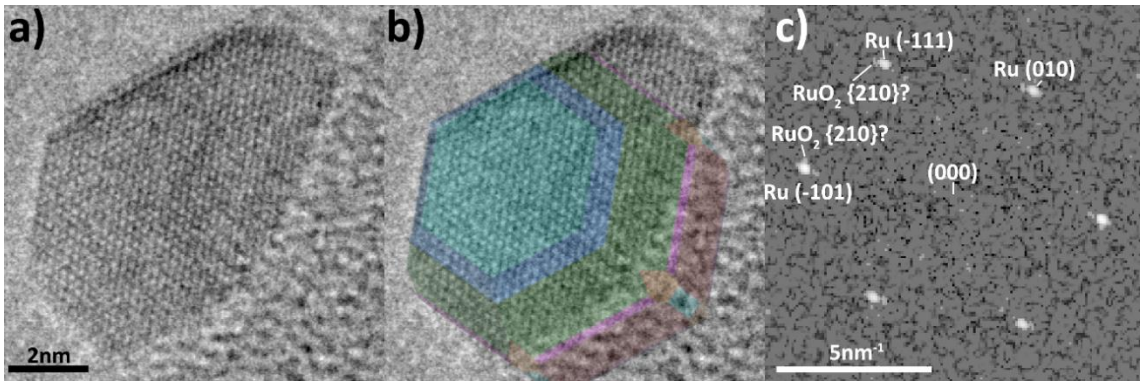

Figure 6-9 Ru Particle With Uncertain Surface. a) Ru particle imaged at 300 kV in 2 Torr CO and 0.7 Torr O_2 at 200°C. b) overlaid Wulff shape showing a rather significant deviation in the top right corner of the image. c) Diffractogram showing clear Ru spots, but uncertain evidence for RuO_2 layers.

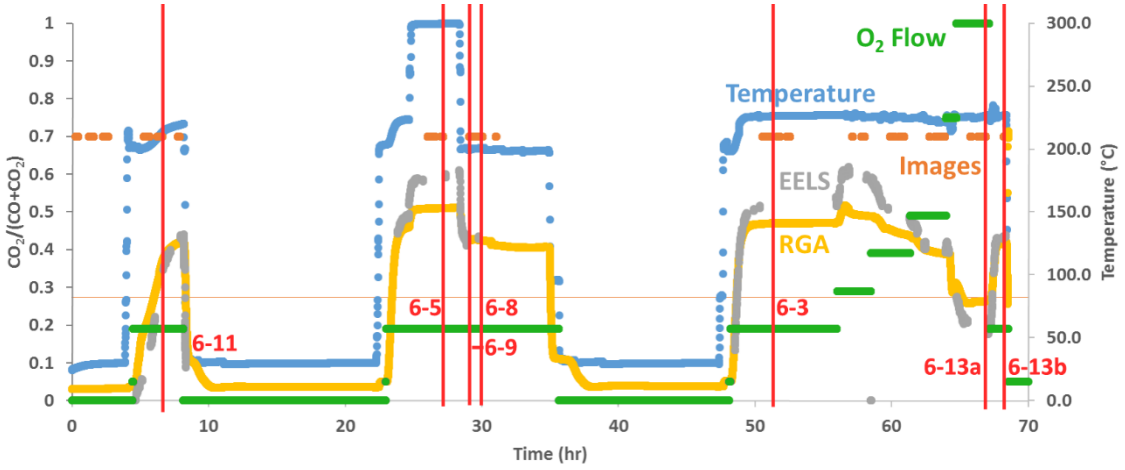

Figure 6-10 Image Acquisition Conditions. The same summary plot shown in Figure 6-6, but with vertical lines indicating the times when the images from this experiment given in this dissertation were acquired; images not noted on this graph were not captured during this experiment.

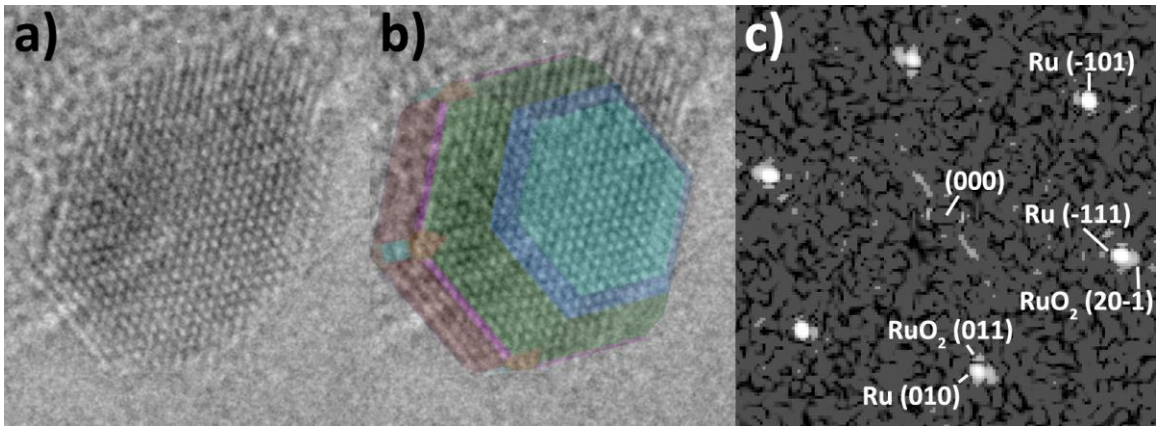

Figure 6-11 Initial 200°C Image. a) Ru particle imaged at 300 kV in 2 Torr CO and 0.7 Torr O_2 at 215°C. b) overlaid Wulff shape showing a slight deviation in the top right corner of the image. c) Diffractogram showing clear Ru spots, a few faint RuO_2 spots, and additional intensity likely from the abrupt termination of the fringes at the particle surface.

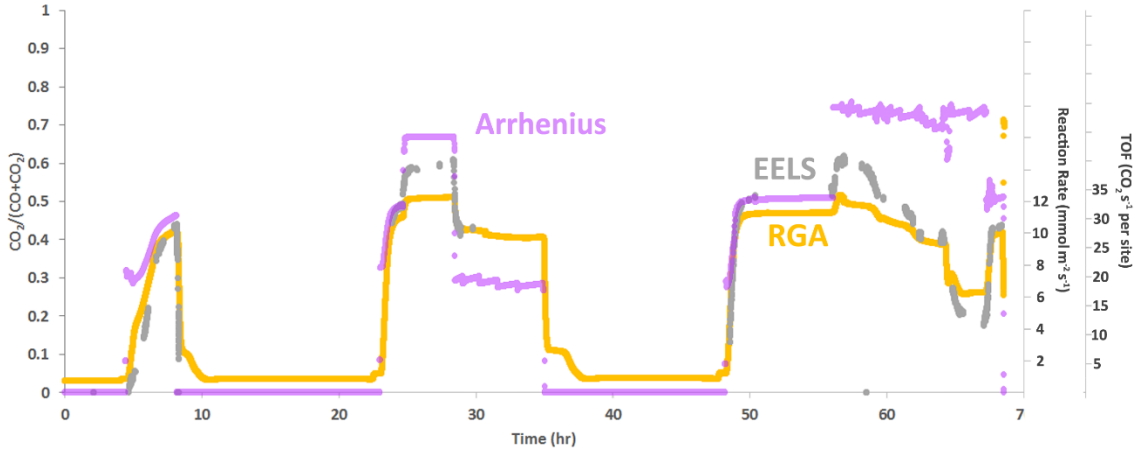

Figure 6-12 Titan *Operando* Catalyst Performance. The CO conversion obtained using both EELS (gray) and RGA (yellow) is plotted for the *operando* experiment summarized in Figure 6-6, along with the conversion calculated based on an Arrhenius fit to *ex-situ* data using equations 2-1 and 2-8 (purple).

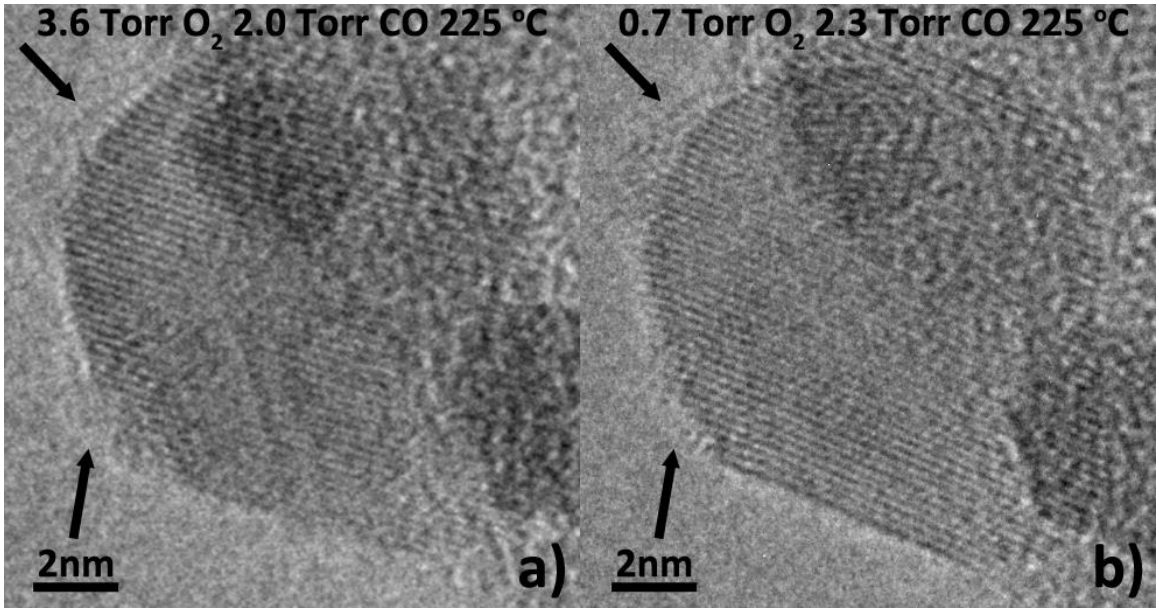

Figure 6-13 Disordered Surface Layers. Ru particle imaged at 300 kV. a) High O_2 condition, showing the formation of disordered surface layers, which are likely oxidized Ru. b) The same particle after the gas composition was returned to slightly less O_2 than a stoichiometric mixture.

Table 6-1 Analyzed Images. Information is given on the images analyzed in Chapter 6 to determine the presence of partial surface oxidation.

Image Name	Experiment	Figure	Surface Oxide Type	Evidence	Confidence
2014-05-28 033	2014-05-28 Pre-Reduced *Operando* Hysteresis	6-1	RuO_2	Moiré	High
2015-02-09 0058	2015-02-09 Titan H_2-O_2	6-2a	RuO_2	Diffractogram	Low
2015-02-09 0098	2015-02-09 Titan H_2-O_2	6-2b	RuO_2	Image, Diffractogram	High
2015-12-02 221i	2015-12-02 Titan *Operando*	6-3	RuO_2	Diffractogram	High
2015-04-24 002l	2015-04-24 Titan O_2 *Operando*	6-4	RuO_2, AO	Image	High
2015-12-02 017i	2015-12-02 Titan *Operando*	6-5	none	Image, Diffractogram	High
2015-12-02 021x	2015-12-02 Titan *Operando*	6-8	none	Image, Diffractogram	High
2015-12-02 018d	2015-12-02 Titan *Operando*	6-9	RuO_2	Diffractogram	Low
2015-12-02 011zc	2015-12-02 Titan *Operando*	6-11	RuO_2	Diffractogram	High
2015-12-02 614g	2015-12-02 Titan *Operando*	6-13a	Disordered Oxide (AO)	Image	High
2015-12-02 714c	2015-12-02 Titan *Operando*	6-13b	Disordered Oxide (AO)	Image	High

Table 6-2 Analyzed Image Conditions. Information on the experimental conditions under which observations of the images analyzed in Chapter 6 were made.

Image Name	Accelerating Voltage (kV)	Temperature (°C)	Gas Pressures (Torr)	Time Under Stated Conditions (h)
2014-05-28 033	200	200	1.33 CO + 0.66 O_2	2.0
2015-02-09 0058	80	200	2 H_2	4.3
2015-02-09 0098	80	200	2H_2 + 0.01 O_2	3.4
2015-12-02 221i	300	225	2 CO + 0.7 O_2	2.5
2015-04-24 002l	80	215	2 CO + 1 O_2	1.6
2015-12-02 017i	300	300	2 CO + 0.7 O_2	2.3
2015-12-02 021x	300	200	2 CO + 0.7 O_2	1.5
2015-12-02 018d	300	200	2 CO + 0.7 O_2	0.7
2015-12-02 011zc	300	215	2 CO + 0.7 O_2	2.3
2015-12-02 614g	300	225	2 CO + 3.6 O_2	2.2
2015-12-02 714c	300	225	2 CO + 0.7 O_2	1.0

7. Summary and Future Work

7.1. Summary

7.1.1. *Ex-Situ* Work

For this work a supported Ru catalyst for CO oxidation was produced and studied in an *ex-situ* reactor. The high activity of the catalyst was confirmed, and a hysteresis in the conversion observed when the sample was reduced. Kinetic parameters were derived from these experiments, and used to estimate the conversion expected during *operando* experiments in the differentially-pumped environmental TEM.

7.1.2. *Operando* Technique

When this work was begun *operando* TEM was a new technique, for which only a single paper had been published (Chenna and Crozier, 2012b). As a part of this work, automated methods for rapidly quantifying low-loss and core-loss EELS of gases, were developed (Miller and Crozier, 2014). Additionally, a new sample preparation method was developed to increase catalytic conversion inside a differentially-pumped ETEM (Miller et al., 2015), and the maximum CO conversion observed was about 80%. A system for mixing gases and delivering them to the ETEM was designed and built, and a method for locating and imaging nanoparticles in zone axis orientations while minimizing electron dose rate was determined.

7.1.3. Ru Shape and Surface Results

After high quality images of Ru nanoparticles observed during CO oxidation were obtained, the shape and surface structures of these particles was investigated. Image registration was applied to maximize signal-to-noise in the acquired images, and fringe spacings were measured with sub-pixel accuracy. A Wulff model structure for Ru was compared to experimental images both by manually rotating the model, and by automatically determining a matching orientation using cross-correlation of shape signatures generated from the experimental data and Wulff model. From this analysis, it was determined that most Ru particles are close to Wulff-shaped during CO oxidation. While thick oxide layers were not observed during CO oxidation, thin RuO_2 layers on the surface of Ru nanoparticles were found by measuring lattice fringes at particle edges in images, and by measuring lattice fringes in diffractograms. The structure of one RuO_2 layer was confirmed by modeling the structure and matching a simulated TEM image to the observed structure. The evidence suggests that RuO_2 layers are not the most active structure for CO oxidation. Disordered RuO_x $(2 < x < 4)$ is proposed to be the most active structure, though proving this is currently challenging due to the structural heterogeneity of the system, and the difficulty inherent to observations of disordered structures.

7.2. Future Work

7.2.1. Other *Operando* Conditions

The majority of the *operando* experiments performed as part of this work used a gas composition close to stoichiometry (2:1 $CO:O_2$). This is the condition under which the

catalyst is most active, and thus seems an obvious condition under which to study the most active structure of the catalyst. However, using a gas composition which is known to deactivate the catalyst over time could also be useful, because the structure of the catalyst before and after this intentional deactivation could be observed. The catalyst is known to deactivate when the gas is oxygen rich. Some researchers, who believe that RuO_2 is the active form of the catalyst, have claimed that this deactivation is related to faceting of the RuO_2 producing more low activity RuO2(100)-c(2× 2) surfaces (Aßmann et al., 2008). Others contend that it is simply due to growth of bulk RuO_2 which is less active for CO oxidation (Goodman et al., 2007a). A suitable gas composition would be 2 Torr O_2 and 1 Torr CO.

As mentioned in section 1.1.1, one of the industrial applications for CO oxidation is to remove CO impurities from H_2 fuel going into fuel cells. This is known as preferential oxidation or PROX. The results presented in Figure 6-2 showing a RuO_2 layer on a Ru particle with only 0.5% O_2 in the H_2 flow into the ETEM indicate that such layers could be present during PROX reactions. This is worthy of further investigation. Since the current design of the gas handling system allows only 2 gases to be flowed simultaneously, to perform such an experiment, the gas handling system would need to be modified, or special gas mixtures purchased.

7.2.2. Other Oxide Supports

All of the data presented in this dissertation was obtained from a single catalyst batch, in which the Ru is supported on amorphous SiO_2 spheres. While the SiO_2 spheres simplify

the system by minimizing metal-support interactions (Cornils et al., 2000), other oxides may also have benefits for the study of Ru catalysts.

MgO has been used as a support for Ru in the past (Aßmann et al., 2008, 2003). Subtle differences were observed, but generally, the catalyst showed similar behavior. MgO, as a crystalline material would likely anchor the Ru particles more firmly than the amorphous SiO_2 used in this work, and MgO readily forms nearly perfect cubes when obtained from the smoke produced by burning Mg metal (Cowley et al., 1979; Heidenreich, 1942). This could possibly lead to a preferred orientation of Ru particles, and make it feasible to rotate particles into a zone axis orientation, a feat which is difficult on the current SiO_2 supported catalyst.

CeO_2 is also a crystalline oxide, and could anchor the Ru particles more firmly than SiO_2. It is also a good material for TEM observation (Cochrane et al., 1989), as it is relatively robust under electron irradiation and less likely to charge under the beam than either SiO_2 or MgO. However, CeO_2 is known to have a strong metal-support interaction (Cochrane et al., 1990; Cavendish, 2012; Su et al., 2015), and is a reducible oxide, which could possibly supply oxygen to the Ru catalyst. This would further complicate the already complex Ru catalyst.

7.2.3. Image Acquisition Modifications

As described in section 3.3.7, most images captured in this work were acquired in sets of 5. This allows some imaging artifacts to be distinguished from real structural features, and provides more information about the drift and noise than a single frame. A series of shorter acquisitions can also often be digitally aligned and averaged to yield better signal

to noise in a single frame. While acquiring a sequence of 5 frames is thus useful, several alternatives might be tried in the future.

Focal series have long been used to increase the resolution of images, and to calculate the exit wave function. In short, the defocus of the TEM is rapidly and systematically changed and at each defocus an image is acquired. Software then uses the series of images to reconstruct the exit wave function. Chang, et al. showed the potential for applying this technique to catalyst nanoparticles, and determined the atomic positions of surface atoms in a Pt particle to within a few picometers by acquiring focal series with an image corrected TEM (Chang et al., 2010). Helveg, et al. also used focal series reconstruction in an aberration-corrected microscope to reduce the dose rate applied to their catalyst sample in the ETEM (Helveg et al., 2015) while still maintaining reasonable image quality. These two applications emphasize two major benefits to acquiring focal series. First, by using focal series to reconstruct the exit wave function, direct interpretation of the contrast is enabled, whereas for usual high resolution TEM images, the contrast cannot always be interpreted so simply (Williams and Carter, 2008). Secondly, by acquiring a series of images, and combining them, more noise can be tolerated in the individual images, as long as the individual frames can be registered accurately (Kisielowski et al., 2015). This allows the beam dose rate to be significantly reduced, which may lead to less beam damage (Egerton et al., 2004; Jiang and Spence, 2012).

Chapter 5 was devoted to the 3D shape of Ru nanoparticles during catalysis, but no tomography was performed. There are several reasons this was not attempted. First, traditional electron tomography requires images be acquired at many tilts, and even when this process is automated, a significant amount of time is required to record the data. If the

catalyst is dynamic and changes orientation during this acquisition, this will likely impede the reconstruction of the 3D structure. Additionally, a higher dose rate would likely be required to improve the signal to noise, and the total dose applied during imaging would thus be higher, leading to more radiation damage, which has been strictly minimized in this work. Since observation of subtle changes in the catalyst are the goal of this research, every effort must be made to minimize changes to the catalyst by the observation itself.

Nevertheless, a middle ground may be possible. It would be ideal to acquire 2-3 tilts of each particle, at the same dose rate currently used. By retaining assumptions about the shape of the particle (that the particles are approximately Wulff-shaped), even just a few tilts could provide significantly more information about the 3D structure of the particles.

The problems with current tomography techniques are the significant electron dose and the long time required for acquisition. In the future, both of these issues may be mitigated by the use of high speed, high DQE direct detection cameras. If every electron which strikes the detector can be detected with precision, and a series of images at 10 tilts acquired in a fraction of a second, then the beam dose rate, total dose, and total acquisition time could all be significantly reduced to the level currently used in this work, and possibly even lower. This is an exciting prospect, and one that could revolutionize studies of catalyst nanoparticles if successful.

One of the challenging aspects of this work is the heterogeneity of the catalyst system being studied. This heterogeneity is inherent to Ru, as it has been observed even on single crystals, as discussed in sections 1.3.2 and 6.4.1. Thus, to obtain an accurate description of the catalyst, images must be acquired from many different particles. As discussed in section 3.3.7, manually searching for catalyst particles in zone-axis orientations is tedious. While

the method of wobbling the objective lens current described in that section made the process quicker, it still requires significant time and energy to be devoted to a task that is repetitive. This could, in principle, be automated. A computer algorithm designed to detect particles which are close to a zone-axis orientation would likely be capable of finding many more particles per hour than a human operator. This would also free the researcher to spend the time thinking about the scientific value of the data being collected. It is unclear at this point how generic such an algorithm could be, and how many researchers would find it useful, but certainly work like that described in this dissertation would be greatly benefited.

7.2.4. Image Simulations and Structure Calculations

An image simulation of the proposed RuO_2 layer on a Ru particle was given in Figure 6-4. Additional simulations of entire Ru particles in non-aberration-corrected images were given in Figure 4-3. Image simulations like these increase confidence that TEM images are being correctly interpreted, and can sometimes lead to the discovery of image features that were previously ignored, since heightened scrutiny is applied to subtle details in the image. More simulations like these should be performed!

Many of the images in Chapter 6 were acquired from particles quite close to a zone axis orientation. Nevertheless, small departures from the ideal orientation exist, complicating the interpretation of image contrast. Systematically tilting the model prior to image simulations and comparing the results to the experimental image might lead to a better understanding of the subtle contrast variations observed. Currently, this is a time consuming task, which should be automated before implementation.

The image simulation shown in Figure 6-4 used a rutile RuO_2 structure, in keeping with the observations of some researchers from single-crystal Ru. This structure seems to match the experimental data fairly well. However, other structures have also been suggested for oxidized Ru surfaces, including non-crystalline phases, and the O-Ru-O trilayer structure, as discussed in section 1.3.2. It would be interesting to also produce models of these structures, and simulate images to compare the results. The results of this comparison would have to be cautiously evaluated however, since simulations never exactly match the experimental data; at some point additional work would yield diminishing returns, and it is possible that each proposed structure might be made to match the experimental data equally well if enough effort was expended, and enough parameters varied.

The simulations presented here are all based on bulk-terminated structures. The atomic positions at surfaces and interfaces have simply been assumed to be identical to their positions in the bulk of the structure. This assumption is certainly not accurate. Some relaxation of the surface atoms is inevitable; this has been observed experimentally using (S)TEM (Chang et al., 2010; Yankovich et al., 2014; H. Yoshida et al., 2012), and is a well-known phenomenon. Density functional theory (Azubel et al., 2014; Chang et al., 2010; Gavnholt, 2009; Shibata et al., 2009) and molecular dynamics (Mejía-Rosales et al., 2007; Pauwels et al., 2000) have both been used to predict the positions of atoms at surfaces and interfaces. These techniques minimize the energy of the entire structure and lead to atomic positions that are different from the bulk-terminated structures. TEM image simulations based on these more realistic structures would reveal whether the calculated structures match the experimental data more closely.

7.2.5. The Way Forward

Several directions for future work have just been discussed. These were straightforward extensions of the work described in this dissertation. However, tackling the broader issue of determining catalyst structure-activity relationships may also require somewhat different approaches. In this work, EELS has been used to measure the catalyst activity by quantifying the gas composition in the ETEM cell. This is a significant step forward from basic *in-situ* experiments in which the activity during observation can only be estimated, and is not actually known. However, the gas composition observed is a product of a large ensemble of particles, making it difficult to clearly identify whether any one observed structure is active. If every particle displayed a single structural feature, this could be unambiguously identified as the structure responsible for the observed catalytic activity. This is not possible for nanoparticles, as these have a range of structures; while this diversity can be reduced, it will likely never be entirely eliminated.

Reduction of this structural diversity is one way to more precisely determine structure-activity relationships. By producing several samples, each consisting of a different model structure, in which individual particles are very similar to one another, various structures can be observed one by one, and the activity of these structures compared (Burda et al., 2005; Somorjai and Park, 2008). *Operando* (S)TEM is ideally suited for such studies, since both the structure and the activity of each sample could be simultaneously determined and unambiguously correlated. It should also be noted that some researchers have focused their attention on single-atom catalysts (Qiao et al., 2011; Yang et al., 2013). Due to their structural simplicity, they may represent a single type of catalytic site, which can be

unambiguously identified as the active site. Again, *operando* (S)TEM could both confirm the presence of single atoms as well as the absence of other larger clusters, and measure the catalytic activity simultaneously.

An alternative to reducing structural diversity is to somehow observe the activity of a single structure at a specific location. This has been successfully achieved by some researchers who use a reaction producing a fluorescent molecule to study the activity of single nanoparticles (Roeffaers et al., 2006; Xu et al., 2008). While the technique cannot currently resolve the location of the active site down to the atomic scale, this approach shows great potential for discriminating between the different structures present in a heterogeneous ensemble of nanoparticles. If this could be performed using a windowed-cell holder which could also be used in the TEM, it might be possible to find highly active and less active particles using the fluorescence technique and then observe those same particles in the TEM all under steady-state reaction conditions. A disadvantage of the technique just described is that the catalyzed reaction must result in a fluorescent molecule. Thus, CO oxidation to CO_2 could not be directly studied using this method. If however, the CO_2 produced by CO oxidation (or any other product molecule) could react with another molecule in the gas phase, resulting in a fluorescent molecule, this technique might be extended. In fact, such a reaction is already used in some advanced CO_2 detectors, though these are not yet used to detect single events (Mills and Hodgen, 2005; Zhou et al., 2015). Single-molecule CO_2 detection by this method may prove to be impractical, but it deserves further consideration.

The existence and effect of heterogeneity in catalyst systems must be acknowledged and confronted. Statistical approaches to this issue are necessary unless true mono-disperse

catalysts characterized by a single structure can be produced, or the activity of individual structures measured. This will be challenging, but *operando* TEM, if able to observe a large number of particles, offers the possibility to statistically link structure and activity, even for heterogeneous systems like that studied in this work.

REFERENCES

Allard, L.F., Bigelow, W.C., Jose-Yacaman, M., Nackashi, D.P., Damiano, J., Mick, S.E., 2009. A new MEMS-based system for ultra-high-resolution imaging at elevated temperatures. Microsc. Res. Tech. 72, 208–215. doi:10.1002/jemt.20673

Allard, L.F., Overbury, S.H., Bigelow, W.C., Katz, M.B., Nackashi, D.P., Damiano, J., 2012. Novel MEMS-Based Gas-Cell/Heating Specimen Holder Provides Advanced Imaging Capabilities for In Situ Reaction Studies. Microsc. Microanal. 18, 656–666. doi:10.1017/S1431927612001249

Alpay, D., Peng, L., Marks, L.D., 2015. Are Nanoparticle Corners Round? J. Phys. Chem. C 119, 21018–21023. doi:10.1021/acs.jpcc.5b07021

Armor, J.N., 2011. A history of industrial catalysis. Catal. Today 163, 3–9. doi:10.1016/j.cattod.2009.11.019

Aßmann, J., Löffler, E., Birkner, A., Muhler, M., 2003. Ruthenium as oxidation catalyst: bridging the pressure and material gaps between ideal and real systems in heterogeneous catalysis by applying DRIFT spectroscopy and the TAP reactor. Catal. Today 85, 235–249. doi:10.1016/S0920-5861(03)00391-2

Aßmann, J., Narkhede, V., Breuer, N.A., Muhler, M., Seitsonen, A.P., Knapp, M., Crihan, D., Farkas, A., Mellau, G., Over, H., 2008. Heterogeneous oxidation catalysis on ruthenium: bridging the pressure and materials gaps and beyond. J. Phys. Condens. Matter 20, 184017. doi:10.1088/0953-8984/20/18/184017

Aßmann, J., Narkhede, V., Khodeir, L., Löffler, E., Hinrichsen, O., Birkner, A., Over, H., Muhler, M., 2004. On the Nature of the Active State of Supported Ruthenium Catalysts Used for the Oxidation of Carbon Monoxide: Steady-State and Transient Kinetics Combined with in Situ Infrared Spectroscopy †. J. Phys. Chem. B 108, 14634–14642. doi:10.1021/jp0401675

Astruc, D., Lu, F., Aranzaes, J.R., 2005. Nanoparticles as Recyclable Catalysts: The Frontier between Homogeneous and Heterogeneous Catalysis. Angew. Chem. Int. Ed. 44, 7852–7872. doi:10.1002/anie.200500766

Azubel, M., Koivisto, J., Malola, S., Bushnell, D., Hura, G.L., Koh, A.L., Tsunoyama, H., Tsukuda, T., Pettersson, M., Hakkinen, H., Kornberg, R.D., 2014. Electron microscopy of gold nanoparticles at atomic resolution. Science 345, 909–912. doi:10.1126/science.1251959

Baker, R.T.K., Barber, M.A., Harris, P.S., Feates, F.S., Waite, R.J., 1972. Nucleation and growth of carbon deposits from the nickel catalyzed decomposition of acetylene. J. Catal. 26, 51–62. doi:10.1016/0021-9517(72)90032-2

Baker, R.T.K., Chludzinski, J.J., 1980. Filamentous carbon growth on nickel-iron surfaces: the effect of various oxide additives. J. Catal. 64, 464–478.

Baker, R.T.K., Harris, P.S., Thomas, R.B., Waite, R.J., 1973. Formation of filamentous carbon from iron, cobalt and chromium catalyzed decomposition of acetylene. J. Catal. 30, 86–95. doi:10.1016/0021-9517(73)90055-9

Bañares, M.A., 2005. Operando methodology: combination of in situ spectroscopy and simultaneous activity measurements under catalytic reaction conditions. Catal. Today 100, 71–77. doi:10.1016/j.cattod.2004.12.017

Bañares, M.., Martínez-Huerta, M.., Gao, X., Fierro, J.L.., Wachs, I.., 2000. Dynamic behavior of supported vanadia catalysts in the selective oxidation of ethane. Catal. Today 61, 295–301. doi:10.1016/S0920-5861(00)00388-6

Banerjee, R., Crozier, P.A., 2012. In Situ Synthesis and Nanoscale Evolution of Model Supported Metal Catalysts: Ni on Silica. J. Phys. Chem. C 116, 11486–11495. doi:10.1021/jp2073446

Barnard, A.S., 2014. Clarifying stability, probability and population in nanoparticle ensembles. Nanoscale 6, 9983. doi:10.1039/C4NR01504E

Bell, A.T., Gates, B.C., Ray, D., Thompson, M.R., 2008. Basic Research Needs: Catalysis for Energy. US Department of Energy Basic Energy Sciences Workshop.

Benton, A.F., 1923. Adsorption and Catalysis in Carbon Monoxide Oxidation. J. Am. Chem. Soc. 45, 900–907.

Bernal, S., Botana, F.J., Calvino, J.J., Lopez-Cartes, C., Perez-Omil, J.A., Rodrıguez-Izquierdo, J.M., 1998. The interpretation of HREM images of supported metal catalysts using image simulation: profile view images. Ultramicroscopy 72, 135–164. doi:10.1016/S0304-3991(98)00009-6

Berzelius, J., 1836. . Ann. Chim. Phys. 61, 146.

Blackman, R.B., Tukey, J.W., 1958. The Measurement of Power Spectra from the Point of View of Communications Engineering - Part I. Bell Syst. Tech. J. 37, 185–282. doi:10.1002/j.1538-7305.1958.tb03874.x

Blaser, H.-U., Malan, C., Pugin, B., Spindler, F., Steiner, H., Studer, M., 2003. Selective Hydrogenation for Fine Chemicals: Recent Trends and New Developments. Adv. Synth. Catal. 345, 103–151. doi:10.1002/adsc.200390000

Blume, R., Havecker, M., Zafeiratos, S., Teschner, D., Kleimenov, E., Knopgericke, A., Schlogl, R., Barinov, A., Dudin, P., Kiskinova, M., 2006. Catalytically active states of Ru(0001) catalyst in CO oxidation reaction. J. Catal. 239, 354–361. doi:10.1016/j.jcat.2006.02.019

Blume, R., Niehus, H., Conrad, H., Böttcher, A., 2004. Oxide-free oxygen incorporation into Ru(0001). J. Chem. Phys. 120, 3871. doi:10.1063/1.1643724

Blume, R., Niehus, H., Conrad, H., Böttcher, A., Aballe, L., Gregoratti, L., Barinov, A., Kiskinova, M., 2005. Identification of Subsurface Oxygen Species Created during Oxidation of Ru(0001). J. Phys. Chem. B 109, 14052–14058. doi:10.1021/jp044175x

Bonzel, H.P., Ku, R., 1972. Mechanisms of the catalytic carbon monoxide oxidation on Pt (110). Surf. Sci. 33, 91–106. doi:10.1016/0039-6028(72)90101-X

Böttcher, A., Conrad, H., Niehus, H., 2000. Characterization of oxygen phases created during oxidation of Ru (0001). J. Chem. Phys. 112, 4779–4787.

Böttcher, A., Niehus, H., 1999. Oxygen adsorbed on oxidized Ru (0001). Phys. Rev. B 60, 14396.

Böttcher, A., Niehus, H., Schwegmann, S., Over, H., Ertl, G., 1997. CO oxidation reaction over oxygen-rich Ru (0001) surfaces. J. Phys. Chem. B 101, 11185–11191.

Böttcher, A., Rogozia, M., Niehus, H., Over, H., Ertl, G., 1999. Transient experiments on CO2 formation by the CO oxidation reaction over oxygen-rich Ru (0001) surfaces. J. Phys. Chem. B 103, 6267–6271.

Bourane, A., 2004. Oxidation of CO on a Pt/Al2O3 catalyst: from the surface elementary steps to light-off tests V. Experimental and kinetic model for light-off tests in excess of O2. J. Catal. 222, 499–510. doi:10.1016/j.jcat.2003.11.019

Bourane, A., 2003. Oxidation of CO on a Pt/Al2O3 catalyst: from the surface elementary steps to light-off tests IV. Kinetic study of the reduction by CO of strongly adsorbed oxygen species. J. Catal. 220, 3–12. doi:10.1016/S0021-9517(03)00267-7

Bourane, A., Bianchi, D., 2002a. Oxidation of CO on a Pt/Al2O3 Catalyst: From the Surface Elementary Steps to Lighting-Off Tests. J. Catal. 209, 114–125. doi:10.1006/jcat.2002.3605

Bourane, A., Bianchi, D., 2002b. Oxidation of CO on a Pt/Al2O3 Catalyst: From the Surface Elementary Steps to Lighting-Off Tests. J. Catal. 209, 126–134. doi:10.1006/jcat.2002.3606

Bourane, A., Bianchi, D., 2001. Oxidation of CO on a Pt/Al2O3 Catalyst: From the Surface Elementary Steps to Light-Off Tests. J. Catal. 202, 34–44. doi:10.1006/jcat.2001.3242

Boyes, E.D., Gai, P.L., 2015. Visualizing reacting single atoms in chemical reactions: Advancing the frontiers of materials research. MRS Bull. 40, 600–609. doi:10.1557/mrs.2015.141

Boyes, E.D., Gai, P.L., 2014. Visualising reacting single atoms under controlled conditions: Advances in atomic resolution in situ Environmental (Scanning) Transmission Electron Microscopy (E(S)TEM). Comptes Rendus Phys. 15, 200–213. doi:10.1016/j.crhy.2014.01.002

Boyes, E.D., Gai, P.L., 1997. Environmental high resolution electron microscopy and applications to chemical science. Ultramicroscopy 67, 219–232. doi:10.1016/S0304-3991(96)00099-X

Brynestad, J., 1976. Iron and Nickel Carbonyl Formation in Steel Pipes and Its Prevention: Literature Survey.

Burcham, L.J., Deo, G., Gao, X., Wachs, I.E., 2000. In situ IR, Raman, and UV-Vis DRS spectroscopy of supported vanadium oxide catalysts during methanol oxidation. Top. Catal. 11, 85–100.

Burda, C., Chen, X., Narayanan, R., El-Sayed, M.A., 2005. Chemistry and Properties of Nanocrystals of Different Shapes. Chem. Rev. 105, 1025–1102. doi:10.1021/cr030063a

Campbell, C.T., 2006. Transition Metal Oxides: Extra Thermodynamic Stability as Thin Films. Phys. Rev. Lett. 96. doi:10.1103/PhysRevLett.96.066106

Cant, N.W., Hicks, P.C., Lennon, B.S., 1978. Steady-state oxidation of carbon monoxide over supported noble metals with particular reference to platinum. J. Catal. 54, 372–383. doi:10.1016/0021-9517(78)90085-4

Cavendish, R., 2012. Structural analysis of nickel doped cerium oxide catalysts for fuel reforming in solid oxide fuel cells. Arizona State University.

Challa, S.R., Delariva, A.T., Hansen, T.W., Helveg, S., Sehested, J., Hansen, P.L., Garzon, F., Datye, A.K., 2011. Relating Rates of Catalyst Sintering to the Disappearance of Individual Nanoparticles during Ostwald Ripening. J. Am. Chem. Soc. 133, 20672–20675. doi:10.1021/ja208324n

Chang, L.Y., Barnard, A.S., Gontard, L.C., Dunin-Borkowski, R.E., 2010. Resolving the Structure of Active Sites on Platinum Catalytic Nanoparticles. Nano Lett. 10, 3073–3076. doi:10.1021/nl101642f

Cheng, X., Shi, Z., Glass, N., Zhang, L., Zhang, J., Song, D., Liu, Z.-S., Wang, H., Shen, J., 2007. A review of PEM hydrogen fuel cell contamination: Impacts, mechanisms, and mitigation. J. Power Sources 165, 739–756. doi:10.1016/j.jpowsour.2006.12.012

Chen, J., Lim, B., Lee, E.P., Xia, Y., 2009. Shape-controlled synthesis of platinum nanocrystals for catalytic and electrocatalytic applications. Nano Today 4, 81–95. doi:10.1016/j.nantod.2008.09.002

Chen, M.S., Cai, Y., Yan, Z., Gath, K.K., Axnanda, S., Goodman, D.W., 2007. Highly active surfaces for CO oxidation on Rh, Pd, and Pt. Surf. Sci. 601, 5326–5331. doi:10.1016/j.susc.2007.08.019

Chenna, S., 2011. In-situ Environmental TEM Studies For Developing Structure-Activity Relationship in Supported Metal Catalyst. Arizona State University, United States -- Arizona.

Chenna, S., Banerjee, R., Crozier, P.A., 2011. Atomic-Scale Observation of the Ni Activation Process for Partial Oxidation of Methane Using In Situ Environmental TEM. ChemCatChem 3, 1051–1059. doi:10.1002/cctc.201000238

Chenna, S., Crozier, P.A., 2012a. In situ environmental transmission electron microscopy to determine transformation pathways in supported Ni nanoparticles. Micron 43, 1188–1194. doi:10.1016/j.micron.2012.04.007

Chenna, S., Crozier, P.A., 2012b. Operando Transmission Electron Microscopy: A Technique for Detection of Catalysis Using Electron Energy-Loss Spectroscopy in the Transmission Electron Microscope. ACS Catal. 2, 2395–2402. doi:10.1021/cs3004853

Chin, S., Alexeev, O., Amiridis, M., 2005. Preferential oxidation of CO under excess H conditions over Ru catalysts. Appl. Catal. Gen. 286, 157–166. doi:10.1016/j.apcata.2005.02.031

Cochrane, H.D., Hutchison, J.L., White, D., 1989. Surface studies of catalytic ceria using atomic-resolution TEM. Ultramicroscopy 31, 138–142.

Cochrane, H.D., Hutchison, J.L., White, D., Parkinson, G.M., Dupas, C., Scott, A.J., 1990. High resolution electron microscopy of ceria-supported catalysts. Ultramicroscopy 34, 10–16. doi:10.1016/0304-3991(90)90051-M

Coloma Ribera, R., van de Kruijs, R.W.E., Kokke, S., Zoethout, E., Yakshin, A.E., Bijkerk, F., 2014. Surface and sub-surface thermal oxidation of thin ruthenium films. Appl. Phys. Lett. 105, 131601.

Coloma Ribera, R., van de Kruijs, R.W.E., Yakshin, A.E., Bijkerk, F., 2015. Determination of oxygen diffusion kinetics during thin film ruthenium oxidation. J. Appl. Phys. 118, 055303. doi:10.1063/1.4928295

Comotti, M., Li, W.-C., Spliethoff, B., Schüth, F., 2006. Support Effect in High Activity Gold Catalysts for CO Oxidation. J. Am. Chem. Soc. 128, 917–924. doi:10.1021/ja0561441

Compton, R.G., Bamford, C.H., Tipper, C.F.H., 1985. Kinetics and Chemical Technology, Comprehensive Chemical Kinetics. Elsevier Science.

Cornils, B., Herrmann, W., Schlogl, R., Wong, C.-H. (Eds.), 2000. Catalysis from A to Z: A Concise Encyclopedia. Wiley-VCH, Weinheim ; New York.

Costa, L. da F., Cesar, R.M., CRC Press, 2001. Shape analysis and classification theory and practice. CRC Press, Boca Raton, FL.

Cowley, J.M., Moodie, A.F., 1957. The scattering of electrons by atoms and crystals. I. A new theoretical approach. Acta Crystallogr. 10, 609–619.

Cowley, R.R., Segall, R.L., Smart, R.S.C., Turner, P.S., 1979. Growth twinning in magnesium oxide smoke crystals. Philos. Mag. A 39, 163–172. doi:10.1080/01418617908236890

Creemer, J.F., Helveg, S., Hoveling, G.H., Ullmann, S., Molenbroek, A.M., Sarro, P.M., Zandbergen, H.W., 2008. Atomic-scale electron microscopy at ambient pressure. Ultramicroscopy 108, 993–998. doi:10.1016/j.ultramic.2008.04.014

Creemer, J.F., Helveg, S., Kooyman, P.J., Molenbroek, A.M., Zandbergen, H.W., Sarro, P.M., 2010. A MEMS Reactor for Atomic-Scale Microscopy of Nanomaterials Under Industrially Relevant Conditions. J. Microelectromechanical Syst. 19, 254–264. doi:10.1109/JMEMS.2010.2041190

Crowther, R.A., DeRosier, D.J., Klug, A., 1970. The Reconstruction of a Three-Dimensional Structure from Projections and its Application to Electron Microscopy. Proc. R. Soc. Math. Phys. Eng. Sci. 317, 319–340. doi:10.1098/rspa.1970.0119

Crozier, P., 1999. Factors affecting the accuracy of lattice spacing determination by HREM in nanometre-sized Pt particles. J. Electron Microsc. 48, 1015–1024.

Crozier, P.A., 2011. Nanocharacterization of Heterogeneous Catalysts by Ex Situ and In Situ STEM, in: Pennycook, S.J., Nellist, P.D. (Eds.), Scanning Transmission Electron Microscopy. Springer New York, New York, NY, pp. 537–582.

Crozier, P.A., Chenna, S., 2011. In situ analysis of gas composition by electron energy-loss spectroscopy for environmental transmission electron microscopy. Ultramicroscopy 111, 177–185. doi:10.1016/j.ultramic.2010.11.005

Crozier, P.A., Hansen, T.W., 2015. In situ and operando transmission electron microscopy of catalytic materials. MRS Bull. 40, 38–45. doi:10.1557/mrs.2014.304

Crozier, P.A., Sharma, R., Datye, A.K., 1998. Oxidation and reduction of small palladium particles on silica. Microsc. Microanal. 4, 278–285.

Crozier, P.A., Wang, R., Sharma, R., 2008. In situ environmental TEM studies of dynamic changes in cerium-based oxides nanoparticles during redox processes. Ultramicroscopy 108, 1432–1440. doi:10.1016/j.ultramic.2008.05.015

Curtin, S., Gangi, J., 2014. 2013 DOE Fuel Cell Technologies Market Report.

Datye, A.K., Xu, Q., Kharas, K.C., McCarty, J.M., 2006. Particle size distributions in heterogeneous catalysts: What do they tell us about the sintering mechanism? Catal. Today 111, 59–67. doi:10.1016/j.cattod.2005.10.013

de Jonge, N., Bigelow, W.C., Veith, G.M., 2010. Atmospheric Pressure Scanning Transmission Electron Microscopy. Nano Lett. 10, 1028–1031. doi:10.1021/nl904254g

DeLaRiva, A.T., Hansen, T.W., Challa, S.R., Datye, A.K., 2013. In situ Transmission Electron Microscopy of catalyst sintering. J. Catal. 308, 291–305. doi:10.1016/j.jcat.2013.08.018

de Ruijter, W.J., Sharma, R., McCartney, M.R., Smith, D.J., 1995. Measurement of lattice-fringe vectors from digital HREM images: experimental precision. Ultramicroscopy 57, 409–422.

Dhar, H.P., 1987. Nature of CO Adsorption during H2 Oxidation in Relation to Modeling for CO Poisoning of a Fuel Cell Anode. J. Electrochem. Soc. 134. doi:10.1149/1.2100333

Egerton, R.F., 2011. Electron energy-loss spectroscopy in the electron microscope, Third edition. ed, The language of science. Springer, New York.

Egerton, R.F., 2007. Limits to the spatial, energy and momentum resolution of electron energy-loss spectroscopy. Ultramicroscopy 107, 575–586. doi:10.1016/j.ultramic.2006.11.005

Egerton, R.F., 1978. Formulae for light-element micro analysis by electron energy-loss spectrometry. Ultramicroscopy 3, 243–251. doi:10.1016/S0304-3991(78)80031-X

Egerton, R.F., Li, P., Malac, M., 2004. Radiation damage in the TEM and SEM. Micron 35, 399–409. doi:10.1016/j.micron.2004.02.003

EIA, 2015. Short Term Energy Outlook. US Energy Information Administration.

Enterkin, J.A., Poeppelmeier, K.R., Marks, L.D., 2011. Oriented Catalytic Platinum Nanoparticles on High Surface Area Strontium Titanate Nanocuboids. Nano Lett. 11, 993–997. doi:10.1021/nl104263j

Fan, C.Y., Wang, J., Jacobi, K., Ertl, G., 2001. The oxidation of CO on RuO2(110) at room temperature. J. Chem. Phys. 114, 10058. doi:10.1063/1.1350817

Feng, X., Chee, S.W., Sharma, R., Liu, K., Xie, X., Li, Q., Fan, S., Jiang, K., 2011. In Situ TEM observation of the gasification and growth of carbon nanotubes using iron catalysts. Nano Res. 4, 767–779. doi:10.1007/s12274-011-0133-x

Flege, J., Hrbek, J., Sutter, P., 2008. Structural imaging of surface oxidation and oxidation catalysis on Ru(0001). Phys. Rev. B 78. doi:10.1103/PhysRevB.78.165407

Fogler, H.S., 2006. Elements of chemical reaction engineering, 4th ed. ed, Prentice Hall PTR international series in the physical and chemical engineering sciences. Prentice Hall PTR, Upper Saddle River, NJ.

Frank, J., 2014. Electron Tomography. Springer.

Fraundorf, P., Qin, W., Moeck, P., Mandell, E., 2005. Making sense of nanocrystal lattice fringes. J. Appl. Phys. 98, 114308. doi:10.1063/1.2135414

Freund, H.-J., Meijer, G., Scheffler, M., Schlögl, R., Wolf, M., 2011. CO Oxidation as a Prototypical Reaction for Heterogeneous Processes. Angew. Chem. Int. Ed. 50, 10064–10094. doi:10.1002/anie.201101378

Fujitani, T., Nakamura, I., Haruta, M., 2014. Role of Water in CO Oxidation on Gold Catalysts. Catal. Lett. 144, 1475–1486. doi:10.1007/s10562-014-1325-2

Gai, P.L., 2002a. Developments in in situ environmental cell high-resolution electron microscopy and applications to catalysis. Top. Catal. 21, 161–173.

Gai, P.L., 2002b. Development of Wet Environmental TEM (Wet-ETEM) for In Situ Studies of Liquid-Catalyst Reactions on the Nanoscale. Microsc. Microanal. 8, 21–28. doi:10.1017/S143192760201005X

Gai, P.L., Kourtakis, K., Boyes, E.D., 2005. In situ nanoscale wet imaging of the heterogeneous catalyzationof nitriles in a solution phase: novel hydrogenation chemistry through nanocatalysts on nanosupports. Catal. Lett. 102, 1–7. doi:10.1007/s10562-005-5195-5

Gai, P.L., Sharma, R., Ross, F.M., 2008. Environmental (S)TEM Studies of Gas–Liquid–Solid Interactions under Reaction Conditions. MRS Bull. 33, 107–114. doi:10.1557/mrs2008.23

Galloway, C.M., Ru, E.C.L., Etchegoin, P.G., 2009. An iterative algorithm for background removal in spectroscopy by wavelet transforms. Appl. Spectrosc. 63, 1370–1376.

Gandía, L.M., Arzamedi, G., Diéguez, P.M. (Eds.), 2013. Renewable hydrogen technologies: production, purification, storage, applications and safety. Elsevier, Amsterdam ; Boston.

Gao, F., Goodman, D.W., 2012. CO oxidation over ruthenium: identification of the catalytically active phases at near-atmospheric pressures. Phys. Chem. Chem. Phys. 14, 6688–6697. doi:10.1039/c2cp40121e

Gao, F., Wang, Y., Cai, Y., Goodman, D.W., 2009. CO oxidation over Ru(0001) at near-atmospheric pressures: From chemisorbed oxygen to RuO2. Surf. Sci. 603, 1126–1134. doi:10.1016/j.susc.2009.02.037

García de Abajo, F.J., Aizpurua, J., 1997. Numerical simulation of electron energy loss near inhomogeneous dielectrics. Phys. Rev. B 56, 15873–15884. doi:10.1103/PhysRevB.56.15873

Gavnholt, J., 2009. The Structure of Individual Nanoparticles and Hot Electron Assisted Chemistry at Surfaces. Technical University of Denmark (DTU).

Gladden, L.F., Mantle, M.D., Sederman, A.J., 2006. Magnetic Resonance Imaging of Catalysts and Catalytic Processes, in: Advances in Catalysis. Elsevier, pp. 1–75.

Goodman, D.W., Peden, C.H.F., Chen, M.S., 2007a. CO oxidation on ruthenium: The nature of the active catalytic surface. Surf. Sci. 601, L124–L126. doi:10.1016/j.susc.2007.08.003

Goodman, D.W., Peden, C.H.F., Chen, M.S., 2007b. Reply to comment on “CO oxidation on ruthenium: The nature of the active catalytic surface” by H. Over, M. Muhler, A.P. Seitsonen. Surf. Sci. 601, 5663–5665. doi:10.1016/j.susc.2007.09.042

Goodman, P., Moodie, A.F., 1974. Numerical evaluations of N-beam wave functions in electron scattering by the multi-slice method. Acta Crystallogr. A 30, 280–290.

Granqvist, C.G., Buhrman, R.A., 1976. Size distributions for supported metal catalysts: Coalescence growth versus ostwald ripening. J. Catal. 42, 477–479.

Grass, M.E., Zhang, Y., Butcher, D.R., Park, J.Y., Li, Y., Bluhm, H., Bratlie, K.M., Zhang, T., Somorjai, G.A., 2008. A Reactive Oxide Overlayer on Rhodium Nanoparticles during CO Oxidation and Its Size Dependence Studied by In Situ Ambient-Pressure X-ray Photoelectron Spectroscopy. Angew. Chem. Int. Ed. 47, 8893–8896. doi:10.1002/anie.200803574

Grob, R.L., Barry, E.F., 2004. Modern practice of gas chromatography. Wiley-Interscience, Hoboken, N.J.

Grogger, W., n.d. DM-Script [WWW Document]. URL http://portal.tugraz.at/portal/page/portal/felmi/DM-Script (accessed 8.21.15).

Gustafson, J., Mikkelsen, A., Borg, M., Lundgren, E., Köhler, L., Kresse, G., Schmid, M., Varga, P., Yuhara, J., Torrelles, X., Quirós, C., Andersen, J.N., 2004. Self-Limited Growth of a Thin Oxide Layer on Rh(111). Phys. Rev. Lett. 92. doi:10.1103/PhysRevLett.92.126102

Hansen, P.L., Wagner, J.B., Helveg, S., Rostrup-Nielsen, J.R., Clausen, B.S., Topsoe, H., 2002. Atom-Resolved Imaging of Dynamic Shape Changes in Supported Copper Nanocrystals. Science 295, 2053–2055. doi:10.1126/science.1069325

Hansen, T.W., 2001. Atomic-Resolution in Situ Transmission Electron Microscopy of a Promoter of a Heterogeneous Catalyst. Science 294, 1508–1510. doi:10.1126/science.1064399

Hansen, T.W., DeLaRiva, A.T., Challa, S.R., Datye, A.K., 2013. Sintering of Catalytic Nanoparticles: Particle Migration or Ostwald Ripening? Acc. Chem. Res. 46, 1720–1730. doi:10.1021/ar3002427

Hansen, T.W., Hansen, P.L., Dahl, S., Jacobsen, C.J., 2002. Support effect and active sites on promoted ruthenium catalysts for ammonia synthesis. Catal. Lett. 84, 7–12.

Hansen, T.W., Wagner, J.B., 2015. Controlled Atmosphere Transmission Electron Microscopy: Principles and Practice. Springer International Publishing.

Hansen, T.W., Wagner, J.B., 2014. Catalysts under Controlled Atmospheres in the Transmission Electron Microscope. ACS Catal. 4, 1673–1685. doi:10.1021/cs401148d

Haruta, M., 1997. Size- and support-dependency in the catalysis of gold. Catal. Today 36, 153–166. doi:10.1016/S0920-5861(96)00208-8

Haruta, M., Kobayashi, T., Sano, H., Yamada, N., 1987. Novel gold catalysts for the oxidation of carbon monoxide at a temperature far below 0.DEG.C. Chem. Lett. 405–408. doi:10.1246/cl.1987.405

Haruta, M., Yamada, N., Kobayashi, T., Iijima, S., 1989. Gold catalysts prepared by coprecipitation for low-temperature oxidation of hydrogen and of carbon monoxide. J. Catal. 115, 301–309. doi:10.1016/0021-9517(89)90034-1

Hashmi, A.S.K., Hutchings, G.J., 2006. Gold Catalysis. Angew. Chem. Int. Ed. 45, 7896–7936. doi:10.1002/anie.200602454

Haw, J.F. (Ed.), 2002. In-situ spectroscopy in heterogeneous catalysis. Wiley-VCH, Weinheim.

Heidenreich, R.D., 1942. Electron Reflections in MgO Crystals with the Electron Microscope. Phys. Rev. 62, 291–292.

Held, G., Uremović, S., Menzel, D., 1995. Rearrangement of stepped Ru(001) surfaces upon oxygen adsorption. Surf. Sci. 331-333, 1122–1128. doi:10.1016/0039-6028(95)00375-4

Helveg, S., 2015. An industrial perspective of the impact of Haldor Topsøe on (in situ) electron microscopy in catalysis. J. Catal. 328, 102–110. doi:10.1016/j.jcat.2014.12.017

Helveg, S., Kisielowski, C.F., Jinschek, J.R., Specht, P., Yuan, G., Frei, H., 2015. Observing gas-catalyst dynamics at atomic resolution and single-atom sensitivity. Micron 68, 176–185. doi:10.1016/j.micron.2014.07.009

Helveg, S., López-Cartes, C., Sehested, J., Hansen, P.L., Clausen, B.S., Rostrup-Nielsen, J.R., Abild-Pedersen, F., Nørskov, J.K., 2004. Atomic-scale imaging of carbon nanofibre growth. Nature 427, 426–429. doi:10.1038/nature02278

Hendriksen, B.L.M., Frenken, J.W.M., 2002. CO Oxidation on Pt(110): Scanning Tunneling Microscopy Inside a High-Pressure Flow Reactor. Phys. Rev. Lett. 89. doi:10.1103/PhysRevLett.89.046101

Herman, G., Lewitt, R., 1979. Overview of image reconstruction from projections. Image Reconstr. Proj. 1–8.

Hess, F., Farkas, A., Seitsonen, A.P., Over, H., 2012. “First-Principles” kinetic monte carlo simulations revisited: CO oxidation over RuO2(110). J. Comput. Chem. 33, 757–766. doi:10.1002/jcc.22902

He, Y.B., Knapp, M., Lundgren, E., Over, H., 2005. Ru(0001) Model Catalyst under Oxidizing and Reducing Reaction Conditions: In-Situ High-Pressure Surface X-ray Diffraction Study. J. Phys. Chem. B 109, 21825–21830. doi:10.1021/jp0538520

Hoffmann, F.M., Weisel, M.W., Peden, C.H.F., 1990. The oxidation of CO over Ru(001) at high pressures: CO residence times and reaction mechanism. J. Electron Spectrosc. Relat. Phenom. 54-55, 779–786. doi:10.1016/0368-2048(90)80270-K

Holse, C., Elkjær, C.F., Nierhoff, A., Sehested, J., Chorkendorff, I., Helveg, S., Nielsen, J.H., 2015. Dynamic Behavior of CuZn Nanoparticles under Oxidizing and Reducing Conditions. J. Phys. Chem. C. doi:10.1021/jp510015v

Howie, A., Walsh, C., 1991. Interpretation of valence loss spectra from composite media. Microsc. Microanal. Microstruct. 2, 171–181. doi:10.1051/mmm:0199100202-3017100

Hug, S.J., Sulzberger, B., 1994. In situ Fourier transform infrared spectroscopic evidence for the formation of several different surface complexes of oxalate on TiO2 in the aqueous phase. Langmuir 10, 3587–3597.

Hunger, M., Wang, W., 2006. Characterization of Solid Catalysts in the Functioning State by Nuclear Magnetic Resonance Spectroscopy, in: Advances in Catalysis. Elsevier, pp. 149–225.

Inokuti, M., 1971. Inelastic Collisions of Fast Charged Particles with Atoms and Molecules—The Bethe Theory Revisited. Rev. Mod. Phys. 43, 297–347. doi:10.1103/RevModPhys.43.297

Irie, H., Kamiya, K., Shibanuma, T., Miura, S., Tryk, D.A., Yokoyama, T., Hashimoto, K., 2009. Visible Light-Sensitive Cu(II)-Grafted TiO2 Photocatalysts: Activities and X-ray Absorption Fine Structure Analyses. J. Phys. Chem. C 113, 10761–10766. doi:10.1021/jp903063z

Jacob, K.T., Mishra, S., Waseda, Y., 2004. Refinement of the Thermodynamic Properties of Ruthenium Dioxide and Osmium Dioxide. J. Am. Ceram. Soc. 83, 1745–1752. doi:10.1111/j.1151-2916.2000.tb01459.x

Janbroers, S., Crozier, P.A., Zandbergen, H.W., Kooyman, P.J., 2011. A model study on the carburization process of iron-based Fischer–Tropsch catalysts using in situ TEM–EELS. Appl. Catal. B Environ. 102, 521–527. doi:10.1016/j.apcatb.2010.12.034

Jeangros, Q., Hansen, T.W., Wagner, J.B., Damsgaard, C.D., Dunin-Borkowski, R.E., Hébert, C., Van herle, J., Hessler-Wyser, A., 2013. Reduction of nickel oxide particles by hydrogen studied in an environmental TEM. J. Mater. Sci. 48, 2893–2907. doi:10.1007/s10853-012-7001-2

Jiang, N., Spence, J.C.H., 2012. On the dose-rate threshold of beam damage in TEM. Ultramicroscopy 113, 77–82. doi:10.1016/j.ultramic.2011.11.016

Jinschek, J.R., Helveg, S., 2012. Image resolution and sensitivity in an environmental transmission electron microscope. Micron 43, 1156–1168. doi:10.1016/j.micron.2012.01.006

Johnsen, R., Chatterjee, B.K., 2011. Flow of binary gas mixtures through small sampling orifices. J. Vac. Sci. Technol. Vac. Surf. Films 29, 011002–011002.

Johnson, D.W., Spence, J.C.H., 1974. Determination of the single-scattering probability distribution from plural-scattering data. J. Phys. Appl. Phys. 7, 771–780. doi:10.1088/0022-3727/7/6/304

Jones, G., Jakobsen, J., Shim, S., Kleis, J., Andersson, M., Rossmeisl, J., Abildpedersen, F., Bligaard, T., Helveg, S., Hinnemann, B., 2008. First principles calculations and experimental insight into methane steam reforming over transition metal catalysts. J. Catal. 259, 147–160. doi:10.1016/j.jcat.2008.08.003

Joo, S.H., Park, J.Y., Renzas, J.R., Butcher, D.R., Huang, W., Somorjai, G.A., 2010. Size Effect of Ruthenium Nanoparticles in Catalytic Carbon Monoxide Oxidation. Nano Lett. 10, 2709–2713. doi:10.1021/nl101700j

Kahlich, M.J., Gasteiger, H.A., Behm, R.J., 1997. Kinetics of the Selective CO Oxidation in H2-Rich Gas on Pt/Al2O3. J. Catal. 171, 93–105. doi:10.1006/jcat.1997.1781

Kalinkin, A.V., Savchenko, V.I., 1982. O2 and CO adsorption on Ru(001) plane. React. Kinet. Catal. Lett. 20, 133–137. doi:10.1007/BF02063598

Kim, S.M., Qadir, K., Seo, B., Jeong, H.Y., Joo, S.H., Terasaki, O., Park, J.Y., 2013. Nature of Rh Oxide on Rh Nanoparticles and Its Effect on the Catalytic Activity of CO Oxidation. Catal. Lett. 143, 1153–1161. doi:10.1007/s10562-013-1087-2

Kim, Y.D., Over, H., Krabbes, G., Ertl, G., 2000. Identification of RuO2 as the active phase in CO oxidation on oxygen-rich ruthenium surfaces. Top. Catal. 14, 95–100.

Kim, Y.D., Schwegmann, S., Seitsonen, A.P., Over, H., 2001. Epitaxial Growth of RuO2 (100) on Ru(10$\bar{1}$0): Surface Structure and Other Properties. J. Phys. Chem. B 105, 2205–2211. doi:10.1021/jp003650y

Kim, Y.H., Yim, S.-D., Park, E.D., 2012. Selective CO oxidation in a hydrogen-rich stream over Ru/SiO2. Catal. Today 185, 143–150. doi:10.1016/j.cattod.2011.07.022

Kim, Y.K., Morgan, G.A., Yates, J.T., 2007. Role of Atomic Step Defect Sites on the Catalytic Oxidation of Carbon Monoxide: Comparison between Ru(001) and Ru(109) Single-Crystal Surfaces. J. Phys. Chem. C 111, 3366–3368. doi:10.1021/jp064729r

Kirkland, J., 1998. Advanced Computing in Electron Microscopy, Journal for the Study of the. Springer US.

Kisielowski, C., Specht, P., Gygax, S.M., Barton, B., Calderon, H.A., Kang, J.H., Cieslinski, R., 2015. Instrumental requirements for the detection of electron beam-induced object excitations at the single atom level in high-resolution transmission electron microscopy. Micron 68, 186–193. doi:10.1016/j.micron.2014.07.010

Kiss, J.T., Gonzalez, R.D., 1984. Catalytic oxidation of carbon monoxide over ruthenium/silicon dioxide. An in situ infrared and kinetic study. J. Phys. Chem. 88, 892–897.

Kolmakov, A., Goodman, D.W., 2002. In situ scanning tunneling microscopy of oxide-supported metal clusters: Nucleation, growth, and thermal evolution of individual particles. Chem. Rec. 2, 446–457. doi:10.1002/tcr.10045

Krebs, R.E., 2006. The history and use of our earth's chemical elements: a reference guide, 2nd ed. ed. Greenwood Press, Westport, Conn.

Kusada, K., Kobayashi, H., Yamamoto, T., Matsumura, S., Sumi, N., Sato, K., Nagaoka, K., Kubota, Y., Kitagawa, H., 2013. Discovery of Face-Centered-Cubic Ruthenium Nanoparticles: Facile Size-Controlled Synthesis Using the Chemical Reduction Method. J. Am. Chem. Soc. 135, 5493–5496. doi:10.1021/ja311261s

Kuwauchi, Y., Takeda, S., Yoshida, H., Sun, K., Haruta, M., Kohno, H., 2013. Stepwise Displacement of Catalytically Active Gold Nanoparticles on Cerium Oxide. Nano Lett. 13, 3073–3077. doi:10.1021/nl400919c

Kuwauchi, Y., Yoshida, H., Akita, T., Haruta, M., Takeda, S., 2012. Intrinsic Catalytic Structure of Gold Nanoparticles Supported on TiO2. Angew. Chem. Int. Ed. 51, 7729–7733. doi:10.1002/anie.201201283

Leapman, R.D., Rez, P., Mayers, D.F., 1980. K, L, and M shell generalized oscillator strengths and ionization cross sections for fast electron collisions. J. Chem. Phys. 72, 1232. doi:10.1063/1.439184

Lee, H., 1980. Carbon monoxide oxidation over Ru (001). J. Catal. 63, 261–264. doi:10.1016/0021-9517(80)90078-0

Lewitt, R., Bates, R., 1978. IMAGE-RECONSTRUCTION FROM PROJECTIONS. 1. GENERAL THEORETICAL CONSIDERATIONS. Optik 50, 19–33.

Li, P., Liu, J., Nag, N., Crozier, P., 2006. In situ synthesis and characterization of Ru promoted Co/Al2O3 Fischer–Tropsch catalysts. Appl. Catal. Gen. 307, 212–221. doi:10.1016/j.apcata.2006.03.051

Li, P., Liu, J., Nag, N., Crozier, P.A., 2009. In situ preparation of Ni–Cu/TiO2 bimetallic catalysts. J. Catal. 262, 73–82. doi:10.1016/j.jcat.2008.12.001

Li, P., Liu, J., Nag, N., Crozier, P.A., 2006. Dynamic nucleation and growth of Ni nanoparticles on high-surface area titania. Surf. Sci. 600, 693–702. doi:10.1016/j.susc.2005.11.023

Li, P., Liu, J., Nag, N., Crozier, P.A., 2005. Atomic-Scale Study of in Situ Metal Nanoparticle Synthesis in a Ni/TiO2 System. J. Phys. Chem. B 109, 13883–13890. doi:10.1021/jp044223d

Liu, K., Wang, A., Zhang, T., 2012. Recent Advances in Preferential Oxidation of CO Reaction over Platinum Group Metal Catalysts. ACS Catal. 2, 1165–1178. doi:10.1021/cs200418w

Li, Y., Somorjai, G.A., 2010. Nanoscale Advances in Catalysis and Energy Applications. Nano Lett. 10, 2289–2295. doi:10.1021/nl101807g

Li, Y., Zakharov, D., Zhao, S., Tappero, R., Jung, U., Elsen, A., Baumann, P., Nuzzo, R.G., Stach, E.A., Frenkel, A.I., 2015. Complex structural dynamics of nanocatalysts revealed in Operando conditions by correlated imaging and spectroscopy probes. Nat. Commun. 6, 7583. doi:10.1038/ncomms8583

López-Haro, M., Cíes, J.M., Trasobares, S., Pérez-Omil, J.A., Delgado, J.J., Bernal, S., Bayle-Guillemaud, P., Stéphan, O., Yoshida, K., Boyes, E.D., Gai, P.L., Calvino, J.J., 2012. Imaging Nanostructural Modifications Induced by Electronic Metal−Support Interaction Effects at Au||Cerium-Based Oxide Nanointerfaces. ACS Nano 6, 6812–6820. doi:10.1021/nn301557u

Madey, T.E., Albert Engelhardt, H., Menzel, D., 1975. Adsorption of oxygen and oxidation of CO on the ruthenium (001) surface. Surf. Sci. 48, 304–328. doi:10.1016/0039-6028(75)90409-4

Malm, J.-O., O'Keefe, M.A., 1997. Deceptive "lattice spacings" in high-resolution micrographs of metal nanoparticles. Ultramicroscopy 68, 13–23. doi:10.1016/S0304-3991(97)00005-3

Manasilp, A., Gulari, E., 2002. Selective CO oxidation over Pt/alumina catalysts for fuel cell applications. Appl. Catal. B Environ. 37, 17–25.

Marks, L.D., Peng, L., 2016. Nanoparticle shape, thermodynamics and kinetics. J. Phys. Condens. Matter 28, 053001. doi:10.1088/0953-8984/28/5/053001

Martynova, Y., Shaikhutdinov, S., Freund, H.-J., 2013. CO Oxidation on Metal-Supported Ultrathin Oxide Films: What Makes Them Active? ChemCatChem 5, 2162–2166. doi:10.1002/cctc.201300212

Martynova, Y., Yang, B., Yu, X., Boscoboinik, J.A., Shaikhutdinov, S., Freund, H.-J., 2012. Low Temperature CO Oxidation on Ruthenium Oxide Thin Films at Near-Atmospheric Pressures. Catal. Lett. 142, 657–663. doi:10.1007/s10562-012-0823-3

Masson, G., Orlandi, S., Rekinger, M., 2014. Global Market Outlook for Photovoltaics.

Mejía-Rosales, S.J., Fernández-Navarro, C., Pérez-Tijerina, E., Blom, D.A., Allard, L.F., José-Yacamán, M., 2007. On the Structure of Au/Pd Bimetallic Nanoparticles. J. Phys. Chem. C 111, 1256–1260. doi:10.1021/jp066328h

Miller, B.K., Barker, T.M., Crozier, P.A., 2015. Novel sample preparation for operando TEM of catalysts. Ultramicroscopy 156, 18–22. doi:10.1016/j.ultramic.2015.05.003

Miller, B.K., Crozier, P.A., 2016a. Shape and Surface Structure of Ru Nanocatalysts During CO Oxidation. ACS Catal. In Preparation.

Miller, B.K., Crozier, P.A., 2016b. Atomic Scale Observation of Thin RuO2 Layers on Individual Nanoparticles During CO Oxidation. J. Phys. Chem. C In Preparation.

Miller, B.K., Crozier, P.A., 2014. Analysis of Catalytic Gas Products Using Electron Energy-Loss Spectroscopy and Residual Gas Analysis for Operando Transmission Electron Microscopy. Microsc. Microanal. 20, 815–824. doi:10.1017/S1431927614000749

Mills, A., Hodgen, S., 2005. Fluorescent Carbon Dioxide Indicators, in: Geddes, C.D., Lakowicz, J.R. (Eds.), Topics in Fluorescence Spectroscopy. Springer US, Boston, MA, pp. 119–161.

Mitchell, D.R.G., Schaffer, B., 2005. Scripting-customised microscopy tools for Digital Micrograph™. Ultramicroscopy 103, 319–332. doi:10.1016/j.ultramic.2005.02.003

Moen, A., Nicholson, D.G., Clausen, B.S., Hansen, P.L., Molenbroek, A., Steffensen, G., 1997. X-ray absorption spectroscopic studies at the cobalt K-edge on a reduced Al2O3-supported rhenium-promoted cobalt Fischer-Tropsch catalyst. Chem. Mater. 9, 1241–1247.

Mortensen, P.M., Hansen, T.W., Wagner, J.B., Jensen, A.D., 2015. Modeling of temperature profiles in an environmental transmission electron microscope using computational fluid dynamics. Ultramicroscopy 152, 1–9. doi:10.1016/j.ultramic.2014.12.007

Nakamura, R., Tokozakura, D., Nakajima, H., Lee, J.-G., Mori, H., 2007. Hollow oxide formation by oxidation of Al and Cu nanoparticles. J. Appl. Phys. 101, 074303. doi:10.1063/1.2711383

Narkhede, V., Aßmann, J., Muhler, M., 2005. Structure-Activity Correlations for the Oxidation of CO over Polycrystalline RuO2 Powder Derived from Steady-State and Transient Kinetic Experiments. Z. Für Phys. Chem. 219, 979–995. doi:10.1524/zpch.219.7.979.67092

Nørskov, J.K., Bligaard, T., Rossmeisl, J., Christensen, C.H., 2009. Towards the computational design of solid catalysts. Nat. Chem. 1, 37–46. doi:10.1038/nchem.121

O'Hanlon, J., 2003. A user's guide to vacuum technology, 3rd ed. ed. Wiley-Interscience, Hoboken NJ.

Oh, S., Sinkevitch, R.M., 1993. Carbon Monoxide Removal from Hydrogen-Rich Fuel Cell Feedstreams by Selective Catalytic Oxidation. J. Catal. 142, 254–262. doi:10.1006/jcat.1993.1205

OKeefe, M.A., 1994. Interpretation of HRTEM images by image simulation: An introduction to theory and practice. Lawrence Berkeley Lab., CA (United States).

Onoda, G.Y., Liniger, E.G., 1990. Random loose packings of uniform spheres and the dilatancy onset. Phys. Rev. Lett. 64, 2727.

Otten, M.T., Coene, W.M.J., 1993. High-resolution imaging on a field emission TEM. Ultramicroscopy 48, 77–91. doi:10.1016/0304-3991(93)90173-U

Over, H., 2012. Surface Chemistry of Ruthenium Dioxide in Heterogeneous Catalysis and Electrocatalysis: From Fundamental to Applied Research. ChemInform 43. doi:10.1021/cr200247n

Over, H., Balmes, O., Lundgren, E., 2009. Direct comparison of the reactivity of the non-oxidic phase of Ru(0001) and the RuO2 phase in the CO oxidation reaction. Surf. Sci. 603, 298–303. doi:10.1016/j.susc.2008.11.012

Over, H., Kim, Y.D., Seitsonen, A.P., Wendt, S., Lundgren, E., Schmid, M., Varga, P., Morgante, A., Ertl, G., 2000. Atomic-scale structure and catalytic reactivity of the RuO2 (110) surface. Science 287, 1474–1476.

Over, H., Muhler, M., 2003. Catalytic CO oxidation over ruthenium—bridging the pressure gap. Prog. Surf. Sci. 72, 3–17. doi:10.1016/S0079-6816(03)00011-X

Over, H., Muhler, M., Seitsonen, A.P., 2007. Comment on "CO oxidation on ruthenium: The nature of the active catalytic surface" by D.W. Goodman, C.H.F. Peden, M.S. Chen. Surf. Sci. 601, 5659–5662. doi:10.1016/j.susc.2007.09.041

Park, E.D., Lee, D., Lee, H.C., 2009. Recent progress in selective CO removal in a H2-rich stream. Catal. Today 139, 280–290. doi:10.1016/j.cattod.2008.06.027

Parkinson, G.M., 1989. High resolution, in-situ controlled atmosphere transmission electron microscopy (CATEM) of heterogeneous catalysts. Catal. Lett. 2, 303–307. doi:10.1007/BF00770228

Pauwels, B., Van Tendeloo, G., Bouwen, W., Theil Kuhn, L., Lievens, P., Lei, H., Hou, M., 2000. Low-energy-deposited Au clusters investigated by high-resolution electron microscopy and molecular dynamics simulations. Phys. Rev. B 62, 10383–10393. doi:10.1103/PhysRevB.62.10383

Peden, C.H., Goodman, D.W., 1986. Kinetics of carbon monoxide oxidation over ruthenium (0001). J. Phys. Chem. 90, 1360–1365.

Peng, Z., Somodi, F., Helveg, S., Kisielowski, C., Specht, P., Bell, A.T., 2012. High-resolution in situ and ex situ TEM studies on graphene formation and growth on Pt nanoparticles. J. Catal. 286, 22–29. doi:10.1016/j.jcat.2011.10.008

Pfnür, H., Menzel, D., 1983. The influence of adsorbate interactions on kinetics and equilibrium for CO on Ru(001). I. Adsorption kinetics. J. Chem. Phys. 79, 2400. doi:10.1063/1.446047

Qadir, K., Joo, S.H., Mun, B.S., Butcher, D.R., Renzas, J.R., Aksoy, F., Liu, Z., Somorjai, G.A., Park, J.Y., 2012. Intrinsic Relation between Catalytic Activity of CO Oxidation on Ru Nanoparticles and Ru Oxides Uncovered with Ambient Pressure XPS. Nano Lett. 12, 5761–5768. doi:10.1021/nl303072d

Qadir, K., Kim, S.M., Seo, H., Mun, B.S., Akgul, F.A., Liu, Z., Park, J.Y., 2013. Deactivation of Ru Catalysts under Catalytic CO Oxidation by Formation of Bulk Ru Oxide Probed with Ambient Pressure XPS. J. Phys. Chem. C 117, 13108–13113. doi:10.1021/jp402688a

Qiao, B., Wang, A., Yang, X., Allard, L.F., Jiang, Z., Cui, Y., Liu, J., Li, J., Zhang, T., 2011. Single-atom catalysis of CO oxidation using Pt1/FeOx. Nat. Chem. 3, 634–641. doi:10.1038/nchem.1095

Raether, H., 1967. Surface plasma oscillations as a tool for surface examinations. Surf. Sci. 8, 233–246. doi:10.1016/0039-6028(67)90085-4

Railsback, J.G., Johnston-Peck, A.C., Wang, J., Tracy, J.B., 2010. Size-Dependent Nanoscale Kirkendall Effect During the Oxidation of Nickel Nanoparticles. ACS Nano 4, 1913–1920. doi:10.1021/nn901736y

Reed, P.D., Comrie, C.M., Lambert, R.M., 1977. Oxygen chemisorption and the carbon monoxide-oxygen interaction on Ru(101). Surf. Sci. 64, 603–616. doi:10.1016/0039-6028(77)90065-6

Regalbuto, J.R., 2007. Handbook of catalyst preparation. Taylor & Francis, Boca Raton.

Reibacher, C., 2014. Instance-Specific Pose Estimation from Silhouette Information for an Accurate Handling of Smoothly-Shaped Goods.

Reuter, K., Ganduglia-Pirovano, M., Stampfl, C., Scheffler, M., 2002. Metastable precursors during the oxidation of the Ru(0001) surface. Phys. Rev. B 65. doi:10.1103/PhysRevB.65.165403

Reuter, K., Scheffler, M., 2006. First-principles kinetic Monte Carlo simulations for heterogeneous catalysis: Application to the CO oxidation at RuO2(110). Phys. Rev. B 73. doi:10.1103/PhysRevB.73.045433

Reuter, K., Scheffler, M., 2003. First-Principles Atomistic Thermodynamics for Oxidation Catalysis: Surface Phase Diagrams and Catalytically Interesting Regions. Phys. Rev. Lett. 90. doi:10.1103/PhysRevLett.90.046103

Rideal, E.K., Taylor, H., 1919. Catalysis in theory and practice. Macmillan and Company, Limited.

Ringe, E., 2014. Nanocrystalline materials: recent advances in crystallographic characterization techniques. IUCrJ 1, 530–539. doi:10.1107/S2052252514020818

Rodríguez, J.A., Hanson, J.C., Chupas, P.J. (Eds.), 2013. In-situ characterization of heterogeneous catalysts. Wiley, Hoboken, New Jersey.

Roeffaers, M.B.J., Sels, B.F., Uji-i, H., De Schryver, F.C., Jacobs, P.A., De Vos, D.E., Hofkens, J., 2006. Spatially resolved observation of crystal-face-dependent catalysis by single turnover counting. Nature 439, 572–575. doi:10.1038/nature04502

Roldan Cuenya, B., 2013. Metal Nanoparticle Catalysts Beginning to Shape-up. Acc. Chem. Res. 46, 1682–1691. doi:10.1021/ar300226p

Roldan Cuenya, B., Behafarid, F., 2015. Nanocatalysis: size- and shape-dependent chemisorption and catalytic reactivity. Surf. Sci. Rep. 70, 135–187. doi:10.1016/j.surfrep.2015.01.001

Rosenhahn, B., Sommer, G., 2005. Pose Estimation in Conformal Geometric Algebra Part I: The Stratification of Mathematical Spaces. J. Math. Imaging Vis. 22, 27–48. doi:10.1007/s10851-005-4781-x

Rosenthal, D., Girgsdies, F., Timpe, O., Blume, R., Weinberg, G., Teschner, D., Schlögl, R., 2009. On the CO-Oxidation over Oxygenated Ruthenium. Z. Für Phys. Chem. 223, 183–208. doi:10.1524/zpch.2009.6032

Rosenthal, D., Girgsdies, F., Timpe, O., Weinberg, G., Schlögl, R., 2011. Oscillatory Behavior in the CO-oxidation over Bulk Ruthenium Dioxide — the Effect of the CO/O2 Ratio. Z. Für Phys. Chem. 225, 57–68. doi:10.1524/zpch.2011.5515

Rossignol, S., G�rard, F., Mesnard, D., Kappenstein, C., Duprez, D., 2003. Structural changes of Ce-Pr-O oxides in hydrogen: a study by in situ X-ray diffraction and Raman spectroscopy. J. Mater. Chem. 13, 3017. doi:10.1039/b306726b

Saavedra, J., Doan, H.A., Pursell, C.J., Grabow, L.C., Chandler, B.D., 2014. The critical role of water at the gold-titania interface in catalytic CO oxidation. Science 345, 1599–1602. doi:10.1126/science.1256018

Salmeron, M., Schlogl, R., 2008. Ambient pressure photoelectron spectroscopy: A new tool for surface science and nanotechnology. Surf. Sci. Rep. 63, 169–199. doi:10.1016/j.surfrep.2008.01.001

Santra, A.K., Goodman, D.W., 2002. Catalytic oxidation of CO by platinum group metals: from ultrahigh vacuum to elevated pressures. Electrochimica Acta 47, 3595–3609.

Schubert, M.M., Hackenberg, S., van Veen, A.C., Muhler, M., Plzak, V., Behm, R.J., 2001. CO Oxidation over Supported Gold Catalysts—“Inert” and “Active” Support Materials and Their Role for the Oxygen Supply during Reaction. J. Catal. 197, 113–122. doi:10.1006/jcat.2000.3069

Sharma, R., 2012. Experimental set up for in situ transmission electron microscopy observations of chemical processes. Micron 43, 1147–1155. doi:10.1016/j.micron.2012.01.007

Sharma, R., 2005. An Environmental Transmission Electron Microscope for in situ Synthesis and Characterization of Nanomaterials. J. Mater. Res. 20, 1695–1707. doi:10.1557/JMR.2005.0241

Sharma, R., Crozier, P.A., 2005. Environmental Transmission Electron Microscopy in Nanotechnology, in: Yao, N., Wang, Z.L. (Eds.), Handbook of Microscopy for Nanotechnology. Kluwer Academic Publishers, Boston, pp. 531–565.

Sharma, V., Crozier, P.A., Sharma, R., Adams, J.B., 2012. Direct observation of hydrogen spillover in Ni-loaded Pr-doped ceria. Catal. Today 180, 2–8. doi:10.1016/j.cattod.2011.09.009

Shaw, E.A., Rayment, T., Walker, A.P., Lambert, R.M., Gauntlett, T., Oldman, R.J., Dent, A., 1991. In situ x-ray diffraction and x-ray absorption investigations of methanol synthesis catalysts derived from CeCu2. Catal. Today 9, 197–202. doi:10.1016/0920-5861(91)85024-3

Sheu, W.-S., Chang, M.-W., 2014. CO oxidation on Ag(111): The catalytic role of H2O. Surf. Sci. 628, 104–110. doi:10.1016/j.susc.2014.05.020

Shibata, N., Goto, A., Matsunaga, K., Mizoguchi, T., Findlay, S.D., Yamamoto, T., Ikuhara, Y., 2009. Interface Structures of Gold Nanoparticles on TiO 2 (110). Phys. Rev. Lett. 102. doi:10.1103/PhysRevLett.102.136105

Simonsen, S.B., Chorkendorff, I., Dahl, S., Skoglundh, M., Sehested, J., Helveg, S., 2011. Ostwald ripening in a Pt/SiO2 model catalyst studied by in situ TEM. J. Catal. 281, 147–155. doi:10.1016/j.jcat.2011.04.011

Simonsen, S.B., Chorkendorff, I., Dahl, S., Skoglundh, M., Sehested, J., Helveg, S., 2010. Direct Observations of Oxygen-induced Platinum Nanoparticle Ripening Studied by In Situ TEM. J. Am. Chem. Soc. 132, 7968–7975. doi:10.1021/ja910094r

Smith R J, B., Loganathan, M., Shantha, M.S., 2010. A Review of the Water Gas Shift Reaction Kinetics. Int. J. Chem. React. Eng. 8. doi:10.2202/1542-6580.2238

Somorjai, G.A., Li, Y., 2010. Introduction to surface chemistry and catalysis, 2nd ed. ed. Wiley, Hoboken, N.J.

Somorjai, G.A., Park, J.Y., 2008. Colloid Science of Metal Nanoparticle Catalysts in 2D and 3D Structures. Challenges of Nucleation, Growth, Composition, Particle Shape, Size Control and Their Influence on Activity and Selectivity. Top. Catal. 49, 126–135. doi:10.1007/s11244-008-9077-0

Song, C., Wang, P., Makse, H.A., 2008. A phase diagram for jammed matter. Nature 453, 629–632. doi:10.1038/nature06981

Stadelmann, P., 2016. JEMS-SAAS [WWW Document]. URL http://www.jems-saas.ch/ (accessed 1.11.16).

Stadelmann, P.A., 1987. EMS - a software package for electron diffraction analysis and HREM image simulation in materials science. Ultramicroscopy 21, 131–145. doi:10.1016/0304-3991(87)90080-5

Stampfl, C., 2005. Surface processes and phase transitions from ab initio atomistic thermodynamics and statistical mechanics. Catal. Today 105, 17–35. doi:10.1016/j.cattod.2005.04.015

Stampfl, C., Scheffler, M., 1999. Density-functional theory study of the catalytic oxidation of CO over transition metal surfaces. Surf. Sci. 433, 119–126.

Stampfl, C., Scheffler, M., 1997. Study of CO oxidation over Ru(0001) at high gas pressures. Surf. Sci. 377-379, 808–812. doi:10.1016/S0039-6028(96)01509-9

Stampfl, C., Schwegmann, S., Over, H., Scheffler, M., Ertl, G., 1996. Structure and stability of a high-coverage (1x1) oxygen phase on Ru (0001). Phys. Rev. Lett. 77, 3371.

Sternberg, 1983. Biomedical Image Processing. Computer 16, 22–34. doi:10.1109/MC.1983.1654163

Stöber, W., Fink, A., Bohn, E., 1968. Controlled growth of monodisperse silica spheres in the micron size range. J. Colloid Interface Sci. 26, 62–69. doi:10.1016/0021-9797(68)90272-5

Su, D.S., Zhang, B., Schlögl, R., 2015. Electron Microscopy of Solid Catalysts: Transforming from a Challenge to a Toolbox. Chem. Rev. 115, 2818–2882.

Takeda, S., Kuwauchi, Y., Yoshida, H., 2015. Environmental transmission electron microscopy for catalyst materials using a spherical aberration corrector. Ultramicroscopy 151, 178–190. doi:10.1016/j.ultramic.2014.11.017

Takeda, S., Yoshida, H., 2013. Atomic-resolution environmental TEM for quantitative in-situ microscopy in materials science. Microscopy 62, 193–203. doi:10.1093/jmicro/dfs096

Ta, N., Liu, J. (Jimmy), Chenna, S., Crozier, P.A., Li, Y., Chen, A., Shen, W., 2012. Stabilized Gold Nanoparticles on Ceria Nanorods by Strong Interfacial Anchoring. J. Am. Chem. Soc. 134, 20585–20588. doi:10.1021/ja310341j

Thomas, J.M., Thomas, W.J., 2015. Principles and practice of heterogeneous catalysis, 2., rev. ed. ed. Wiley-VCH, Weinheim.

Tinnemans, S.J., Mesu, J.G., Kervinen, K., Visser, T., Nijhuis, T.A., Beale, A.M., Keller, D.E., van der Eerden, A.M.J., Weckhuysen, B.M., 2006. Combining operando techniques in one spectroscopic-reaction cell: New opportunities for elucidating the active site and related reaction mechanism in catalysis. Catal. Today 113, 3–15. doi:10.1016/j.cattod.2005.11.076

Tsen, S.-C.Y., Crozier, P.A., Liu, J., 2003. Lattice measurement and alloy compositions in metal and bimetallic nanoparticles. Ultramicroscopy 98, 63–72. doi:10.1016/S0304-3991(03)00119-0

Uchiyama, T., Yoshida, H., Kuwauchi, Y., Ichikawa, S., Shimada, S., Haruta, M., Takeda, S., 2011. Systematic Morphology Changes of Gold Nanoparticles Supported on CeO2 during CO Oxidation. Angew. Chem. Int. Ed. 50, 10157–10160. doi:10.1002/anie.201102487

Vendelbo, S.B., Elkjær, C.F., Falsig, H., Puspitasari, I., Dona, P., Mele, L., Morana, B., Nelissen, B.J., van Rijn, R., Creemer, J.F., Kooyman, P.J., Helveg, S., 2014a. Visualization of oscillatory behaviour of Pt nanoparticles catalysing CO oxidation. Nat. Mater. 13, 884–890. doi:10.1038/nmat4033

Vendelbo, S.B., Elkjær, C.F., Falsig, H., Puspitasari, I., Dona, P., Mele, L., Morana, B., Nelissen, B.J., van Rijn, R., Creemer, J.F., Kooyman, P.J., Helveg, S., 2014b. Visualization of oscillatory behaviour of Pt nanoparticles catalysing CO oxidation. Nat. Mater. 13, 884–890. doi:10.1038/nmat4033

Vendelbo, S.B., Kooyman, P.J., Creemer, J.F., Morana, B., Mele, L., Dona, P., Nelissen, B.J., Helveg, S., 2013. Method for local temperature measurement in a nanoreactor for in situ high-resolution electron microscopy. Ultramicroscopy 133, 72–79. doi:10.1016/j.ultramic.2013.04.004

Vuurman, M.A., Wachs, I.E., 1992. In situ Raman spectroscopy of alumina-supported metal oxide catalysts. J. Phys. Chem. 96, 5008–5016.

Wagner, J.B., Cavalca, F., Damsgaard, C.D., Duchstein, L.D.L., Hansen, T.W., 2012. Exploring the environmental transmission electron microscope. Micron 43, 1169–1175. doi:10.1016/j.micron.2012.02.008

Wagner, J.B., Hansen, P.L., Molenbroek, A.M., Topsøe, H., Clausen, B.S., Helveg, S., 2003. In Situ Electron Energy Loss Spectroscopy Studies of Gas-Dependent Metal−Support Interactions in Cu/ZnO Catalysts. J. Phys. Chem. B 107, 7753–7758. doi:10.1021/jp0277863

Wang, C.M., Baer, D.R., Thomas, L.E., Amonette, J.E., Antony, J., Qiang, Y., Duscher, G., 2005. Void formation during early stages of passivation: Initial oxidation of iron nanoparticles at room temperature. J. Appl. Phys. 98, 094308. doi:10.1063/1.2130890

Wang, J., Fan, C.Y., Jacobi, K., Ertl, G., 2002. The Kinetics of CO Oxidation on RuO2 (110): Bridging the Pressure Gap. J. Phys. Chem. B 106, 3422–3427. doi:10.1021/jp014109k

Wang, J., Fan, C.Y., Jacobi, K., Ertl, G., 2001. Adsorption and reaction of CO on RuO 2 (110) surfaces. Surf. Sci. 481, 113–118.

Wang, R., Crozier, P.A., Sharma, R., 2009. Structural Transformation in Ceria Nanoparticles during Redox Processes. J. Phys. Chem. C 113, 5700–5704. doi:10.1021/jp8107232

Wang, T., Jelic, J., Rosenthal, D., Reuter, K., 2013. Exploring Pretreatment-Morphology Relationships: Ab Initio Wulff Construction for RuO2 Nanoparticles under Oxidising Conditions. ChemCatChem 5, 3398–3403. doi:10.1002/cctc.201300168

Weckhuysen, B.M., 2003. Determining the active site in a catalytic process: Operando spectroscopy is more than a buzzword. Phys. Chem. Chem. Phys. 5, 4351. doi:10.1039/b309650p

Weckhuysen, B.M., 2002. Snapshots of a working catalyst: possibilities and limitations of in situ spectroscopy in the field of heterogeneous catalysis. Chem. Commun. 97–110. doi:10.1039/b107686h

Wieckowski, A., 2009. Fuel cell catalysis a surface science approach. Wiley, Hoboken, N.J.

Williams, D.B., Carter, C.B., 2008. Transmission electron microscopy: a textbook for materials science, 2nd ed. ed. Springer, New York.

Winterbottom, W.., 1967. Equilibrium shape of a small particle in contact with a foreign substrate. Acta Metall. 15, 303–310. doi:10.1016/0001-6160(67)90206-4

Wulff, G., 1901. XXV. Zur Frage der Geschwindigkeit des Wachsthums und der Auflösung der Krystallflächen. Z. Für Krist. - Cryst. Mater. 34. doi:10.1524/zkri.1901.34.1.449

Xin, H.L., Alayoglu, S., Tao, R., Genc, A., Wang, C.-M., Kovarik, L., Stach, E.A., Wang, L.-W., Salmeron, M., Somorjai, G.A., Zheng, H., 2014. Revealing the Atomic Restructuring of Pt–Co Nanoparticles. Nano Lett. 14, 3203–3207. doi:10.1021/nl500553a

Xin, H.L., Pach, E.A., Diaz, R.E., Stach, E.A., Salmeron, M., Zheng, H., 2012. Revealing Correlation of Valence State with Nanoporous Structure in Cobalt Catalyst Nanoparticles by In Situ Environmental TEM. ACS Nano 6, 4241–4247. doi:10.1021/nn3007652

Xu, W., Kong, J.S., Yeh, Y.-T.E., Chen, P., 2008. Single-molecule nanocatalysis reveals heterogeneous reaction pathways and catalytic dynamics. Nat. Mater. 7, 992–996. doi:10.1038/nmat2319

Yaguchi, T., Suzuki, M., Watabe, A., Nagakubo, Y., Ueda, K., Kamino, T., 2011. Development of a high temperature-atmospheric pressure environmental cell for high-resolution TEM. J. Electron Microsc. (Tokyo) 60, 217–225. doi:10.1093/jmicro/dfr011

Yamamoto, S., Bluhm, H., Andersson, K., Ketteler, G., Ogasawara, H., Salmeron, M., Nilsson, A., 2008. In situ x-ray photoelectron spectroscopy studies of water on metals and oxides at ambient conditions. J. Phys. Condens. Matter 20, 184025. doi:10.1088/0953-8984/20/18/184025

Yang, X.-F., Wang, A., Qiao, B., Li, J., Liu, J., Zhang, T., 2013. Single-Atom Catalysts: A New Frontier in Heterogeneous Catalysis. Acc. Chem. Res. 46, 1740–1748. doi:10.1021/ar300361m

Yankovich, A.B., Berkels, B., Dahmen, W., Binev, P., Sanchez, S.I., Bradley, S.A., Li, A., Szlufarska, I., Voyles, P.M., 2014. Picometre-precision analysis of scanning transmission electron microscopy images of platinum nanocatalysts. Nat. Commun. 5. doi:10.1038/ncomms5155

Yokosawa, T., Alan, T., Pandraud, G., Dam, B., Zandbergen, H., 2012. In-situ TEM on (de)hydrogenation of Pd at 0.5–4.5bar hydrogen pressure and 20–400°C. Ultramicroscopy 112, 47–52. doi:10.1016/j.ultramic.2011.10.010

Yoo, S.-H., Lee, J.-H., Jung, Y.-K., Soon, A., 2016. Exploring stereographic surface energy maps of cubic metals via an effective pair-potential approach. Phys. Rev. B 93. doi:10.1103/PhysRevB.93.035434

Yoshida, H., Kohno, H., Takeda, S., 2012. In situ structural analysis of crystalline Fe–Mo–C nanoparticle catalysts during the growth of carbon nanotubes. Micron 43, 1176–1180. doi:10.1016/j.micron.2012.04.008

Yoshida, H., Kuwauchi, Y., Jinschek, J.R., Sun, K., Tanaka, S., Kohyama, M., Shimada, S., Haruta, M., Takeda, S., 2012. Visualizing Gas Molecules Interacting with Supported Nanoparticulate Catalysts at Reaction Conditions. Science 335, 317–319. doi:10.1126/science.1213194

Yoshida, H., Matsuura, K., Kuwauchi, Y., Kohno, H., Shimada, S., Haruta, M., Takeda, S., 2011. Temperature-Dependent Change in Shape of Platinum Nanoparticles Supported on CeO_2 during Catalytic Reactions. Appl. Phys. Express 4, 065001. doi:10.1143/APEX.4.065001

Zhang, J. (Ed.), 2008. PEM fuel cell electrocatalysts and catalyst layers: fundamentals and applications. Springer, London.

Zhang, S., Shan, J., Zhu, Y., Frenkel, A.I., Patlolla, A., Huang, W., Yoon, S.J., Wang, L., Yoshida, H., Takeda, S., Tao, F. (Feng), 2013a. WGS Catalysis and In Situ Studies of CoO1–x, PtCon/Co3O4, and PtmCom′/CoO1–x Nanorod Catalysts. J. Am. Chem. Soc. 135, 8283–8293. doi:10.1021/ja401967y

Zhang, S., Shan, J., Zhu, Y., Nguyen, L., Huang, W., Yoshida, H., Takeda, S., Tao, F. (Feng), 2013b. Restructuring Transition Metal Oxide Nanorods for 100% Selectivity in Reduction of Nitric Oxide with Carbon Monoxide. Nano Lett. 13, 3310–3314. doi:10.1021/nl4015292

Zhou, X., Lee, S., Xu, Z., Yoon, J., 2015. Recent Progress on the Development of Chemosensors for Gases. Chem. Rev. 115, 7944–8000. doi:10.1021/cr500567r

Zitová, B., Flusser, J., 2003. Image registration methods: a survey. Image Vis. Comput. 21, 977–1000. doi:10.1016/S0262-8856(03)00137-9

Zucker, R.V., Chatain, D., Dahmen, U., Hagège, S., Carter, W.C., 2012. New software tools for the calculation and display of isolated and attached interfacial-energy minimizing particle shapes. J. Mater. Sci. 47, 8290–8302. doi:10.1007/s10853-012-6739-x

APPENDIX I

RIG 150 TEMPERATURE GRADIENT

The RIG 150 reactor is designed to flow gases down through a vertically oriented quartz tube, shown in Figure A 2. As described in section 2.2.1, the 12 inch tube has a frit about 4 inches from the bottom to keep the catalyst at a good position in the vertical tube furnace of the RIG-150. The location of the tip of a thermocouple used to control the temperature can be varied, and should be set as close to the top of the catalyst bed as possible. This is because the temperature in the furnace is not uniform along the length of the quartz tube. For precise measurement of temperatures, this non-uniformity should be characterized and accounted for. To do this, a second thermocouple was placed in the furnace alongside the quartz tube, and the height of this second thermocouple was varied systematically, to measure the difference in temperature between the ideal thermocouple location (at the frit, with the original thermocouple tip) and the 2nd thermocouple tip. This difference is plotted in Figure A 1, and reached a maximum of just over 150°C. This is quite significant.

This gradient can be accounted for if the distance of the thermocouple (D_{TC}) from the frit, as well as the mean distance of the catalyst bed (D_C) from the frit are known. The temperature to set the RIG 150 furnace to, as a function of T_D, the desired catalyst bed temperature is given in Equation A1. If the temperature was already measured, and the actual temperature at the catalyst bed must be calculated, the formula for this is given in Equation A2. The difference between the set (T_{Set}) and desired/actual temperature (T_D) is small if the thermocouple is close to the bed and the bed is short. For the *ex-situ* reactor experiments described in section 2.2.2, D_{TC} is 16 mm and D_C is only 5 mm the catalyst bed is between 2°C and 4°C cooler than the thermocouple indicated.

A1 $$T_{Set} = 3.2 + 1.374 * D_{TC} + (1.012 + .00503 * D_{TC}) * \frac{T_D - 3.2 - 1.374 * D_C}{1.012 + .00503 * D_C}$$

A2 $$T_D = 3.2 + 1.374 * D_C + (1.012 + .00503 * D_C) * \frac{T_{Set} - 3.2 - 1.374 * D_{TC}}{1.012 + .00503 * D_{TC}}$$

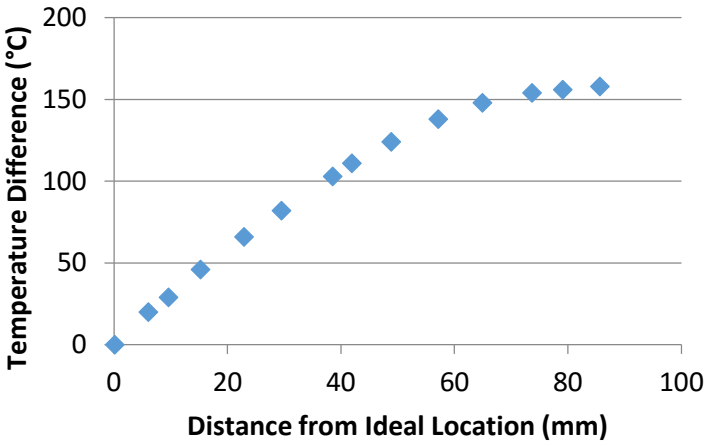

Figure A 1 Temperature Difference. The difference in temperature between the ideal location, where the original thermocouple was positioned, and the location of a second thermocouple, used to measure the temperature gradient along the reactor tube.

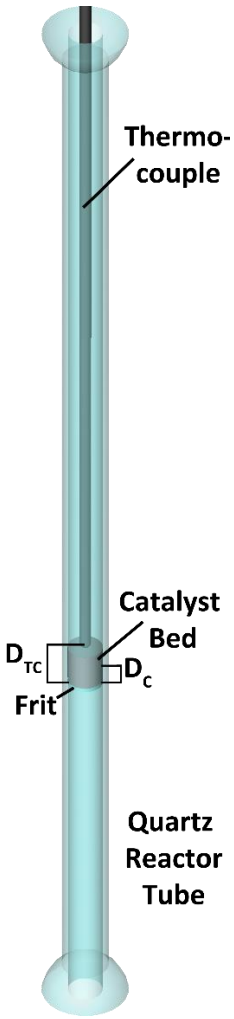

Figure A 2 RIG 150 Reactor Tube. Model showing the position of the catalyst bed and thermocouple as used in this work.

APPENDIX II

GC METHOD PARAMETERS

The GC software used for acquisition of data during *ex-situ* reactor experiments was called Galaxy. It is now known as Compass CDS, and is essentially identical. Methods may be created to set the parameters of the GC system during acquisition of a chromatogram. All parameters set in the method used to obtain the data shown in Figure 2-3 to Figure 2-6 are given below. This method was used on a Varian 3900 GC with a 10m long Varian PLOT column (MolSieve5A) with a 0.32 mm diameter.

Control Parameters	
Injector	
Set point:	120 °C
Oven	
Stabilization Time:	0 min
Heater:	on
Rate- Initial Step:	30 °C
Rate- Initial Time:	10 min
Column Pneumatics	
Rate- Initial Step:	4.8psi
Rate- Initial Time:	10 min
Flow- Initial Flow:	15 mL/min
Detector	
Heater:	on
Set point:	100 °C
Electronics:	YES
Time Constant:	Fast
Carrier Gas:	He/H_2
Filament Temp Limit:	390 °C
Filament Temperature:	250 °C
TCD Range:	5
TCD Auto zero:	YES
TCD Polarity:	Negative
TCD Attenuation:	1024
Detector EFC Flow:	15mL/min
Detector EFC Reference Flow:	30mL/min
External Events	
Event Table 1-Time:	Initial
Event Table 1- External Event State 1:	NO
Event Table 1- External Event State 2:	NO
Event Table 1-Time:	0.01
Event Table 2- External Event State 1:	YES
Event Table 2- External Event State 2:	NO

Miscellaneous

Acquisition Frequency:	20 Hz
Driver Behavior- Reset Program…	YES
Driver Behavior- Start Automatically…	YES

Export Parameters

(For export parameters, see Figure A 3, below.)

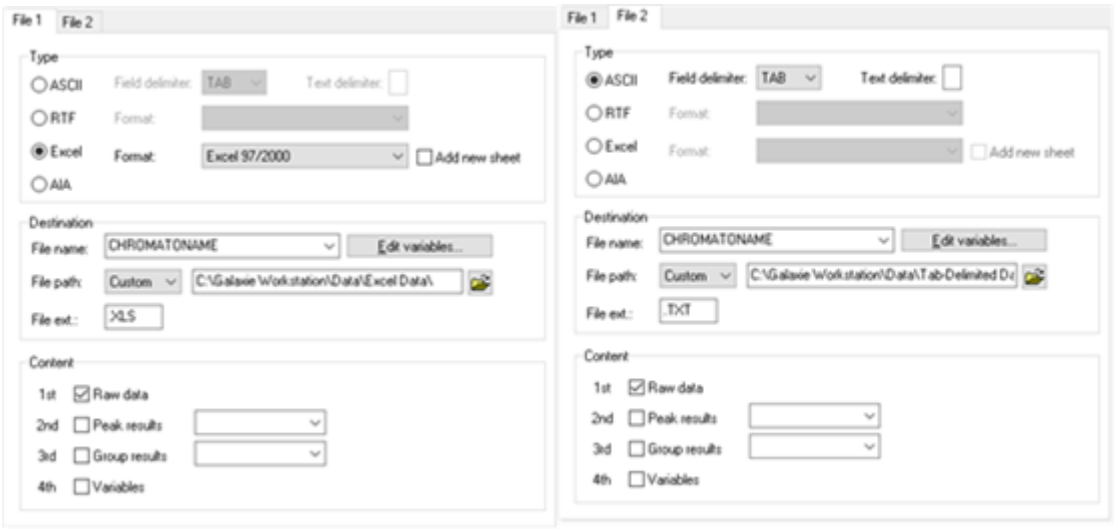

Figure A 3 GC Method Export Dialog. The export dialog from the Galaxy/Compass CDS software, with the options used in this work. Two types of files are exported containing the raw data: a tab delimited text file, and an Excel file.

APPENDIX III

GC DATA ANALYSIS

Analysis of the data acquired during GC experiments was automated using a MATLAB code named GCDataQuant. The code first allows the user to open any number of text or excel files with data from the Galaxie/CompassCDS software. The data is then checked for consistency, to determine whether every chromatograph has the same number of data points. If the selected files do not all have the same number of data points, but only 1 file is different (the last run on the GC may have been ended early) then this file is ignored, and the analysis continues with the other files. If several files have chromatograms of different lengths, then the file with the minimum number of data points is used to determine the number of data points read from all the selected files. A basic linear fit background subtraction is then performed, and the background noise level estimated by fitting a histogram of the log of the values in the chromatographs with a Gaussian.

The code then proceeds with a detailed background subtraction procedure designed to accurately subtract a background that has no functional dependence, varies from one chromatogram to the next, and is several orders of magnitude smaller than the signal peaks. This was achieved using an iterative procedure that is given in a separate function, called GCDataIterativeBGFit. Basically, this code works by first finding the mean and maximum values of each chromatograph, and setting all points larger than half the maximum to the mean value. (The mean value is much closer to 0 than half the maximum since the peaks are very tall and narrow.) After this is done, the resulting chromatograph is fit by straight line, and this line subtracted from the chromatograph. The new chromatograph's max and mean are again found, and the process repeated until the maximum value is less than 2 times the noise threshold determined from the analysis of the log histogram. A 7^{th} degree polynomial fit is then subtracted from the chromatograph, to make it more flat. Another

iterative process is then begun, this time setting all points larger than 75% of the max value to the mean value until the max value is less than the set noise threshold. A final 7^{th} degree polynomial fit is subtracted, and the resulting noise signal is plotted, as seen in the middle plot of Figure A 4. All of the linear and polynomial fits are then summed together, and considered to be the background of the original chromatograph. This background is plotted, as seen in Figure A 5 and subtracted from the original data, to yield a background subtracted chromatograph, shown on a log scale in Figure A 4 and a linear scale in Figure A 6.

After background subtraction of every chromatograph the user opened, the user selects a peak with which to align all the chromatographs. This is done using local cross-correlation around the selected peak. The user then selects a point before and after each peak to be integrated, and the integrated intensity of each peak over the set of chromatograms is plotted. The integrated intensity is proportional to the concentration of a gaseous species. The immediate display of a plot of the peak areas over time allows the user to quickly determine whether the results match what was expected.

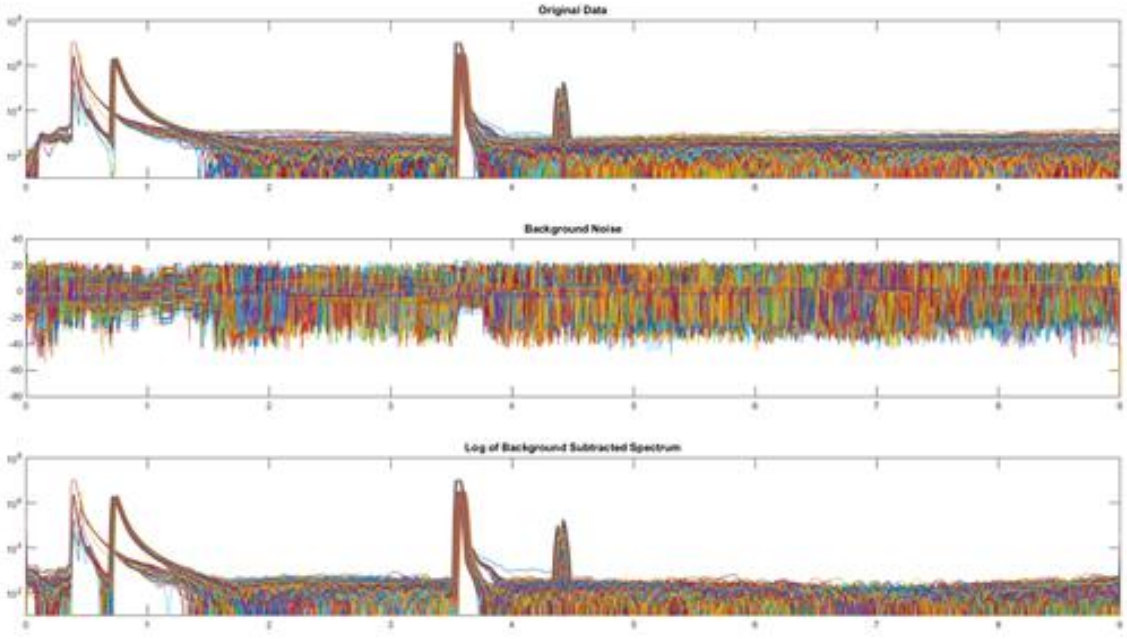

Figure A 4 GC Data Background Fitting. Top: The data after subtracting an initial linear fit to the data. Middle: The resulting noise residual after the iterative background fitting procedure. Bottom: The background subtracted chromatographs plotted on a log scale.

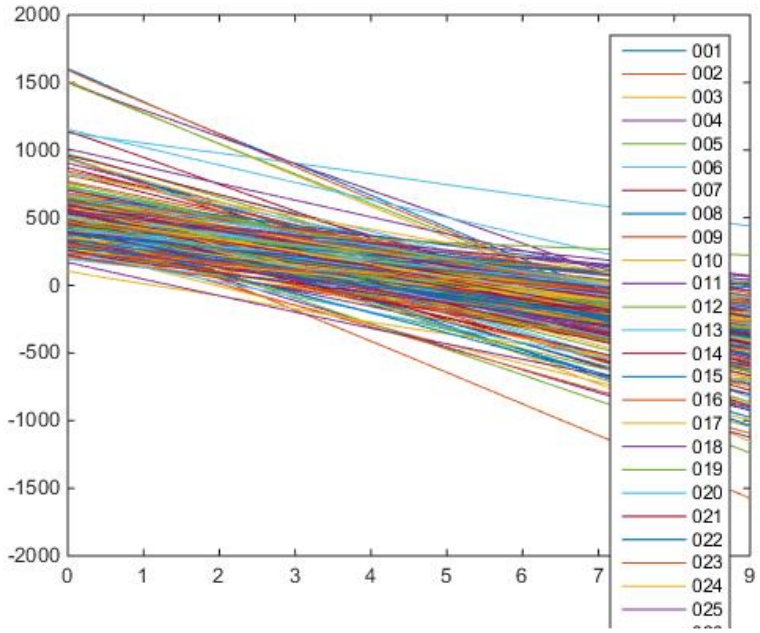

Figure A 5 Fit Backgrounds. The summed background signals obtained using the iterative background fitting approach.

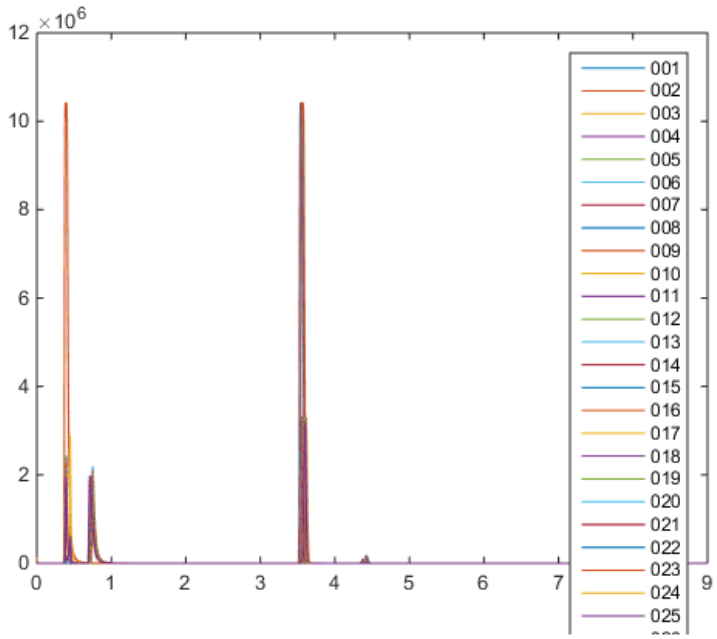

Figure A 6 Background Subtracted Chromatographs. Chromatographs after the backgrounds in Figure A 5 have been subtracted.

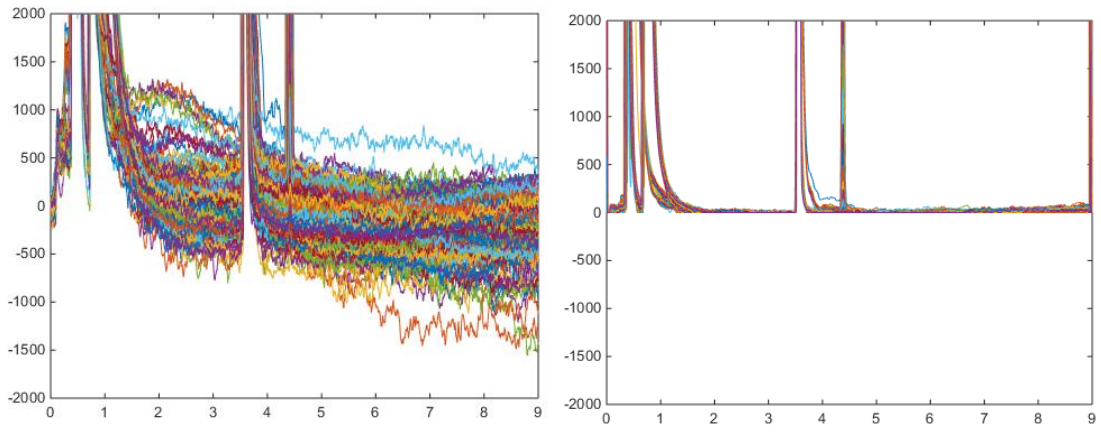

Figure A 7 Background Noise. Background noise before and after background subtraction, showing the significant reduction in the noise signal, and the flat baseline.

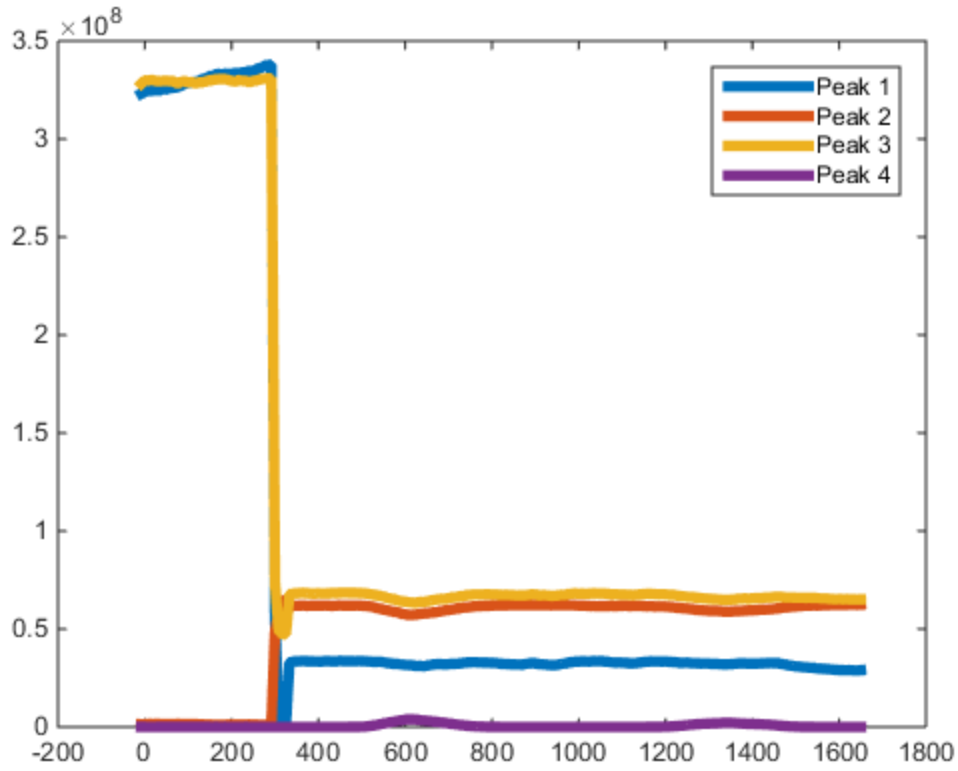

Figure A 8 Peak Areas Graph. The resulting plot after the peaks in the chromatographs have been integrated. Each line corresponds to one of the peaks in Figure A 6.

GCDataQuant MATLAB Code

```
clear
close all
%Loading Data Files
%XXXXXXXXXXXXXXXXXXXXXXXXXXXXXXXXXXXXXXXXXXXXXXXXXXXXXXXXXXXXXXXXXXXXXXXXXXXXX
XXX
global PN
if ~exist('PN','var')
   [FNames,PN,FT]=uigetfile({'*.xls';'*.txt'},'Select Series of Files with GC Data','multiselect','on');
end
if PN==0
   [FNames,PN,FT]=uigetfile({'*.xls';'*.txt'},'Select Series of Files with GC Data','multiselect','on');
elseif exist('PN','var')
   [FNames,PN,FT]=uigetfile({'*.xls';'*.txt'},'Select Series of Files with GC Data',PN,'multiselect','on');
end
%add the path PN to the matlab path list
addpath(PN);
```

```
%count number of Chromatograms
NumChrom=length(FNames);
%Get list of all files in the Path Directory
FileList=dir(PN);
%Parameters
%XXXXXXXXXXXXXXXXXXXXXXXXXXXXXXXXXXXXXXXXXXXXXXXXXXXXXXXXXXXXXXXXXXXXXXX
XXX
%The time between GC runs (min)
TimeStep=8.333;
%Time in Min for use in the smoothing function
SmoothTime=.02;
%Slope Constant (PSC/dt=Threshold Slope)
PeakSlopeConst=8.333333;
%XXXXXXXXXXXXXXXXXXXXXXXXXXXXXXXXXXXXXXXXXXXXXXXXXXXXXXXXXXXXXXXXXXXXXXX
XXX
%Import the GC Data from either tab delimited text or Excel file
[DataLength,DataLengthMode,DL,SpecNs,OriginalData]=GCDataImport(FNames,FT,0,[]);
%Give User Helpful error messages if the data is not all the same length
%If DL is 1 (only one file was a different length)
if DL==1
    for i=1:NumChrom
        % if the data in a file is normal, extract the data
        if DataLength(i)==DataLengthMode
            SpecO(:,i)=OriginalData(i).SpecO;
            TimeO=OriginalData(i).Time;
        else
            break
        end
    end
    %Remove the filename which had a differnt number of data points
    FNames(i)=[];
    NumChrom=NumChrom-1;
    %Retry to import the data
    [DataLength,DataLengthMode,DL,SpecNs,OriginalData]=GCDataImport(FNames,FT,0,[]);
    %Give the user a warning that a data file was ignored
    warning('One Chromatogram was a different length than the rest of the loaded data files. This data file has been ignored')
    for i=1:NumChrom
        SpecO(:,i)=OriginalData(i).SpecO;
        TimeO=OriginalData(i).Time;
    end
    %If DL is 0
elseif DL==0
    %Extract the data
    for i=1:NumChrom
        SpecO(:,i)=OriginalData(i).SpecO;
        TimeO=OriginalData(i).Time;
    end
    %If DL is another number (several Data files are a different length)
else
    %Find the minimum length of the data files
    DataNum=min(DataLength);
    %Import the data from the data files, using the minumum data legnth
    [DataLength,DataLengthMode,DL,SpecNs,OriginalData]=GCDataImport(FNames,FT,1,DataNum);
    %Extract the data
```

```
    for i=1:NumChrom
        SpecO(:,i)=OriginalData(i).SpecO;
        TimeO=OriginalData(i).Time;
    end
    %Warn the user about the data being cropped
    warning('The Chromatograms you have loaded have several different lengths. They have been cropped to the same length')
    %Optional figure to visualize data lengths:
    %     figure(11)
    %     bar(DataLength,'basevalue',min(DataLength))
end
%Preliminary Background Subtraction
%XXXXXXXXXXXXXXXXXXXXXXXXXXXXXXXXXXXXXXXXXXXXXXXXXXXXXXXXXXXXXXXXXXXXXXX
XXX
%Initial linear background fit (to remove constant offsets, etc)
for i=1:NumChrom
    BGRough(:,i)=polyval(polyfit(TimeO,SpecO(:,i),1),TimeO);
end
%Calculate background subtracted spectra based on BGRough
SpecBGR=SpecO-BGRough;
%Calculate spacing between data points
dt=(TimeO(4)-TimeO(2))/2;
%Smooth the Background subtracted spectra using window of size SmoothTime
Sm=ceil(SmoothTime/dt);
for i=1:NumChrom
    G=gausswin(Sm,sqrt(Sm/2));
    %The 20*i term here allows the backgrounds to not overlap when they are
    %ploted, and has no effect whatever on the quantification
    SpecBGRS(:,i)=0*i+convn(SpecBGR(:,i),G/sum(G),'same');
end
%Acceptable Background maxima
for i=1:NumChrom
    %Calculate (heavily) smoothed spectra
    SpecS(:,i)=smooth(SpecO(:,i),numel(TimeO)/100,'sgolay',3);
    %Take derivative of both smoothed and original spectra
    DiffS(:,i)=(diff(SpecS(:,i)));
    DiffO(:,i)=(diff(SpecO(:,i)));
end
%subtract the smoothed and orignial derivatives
DerivativeDiff=abs(DiffS-DiffO)+.01;
%compute histogram of the logarithm of the difference
[Hist,BinCenter]=hist(log10(DerivativeDiff(:)),200);
%Fit the histogram with a gaussian
f=fit(BinCenter',Hist','gauss1');
%calculate the mean noise from the fit parameters
CV=coeffvalues(f);
NoiseMean=10^CV(2);
%Set BGMax based on this mean noise value
BGMax=NoiseMean*3;
%Plot the histogram and fit in a new figure
figure(10); plot(BinCenter,f(BinCenter'),'o'); hold on; plot(BinCenter,Hist); plot(log10(BGMax)*[1,1],[0,f(log10(BGMax))])
%Perform iterative background fitting
[SpecBGSub,NoiseMax]=GCDataIterativeBGFit(NumChrom,TimeO,SpecO,SpecBGRS,BGMax,BGRough,SpecNs);
%Peak Alignment
%XXXXXXXXXXXXXXXXXXXXXXXXXXXXXXXXXXXXXXXXXXXXXXXXXXXXXXXXXXXXXXXXXXXXXXX
```

```
XXX
%Create new Chromatogram for integration with values within the magnitude
%of the noise set to 0, so that only peaks are summed, and the exact limits
%of integration are not important for isolated peaks
SpecInt=SpecBGSub;
SpecInt(SpecBGSub<NoiseMax)=0;
%Plot these Chromatograms in a new plot
figure(1)
plot(TimeO,SpecInt+1)
set(gcf,'name','Click a Peak to align the spectra')
legend(SpecNs)
%Have the user pick one peak to align all the Chromatograms with
[t,~]=ginput(1);
set(gcf,'name','Background Subtracted Chromatograms')
%Align the chromatograms using the selected peak
CCWidth=round(.1*DataLengthMode);
CCMask=zeros(DataLengthMode,1);
CCMask(1:CCWidth)=1;
dTime=TimeO(2)-TimeO(1);
CCMask=circshift(CCMask,round(t/dTime)-round(CCWidth/2));
SpecIntShift=SpecInt;
for j=1:2
    SpecSum=mean(SpecIntShift,2);
    SpecSumNorm=SpecSum/max(SpecSum);
    SpecNormDiff=smooth(diff(smooth(SpecSumNorm,100,'sgolay',2)),100,'sgolay',1);
    SND=SpecNormDiff-.1*max(SpecNormDiff); SND(SND<0)=0;
    SNDD=abs(diff(SND));
    [~,P]=findpeaks(SNDD); P=diff(P);
    PWidths=P(1:2:end);
    MaxLag=round(1.5*mean(PWidths));
    for  i=1:NumChrom
        [CC,Lags]=xcorr(diff(CCMask.*SpecSum),diff(SpecIntShift(:,i).*CCMask),MaxLag);
        [~,CCMax]=max(CC);
        CCShift(i)=Lags(CCMax(1));
        SpecIntShift(:,i)=circshift(SpecIntShift(:,i),CCShift(i));
    end
end
%Plot the Shifted Spectra as   t vs I/log(I)
figure(7)
plot(TimeO,SpecIntShift./log(SpecIntShift+2))
set(gcf,'name','Select Points Before and After Each Peak to be Analyzed')
legend(SpecNs)
%Peak Integration, Plotting
%XXXXXXXXXXXXXXXXXXXXXXXXXXXXXXXXXXXXXXXXXXXXXXXXXXXXXXXXXXXXXXXXXXXXXXXXXX
XXX
%Again have the user select points before and after every peak to be
%analyzed
[t2,~]=ginput;
set(gcf,'name','Aligned, Background Subtracted Chromatograms')
%Count the number of points selected by the user
L2=length(t2);
%Check that the user has input an even number of points
if mod(L2,2)
    error('number of points selected should be even')
```

```
elseif L2==2
   error('Please select at least 2 peaks to integrate')
else
   %Find the indices closest to the user-selected points in the Figure
   for l=1:L2
      [~,Indi]=min(abs(TimeO-t2(l)));
      Ind2(l)=Indi;
   end
   %Integrate each of the peaks selected by the user
   for k=1:2:L2
      i=(k+1)/2;
      PeakArea(i,:)=sum(SpecIntShift(Ind2(k):Ind2(k+1),:));
   end
end
%Create a time vector for plotting the peaks as a function of time
TimeTemp=[-1:NumChrom-2]*TimeStep;
%Plot the integrated peaks as a function of time
figure(6)
plot(TimeTemp',PeakArea,'linewidth',4)
legend('Peak 1','Peak 2','Peak 3','Peak 4','Peak 5','Peak 6','Peak 7')
PeakArea=PeakArea';
```

GCDataImport MATLAB Function

```
function [DataLength,DataLengthMode,DL,SpecNs,OriginalData]=GCDataImport(FN,FT,DiffLengths,DataNum)
%check that there are several data files
if ~iscell(FN)
error('Please Open More than 1 data file when running this code')
end
NumChrom=length(FN);
for i=1:NumChrom
   %Put all filenames into a character variable
   SpecNames=char(FN);
   %Extract the run-number suffix from the data file names
   SpecN=strtrim(SpecNames(i,:));
   SpecNstr(i,:)=SpecN(end-6:end-4);
end
%if run-number only has one digit, remove letter, and add leading 0
SpecNstr(isletter(SpecNstr))='0';
SpecInts=str2num(SpecNstr);
%Convert to cell variable
SpecNs=cellstr(SpecNstr);
[~,SortInd]=sort(SpecInts);
FN=FN(SortInd);
SpecNs=SpecNs(SortInd);

%Read From Excel Files
if FT==1
   %Read the data into a structure called Original Data
   for i=1:NumChrom
      OriginalData(i).Time=xlsread(FN{1},'A:A');
      OriginalData(i).SpecO=xlsread(FN{i},'B:B');
      if DiffLengths
```

```
            OriginalData(i).SpecO=OriginalData(i).SpecO(1:DataNum);
            OriginalData(i).Time=OriginalData(i).Time(1:DataNum);
       end
       DataLength(i)=length(OriginalData(i).SpecO);
    end
end
%Read From Text Files
if FT==2
    for i=1:NumChrom
        %Get data from tab-delimited text files
        OriginalData(i)=tdfread(FN{i});
    end
    [OriginalData.SpecO]=OriginalData.Value;
    OriginalData=rmfield(OriginalData,'Value');
    for i=1:NumChrom
        %Extract chromatogram
        if DiffLengths
            OriginalData(i).SpecO=OriginalData(i).SpecO(1:DataNum);
            OriginalData(i).Time=OriginalData(i).Time(1:DataNum);
        end
        DataLength(i)=length(OriginalData(i).SpecO);
    end
end
DataLengthMode=mode(DataLength);
DL=DataLength==DataLengthMode;
DL=numel(DL)-sum(DL);
```

GCDataIterativeBGFit MATLAB Function

```
function [SpecBGSub,NoiseMax]=GCDataIterativeBGFit(NumChrom,TimeO,SpecO,SpecBGRS,BGMax,BGRough,SpecNs)
BGMaxRough=2*BGMax;
%iterative background fitting!!
%XXXXXXXXXXXXXXXXXXXXXXXXXXXXXXXXXXXXXXXXXXXXXXXXXXXXXXXXXXXXXXXXXXXXX
XXX
%Pause Switch: if you want to see the background subtraction process
%as it occurs visualy set this to 1
Pause=0;
%Initiallize the background function (fitted functions will be summed
% together later)
BG=zeros(length(TimeO),NumChrom);
%Get Screen resolution for figures
ScreenSize=get( groot, 'Screensize' );
%Loop once for each Chromatogram
figure(3)
set(gcf,'Position',ScreenSize)
for i=1:NumChrom
    %Begin with the smoothed, Rough-Background subtracted chromatograms
    SpecBGS=SpecBGRS(:,i);
    if Pause==1
        subplot(3,3,4:6)
        plot(TimeO,SpecBGS)
        pause (.5)
    end
```

```
%Continue iterating until the spectrum maximum falls below BGMax1
while max(SpecBGS)>BGMaxRough
   %Set all points in the Chrom which are larger than half the maximum
   %value to the mean value over the entire run
   SpecBGS(abs(SpecBGS)>.5*max(SpecBGS))=mean(SpecBGS);
   %Fit a linear function to the chrom
   BGi=polyval(polyfit(TimeO,SpecBGS,1),TimeO);
   %Subtract the linear function from the chromatogram
   SpecBGS=SpecBGS-BGi;
   %Add this linear function to the total background function, which will
   %eventually be subtracted from the raw data
   BG(:,i)=BG(:,i)+BGi;
   %subplot(3,1,2)
   if Pause==1
      subplot(3,3,4:6)
      plot(TimeO,SpecBGS)
      pause (.5)
   end
end
%Plot the current background subtracted chromatogram
subplot(3,3,4:6)
plot(TimeO,SpecBGS)
%Fit the background with 7th degree polynomial function
BGf=polyval(polyfit(TimeO,SpecBGS,7),TimeO);
%Subtract this fit from the chromatogram
SpecBGS=SpecBGS-BGf;
%Add this function to the total Background
BG(:,i)=BG(:,i)+BGf;
if Pause==1
   subplot(3,3,4:6)
   plot(TimeO,SpecBGS)
   pause (.5)
end
%Continue iterating (slower) until the spectrum maximum falls below BGmax2
while max(SpecBGS)>BGMax
   %Set all points in the Chrom which are larger than 3/4 the maximum
   %value to the mean value over the entire run
   SpecBGS(SpecBGS>.75*max(SpecBGS))=mean(SpecBGS);
   %Fit a linear function to the chrom
   BGi=polyval(polyfit(TimeO,SpecBGS,1),TimeO);
   %Subtract the linear function from the chromatogram
   SpecBGS=SpecBGS-BGi;
   %Add this linear function to the total background function, which will
   %eventually be subtracted from the raw data
   BG(:,i)=BG(:,i)+BGi;
   if Pause==1
      subplot(3,3,4:6)
      plot(TimeO,SpecBGS)
      pause (.5)
   end
end
%Final 7th degree polynomial background fit
BGf2=polyval(polyfit(TimeO,SpecBGS,7),TimeO);
SpecBGS=SpecBGS-BGf2;
```

```
   if Pause==1
      subplot(3,3,4:6)
      plot(TimeO,SpecBGS)
      pause (2)
   end
   %This is the final function added to the total background
   BG(:,i)=BG(:,i)+BGf2;
   %The Chromatogram left over after all the subtractions, and set-to-mean-value
   %iterations is saved as a column in the Noise matrix
   Noise(:,i)=SpecBGS;
end
%Find the maximum value of the noise from all Chromatograms
NoiseMax=max(max(Noise));
%Subtract the total background from the smoothed Chromatograms computed
%earlier
SpecBGSub=SpecBGRS-BG;
%Plot the noise
figure(3)
subplot(3,3,4:6)
plot(TimeO,Noise)
title('Background Noise')
%Plot the Final Background-Subtracted Chromatograms on a log scale
subplot(3,3,7:9)
SpecBGSubPlot=SpecBGSub;
SpecBGSubPlot(abs(SpecBGSubPlot)<.75*BGMax)=10;
semilogy(TimeO,abs(SpecBGSubPlot))
title('Log of Background Subtracted Spectrum')
axis([min(TimeO),max(TimeO),10,10^ceil(log10(max(SpecBGSub(:))))])
%Plot the original smoothed data
figure(3)
subplot(3,3,1:3)
semilogy(TimeO,abs(SpecO))
title('Original Data')
axis([min(TimeO),max(TimeO),10,10^ceil(log10(max(SpecO(:))))])
%Plot the total Background functions for all the Chromatograms
figure(5)
plot(TimeO,BG+BGRough)
set(gcf,'name','Background functions subtracted from the original data')
legend(SpecNs)
%Optional Plots (These make this code slow)
%XXXXXXXXXXXXXXXXXXXXXXXXXXXXXXXXXXXXXXXXXXXXXXXXXXXXXXXXXXXXXXXXXXXXXXXXXXXXXXXXXXXXXXXXXXXXXXXXXXXXXXX
fig=0;
if fig==1
   figure(2)
   [Y,T]=meshgrid(TimeO,[1:NumChrom]);
   waterfall(T,Y,(log10(SpecBGSub-ones(length(SpecBGSub),1)*min(SpecBGSub,[],1)+1))')
   figure(4)
   ribbon(TimeO,(log10(SpecBGSub-ones(length(SpecBGSub),1)*min(SpecBGSub,[],1)+1)),.25)
   shading interp
   legend(SpecNs)
end
```

APPENDIX IV

TITAN GAS HANDLING SYSTEM DESIGN

Switching to the Titan ETEM provided an opportunity to overhaul the design of the gas mixing system because the microscope does not include all the components necessary for flowing gas mixtures. The microscope does include 3 gas inlets, each with its own leak valve; however, the inlets are not designed for mixing gases and the 2 so-called reactant gas inlets cannot be simultaneously opened to mix two reactants. This means that any gas mixing must be completed outside the microscope, before flowing the gas mixture into the ETEM. A gas handling system was therefore designed as part of this work, with some input from Jimmy Liu and Peter Crozier. It was built with a bit of help from other graduate students, and one undergraduate who helped build the supporting cart.

A basic diagram of the system is given in Figure A 9. The system consists of 2 mass flow controllers (MFCs), which are each attached to 3 gas cylinders, for a total of 6 available gases. The MFCs flow gas into a small mixing chamber, which is then connected to all 3 gas inlets on the ETEM, as well as to a large tank of N_2 for purging. Two gauges measure the pressure in the mixing chamber and just before the pumps.

A complete schematic diagram of the system is given in Figure A 10. The 6 gasses originally planned are shown, with flammable gases H_2, CH_4, and CO connected to the top MFC, and non-flammable O_2, CO_2, and air connected to the bottom mass flow controller via ¼ inch stainless steel lines. These lines are also connected (through valves VM1 and VM2) to a larger ½ inch stainless steel line, which allows them to be efficiently pumped by the turbopump, bypassing the mass flow controllers. The mass flow controllers are both connected to the mixing chamber, which also connects to all three inlets of the titan, as well as the 2 inch vacuum line to which the turbopump connects. The 3 inlets to the microscope are all intended for different experiments. The bottom line is designed for

experiments using CO, for which additional filters are necessary, as discussed in section 3.3.2. The top inlet line is used for experiments with water vapor, and has a liquid water vessel attached. The middle line is for other experiments which do not require either the filters nor water vapor, and also connects to the large N_2 tank.

The system is designed to enable rapid and efficient pumping so that pump-purge cycles can be quickly performed during experiments when switching gases. The turbo pump is quite large for such a small system, with a pumping speed of 230 l/s. However, if a high pressure of gas is present in the lines from the gas tanks to the mass flow controllers, and these lines need to be pumped, the turbo pump cannot handle such a large amount of gas. This happens frequently when pump-purge cycles are performed. For this reason, a bypass is built into the system, allowing the backing pump to directly pump the system by opening valve VL2, with the turbo pump still running, but closed off completely from the rest of the system by valves VL3 and VL4. After only a few seconds the bypass can be closed and the turbo pump engaged again to achieve a pressure close to 10^{-5} Torr in a minute or two.

The entire gas handling system operates using manual valves. This reduced the initial cost of the system. It also makes it easier for users to get a good sense of what is actually happening in the system. It is likely more difficult to make dumb mistakes when operating manual valves than when pressing buttons on a control panel or graphical user interface. A photo of the system during construction is shown in Figure A 11.

The mass flow controllers are the heart of the gas handling system, enabling stable and precise gas flow rates over long time periods. The MFCs chosen for this system are built by Alicat, and operate via a laminar flow rate measurement. Basically, within the mass

flow controller, the gas flow is divided into many small channels, where the flow becomes laminar. The pressure drop over this region of laminar flow is then measured to determine the flow rate. The two mass flow controllers have two different maximum flow rates. The top flow controller can flow 20 sccm while the lower MFC can flow up to 10 sccm. Each MFC can reliably flow as little as 0.5% of its maximum rate.

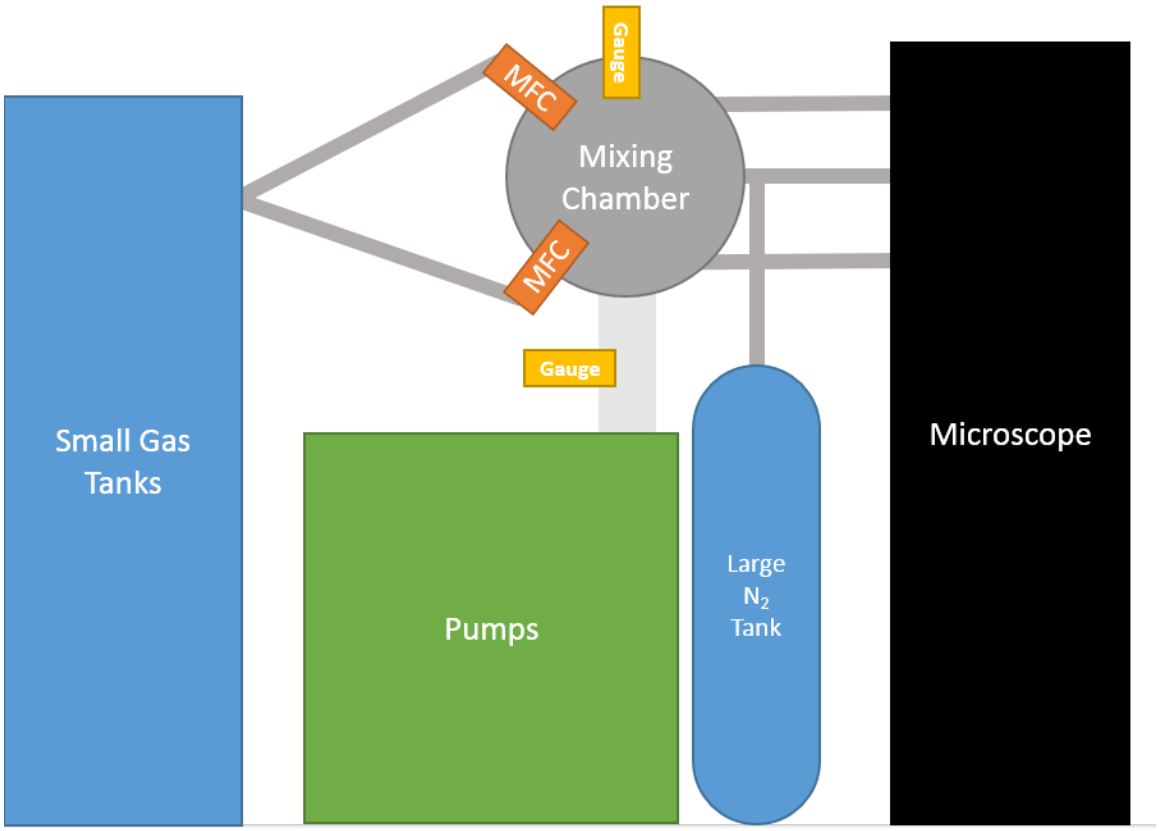

Figure A 9 Gas Handling System Diagram- Basic. Simple schematic diagram showing the major components of the gas handling system built for the Titan microscope.

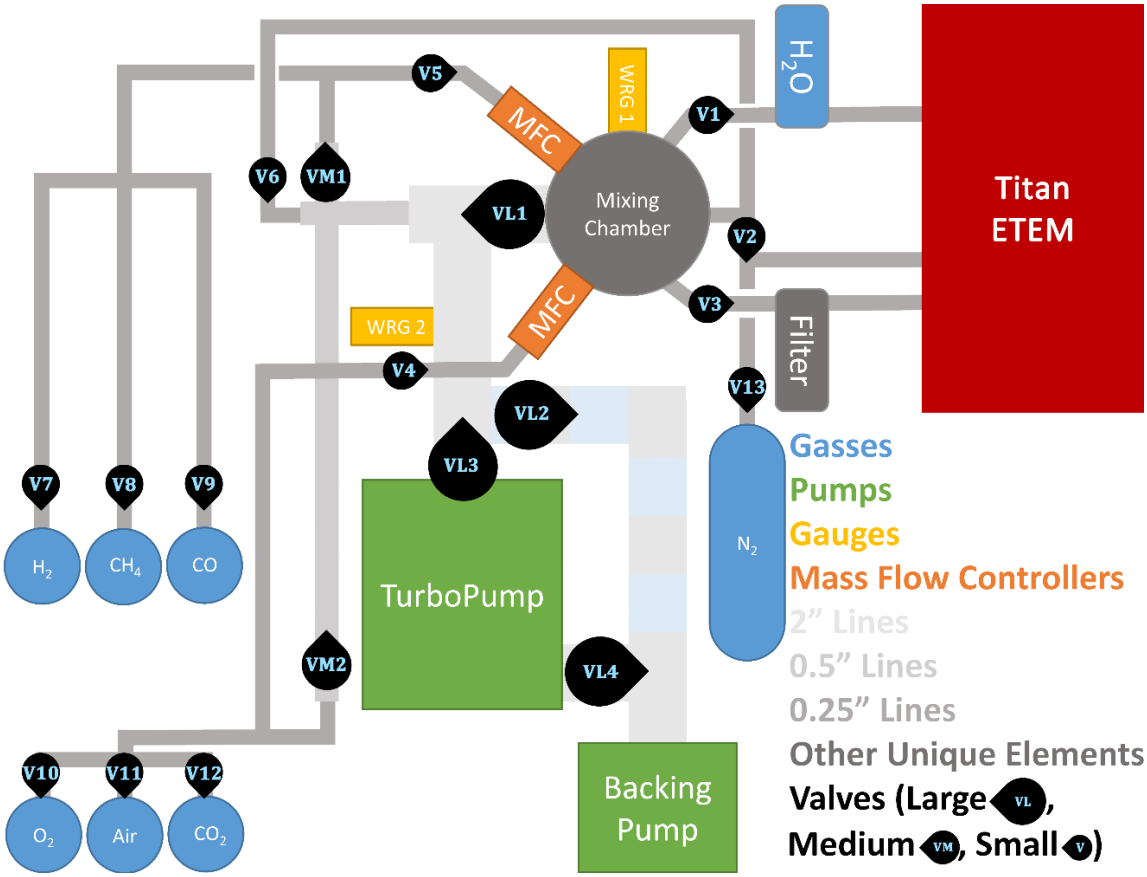

Figure A 10 Gas Handling System Diagram- Full. Full schematic diagram of the gas handling system built for the Titan ETEM showing every valve, gauge, pump, MFC, and the 3 different sizes of stainless steel tubing used.

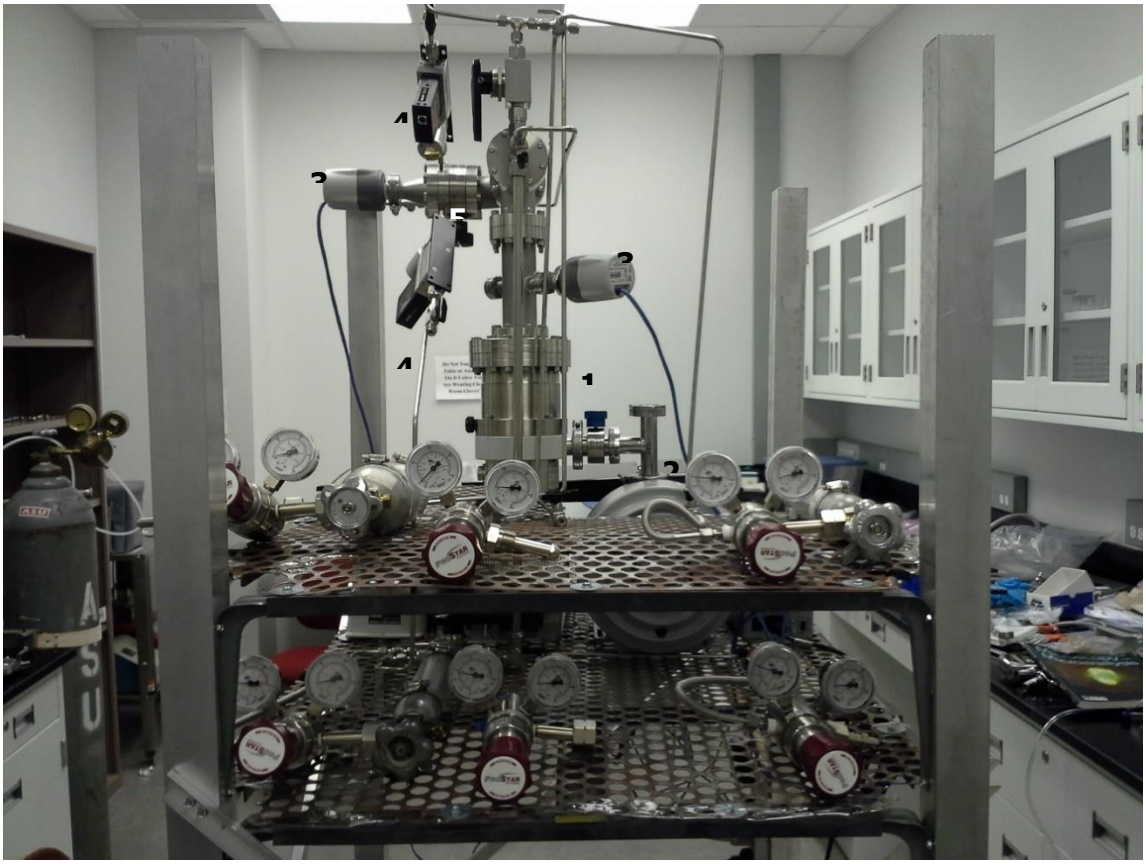

Figure A 11 Titan Gas Handling System. The gas handling system during construction. In the foreground are the regulators and a few gas tanks. In the background are the turbo pump[1] and scroll pump[2], along with the gauges[3], mass flow controllers[4] and the mixing chamber[5].

APPENDIX V

LOW-LOSS EELS CODE

As part of this work, a MATLAB code was written to automate the process of finding the gas composition within the ETEM by fitting low-loss EELS spectra with a linear combination of reference spectra by a constrained weighted least squares method (Miller and Crozier, 2014). The code can perform this operation on a single spectrum, multiple spectra, on a STEM-EELS data cube, or on the data cube generated by the multiple EELS acquisition code referenced in section 3.3.4 (Mitchell and Schaffer, 2005). The main code handles the input of these different formats, and passes the resulting 1D EELS spectra to the function LL_EELS_CC, which contains the core of the fitting functionality, as described below. If the input is a multiple EELS acquisition code data cube, the MATLAB code integrates the 2D detector image in an intelligent way to reduce noise (see Appendix VI).

In addition to performing the constrained least squares fit, the MATLAB code automatically shifts the energy scale and accounts for the background. The code first normalizes the reference spectra so their integrated intensities are all unity over the energy range of 4 to 44 eV. To automatically shift the spectra to the correct energy loss, the reference spectra and the mixture spectrum are aligned roughly using cross correlation in case the mixture spectrum has a significantly incorrect energy calibration. Next, the linear combination of selected gases that best fits the spectrum from the gas mixture in the TEM is computed by a constrained weighted non-linear least squares method, where the peaks in the mixture spectrum are given a higher weighting, by setting the weights equal to the square of the intensity. This least squares fit is repeated many times, while shifting the mixture spectrum slightly relative to the (precisely calibrated) reference spectra to get a precise, automatic energy calibration of the mixture spectrum, as shown in Figure 3-18,

where an optimal fit is given in green and the poorest fits in red. The results of this shifting can also be seen in Figure A 12 where the right window contains a plot showing the initial cross-correlation based energy shift on the far right, and the lower plot gives the root mean squared error of the fit as a function of the mixture spectrum shift.

After the ideal fit is found, it is seen that the residuals often show a clear functional dependence, as seen in Figure A 12, and described in section 3.3.4. This is due to the zero loss tails of the reference and mixture spectra being slightly different. No background removal was performed on either the reference or mixture spectra to attempt to completely remove the zero loss tails; instead the backgrounds of the reference and mixture spectra were matched. This is done by fitting the residuals using an inverse power law, and this fit is subtracted from the measured spectrum. The power law fit can be seen in the right window of Figure A 12, where the red region is fit, and the blue region ignored, since this region is dominated by the gas signals, rather than the background intensity. This procedure is equivalent to performing a background subtraction on both the mixture and reference spectra, to remove the zero loss tails, but is more robust in this case, where only a small window prior to the peak onset is available, making a more traditional background subtraction difficult. After the residual fit has been subtracted, (shown in Figure A 13) the background-matched spectrum is taken through the steps of fitting and shifting again to determine a new optimized fit. This process of matching the background is repeated as necessary until no clear power law dependence of the residuals is found. In this case, subtracting the power law fit to the residuals once was sufficient; this is usual, and no more than 3 subtractions have ever been necessary. No procedure for deconvolution of plural scattering was applied, since plural scattering is minimal at the gas pressures used, where

the electron mean free path is much larger than the pole piece gap. Once the linear combination coefficients have been determined, information about the reference spectra is used to compute the gas partial pressures, as detailed in (Crozier and Chenna, 2011).

The low loss EELS code gave good results for experimental 50-50 mixtures of CO and CO_2 as shown in Figure 3-17 of the text. However, it is unclear from this test whether the deviation of the measured gas composition from a precise 50-50 mixture is due to a flaw in the linear combination fit method, the MATLAB code, or the experimental gas mixture itself. It is likely that the error is in the mixture itself, as the method used to mix the gases in the Tecnai system is basic, and does not account for the differential effusion of gases of different mass. A method for testing the precision of the MATLAB code itself was therefore devised. A simulated mixture spectrum was produced from single gas reference spectra by a linear combination with known coefficients. This spectrum was then scaled and Poisson noise added, as seen in Figure A 15, so that it had the same signal to noise as an experimental spectrum acquired for 4s (the standard acquisition time used in this work). A series of simulated spectra were then produced, with linear combination coefficients consistent with CO conversions of between 1 and 100%. The simulated spectra were then fit using the MATLAB code. The resulting calculated gas compositions are compared to the expected value in Figure A 15. The precision of the code was shown to be quite good, and a second CO conversion range, 0.1 to 10% was explored, and is also shown in Figure A 15. The root mean squared error over the entire 1 to 100% range was found to be just 0.2%, and the fit was accurate even for small CO conversions, where the CO_2 mole fraction was below 1%.

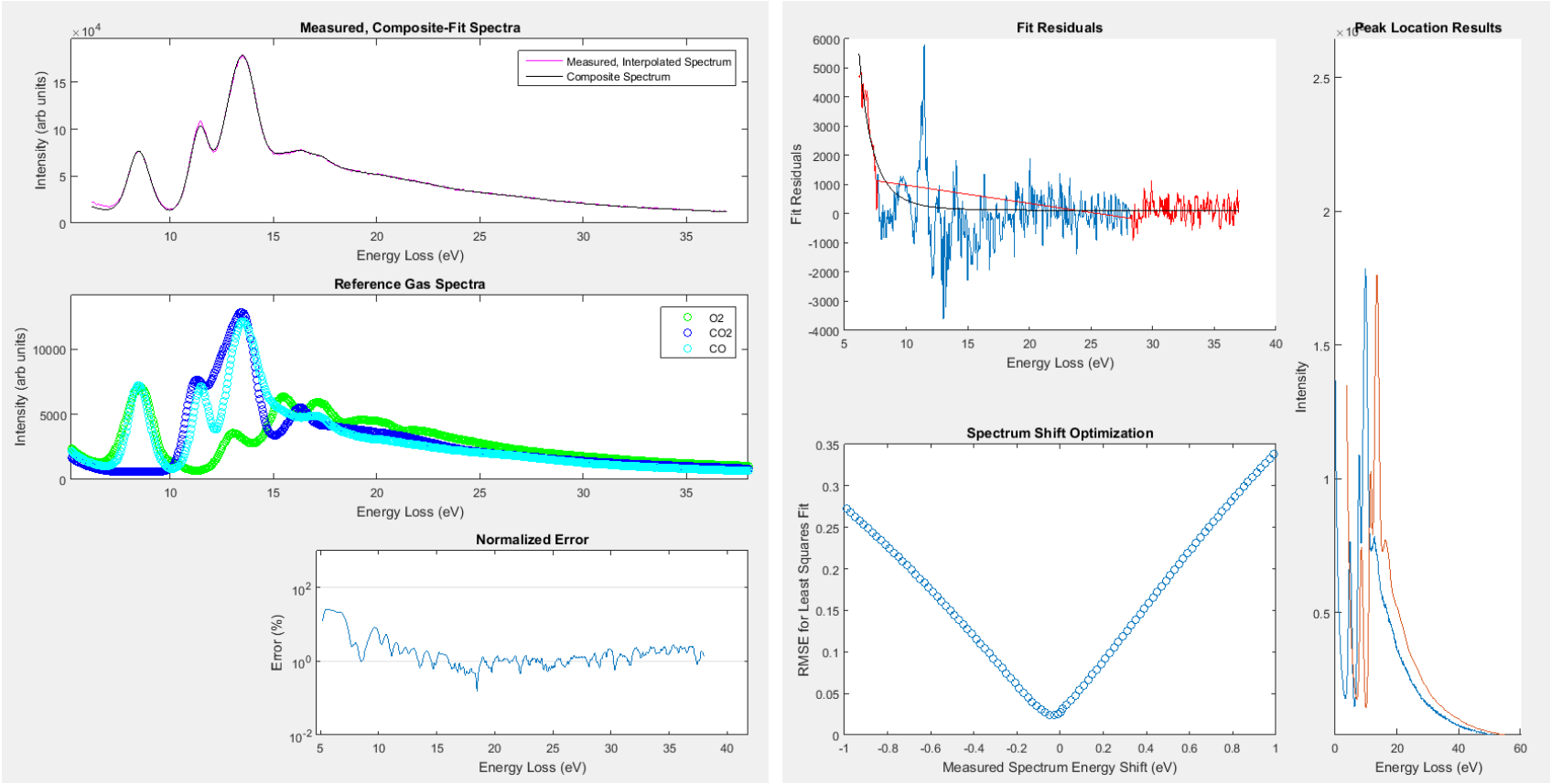

Figure A 12 LL EELS MATLAB Code 1. Low-loss EELS code windows shown prior to background matching. In the left window are three plots. The upper plot shows the measured and linear combination spectra plotted together for visual comparison. The middle plot shows the 3 reference gas spectra. The lower plot shows the percent error along the spectra. In the right window are three more plots. The upper left plot shows the fit residuals along with a power-law fit to the residuals colored red. The lower left plot shows the error of the fit as a function of the energy shift applied to the measured spectrum, which should display a clear global minimum. The right plot shows the large shift applied to the spectrum during the initial energy calibration.

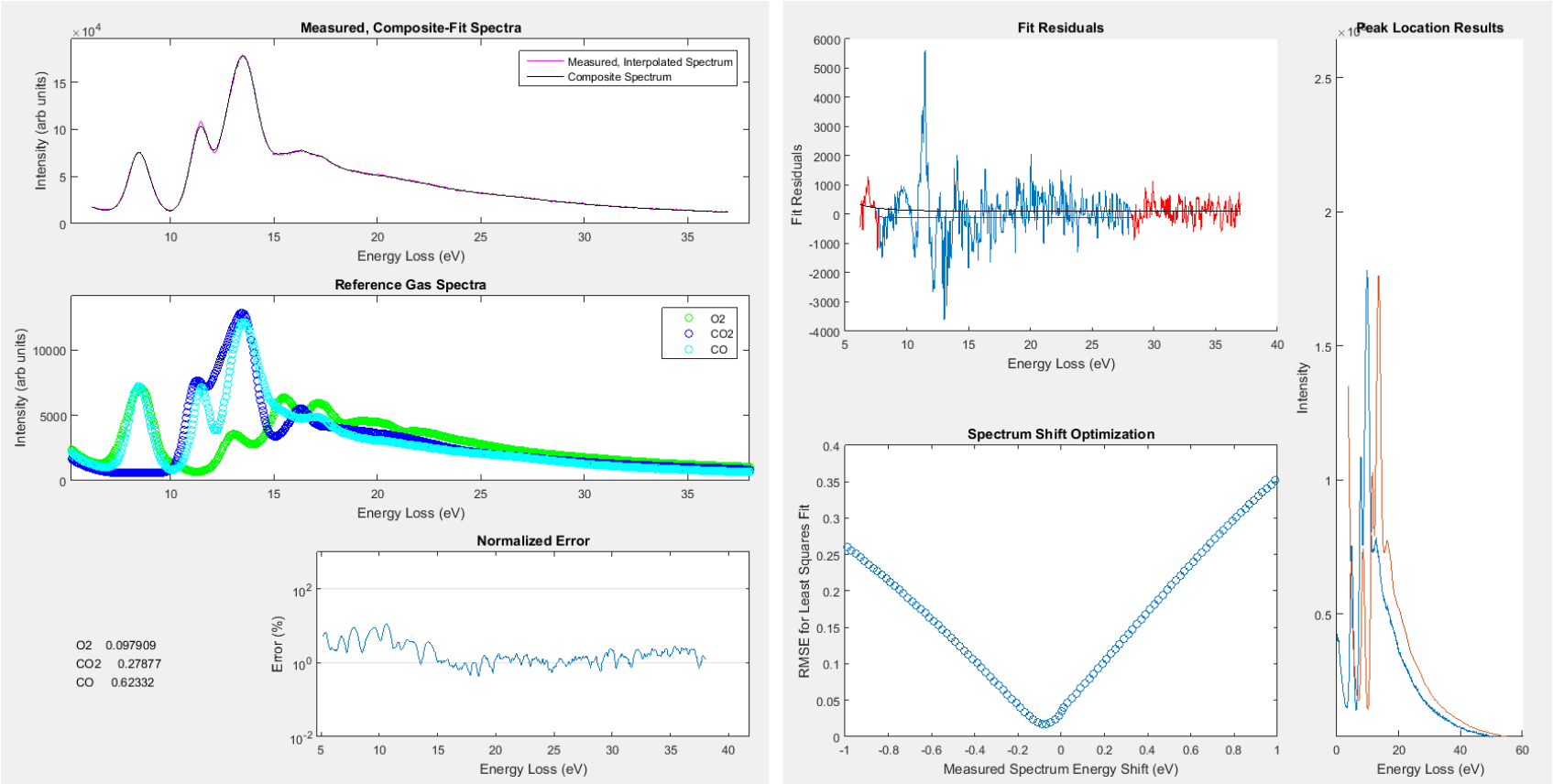

Figure A 13 LL EELS MATLAB Code 2. Low-loss EELS code windows shown after background matching. The upper left corner of the right window shows that the fit residuals no longer display an obvious functional dependence. The gas composition determined from the fit is given in the lower left corner of the left window.

Figure A 14 Simulated Noisy Spectrum. A linear combination of reference spectra was suitably scaled to create the combined spectrum in purple, and is shown in green after addition of Poisson noise.

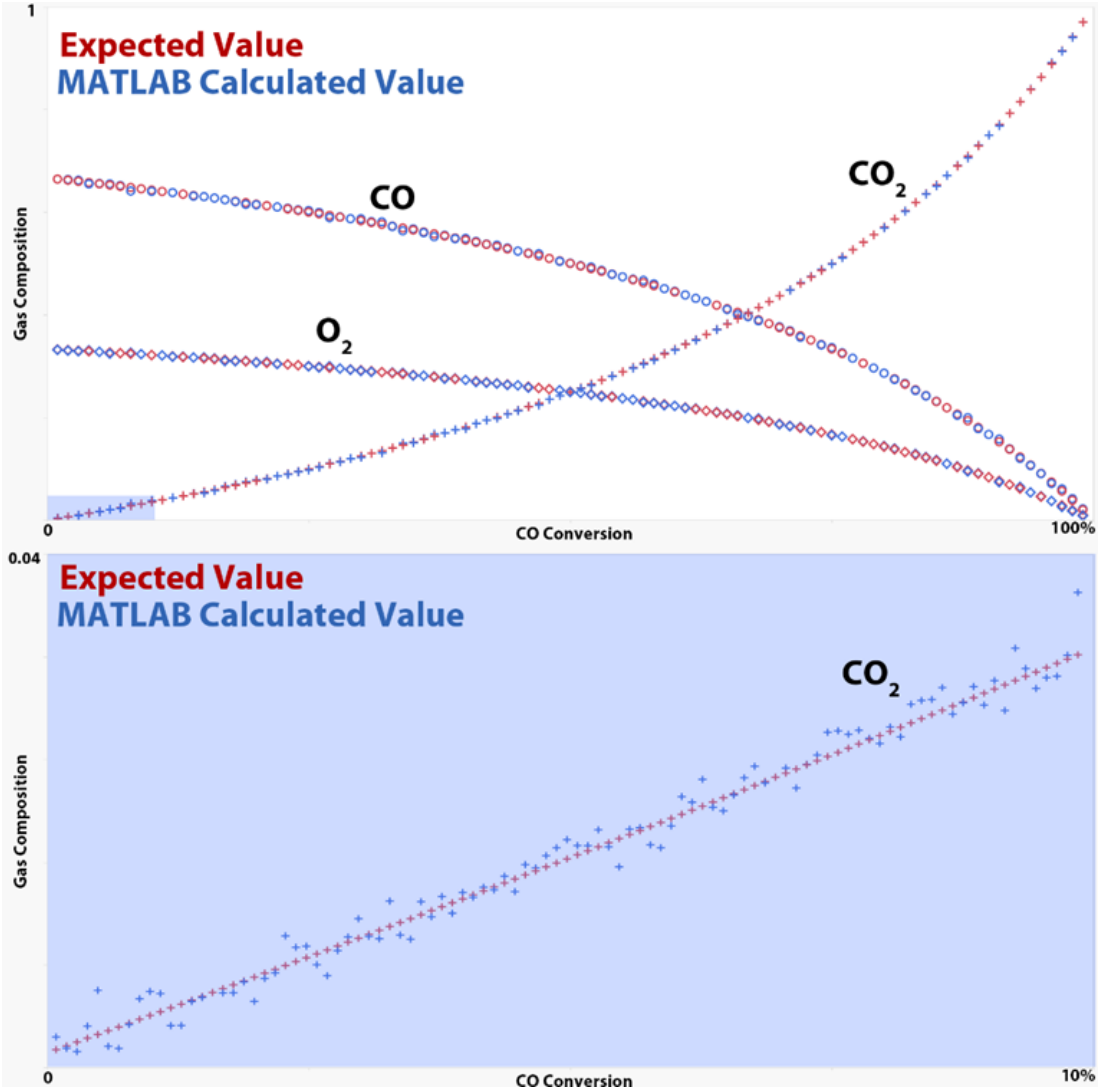

Figure A 15 LL EELS Code Precision. The good match between the expected value of the gas composition and the value calculated by the MATLAB code is shown here for a range of compositions corresponding to, Top: between 1 and 100% CO conversion. Bottom: between 0.1 and 10% CO conversion.

EELS_LL_Analysis MATLAB Code

```
%Choose which type of file(s) you wish to analyze, by setting this
%parameter to 1, 2, 3, or 4
% 1: Single DM3
% 2: EELS Image DataCube DM3 (from MultipleEELS Code)
% 3: Spectrum Image
% 4: Multiple DM3 files
clear
global IndexT NumSpec Path
FileType=2;
```

```
WholeFolder=0;
%XXXXXXXXXXXXXXXXXXXXXXXXXXXXXXXXXXXXXXXXXXXXXXXXXXXXXXXXXXXXXXXXXXXXXXXXXXXXXXX
XXX
%Read Excel File with Reference Spectra for Gases
ReferenceFile='EELSReferenceSpectra2';
[RefSpectra,Titles]=xlsread(ReferenceFile);

%First select gases to extract from Reference File
%Get User Input about what Gases are expected to contribute to Obeserved
%Spectrum
Gas=input('What is the First Gas in the Spectrum? ','s');
if isempty(Gas)
    IndexT=IndexT;
    NumSpec=NumSpec;
else
    %Put First User Input into Cell Array "CompName"
    CompName{1}=Gas;
    i=1;
    %Put Additional User inputs into same Cell Array until user stops entering
    %gases
    while ~isempty(Gas)
        i=i+1;
        Gas=input('What is the Next Gas in the Spectrum? (If done, leave blank) ','s');
        CompName{i}=Gas;
    end
    %Delete Last Input from Cell Array (Input was nothing [] )
    CompName(end)=[];
    %Find number of User input Spectra
    NumSpec=size(CompName,2);
    %Initialize IndexT
    IndexT=zeros(1,size(Titles,2));
    %Find which collumns correspond to the user input gas names
    for i=1:NumSpec
        %Compare strings input by user to those read from Excel file
        Index=strcmp(Titles,CompName{i});
        %Gather these into one vector
        IndexT=Index+IndexT;
    end
end
%Set NonNeg to 1 if you want the computed linear coefficients to be only positive
NonNeg=1;

%XXXXXXXXXXXXXXXXXXXXXXXXXXXXXXXXXXXXXXXXXXXXXXXXXXXXXXXXXXXXXXXXXXXXXXXXXXXXXXX
XXX
%end

%XXXXXXXXXXXXXXXXXXXXXXXXXXXXXXXXXXXXXXXXXXXXXXXXXXXXXXXXXXXXXXXXXXXXXXXXXXXXXXX
XXX
%Now begin to extract measured data and call main computational function
if FileType==1
    %Select File using dialog box and after first instance keep opening from same
    %folder.
    if ~exist('Path','var')
        [FName,Path]=uigetfile({'*.dm3','Digital Micrograph File (dm3)'},'Select a DM3 file');
```

```
    end
    if Path==0
        [FName,Path]=uigetfile({'*.dm3','Digital Micrograph File (dm3)'},'Select a DM3 file');
    elseif exist('Path','var')
        [FName,Path]=uigetfile(strcat(Path,'*.dm3'),'Select a DM3 file');
    end
    %Use DM3Import Function (Robert McLeod) to get data from DM3
    DM3Data=DM3Import(strcat(Path,FName));
    %Get the EELS dispersion
    Dispersion=DM3Data.xaxis.scale;
    %Get the start energy (this is really not important, since the code
    %automatically shifts the energy calibration
    EStart=0;
    %Get the EELS Spectrum!!
    MSpec=(DM3Data.image_data);
    MSpec=real(MSpec);
    %Create the energy vector for the spectrum
    MSpecE=EStart:Dispersion:EStart+Dispersion*(length(MSpec)-1);
    %Run the EELS Low Loss fitting code
    [CNorms,RMSEs,ResidualsPs,MeasSpecNames,Wps,MSpecEP,MSpecP] =
LL_EELS_CC(MSpecE,MSpec,FName,IndexT,RefSpectra,Titles,NonNeg);
end

if FileType==2
    NumFilesLeft=1;
    % 1 out of AnalIntval spectra will be analyzed
    AnalIntval=1;
    %Select File using dialog box and after first instance keep opening from same
    %folder.
    if ~exist('Path','var')
        [FName,Path]=uigetfile({'*.dm3','Digital Micrograph File (dm3)'},'Select an EELS Data Cube File');
        if WholeFolder==1
            DirStruct=dir(Path);
            NumFilesLeft=size(DirStruct,1)-2;
        end
    end
    if Path==0
        [FName,Path]=uigetfile({'*.dm3','Digital Micrograph File (dm3)'},'Select an EELS Data Cube File');
    elseif exist('Path','var')
        [FName,Path]=uigetfile(strcat(Path,'*.dm3'),'Select an EELS Data Cube File');
        if WholeFolder==1
            DirStruct=dir(Path);
            NumFilesLeft=size(DirStruct,1)-2;
        end
    end

    while NumFilesLeft>0
        if WholeFolder
        FName=DirStruct(NumFilesLeft+2).name;
        end
        CubeSize=ReadDM3_size(strcat(Path,FName));
        for i=1:CubeSize(3)
            DataCubeO(:,:,i)=ReadDM3_slice(strcat(Path,FName),CubeSize,i);
            %Because ReadDM3_slice is reading using improper format, negative
```

```
        %numbers must be set to 0 (else they are read as very large numbers)
        DataCubeO(:,:,i)=DataCubeO(:,:,i).*uint16(~(DataCubeO(:,:,i)>16385));
        DataCubeMed(:,:,i)=medfilt2(DataCubeO(:,:,i),[5,1]);
      end
      %Specify the Dispersion
      Dispersion=.05;
      %Find the maximum pixel row in the non-dispersive direction
      IntP=sum(DataCubeMed,1);
      IntP=sum(IntP,3);
      [~,IntM]=max(IntP);
      %Number of non-dispersive channels to integrate (actual integration
      %uses IntRange+1 channels
      IntRange=(min(IntM,CubeSize(2)-IntM)-1)*2;
      IntBreaks=[IntM-round(IntRange/2),IntM+round(IntRange/2)];
      Spectra=squeeze(sum(DataCubeO(:,IntBreaks(1):IntBreaks(2),:),2));
      MSpecE=0:Dispersion:Dispersion*1023;

      %Run the EELS Low Loss fitting code once for every spectrum
      for i=1:AnalIntval:CubeSize(3)
        MSpec=Spectra(:,i)';
        [CNorms,RMSEs,ResidualsPs,MeasSpecNames,Wps,MSpecEP,MSpecP] =
LL_EELS_CC(MSpecE,MSpec,FName,IndexT,RefSpectra,Titles,NonNeg);
      end
      NumFilesLeft=NumFilesLeft-1;
    end
end

if FileType==3
    %Select File using dialog box and after first instance keep opening from same
    %folder.
    if ~exist('Path','var')
        [FName,Path]=uigetfile({'*.dm3','Digital Micrograph File (dm3)'},'Select a DM3 Spectrum Image file');
    end
    if Path==0
        [FName,Path]=uigetfile({'*.dm3','Digital Micrograph File (dm3)'},'Select a DM3 Spectrum Image file');
    elseif exist('Path','var')
        [FName,Path]=uigetfile(strcat(Path,'*.dm3'),'Select a DM3 Spectrum Image file');
    end


    addpath(Path);
    DM3Data=DM3Import(FName);
    Dispersion(i)=DM3Data.xaxis.scale;
    MSpecCube=DM3Data.image_data;
    CubeSize=size(MSpecCube);
    MSpecE=(0:Dispersion(1,i):Dispersion(1,i)*(CubeSize(3)/2-1));
    counter=1;
    for i=1:CubeSize(1)
        for j=1:CubeSize(2)
            MSpec=MSpecCube(i,j,1:CubeSize(3)/2);
            MSpec=MSpec(:)';
            %Give the user an indication of how far the script has progressed
            disp(strcat('Processing Spectrum #',num2str(counter),{' out of '},num2str(CubeSize(1)*CubeSize(2))))
            [CNorms,RMSEs,ResidualsPs,MeasSpecNames,Wps,MSpecEP,MSpecP] =
```

```
LL_EELS_CC(MSpecE,MSpec,FName,IndexT,RefSpectra,Titles,NonNeg);
            counter=counter+1;
            %Place the output values from the EELS code for each SI pixel into matrices
            CNormCube(i,j,:)=CNorms(:,end);
            RMSECube(i,j)=RMSE(end);
            MeasSpecNamesCube{i,j}=MeasSpecNames{end};
            WpsCube(i,j)=Wps(end);
        end
    end
end

if FileType==4
    if ~exist('Path','var')
        [FName,Path]=uigetfile({'*.dm3','Digital Micrograph File (dm3)'},'Select Multipe DM3 files containing single
spectra','multiselect','on');
    end
    if Path==0
        [FName,Path]=uigetfile({'*.dm3','Digital Micrograph File (dm3)'},'Select Multipe DM3 files containing single
spectra','multiselect','on');
    elseif exist('Path','var')
        [FName,Path]=uigetfile(strcat(Path,'*.dm3'),'Select Multipe DM3 files containing single spectra','multiselect','on');
    end

    NumSpec=length(FName);
    if ~strcmp(class(FName),'cell')
        error('To select one spectrum, please use FileType 1 (EELS_LL_Analysis: Line 8)')
    end
    %Run the EELS Low Loss fitting code once for every spectrum
    for i=1:NumSpec
        DM3Data=DM3Import(strcat(Path,FName{i}));
        %Get the EELS dispersion
        Dispersion=DM3Data.xaxis.scale;
        %Get the start energy (this is really not important, since the code
        %automatically shifts the energy calibration
        EStart=0;
        %Get the EELS Spectrum!!
        MSpec=real(DM3Data.image_data);
        NumChannels=length(MSpec);
        %Create the energy vector for the spectrum
        MSpecE=EStart:Dispersion:EStart+Dispersion*(length(MSpec)-1);
        %Give the user an indication of how far the script has progressed
        disp(strcat('Processing DM3 file #',num2str(i),{' out of '},num2str(NumSpec)))
        %Run the EELS Low Loss fitting code
        [CNorms,RMSEs,ResidualsPs,MeasSpecNames,Wps,MSpecEP,MSpecP] =
LL_EELS_CC(MSpecE,MSpec,FName,IndexT,RefSpectra,Titles,NonNeg);
        %Run the EELS Low Loss fitting code, without any graphical output

%[T,CNorms,RMSEs,ResidualsPs,MeasSpecNames,Wps,MSpecEP,MSpecP]=evalc('LL_EELS_CC(MSpecE,MSpec,FName,Ind
exT,RefSpectra,Titles,NonNeg)');
    end

end
```

3rd Party Codes Used: DM3Import, ReadDM3_size, ReadDM3_slice

LL_EELS_CC Function

```
function [CNorms,RMSEs,ResidualsPs,MeasSpecNames,Wps,MSpecEP,MSpecP] =
LL_EELS_CC(MSpecE,MSpec,FName,IndexT,RefSpectra,Titles,NonNeg)

%Function LL_EELS Low-Loss Electron Energy-Loss of gases least squares
%fitting

%Inputs:
%MSpecE -       a vector of Energy losses (eV)
%MSpec -        a vector of counts (the spectrum)
%FName -        the file name of the DM3 file
%IndexT -       a logical vector determining which gases from the reference
            %file will be used for the linear fit
%RefSpectra-    The reference spectra read from the reference file
%Titles -       The names of reference gases from the reference file
%NonNeg -       A logical value, specifying whether the results of the
            %linear combination fit will be constrained to positive
            %values (1- positive 0- may result in negative values)

%Outputs:
%CNorms -       The determined gas composition
%RMSEs -        The root mean squared error of the fit
%ResidualsPs -  The final residuals of the fit
%MeasSpecNames- The name of the measured spectrum (from the file name)
%Wps -          The weighting exponent used
%MSpecEP -      Energy values of the interpolated spectrum
%MSpecP -       Intensity values of the interpolated spectrum


%XXXXXXXXXXXXXXXXXXXXXXXXXXXXXXXXXXXXXXXXXXXXXXXXXXXXXXXXXXXXXXXXXXXXXXX
XXX
%User Defined Variables XXXXXXXXXXXXXXXXXXXXXXXXXXXXXXXXXXXXXXXXXXXXXXXXXXX
%XXXXXXXXXXXXXXXXXXXXXXXXXXXXXXXXXXXXXXXXXXXXXXXXXXXXXXXXXXXXXXXXXXXXXXX
XXX
%Weighting Exponent
Wp=2;
%Span Used to smooth data before finding peaks
SmoothSpan=24;
%Minimum Peak Height for measured spectrum
PHMeas=.00007;
%Minimum Peak Height for reference spectra
PHRef=.2;
%Minimum Index at which a peak can be found
PiMin=20;
%Domain Spacing (eV)
DomainSpace=.01;
%Domain Minimum (eV)
DomainMin=5.2;
%Multiplier used to determine domain maximum
DomainMaxMult=.8;
%nshift*domainspace is the amount the spectrum is shifted when searching
%for optimum match
```

```
nshift=100;
%Used to change height of the reference peaks when they are plotted
RefPlotMult=2000000;
%Change the sensitivity to incorrect background fitting- lower# - more
%sensitive (default is 2)
RratioN=2;
%Choose indices of MSpecInterpEn where the residuals fit is interupted
ResFitCut1=150;
ResFitCut2=2200;

%If NonNeg is not specified, set to 0.
if ~exist('NonNeg')
   NonNeg=0;
end
%COveride is empty if the coefficients are to be found
COveride=[];
%Use the following line to set fit coefficients, rather than finding them
%COveride=input('To Revert to Default Coefficients type 0. To Set Coefficients Manually, give them as row vector, in the order
they appear in the Reference File');
%Basically divide number of values in IndexT by two (because the Excel file
%only has a title every other collumn)
IndexT2=IndexT(1:2:end);
NumSpec=sum(IndexT2);
%Get List of Gas Names in Order that they will be Plotted (for Legend)
CompNamesO=Titles(IndexT==1);
%Count Reference Spectra read from file
NumRefSpec=size(RefSpectra,2)/2;
%Reshape Reference Spectra data from one matrix into 2: one with energy
%values, and one with intesity values
for i=1:NumRefSpec
   RefSpectraI(:,i)=RefSpectra(:,2*i);
   RefSpectraE(:,i)=RefSpectra(:,2*i-1);
end
%Initialize index
iRS=1:NumRefSpec;
%set to 0 all index values for which IndexT2 is 0 (User didn't include that
%gas)
iRS=iRS.*IndexT2;
%Delete all index values that are 0s (indices can't be 0 in MATLAB)
iRS(iRS==0)=[];
%Initialize Plot
figure(1)
%Clear figure, so previous data is never shown
clf
%Set Figure size to fill half the screen
fullscreen = get(0,'ScreenSize');
set(gcf,'OuterPosition',[0 64 fullscreen(3)/2 fullscreen(4)-64])
%Give a name to the top axis of the figure
SpectraPlot=subplot(3,3,[1 2 3]);
hold on
%Initialize k
k=1;
%Extract User Specified Gases Data from the full set of Reference data
for j=iRS
```

```
    %Normalize EELS intensity data
    SpectraI(:,k)=RefSpectraI(2:end,j)/sum(RefSpectraI(2:end,j));
    SpectraE(:,k)=RefSpectraE(2:end,j);
    %Pressure of reference gases
    Pr(k,1)=RefSpectraI(1,j);
    %t/lambda of reference gases
    TL(k,1)=RefSpectraE(1,j);
    %Plot the Spectra of Specified Gases
    %Colors to cycle through
    Color={'r','g','b','c','m','k'};
    %Mod used to cycle through colors in case there are more spectra than
    %colors
    plot(subplot(3,3,[4 5 6]),SpectraE(:,k),SpectraI(:,k)*RefPlotMult,Color{mod(k,6)+1},'linestyle','none','marker','o')
    hold on
    k=k+1;
end
%Use t/lambda and pressure from reference gas spectra to compute correction
%factor for composition
Correction=Pr.*(1+1./(exp(TL)-1));
assignin('base','Cor',Correction)
%XXXXXXXXXXXXXXXXXXXXXXXXXXXXXXXXXXXXXXXXXXXXXXXXXXXXXXXXXXXXXXXXXXXXXXXX
XXX
%XXXXXXXXXXXXXXXXXXXXXXXXXXXXXXXXXXXXXXXXXXXXXXXXXXXXXXXXXXXXXXXXXXXXXXXX
XXX
%XXXXXXXXXXXXXXXXXXXXXXXXXXXXXXXXXXXXXXXXXXXXXXXXXXXXXXXXXXXXXXXXXXXXXXXX
XXX
%This Section Calibrates the Experimental Spectrum XXXXXXXXXXXXXXXXXX
span=SmoothSpan;
window=ones(span,1)/span;
%MSpecS=conv(MSpec(1,:),window,'same');
MSpecS=smooth(MSpec,SmoothSpan,'sgolay',2);
MSpecS=smooth(MSpecS,SmoothSpan,'sgolay',2);
dE=SpectraE(2)-SpectraE(1);
DomainCC=0:dE:floor(max(SpectraE(:))*DomainMaxMult);
MSpecInterpICC=spline(MSpecE,MSpecS,DomainCC)';
MSpecInterpECC=DomainCC';
[r,Lags]=xcorr(sum(SpectraI,2)/max(SpectraI(:)*3),MSpecInterpICC/max(MSpecInterpICC(:)));
[~,rmax]=max(r);
Lag=Lags(rmax(1));
EDiff=Lag*dE;
MSpecEO=MSpecE;
MSpecE=MSpecE+EDiff+min(SpectraE(:));
%XXXXXXXXXXXXXXXXXXXXXXXXXXXXXXXXXXXXXXXXXXXXXXXXXXXXXXXXXXXXXXXXXXXXX
%Trim Final Data before fitting
%Interpolate all the Reference Spectra and Plot the Interpolation
Domain=DomainMin:DomainSpace:floor(max(SpectraE(:))*DomainMaxMult);
for k=1:NumSpec
    SpectraInterpI(:,k)=spline(SpectraE(:,k),SpectraI(:,k),Domain)';
    SpectraInterpE(:,k)=Domain';
end
legend(CompNamesO)
xlabel('Energy Loss (eV)')
ylabel('Intensity (arb units)')
title('Reference Gas Spectra')
```

```
%Initialize Shift, R
Shift=0;
R=2;
m=0;
while R>0
   if m~=0
      figure(1)
      SpectraPlot=subplot(3,3,[1 2 3]);
      set(SpectraPlot,'visible','off')
   end
   MSpecE=MSpecE-Shift;
   %Further Background Subtract
   if R~=2;
      MSpec=real(MSpec-ResFit(MSpecE)');
   end
   %Interpolate the Measured Spectrum
   MSpecInterpI=spline(MSpecE,MSpec,Domain)';
   MSpecInterpE=Domain';
   %This is the Section of code that solves the linear combination problem
   %nshift*(Domain Spacing) is the amount (+-) that the spectrum is shifted
   %through to search for optimum shift value
   %Use an even number for nshift
   %Create Shiftable Measured Spectrum, to preserve original values
   MSpecInterpIn=MSpecInterpI;
   %Take Center values from Reference Spectra
   eM=SpectraInterpI(nshift:end-nshift,:);
   %Place Cropped Spectrum into (last) collumn of matrix A
   EShift=[];
   A(:,nshift*2+1)=MSpecInterpIn(nshift:end-nshift);
   %Produce Weighting Matrix
   W=diag((abs(A(:,nshift*2+1))).^Wp,0);
   % Normal Linear Combination
   C=(eM'*W*eM)\eM'*W*A(:,nshift*2+1);
   % Non-Negative Non-Linear least squares linear combination used if NonNeg is 1
   if NonNeg==1
      C=lsqnonneg(eM,A(:,nshift*2+1));
   end
   %Produce Composite Spectrum using coefficients and Reference Spectra
   CompSpectra=SpectraInterpI*C;
   RMSE(1,2*nshift+1)=sqrt(sum((CompSpectra(nshift:end-nshift)-MSpecInterpI(nshift:end-
nshift)).^2)/length(CompSpectra(nshift:end-nshift)))/mean(CompSpectra(nshift:end-nshift));
   %The next 2 loops shift the measured spectrum, and calculate the RMSE to
   %find the best possible fit
   %The 1st loop shifts the spectrum forward, the 2nd shifts it backwards
   for n=1:2:nshift
      MSpecInterpIn=[0;MSpecInterpIn];
      MSpecInterpIn(end)=[];
      EShift(end+1)=DomainSpace*n;
      A(:,n)=MSpecInterpIn(nshift:end-nshift);
      W=diag((abs(A(:,n))).^Wp,0);
      C=(eM'*W*eM)\eM'*W*A(:,n);
      % Non-Negative Non-Linear least squares linear combination used if NonNeg is 1
      if NonNeg==1
         C=lsqnonneg(eM,A(:,n));
```

```
    end
    %Compute Composite Spectrum
    CompSpectra=SpectraInterpI*C;
    RMSE(n)=sqrt(sum((CompSpectra(nshift:end-nshift)-MSpecInterpIn(nshift:end-nshift)).^2)/length(CompSpectra(nshift:end-nshift)))/mean(CompSpectra(nshift:end-nshift));
  end
  MSpecInterpIn=MSpecInterpI;
  for n=1:2:nshift
    MSpecInterpIn(end+1)=0;
    MSpecInterpIn(1)=[];
    EShift(end+1)=-DomainSpace*n;
    A(:,n+nshift)=MSpecInterpIn(nshift:end-nshift);
    W=diag((abs(A(:,n+nshift))).^Wp,0);
    C=(eM'*W*eM)\eM'*W*A(:,n+nshift);
    % Non-Negative Non-Linear least squares linear combination used if NonNeg is 1
    if NonNeg==1
      C=lsqnonneg(eM,A(:,n+nshift));
    end
    %Compute Composite Spectrum
    CompSpectra=SpectraInterpI*C;
    RMSE(nshift+n)=sqrt(sum((CompSpectra(nshift:end-nshift)-MSpecInterpIn(nshift:end-nshift)).^2)/length(CompSpectra(nshift:end-nshift)))/mean(CompSpectra(nshift:end-nshift));
  end
  EShift(end+1)=0;
  A(:,RMSE==0)=[];
  RMSE(RMSE==0)=[];
  [~,RM]=min(RMSE);
  %Report on the shift (in eV) that gives the best fit
  if RM<=nshift/2
    Shift=DomainSpace*RM;
  else if RM==nshift+1
      Shift=0;
    else if RM>nshift/2
        Shift=-1*DomainSpace*(RM-nshift/2);
      end
    end
  end
  %Extract Best Cropped Spectrum from A
  MSpecInterpIn=A(:,RM);
  %Create Corresponding Cropped Energy Vector
  MSpecInterpEn=MSpecInterpE(nshift:end-nshift,:);
  W=diag(abs(A(:,RM)).^Wp,0);
  C=(eM'*W*eM)\eM'*W*A(:,RM);
  % Non-Negative Non-Linear least squares linear combination used if NonNeg is 1
  if NonNeg==1
    C=lsqnonneg(eM,A(:,RM));
  end
  CFit=C;
  %Ratio Override
  if ~isempty(COveride)
    if COveride==0
      C=[.492;.462];
    else
      C=COveride'/sum(COveride);
```

```
        CCC(1,1)=1;
        for i=2:length(C)
            CCC(i,1)=C(i,1)/C(1,1)*Correction(1,1)/Correction(i,1);
        end
        C=CCC*sum(MSpecInterpI)/sum(SpectraInterpI*CCC);
    end
end

%Correct for effects of constituent Pressures/extintion distances
%Correction comes from first row of reference spectra data
CC(1,1)=1;
for i=2:length(C)
    CC(i,1)=C(i,1)/C(1,1)*Correction(i,1)/Correction(1,1);
end
%Normalize constituent ratios so that they sum to 1
CNorm=CC/sum(CC);
%Compute Composite Spectrum
CompSpectra=SpectraInterpI*C;
Residuals=MSpecInterpIn-CompSpectra(nshift:end-nshift);
size(Residuals)
RMSE_=sqrt(sum((CompSpectra(nshift:end-nshift)-MSpecInterpIn).^2)/length(CompSpectra(nshift:end-
nshift)))/mean(CompSpectra(nshift:end-nshift))
figure(1)
SpectraPlot=subplot(3,3,[1 2 3]);
hold off
LegendText={'Measured, Interpolated Spectrum','Composite Spectrum'};
LinesPlot=plot(SpectraPlot,MSpecInterpEn,MSpecInterpIn,Color{5},MSpecInterpEn,CompSpectra(nshift:end-
nshift),Color{6});
axis([min(MSpecInterpE),max(MSpecInterpE),0,1.1*max(MSpecInterpI)])
xlabel('Energy Loss (eV)')
ylabel('Intensity (arb units)')
title('Measured, Composite-Fit Spectra')
legend(LegendText)
delete(findobj('tag','ComponentNames'))
RefPlot=subplot(3,3,[4 5 6]);
axis(RefPlot,[min(MSpecInterpE),max(MSpecInterpE),0,1.1*max(max(SpectraI*RefPlotMult))])
h=figure(2);
set(h,'name','EELS Fitting Diagnostic Plots')
set(gcf,'OuterPosition',[fullscreen(3)/2 64 fullscreen(3)/2 fullscreen(4)-64])
clf (2)
subplot(2,3,[1 2])
hold on
plot(MSpecInterpEn,Residuals)
xlabel('Energy Loss (eV)')
ylabel('Fit Residuals')
title('Fit Residuals')
subplot(2,3,[4 5])
plot(EShift,RMSE,'o')
assignin('base','RMSEPlot',RMSE);
assignin('base','RMSEPlotE',EShift);
xlabel('Measured Spectrum Energy Shift (eV)')
ylabel('RMSE for Least Squares Fit')
title('Spectrum Shift Optimization')
MSpecInterpEnP=[MSpecInterpEn(1:ResFitCut1);MSpecInterpEn(ResFitCut2:end)];
```

```
    ResidualsP=[Residuals(1:ResFitCut1);Residuals(ResFitCut2:end)];
    Power3=@(a,b,c,x) 1000*(x-b).^c+a;
    ResFit=fit(MSpecInterpEnP,ResidualsP,'power2','startpoint',[1000,-4,-.1]);
    ResidualsF=ResidualsP-ResFit(MSpecInterpEnP);
    assignin('base','ResidualsP',ResidualsP)
    assignin('base','ResidualsE',MSpecInterpEnP)
    subplot(2,3,[1 2])
    plot(MSpecInterpEnP,ResidualsP,'r')
    plot(MSpecInterpEn,ResFit(MSpecInterpEn),'k')
    ResRatio=sum(abs(ResidualsP))/sum(abs(ResidualsF));
    subplot(2,3,[3 6])
    hold on
    axis([0,1.1*max(MSpecE),min(MSpecS),1.5*max(MSpecS)])
    plot(MSpecEO,MSpec,MSpecE,MSpecS)
    xlabel('Energy Loss (eV)')
    ylabel('Intensity')
    title('Peak Location Results')
    R=ResRatio>=RratioN;
    nshift=2*round(nshift/2);
    RMSe=RMSE;
    clear A
    clear RMSE
    clear EShift
    if R==0
        h=figure (1);
        set(h,'name','EELS Fitting Results')
        TextBox2=subplot(3,3,7);
        CString=cellstr(num2str(CNorm))';
        Y=(.25:-.05:0)*2;
        X=ones(length(Y),1)*.05;
        X2=X-.025;
        Components=text(X2(1:length(CNorm)),Y(1:length(CNorm)),strcat(CompNamesO,{'
'},CString),'units','normalized','parent',TextBox2,'tag','ComponentNames');
        set(gca,'visible','off')
    end
    figure(1)
    ErrorPlot=subplot(3,3,[8 9]);
    ErrorCurve=abs(CompSpectra-MSpecInterpI)./abs(MSpecInterpI)*100;
    span = 50;
    window = ones(span,1)/span;
    ErrorCurve = convn(ErrorCurve,window,'same');
    semilogy(Domain',ErrorCurve);
    axis([.9*min(Domain),1.1*max(Domain),10^-2,1000])
    xlabel('Energy Loss (eV)')
    ylabel('Error (%)')
    title('Normalized Error')
    set(gca,'YGrid','on')
    pause(.1)
    m=m+1;
end
%Collect data for output
CNorm=padarray(CNorm,4-length(CNorm),0,'post');
ResidualsP=padarray(ResidualsP,4000-length(ResidualsP),0,'post');
global RMSEs CNorms MeasSpecNames Wps nshifts MSpecEP MSpecP
```

```
if ~exist('RMSEs','var')
    RMSEs{1}=RMSE_;
    MeasSpecNames{1}=MeasSpecName;
    CNorms{1}=CNorm;
    ResidualsPs{1}=ResidualsP;
else
    MSpecEP{end+1}=MSpecInterpEn;
    MSpecP{end+1}=MSpecInterpIn;

    MeasSpecNames{end+1}={FName};
    Wps{end+1}=Wp;
    nshifts{end+1}=nshift;
    RMSEs{end+1}=RMSE_;
    CNorms{end+1}=CNorm;
    ResidualsPs(1).Ps=[];
    ResidualsPs(end+1).Ps=ResidualsP;
    assignin('base','Ref_Spec',SpectraInterpI)
    assignin('base','Meas_Spec',MSpecInterpI)
    assignin('base','CNorm',CNorm)
end
```

APPENDIX VI

CORE-LOSS EELS CODE

Core-loss quantification was similar to the low-loss method, and used a linear combination of reference spectra to fit the spectrum from a gas mixture. Like the low-loss code, the core-loss main code handles input of either a single spectrum, multiple spectra, a STEM-EELS data cube, or the data cube generated by the multiple EELS acquisition code referenced in section 3.3.4 (Mitchell and Schaffer, 2005). It then passes the resulting 1D EELS spectra to the function CL_EELS, which contains the core of the fitting functionality, as described below.

If the input is a multiple EELS acquisition code data cube, the MATLAB code integrates the 2D detector image in an intelligent way to reduce noise. The code first performs a median filter using a vertical (non-dispersive direction) 7 pixel region for the filter kernel; this vertical kernel ensures that the data is not distorted in the dispersive (horizontal) direction, but still filters out X-rays effectively. The filtered data is then summed in the dispersive direction to determine the row with maximum integrated intensity. The largest possible symmetric region around this maximum (as seen in Figure A 16) is then selected for the integration in the non-dispersive direction, resulting in a 1D spectrum. This reduces the amount of noise included in the integration when the intensity on the camera was not centered in the vertical (non-dispersive) direction.

For all the core-loss spectra, including the reference spectra, the backgrounds were fit with an inverse power law, which was then subtracted. The user is prompted to select the region over which to fit the background for each DM3 file. (This is in contrast to the low-loss method, where the backgrounds of the reference and mixture spectra are matched rather than subtracted, as described in section 3.3.4 and Appendix V). After background subtraction, a non-negative non-linear least squares approach was used to find the linear

combination of reference spectra from CO and CO_2 which best fit the mixture spectrum. Because core-loss spectra were often subject to slight misalignments causing the peaks to be broadened relative to their ideal width, the reference spectra were adjusted to account for this. As shown in the top of Figure A 18, a series of Gaussian functions were convolved with the reference spectra, causing them to be systematically broadened. Each set of broadened reference spectra was fit to the measured spectrum and the closest match was selected.

For each spectrum in a DM3 file, the linear combination fit is performed, and the residuals plotted in the lower graph of Figure A 17. Also plotted after each fit are the background subtracted spectrum compared to the fit spectrum, and compared to all the previous spectra from the DM3 file. Finally, after all spectra from the file have been fit, PCA (principle component analysis) is performed, and the first 3 components plotted, as seen in the bottom of Figure A 18. Unfortunately, unlike the low-loss code, the measured spectra are not shifted precisely by the core-loss code, so the 2^{nd} and 3^{rd} PCA components are mainly a result of the variously shifted spectra. To fix this the code would require extensive modification which has not been attempted.

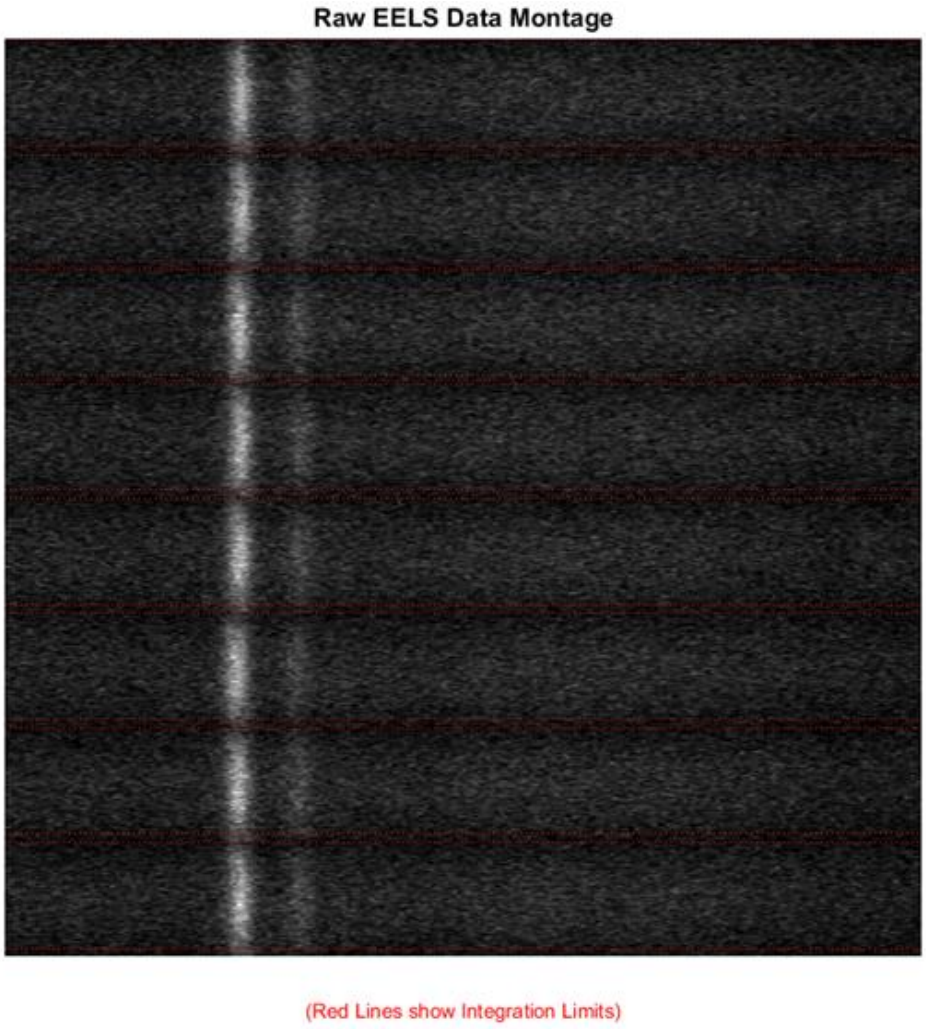

Figure A 16 EELS 2D Integration Limits. The MATLAB figure produced by the core-loss EELS code if data acquired using the multiple EELS script. The figure displays a series of up to 8 2D images of the detector, along with the vertical integration limits automatically determined by the code as red lines.

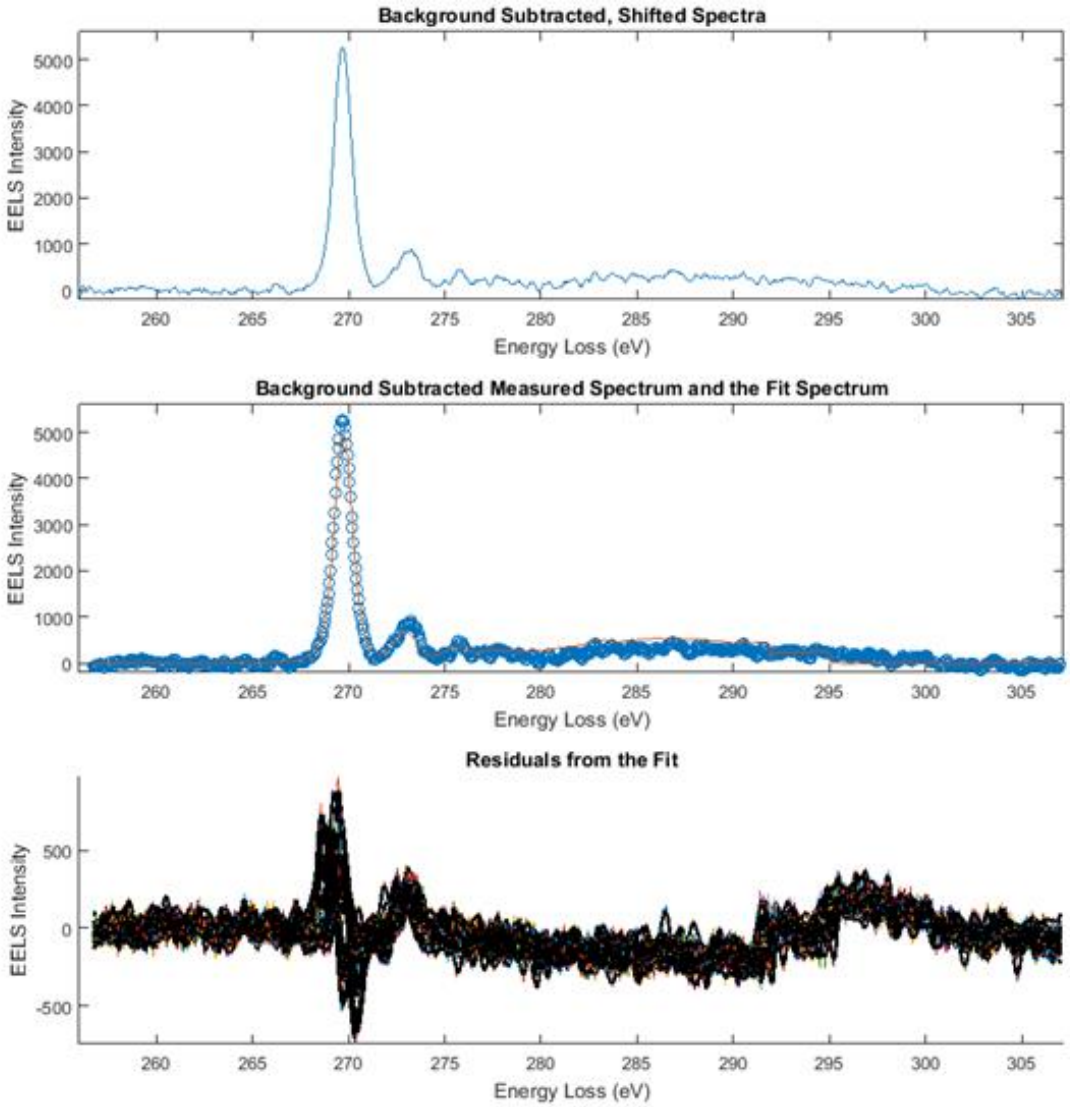

Figure A 17 EELS Core-Loss Code Figure 1. Top: single background subtracted spectrum. Middle: the same spectrum compared with the linear combination fit spectrum. Bottom: the residuals from fitting all 30 spectra contained in the selected DM3 file.

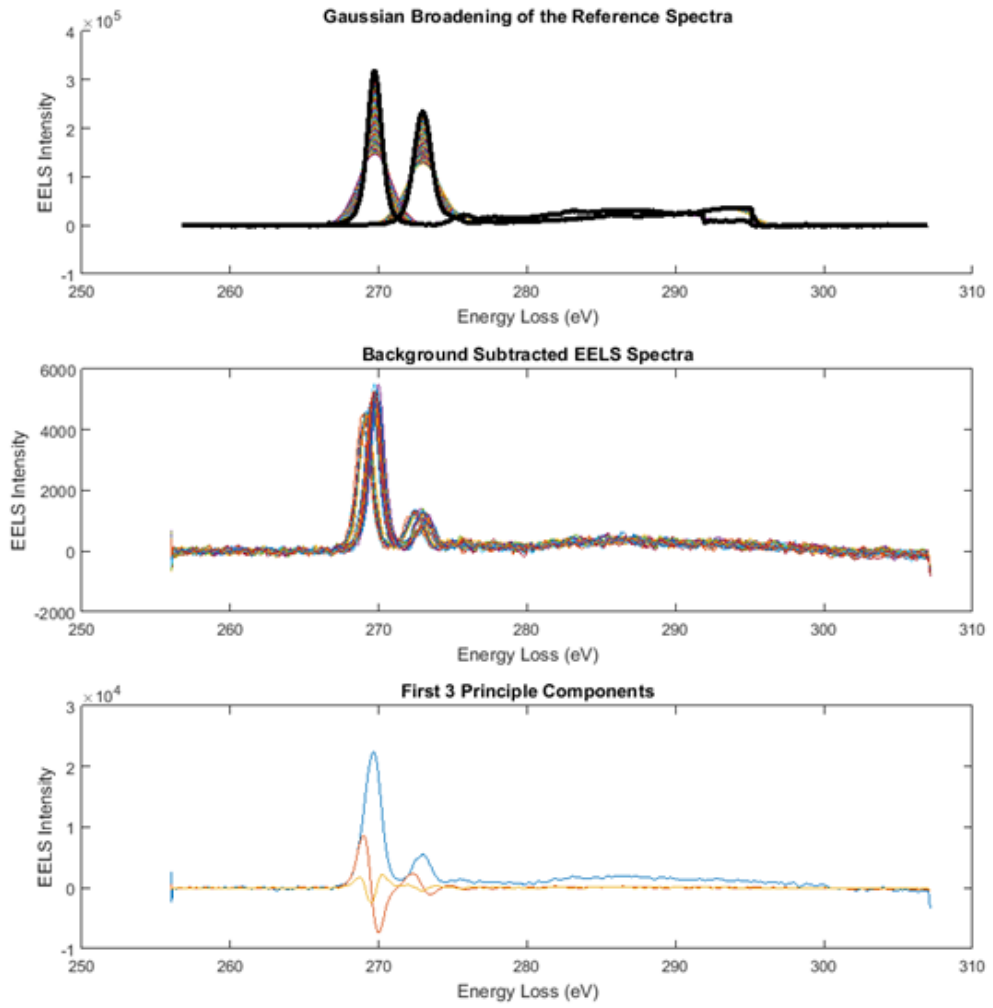

Figure A 18 EELS Core-Loss Code Figure 2. Top: A series of broadened reference spectra, with the matching broadening chosen shown in black. Middle: All 30 background subtracted EELS spectra from the selected DM3 file. Bottom: First 3 principle components from a PCA analysis of the 3O background subtracted spectra.

EELS_CL_Analysis MATLAB Code

```
%Code to analyze Core-loss EELS spectra
clear
close all
%Choose which type of file(s) you wish to analyze, by setting this
%parameter to 1, 2, 3, or 4
% 1: Single DM3
% 2: EELS Image DataCube DM3 (from MultipleEELS Code)
% 3: Spectrum Image
```

```
% 4: Multiple DM3 files
FileType=2;
%If NonNeg is set to 1, the fitting code uses a non-negative least squares
%algorithm
NonNeg=1;
%If WholeFolder is set to 1, the code will run for every DM3 file found in
%the directory selected by the user
WholeFolder=0;
%Set Path as a global variable
global Path
%Specify Reference Spectra file
RefData=xlsread('COCO2Reference');
%XXXXXXXXXXXXXXXXXXXXXXXXXXXXXXXXXXXXXXXXXXXXXXXXXXXXXXXXXXXXXXXXXXXXXXXX
XXX
%Now begin to extract measured data and call main computational function
if FileType==1
    %Select File using dialog box and after first instance keep opening from same
    %folder.
    if ~exist('Path','var')
        [FName,Path]=uigetfile({'*.dm3','Digital Micrograph File (dm3)'},'Select a DM3 file');
    end
    if Path==0
        [FName,Path]=uigetfile({'*.dm3','Digital Micrograph File (dm3)'},'Select a DM3 file');
    elseif exist('Path','var')
        [FName,Path]=uigetfile(strcat(Path,'*.dm3'),'Select a DM3 file');
    end
    %Use DM3Import Function (Robert McLeod) to get data from DM3
    DM3Data=DM3Import(strcat(Path,FName));
    %Get the EELS dispersion
    Dispersion=DM3Data.xaxis.scale;
    %Get the start energy (this is really not important, since the code
    %automatically shifts the energy calibration
    EStart=(DM3Data.xaxis.origin);
    if EStart<0;
        EStart=0;
    end
    %Get the EELS Spectrum!!
    MSpec=real(DM3Data.image_data);
    %Create the energy vector for the spectrum
    MSpecE=EStart:Dispersion:EStart+Dispersion*(length(MSpec)-1);
    %Run the EELS Core Loss fitting code
    [BGSSpec,BGSSpecE,CNorms,RMSEs,FNames]=CL_EELS(MSpecE',MSpec,RefData,FName,NonNeg,1);
end

if FileType==2
    % 1 out of AnalIntval spectra will be analyzed
    AnalIntval=1;
    % initialize this variable in case WholeFolder is not set to 1
    NumFilesLeft=1;
    %Specify the Dispersion
    Dispersion=.05;
    %Select File using dialog box and after first instance keep opening from same
    %folder.
    if ~exist('Path','var')
```

```
    [FName,Path]=uigetfile({'*.dm3','Digital Micrograph File (dm3)'},'Select an EELS Data Cube File');
end
if Path==0
    [FName,Path]=uigetfile({'*.dm3','Digital Micrograph File (dm3)'},'Select an EELS Data Cube File');
elseif exist('Path','var')
    [FName,Path]=uigetfile(strcat(Path,'*.dm3'),'Select an EELS Data Cube File');
    if WholeFolder==1
        DirStruct=dir(Path);
        NumFilesLeft=size(DirStruct,1)-2;
    end
end
%loop once for every file in the folder if WholeFolder is set to 1
while NumFilesLeft>0

    if WholeFolder==1
        %Set the file name to the next name in the directory
        FName=DirStruct(NumFilesLeft+2).name;
    end
    %Read the size of the Data from the DM3 file
    CubeSize=ReadDM3_size(strcat(Path,FName));
    for i=1:CubeSize(3)
        %Read the data from the DM3 file
        DataCubeO(:,:,i)=ReadDM3_slice(strcat(Path,FName),CubeSize,i);
        %Because ReadDM3_slice is reading using improper format, negative
        %numbers must be set to 0 (else they are read as very large numbers)
        DataCubeO(:,:,i)=DataCubeO(:,:,i).*uint16(~(DataCubeO(:,:,i)>16385));
        %Median filter the images, taking the median from a vertical
        %column of 7 pixels (this is better than taking the median from
        %a square region for this EELS data.)
        DataCubeMed(:,:,i)=medfilt2(DataCubeO(:,:,i),[7,1]);
        %For the first up to 8 spectra, save the 2D display so that
        %they can be displayed in a figure
        if i<9
            DataCubeDisp(:,:,1,i)=DataCubeMed(:,:,i);
        end
    end
    %Figure 1 shows the original 2D data, along with the integration
    %range used
    figure(1)
    %Display the data
    montage(imrotate(mat2gray(DataCubeDisp),90))
    %Find the maximum pixel row in the non-dispersive direction
    IntP=sum(DataCubeMed,1);
    IntP=sum(IntP,3);
    [~,IntM]=max(IntP);
    %Number of non-dispersive channels to integrate (actual integration
    %uses IntRange+1 channels
    IntRange=(min(IntM,CubeSize(2)-IntM)-1)*2;
    %Integration Limits
    IntLims=[IntM-round(IntRange/2),IntM+round(IntRange/2)];
    %Integrate the data between the integration limits
    Spectra=squeeze(sum(DataCubeMed(:,IntLims(1):IntLims(2),:),2));
    %Create a dummy energy loss vector starting at 0
    MSpecE=(0:Dispersion:Dispersion*(CubeSize(1)-1))';
```

```
    %Plot lines on figure 1 to show where the
    %integration limits were set in the non-dispersive direction
    for i=1:CubeSize(3)
       %Set positions
       HlinePos(2*i)=IntLims(2)+length(IntP)*(i-1);
       HlinePos(2*i-1)=IntLims(1)+length(IntP)*(i-1);
    end
    %Plot lines
    hline(1+(size(DataCubeMed,2)*size(DataCubeMed,3))-HlinePos)
    %Figure 1 text
    title('Raw EELS Data Montage','fontsize',14)
    xlabel('(Red Lines show Integration Limits)','color','r')
    %Run the EELS Core Loss fitting code once for every AnalIntval spectrum
    figure(2)
    for i=1:AnalIntval:CubeSize(3)
       %Extract the current measured spectrum
       MSpec=Spectra(:,i)';
       %Run Fitting Code
       [BGSSpec(:,i),BGSSpecE(:,i),CNorms,RMSEs,FNames]=CL_EELS(MSpecE,MSpec,RefData,FName,NonNeg,i);
    end
    %Plot the Background Subtracted Spectra from the DM3 file in Figure 3

    figure(3)
    subplot(3,1,2)
    plot(BGSSpecE,BGSSpec)
    title('Background Subtracted EELS Spectra')
    xlabel('Energy Loss (eV)')
    ylabel('EELS Intensity')
    %Compute principle components from the Background subtracted
    %spectra
    [coeff,PCAComp,latent]=pca(BGSSpec,'centered',false);
    %Also Plot the first 3 principle components in Figure 3
    figure(3)
    subplot(3,1,3)
    plot(BGSSpecE(:,1:3),PCAComp(:,1:3))
    title('First 3 Principle Components')
    xlabel('Energy Loss (eV)')
    ylabel('EELS Intensity')
    %Update the NumFilesLeft index
    NumFilesLeft=NumFilesLeft-1;

  end
  for i=1:size(CNorms,1)
     CNs(i,:)=CNorms{i};
  end
  if std(CNs)~=0
     SpecIndex=[1:size(CNs,1)]'*[1,1];
     figure(4)
     plot(SpecIndex,CNs)
     xlabel('Spectrum Number')
     ylabel('Mol Fraction CO, CO2')
     legend({'CO2','CO'})
  end
end
```

```
if FileType==3
   %Select File using dialog box and after first instance keep opening from same
   %folder.
   if ~exist('Path','var')
      [FName,Path]=uigetfile({'*.dm3','Digital Micrograph File (dm3)'},'Select a DM3 Spectrum Image file');
   end
   if Path==0
      [FName,Path]=uigetfile({'*.dm3','Digital Micrograph File (dm3)'},'Select a DM3 Spectrum Image file');
   end
   if exist('Path','var')
      [FName,Path]=uigetfile(strcat(Path,'*.dm3'),'Select a DM3 Spectrum Image file');
   end
   addpath(Path);
   DM3Data=DM3Import(FName);
   Dispersion=DM3Data.xaxis.scale;
   MSpecCube=DM3Data.image_data;
   CubeSize=size(MSpecCube);
   MSpecE=(0:Dispersion(1):Dispersion(1)*(CubeSize(3)-1));
   counter=1;
   for i=1:CubeSize(1)
      for j=1:CubeSize(2)
         MSpec=MSpecCube(i,j,1:CubeSize(3));
         MSpec=MSpec(:)';
         %Give the user an indication of how far the script has progressed
         disp(strcat('Processing Spectrum #',num2str(counter),{' out of '},num2str(CubeSize(1)*CubeSize(2))))
         [BGSSpec,BGSSpecE,CNorms,RMSEs,FNames]=CL_EELS(MSpecE,MSpec,RefData,FName,NonNeg,counter);
         counter=counter+1;
         %Place the output values from the EELS code for each SI pixel into matrices
         BGSSpecCube(j,i,:)=BGSSpec;
         BGSSpecECube(j,i,:)=BGSSpecE;
      end
   end
   figure(6)
   BGSC=reshape(BGSSpecCube,[size(BGSSpecCube,1)*size(BGSSpecCube,2),1024])';
   BGSEC=reshape(BGSSpecECube,[size(BGSSpecCube,1)*size(BGSSpecCube,2),1024])';
   plot(BGSEC(:,1),mean(BGSC,2))
   axis([min(BGSSpecECube(:)),max(BGSSpecECube(:)),median(BGSSpecCube(:))-
std(BGSSpecCube(:))/2,max(BGSSpecCube(:))+std(BGSSpecCube(:))/2])
   figure(7)
   title('First 3 Principle Components')
   [C,PCAComp,L]=pca(BGSC,'centered',false,'numcomponents',5);
   plot(BGSEC(:,1),sum(PCAComp(:,2:5),2))
   axis([min(BGSSpecECube(:)),max(BGSSpecECube(:)),median(BGSSpecCube(:))-
std(BGSSpecCube(:))/2,max(BGSSpecCube(:))+std(BGSSpecCube(:))/2])
end

if FileType==4
   if ~exist('Path','var')
      [FName,Path]=uigetfile({'*.dm3','Digital Micrograph File (dm3)'},'Select Multipe DM3 files containing single
spectra','multiselect','on');
   end
   if Path==0
      [FName,Path]=uigetfile({'*.dm3','Digital Micrograph File (dm3)'},'Select Multipe DM3 files containing single
spectra','multiselect','on');
```

```
    end
    if exist('Path','var')
        [FName,Path]=uigetfile(strcat(Path,'*.dm3'),'Select Multipe DM3 files containing single spectra','multiselect','on');
    end
    NumSpec=length(FName);
    if ~strcmp(class(FName),'cell')
        error('To select one spectrum, please use FileType 1 (EELS_LL_Analysis: Line 8)')
    end
    %Run the EELS Low Loss fitting code once for every spectrum
    for i=1:NumSpec
        DM3Data=DM3Import(strcat(Path,FName{i}));
        %Get the EELS dispersion
        Dispersion=DM3Data.xaxis.scale;
        %Get the start energy (this is really not important, since the code
        %automatically shifts the energy calibration
        EStart=(DM3Data.xaxis.origin);
        %Get the EELS Spectrum!!
        MSpec=real(DM3Data.image_data);
        NumChannels=length(MSpec);
        %Create the energy vector for the spectrum
        MSpecE=EStart:Dispersion:EStart+Dispersion*(length(MSpec)-1);
        %Give the user an indication of how far the script has progressed
        disp(strcat('Processing DM3 file #',num2str(i),{' out of '},num2str(NumSpec)))
        %Run the EELS Core Loss fitting code
        [BGSSpec,BGSSpecE,CNorms,RMSEs,FNames]=CL_EELS(MSpecE,MSpec,RefData,FName,NonNeg);
        %Run the EELS Core Loss fitting code, without any graphical output
        %[T,BGSSpec,CNorms,RMSEs,FNames]=evalc('CL_EELS(MSpecE,MSpec,RefData,FName,NonNeg)');
    end
end
```

3rd Party Codes Used: DM3Import, hline, ReadDM3_size, ReadDM3_slice

CL_EELS MATLAB Function

```
function [BGSSpec,BGSSpecE,CNorms,RMSEs,FNames]=CL_EELS(MSpecE,MSpec,RefData,FName,NonNeg,I)
%Inputs
%MSpecE -      Energy loss values of the measured spectrum
%MSpec -       Intensity values of the measured spectrum
%RefData -     Reference Spectra
%FName -       File Name of EELS data
%NonNeg -      1 if the code should use a non-negative non-linear algorithm
%I -           Index indicating if this is the first spectrum from the
              %data file which has been passed to this function

%Outputs
%BGSSpec -     Background Subtracted Spectrum intensities
%BGSSpecE -    Background Subtracted Spectrum energy losses
%CNorms -      gas composition computed
%RMSEs -       Root mean squared error of the least squares fit
%FNames -      File name of EELS Data
```

```
%User-Set Parameters XXXXXXXXXXXXXXXXXXXXXXXXXXXXXXXXXXXXXXXXXXXXXXXXXXXXXX
%XXXXXXXXXXXXXXXXXXXXXXXXXXXXXXXXXXXXXXXXXXXXXXXXXXXXXXXXXXXXXXXXXXXXXXXXXXXXX
%If this line is not commented out, the code will assume analysis of CO/CO2
SpecIsCarbonk=1;
%Full width half max (in data points, not eV) to be used for fitting of peaks in auto-alignment
FWHM=24;
%Number of interpolated points per actual data point for peak fitting
PeakInterpMult=20;
%True Peak position (eV) of the peak that will be fitted and aligned
TruePeakPos=285;
%Specify the Dispersion
Dispersion=abs(MSpecE(2)-MSpecE(1));
CO_CO2_PeakSep=65;
global ResidualLims
%Fit the main Peak in the EELS Core Loss Spectrum
%Find the maximum point in each EELS spectrum
[SpecMax,MaxI]=max(MSpec);
if MaxI~=1
    %Set the limits for the peak fitting for each spectrum
    PeakLimitsR=[MaxI-round(FWHM/2);MaxI+round(FWHM/2)];
    %Extract the portion of the measured spectrum around the largest peak
    MSpecPeak=MSpec(PeakLimitsR(1):PeakLimitsR(2));
    %Extract the portion of the energy spectrum around the largest peak
    MSpecPeakE=MSpecE(PeakLimitsR(1):PeakLimitsR(2))';
    %Create a new energy vector with PeakInterpMult times as many points as MSpecPeakE
    MSpecPeakEInterp=(MSpecE(PeakLimitsR(1)):Dispersion/PeakInterpMult:MSpecE(PeakLimitsR(2)))';
    %Calculate numerical second derivative around peak
    MSpecPeakDer=diff(MSpecPeak,2);
    %Find where the second derivative is positive
    DerLogic=MSpecPeakDer>0;
    %Pad, since the second derivative has fewer points than the original data
    DerLogic=logical([1,DerLogic,1]);
    %Fit the peak data with a parabola where the second derivative is negative
    [PeakFit,PFitQual]=fit(MSpecPeakE',log(MSpecPeak'),'poly2','exclude',DerLogic','normalize','on');
    %Extract, store the R-squared goodness-of-fit parameter of the peak fit
    R2=PFitQual.rsquare;
    %Find (the index) where the fit's peak is
    [~,PIInterp]=max(PeakFit(MSpecPeakEInterp));
    %Extract the energy in eV where the peak maximum is
    PeakEInterp=MSpecPeakEInterp(PIInterp);
    %Find the nearest point in the MSpecE vector to the precise peak position
    PeakE=Dispersion*(round(PeakEInterp/Dispersion));
    if min(R2)<.65
        warning('Peak fitting of at least one spectrum is not good')
    end
    %Calculate the number of indices to shift the spectrum
    Shift=round((TruePeakPos-PeakE)/Dispersion);
    %Shift the measured spectrum by [Shift] indices
    MSpecShift=circshift(MSpec,Shift);
    %clear derlogic, because it's size is different for each peak
    clear DerLogic
else
    MSpecShift=MSpec;
end
```

```
%Fit the background before the peaks, subtract BG
%Find the peak maximum based on a sum of all the (shifted) spectra from the cube
[~,PI]=max(sum(MSpecShift,1));
pause(.02)
F2=figure(2);
fullscreen = get(0,'ScreenSize');
set(F2,'OuterPosition',[0 64 fullscreen(3)/2 fullscreen(4)-64])
set(F2,'name','EELS Core Loss Fitting Plots')
%Have user input the range for background fitting from the plot
global BGLimits
if exist('i')
    if I==1
        F21=subplot(3,1,1);
        plot(F21,MSpecShift)
        ylabel('EELS Intensity')
        xlabel('Index')
        title('Select Range for Background Fit')
        [BGLimits,~]=ginput(2);
        %Sort and round the limits (indices) to the nearest integer
        BGLimits=sort(round(BGLimits));
    end
else
    subplot(3,1,1)
    plot(F21,MSpecShift)
    ylabel('EELS Intensity')
    xlabel('Index')
    title('Select Range for Background Fit')
    [BGLimits,~]=ginput(2);
    %Sort and round the limits (indices) to the nearest integer
    BGLimits=sort(round(BGLimits));
end
%Fit the background with a power law
BGfit=fit(MSpecE(BGLimits(1):BGLimits(2),1),MSpecShift(BGLimits(1):BGLimits(2))','power1');
%Extrapolate intensity values of fit to all the energy values in MSpecE
BG=BGfit(MSpecE)';
%set any NAN values in BG to 0
BG(isnan(BG))=0;
%Subtract the extrapolated background from the shifted data
MSpecBGS=MSpecShift-BG;
%Produce a calibrated Energy vector
MSpecECal=MSpecE+(285-29);
%Plot the background subtracted, and aligned measured spectra
subplot(3,1,1)
plot(MSpecECal(2:end),MSpecBGS(2:end))
title('Background Subtracted, Shifted Spectra')
xlabel('Energy Loss (eV)')
ylabel('EELS Intensity')
axis([min(MSpecECal),max(MSpecECal),median(MSpecBGS)-std(MSpecBGS)/2,max(MSpecBGS)+std(MSpecBGS)/2])
BGSSpec=MSpecBGS;
BGSSpecE=MSpecECal;
%CO Oxidation AnalysisXXXXXXXXXXXXXXXXXXXXXXXXXXXXXXXXXXXXXXXXXXXXXXXXXXXXX
%XXXXXXXXXXXXXXXXXXXXXXXXXXXXXXXXXXXXXXXXXXXXXXXXXXXXXXXXXXXXXXXXXXXXXXX
XXX
%If the variable SpecIsCarbonk exists, then the code will analyze the
```

```
%spectra assuming CO oxidation is occuring
if exist('SpecIsCarbonk')
   % Read, Shift the Reference Spectra Data for CO, CO2
   %read the xls file
   %Get the data for the 2 spectra
   CO2Spec=RefData(:,1);
   COSpec=RefData(:,2);
   %Find the index of the CO spectrum peak
   [~,RefPeak(1)]=max(COSpec);
   %Shift the reference spectra to match the measured peak position
   COSpecShift=circshift(COSpec,-(RefPeak(1)-PI));
   CO2SpecShift=circshift(CO2Spec,-(RefPeak(1)-PI-CO_CO2_PeakSep));
   %If the CO2 peak is larger than the CO peak, shift the spectra further
   Peak2=findpeaks(smooth(MSpecBGS(MaxI-90:MaxI-40),20,'sgolay',2),'NPeaks',1);
   if Peak2>.1*SpecMax
      COSpecShift=circshift(COSpecShift,-CO_CO2_PeakSep);
      CO2SpecShift=circshift(CO2SpecShift,-CO_CO2_PeakSep);
   end
   AO=[CO2SpecShift,COSpecShift];
   % Perform a Linear Combination Fit Using Reference Spectra XXXXXXXXXXX

%XXXXXXXXXXXXXXXXXXXXXXXXXXXXXXXXXXXXXXXXXXXXXXXXXXXXXXXXXXXXXXXXXXXXXXXXXXXXXXXXXXXXXXX
   % Shift the Measured Spectrum More Precisely
   %Choose the limits for the reference fitting
   FitLim=[BGLimits(1),length(COSpec)-3];
   %Determine ideal spectrum shift
   for i=1:15
      A_ISS=circshift(AO,i-8);
      A_ISS=A_ISS(FitLim(1):FitLim(2),:);
      B_ISS=MSpecBGS(FitLim(1):FitLim(2))';
      C_ISS=A_ISS\B_ISS;
      Resid_ISS=B_ISS-A_ISS*C_ISS;
      RMSE_ISS(i)=sqrt(mean(Resid_ISS.^2))/mean(B_ISS);
   end
   [~,MS]=min(RMSE_ISS); MS=-(MS-8);
   MSpecFit=circshift(MSpecBGS,MS)';
   MSpecFit=MSpecFit(FitLim(1):FitLim(2));
   % Fit Residuals, Subtract From Measured Spec
   FitE=MSpecE(FitLim(1):FitLim(2));
   FitECal=MSpecECal(FitLim(1):FitLim(2));
   C_RF=AO(FitLim(1):FitLim(2),:)\MSpecFit;
   Exclude=FitE<35 & FitE>25;
   ResFit=fit(FitE,MSpecFit-AO(FitLim(1):FitLim(2),:)*C_RF,'power2','exclude',Exclude);
   MSpecFit_RF=MSpecFit-ResFit(FitE);
   % Find ideal gaussian blur to apply to Reference Spectra
   F3=figure(3);
   set(F3,'name','Additional EELS Core Loss Fitting Plots')
   set(gcf,'OuterPosition',[fullscreen(3)/2 64 fullscreen(3)/2 fullscreen(4)-64])
   F31=subplot(3,1,1);
   cla(F31)
   hold on
   A_GB_All=[];
   for i=1:100
      Gauss=gausswin(i);
```

```
        Gauss=Gauss/sum(Gauss);
        A_GB=[conv(CO2SpecShift(FitLim(1):FitLim(2)),Gauss,'same'),conv(COSpecShift(FitLim(1):FitLim(2)),Gauss,'same')];
        B_GB=MSpecFit_RF;
        C_GB=A_GB\B_GB;
        Resid_GB=B_GB-A_GB*C_GB;
        RMSE_GB(i)=sqrt(mean(Resid_GB.^2))/mean(B_GB);
        A_GB_All=[A_GB_All,A_GB];
    end
    plot(FitECal,A_GB_All)
    title('Gaussian Broadening of the Reference Spectra')
    xlabel('Energy Loss (eV)')
    ylabel('EELS Intensity')
    [~,MGB]=min(RMSE_GB);

A_Final=[conv(CO2SpecShift(FitLim(1):FitLim(2)),gausswin(MGB)/sum(gausswin(MGB)),'same'),conv(COSpecShift(FitLim(1
):FitLim(2)),gausswin(MGB)/sum(gausswin(MGB)),'same')];
    plot(FitECal,A_Final,'k','linewidth',3)
    C_Final=A_Final\B_GB;
    if NonNeg==1
        C_Final=lsqnonneg(A_Final,B_GB);
    end
    FinalFit=A_Final*C_Final;
    CNorm=C_Final/sum(C_Final);
    RMSE=sqrt(mean((MSpecFit_RF-FinalFit).^2))/mean(MSpecFit_RF);
    %Plotting Results
    F2=figure(2);
    subplot(3,1,2)
    pause(.02)
    plot(FitECal,sum(MSpecFit_RF,2),'o',FitECal,sum(FinalFit,2))
    title('Background Subtracted Measured Spectrum and the Fit Spectrum')
    xlabel('Energy Loss (eV)')
    ylabel('EELS Intensity')
    axis([min(MSpecECal),max(MSpecECal),median(MSpecBGS)-std(MSpecBGS)/2,max(MSpecBGS)+std(MSpecBGS)/2])
    F2=figure(2);
    subplot(3,1,3)
    hold on
    FinalFitResiduals=MSpecFit_RF-FinalFit;
    ResidualLims=[ResidualLims;[min(FinalFitResiduals(:)),max(FinalFitResiduals(:))]];
    plot(FitECal,FinalFitResiduals)
    plot(FitECal,smooth(mean(FinalFitResiduals,2)),'k','linewidth',2)
    title('Residuals from the Fit')
    xlabel('Energy Loss (eV)')
    ylabel('EELS Intensity')
    axis([min(MSpecECal),max(MSpecECal),min(ResidualLims(:,1)),max(ResidualLims(:,2))])
else
    CNorm=1;
    RMSE=1;
    FNameM=FName;
end
% Save Global Variables
global CNorms FNames RMSEs
CNorms=[CNorms;{CNorm'}];
FNames=[FNames;{FName}];
RMSEs=[RMSEs;{RMSE'}];
```

APPENDIX VII

DIFFRACTOGRAM ANALYSIS AND IMAGE REGISTRATION CODE

A MATLAB code was written for performing Fourier filtering and measurement of image spacings with sub-pixel accuracy. The code begins by letting the user choose a DM3 file to open; this file can contain either a single image frame, or multiple image frames. A dialog opens, and the image calibration can be specified by the user, or the calibration in the DM3 file can be retained. If the file contains a single image frame, the code recognizes this and skips image registration. If multiple image frames are present, the user is asked whether the frames should be analyzed using image registration. If the user does not request image registration, the user is prompted to select which of the image frames to use for the diffractogram analysis.

If image registration is requested, the code calls the ImageRegMutualInfo function written for this purpose two times. The first call to this image registration function begins with a rough alignment of the entire image using an efficient Fourier-space technique called phase correlation (Zitová and Flusser, 2003); this ensures that large shifts due to severe sample drift are corrected. The registration function then sets various parameters used by MATLAB's built-in image registration function, which is set in the code to use a mutual information based metric. The results of this registration are displayed to the user by cycling through the series of un-registered and registered frames shown side-by-side. The code then outputs a montage, as seen in Figure A 19 where the difference between the first (fixed) and subsequent (registered) frames is shown. An averaged image is also shown, and the user prompted to select a region of the image for further, more precise alignment. This region is then passed back to the ImageRegMutualInfo function and this second call skips the rough phase-correlation alignment, and uses different parameters for a more precise, and computationally intensive alignment of this small region. The results of this alignment

are again displayed as a series of cycled image frames, so that the user can visually appraise the effectiveness of the alignment, and a second montage (also shown in Figure A 19) is output. It is clear from Figure A 19 that this second pass by the image registration code significantly improves the alignment. The user is now prompted to select which of the aligned frames to include in an averaged image which will be used for the rest of the code; this allows frames which were not correctly aligned to be excluded from the averaged image. An averaged image obtained from 5 frames using this code is shown compared with a single frame in Figure 4-4 of the text. A larger view of the averaged image in grayscale is shown in Figure A 20.

Now, whether a single frame DM3 file was opened, or a single frame selected from those contained in the file, or the frames aligned and averaged, a single image frame remains. The user is now prompted to select a region of interest from this image to be used to compute the diffractogram by clicking on points in the image that define a polygon. This allows a region of arbitrary shape to be selected, so that individual particles may be outlined, and adjacent regions excluded. If the user right clicks on the image instead, the entire displayed region is used. It should be noted here that if a polygonal region of interest is selected, care should be taken in the interpretation of the diffractogram, since large diagonal edges will result in artifacts the diffractogram, as shown in Figure A 21. Rectangular regions of interest do not result in this type of artifact, because the region of interest is padded with zeros to fill a rectangular area to which a rectangular Hann window (Blackman and Tukey, 1958) is applied prior to computation of the diffractogram, reducing the effect of rectangular edges. The resulting rectangular area with the Hann window applied is then padded with zeros to fill a square region which is $2^n x 2^n$ where n is chosen

to minimize the amount of padding needed. The FFT is computed using the built-in MATLAB function, and the result is multiplied by its complex conjugate to obtain the diffractogram, which is displayed in a new MATLAB plot.

The user is now prompted to select points to be measured in the diffractogram by dragging rectangular boxes around the desired spots. The code uses the algorithm described by de Ruijter (de Ruijter et al., 1995) to find the maximum intensity position with sub-pixel accuracy. Using the image calibration, the exact fringe spacing is calculated. As many points as desired can be selected, and mistakenly selected spots can be deleted, as seen in Figure A 22. An image of this annotated diffractogram is saved for future reference, as are the fringe spacings, intensities, and angles between spacings. The first 3 spots selected by the user are used to produce filtered images, shown in Figure A 23. These are produced by retaining only a small square region of the original FFT around each selected spot which is $1/64^{th}$ the size of the diffractogram; this is multiplied by a Gaussian filter to emphasize the central point in the small region, and the inverse FFT computed. Above each filtered image, shown in Figure A 23 the measured spacing is labeled. If the user zooms in on any of the four images in the MATLAB figure, all 4 are similarly zoomed automatically, as seen in Figure 4-6 of the text.

Next, the diffractogram is further processed to emphasize spots from fringe spacings and remove the intensity resulting from amorphous material in the image, as well as the central peak. The resulting processed diffractogram is shown in Figure A 24. This is achieved by first subtracting a simple mean background intensity computed iteratively in a similar (but simpler) way to the background determination described in Appendix III. This results in some pixels having a negative value. These are set to 0. A rotational average

is then applied to the data, and pixels outside a circle inscribed in the FFT square are also set to zero. The rotational average profile is then fit by 4 Gaussian functions, and this fit is then subtracted from the diffractogram. The mean value of all the positive pixels is then multiplied by 3, and this is used as a noise floor, below which all positive pixels are set to 0. Negative values whose magnitudes are larger than 2 times this noise floor are set to -2 times the noise floor. This somewhat complicated procedure seems to do a good job of retaining peaks in the diffractogram while removing the central spot and most of the amorphous contrast. Finally, important information generated by the code is placed in a data structure and saved in a .mat file. This includes information on the region of interest including the image pixels, information on the measured fringe spacings, and an annotated image of the diffractogram figure. If image registration was performed, an average image as well as a tiff containing all the registered frames is also saved.

For more analysis of many different spots, and comparison of these to calculated lattice spacings, an additional MATLAB code, called DM3FringeFurtherAnalysis can subsequently be run. This code uses the image, diffractogram, and FFT calculated by DM3FringeAnalysis, but is capable of importing CIF files of crystal structures, calculating possible spacings from those structures and then matching the spacings measured in the diffractogram to the calculated spacings. The interactive figure produced by this code is shown in Figure 4-7 of the text. If the user does not have a CIF file of the crystal structure, lattice parameters and angles may also be entered manually. The calculation of spacings by the CrystalSpacings function does not include calculation of the structure-factors, and so does not consider the possibility of forbidden spacings, nor does it calculate the

probability of the spacings it computes. The code merely uses the general form of the reciprocal metric tensor to calculate the d-spacings, given lattice parameters and angles.

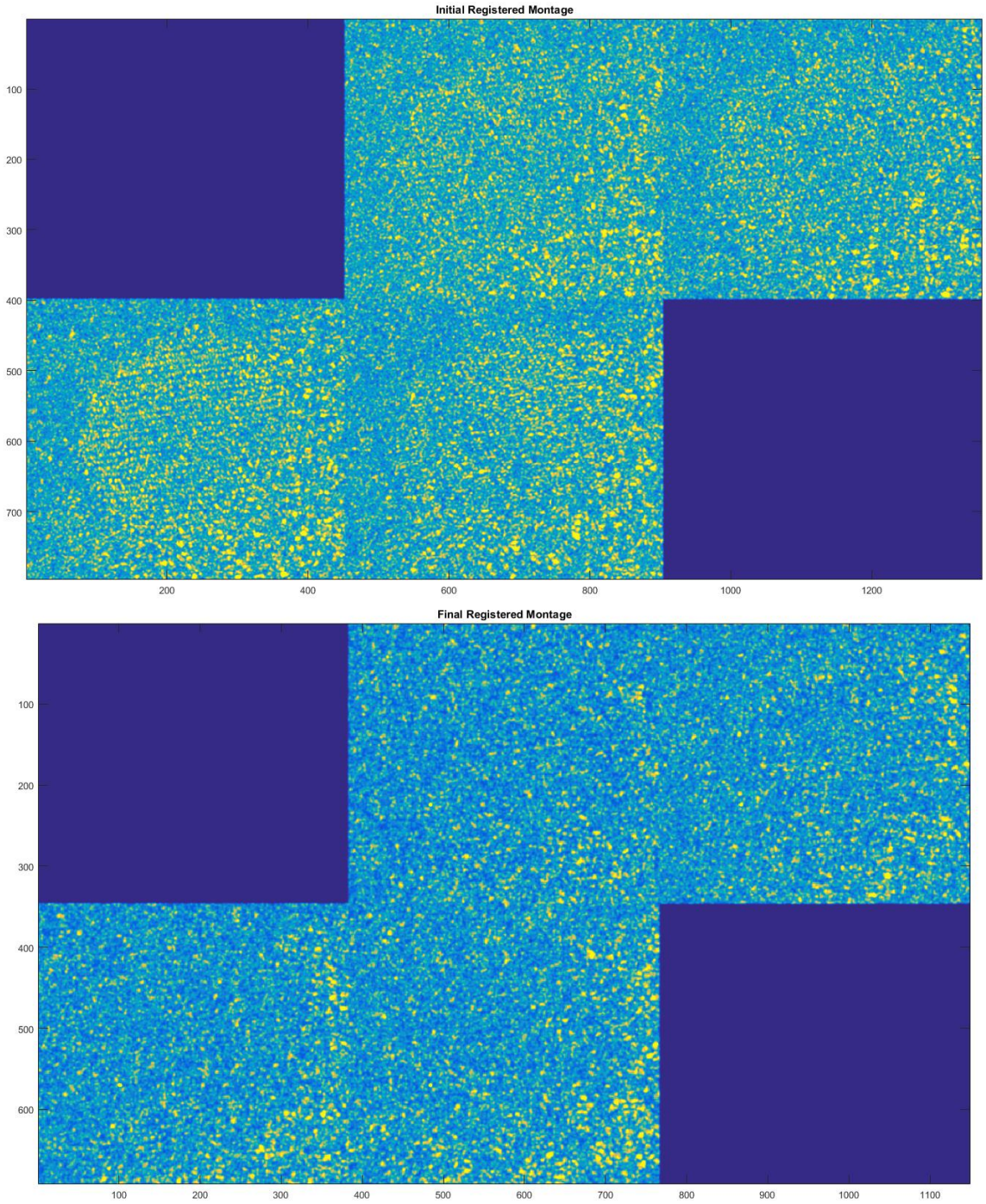

Figure A 19 Montages of Registered Frames. Top: Montage of registered frames produced during the first call to the ImageRegMutualInfo function, showing rough alignment. Bottom: Montage of registered frames from the second call to the ImageRegMutualInfo function, showing better alignment. Each montage is a difference between the first frame and each frame in the DM3 file (note that the first frame difference is exactly 0 at all pixels).

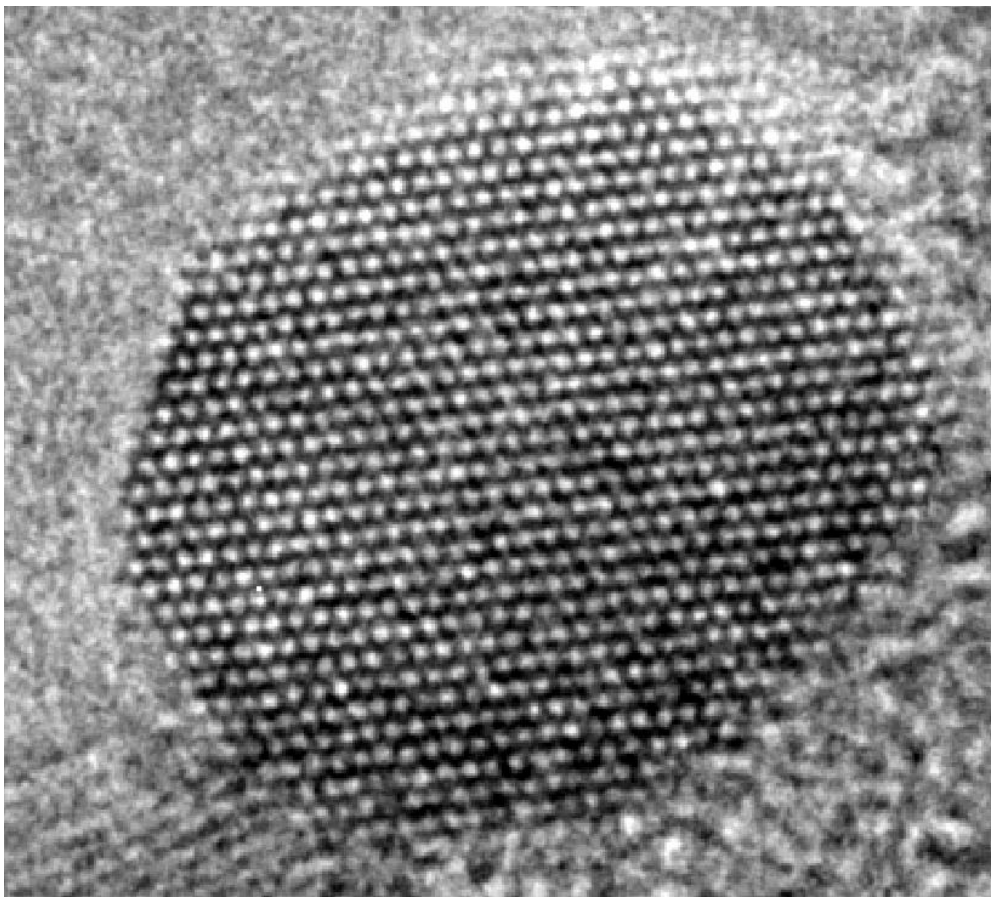

Figure A 20 Aligned, Averaged Image. The averaged image produced from the aligned frames selected by the user. A region of interest in this image is used to calculate the diffractogram.

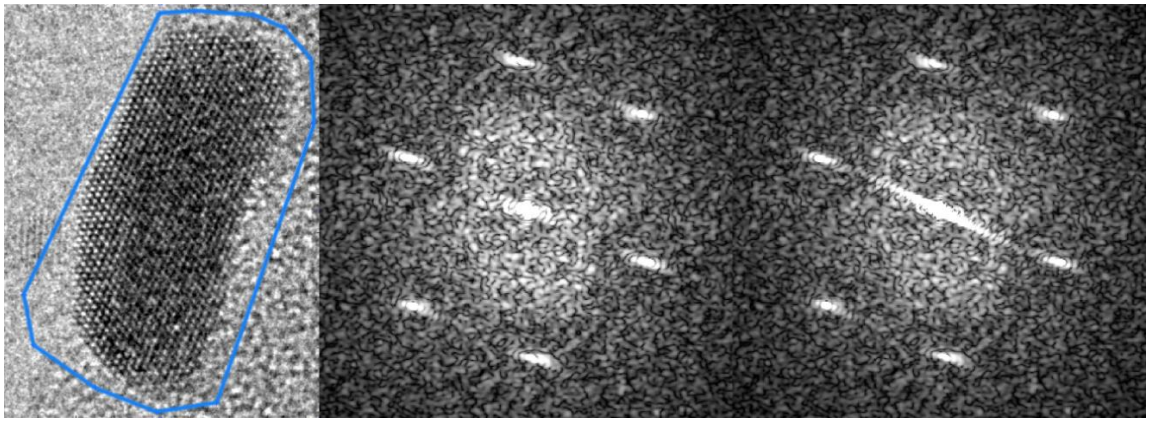

Figure A 21 Diffractogram ROI Artifact. Left: Image with polygonal region of interest (ROI) around particle. Center: Diffractogram produced from the entire displayed image region. Right: Diffractogram produced using only the area within the region of interest, showing a streaking artifact from the abrupt diagonal edges of the ROI.

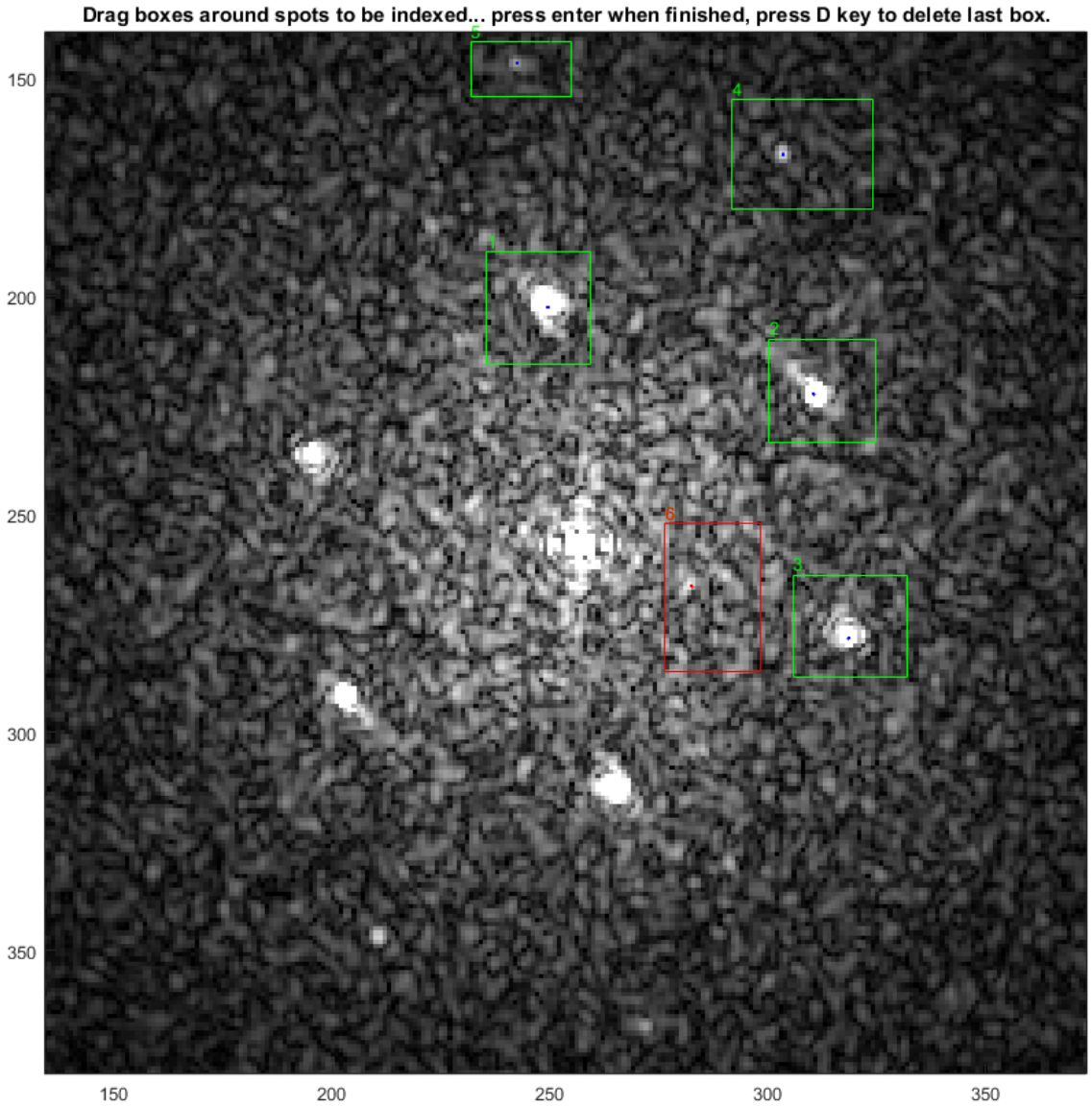

Figure A 22 Measured Diffractogram. A diffractogram with 5 spots measured to sub-pixel accuracy. A 6th spot was mistakenly selected, and deleted (red). The first 3 spots selected are used to produce the filtered images, shown in Figure A 23. Only the central portion of the diffractogram is displayed here.

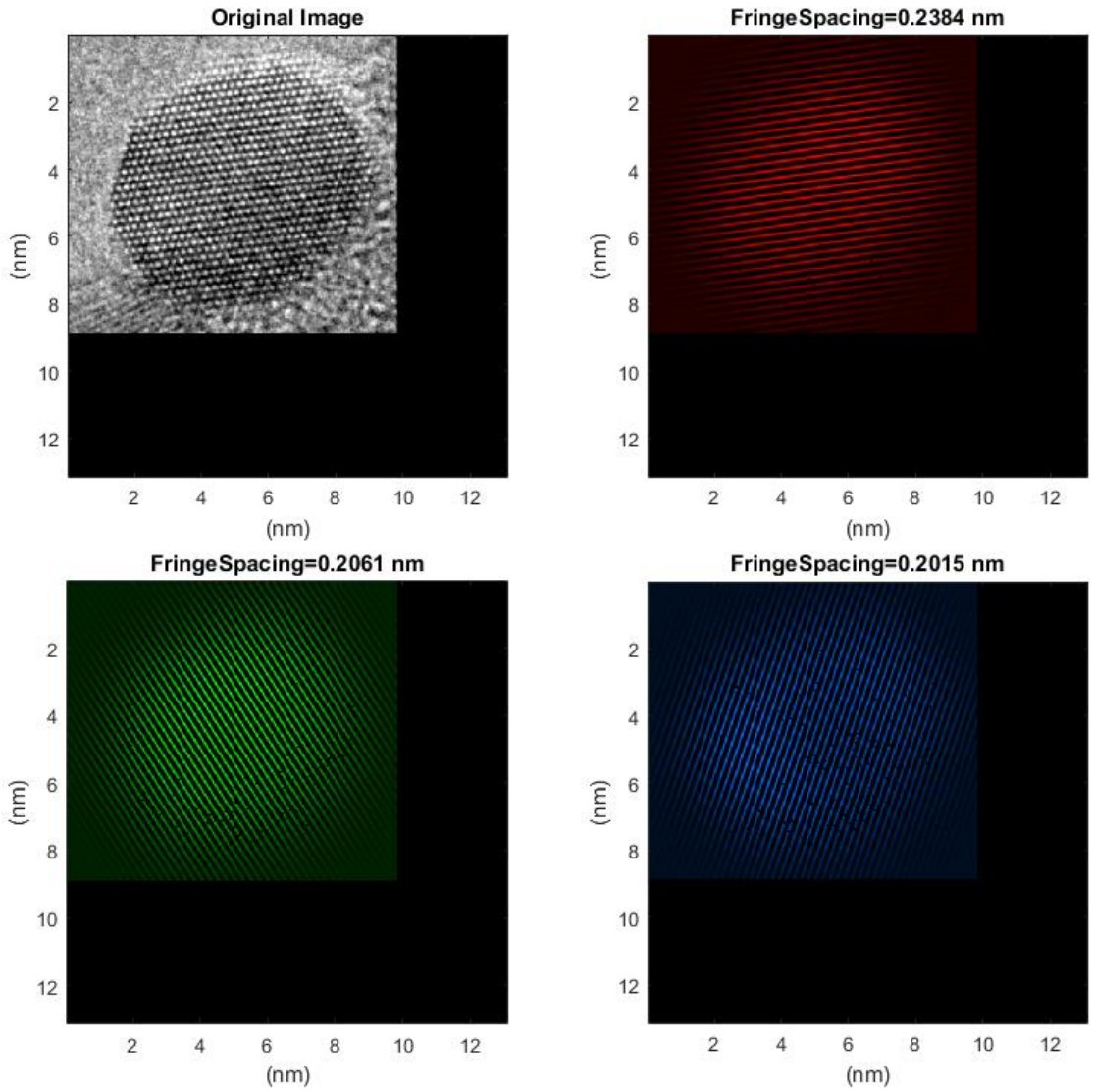

Figure A 23 Fourier Filtering. The first 3 spots selected in Figure A 22 were used to produce these filtered images, which show the spatial distribution of the spacings in the image. In the MATLAB figure, zooming in on any of the four images causes all the images to be similarly zoomed, as seen in Figure 4-6 of the text.

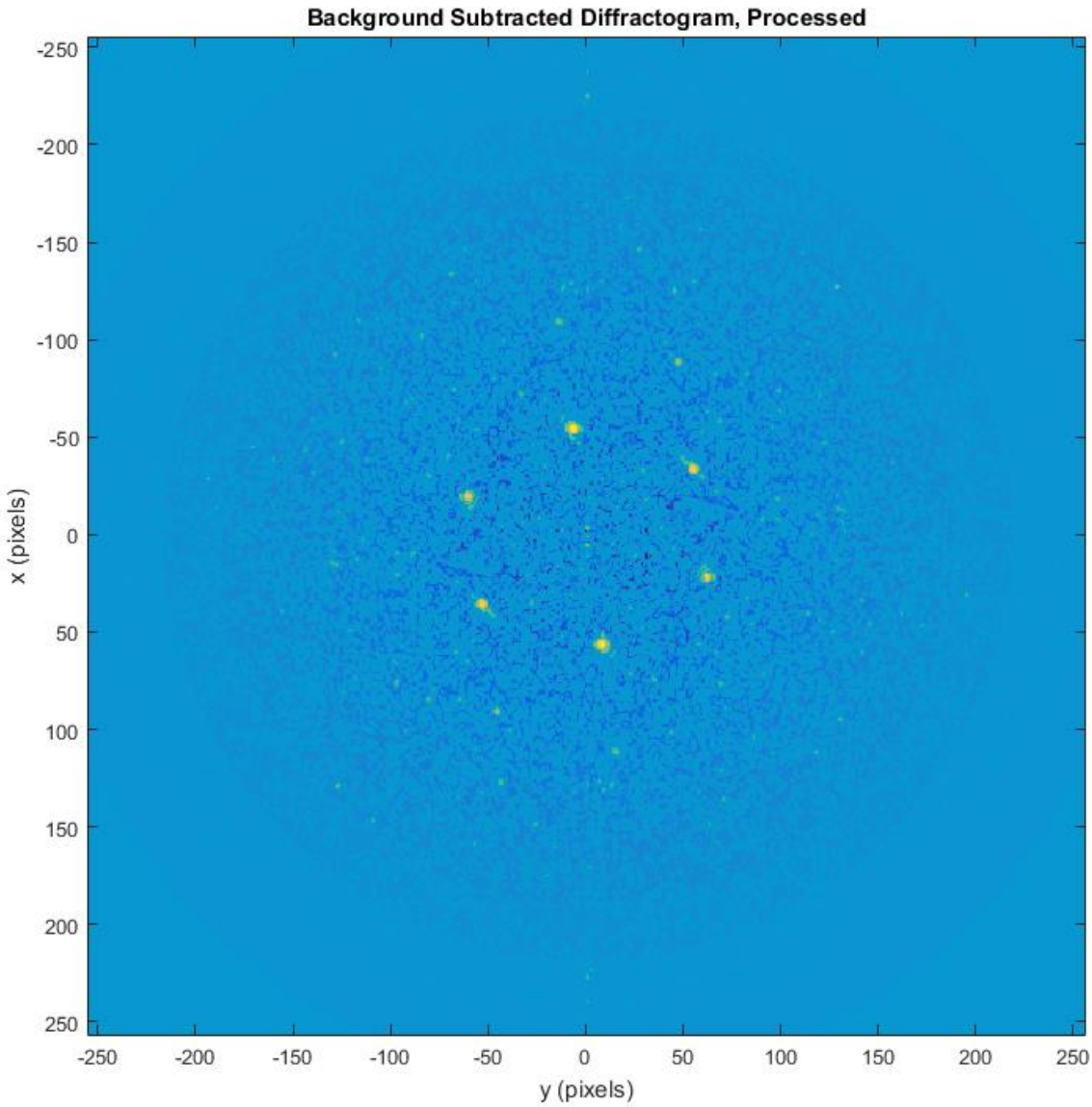

Figure A 24 Processed Diffractogram. The full diffractogram based on that shown in Figure A 22 resulting from the background subtraction and noise suppression described in this appendix. See also Figure 4-9 for a comparison between a processed and unprocessed diffractogram.

DM3FringeAnalysis MATLAB Code

```
clear
close all
%Select File using dialog box and after first instance keep opening from same
%folder.
global Path
```

```
if ~exist('Path','var')
   [FName,Path]=uigetfile({'*.dm3','DM3 File'},'Select a DM3 File');
end
if Path==0
   [FName,Path]=uigetfile({'*.dm3','DM3 File'},'Select a DM3 File');
elseif exist('Path','var')
   [FName,Path]=uigetfile(strcat(Path,'*.dm3'),'Select a DM3 File');
end
%Set whether fourier filtering is performed 1-yes 0-no
FFT=1;
%Set whether background subtraction of center region of FFT is performed
DiffBGS=1;
%Read the DM3 file, including the original image calibration
[ImO,MagCalO,Units]=ReadDMFile(strcat(Path,FName));
ScreenSize=get(0,'screensize');
ImO=single(ImO);
global Cal
if isempty(Cal)
   Cal=0;
end
UserCal=[];
%Set the magnification calibration
while isempty(UserCal)
   UserCal=(inputdlg('Type the image scale calibration (nm/pixel), or enter 0 to use calibration found in DM3 file.','Image
Calibration',1,{num2str(Cal)}));
   UserCal=str2num(UserCal{1});
   Cal=UserCal;
   if UserCal==0
      UserCal=double(MagCalO);
   end
end

%print the file name to the command window
FName
%Image Registration Section XXXXXXXXXXXXXXXXXXXXXXXXXXXXXXXXXXXXXXXXXXXXXXXXXXXX
%XXXXXXXXXXXXXXXXXXXXXXXXXXXXXXXXXXXXXXXXXXXXXXXXXXXXXXXXXXXXXXXXXXXXXXXXXXXXXXX
XXX
if ndims(ImO)==3
   ImReg=inputdlg('Do you want to analyze a stack using image Registration? 1-yes 0-no','Image Registration?',1,{num2str(1)});
   ImReg=str2num(ImReg{1});
else
   ImReg=0;
end
if ImReg
   for i=1:size(ImO,3)
      ImOTrans(:,:,i)=ImO(:,:,i)';
   end
   ImO=ImOTrans;
   Fraction=16;
   Scale1=.25;
   RunNum=1;
   try
      figure(2)
      Fig2Ax=gca;
```

```
    title('Please Wait. Image Registration in Progress')
    drawnow
    [ImRegMontage,ImRegStack,ImDiffMontage]=ImageRegMutualInfo(ImO,Fraction,Scale1,RunNum);
  catch
    figure(2)
    title('Image Registration Failed!')
  end
  figure(1)
  Fig1Ax=gca;
  Fig1Image=imfilter(ImDiffMontage,fspecial('gaussian',[6,6],1));
  set(gcf,'OuterPosition',[0,round(ScreenSize(4)/20),ScreenSize(3),ScreenSize(4)-round(ScreenSize(4)/20)]);
  axes(Fig1Ax)
  imagesc(Fig1Image,prctile(Fig1Image(:),[1,99]))
  title('Initial Registered Montage')
  axis('image')
  Fraction=floor(Fraction*numel(ImRegStack)/numel(ImO));
  Scale2=.5;
  RunNum=RunNum+1;
  try
    figure(2)
    title('Please Wait. Image Registration in Progress')
    drawnow
    [ImRegMontage,ImRegStack,ImDiffMontage]=ImageRegMutualInfo(ImRegStack,Fraction,Scale2,RunNum);
  catch
    figure(2)
    title('Image Registration Failed!')
  end
  figure(2)
  set(gcf,'OuterPosition',[0,round(ScreenSize(4)/20),ScreenSize(3),ScreenSize(4)-round(ScreenSize(4)/20)]);
  axes(Fig2Ax)
  Fig2Image=imfilter(ImDiffMontage,fspecial('gaussian',[6,6],1));
  imagesc(Fig2Image,prctile(Fig1Image(:),[1,99]))
  axis('image')
  title('Final Registered Montage, Select Frames to be Averaged')
  MontageSize(2)=size(ImDiffMontage,1)/size(ImRegStack,1); MontageSize(1)=size(ImDiffMontage,2)/size(ImRegStack,2);
  RegImSelectXY=ginput();

RegImSelectij=circshift(ceil(([1/size(ImRegStack,2);1/size(ImRegStack,1)]*ones(1,size(RegImSelectXY,1)))'.*RegImSelectXY),
1,2);
  RegImSelected=sub2ind(MontageSize,RegImSelectij(:,2),RegImSelectij(:,1));
  RegImSelected(RegImSelected>size(ImRegStack,3))=[];
  title('Final Registered Montage')
  ImOR=mean(ImRegStack(:,:,[1;RegImSelected]),3);
  figure(13)
  Fig12a=subplot(1,2,1);
  imagesc([1:size(ImRegStack,2)]*UserCal,[1:size(ImRegStack,1)]*UserCal,ImRegStack(:,:,1),prctile(ImRegStack(:),[1,99]))
  title('First Frame Image')
  axis('image')
  xlabel('(nm)')
  ylabel('(nm)')
  Fig12b=subplot(1,2,2);
  imagesc([1:size(ImRegStack,2)]*UserCal,[1:size(ImRegStack,1)]*UserCal,ImOR,prctile(ImRegStack(:),[1,99]))
  title('Average Image')
  axis('image')
```

```
   xlabel('(nm)')
   ylabel('(nm)')
   linkaxes([Fig12a,Fig12b])
   close([3,4,5,6])
   TiffLims=double(prctile(ImRegStack(:),[.1,99.9]));
   for i=1:size(ImO,3)
      imwrite(mat2gray(double(ImRegStack(:,:,i)),TiffLims),strcat(Path,FName,'RegStack.tif'),'writemode','append')
      pause(.02)
   end
   imwrite(mat2gray(double(ImOR),TiffLims),strcat(Path,FName,'Reg.tif'),'writemode','append')
else
   for i=1:size(ImO,3)
      ImOR(:,:,i)=ImO(:,:,i)';
   end
end
%End Registration Section XXXXXXXXXXXXXXXXXXXXXXXXXXXXXXXXXXXXXXXXXXXXXXXXXXXXXX

%Set Scale of Image shown on screen (to speed up display of image)
DispScale=1;
%Specify width of the border (nm) to be used around the outlined region of interest when
%computing the diffractogram
BorderWidth=1;
%Set the Scale (nm/pixel) for the original image
ImOScale=UserCal;
%Set scale of reduced image to correct value (nm)
ImSmallScale=ImOScale/DispScale;
%Plotting, and Adjusting to center region of interest in Figure XXXXXXXXXXX
n=1;
%Initialize Figure 3
h=figure(3);
drawnow
ScreenSize=get(0,'screensize');
set(h,'OuterPosition',[0,round(ScreenSize(4)/20),ScreenSize(3),ScreenSize(4)-round(ScreenSize(4)/20)]);
%Set the name of Figure 3 including the slice number from the image stack
Fig1NameStr=strcat('TEM Image, Slice #',num2str(n));
set(h,'name',Fig1NameStr)
ImSmall(:,:,n)=imresize(ImOR(:,:,n),DispScale);
%Blur the image that will be displayed in figure 3 using default gaussian blur
Figure3Image=imfilter(ImSmall(:,:,n),fspecial('gaussian'));
%Plot the image with the coordinates set to normal x-y mode, rather than
%standard for images, with a gray colormap
imagesc(Figure3Image,double(prctile(double(ImSmall(:)),[1,99])));
%axis('image')
colormap(gray);
axis('image')
xlabel('(pixels)')
ylabel('(pixels)')
%Save a handle to this axis
Fig3Axis=gca;
%Zoom and Pan to center the region of interest
%For the first image, zoom in and pan
if n==1
   title('Zoom in On Region of Interest, then press enter (Either Click Once, or Click-and-Drag to Zoom in on Region.)')
   %Zoom in on Just part of the Figure
```

```
    zoom on
    k=0;
    while k~=1
        k=waitforbuttonpress;
    end
    %Set this as Default Zoom
    zoom reset
    %For the second, and subsequent images, pan only
else
    %set the zoom level to previously defined default
    zoom out
    %Pan in on image
    title('Pan (to Center Region of Interest), then press enter')
    pan on
    k=0;
    while k~=1
        k=waitforbuttonpress;
    end
    pan off
end
%Have user select which image from the image stack to use if it is a stack
%and image registration was not performed
if ~ImReg && size(ImOR,3)>1
    XLimits=floor(get(gca,'XLim')); YLimits=floor(get(gca,'YLim'));
    XLimits(XLimits==0)=1;YLimits(YLimits==0)=1;
    for m=1:size(ImOR,3)
        if DispScale~=1
            ImS(:,:,m)=imresize(ImOR(:,:,m),DispScale);
            ImCrop(:,:,m)=ImS(YLimits(1):YLimits(2),XLimits(1):XLimits(2),m);
        else
            ImOp(:,:,m)=ImOR(:,:,m);
            ImCrop(:,:,m)=ImOp(YLimits(1):YLimits(2),XLimits(1):XLimits(2),m);
        end
    end
    ImCrops=reshape(ImCrop,size(ImCrop,1),size(ImCrop,2)*size(ImCrop,3));
    clear('ImCrop')
    imagesc(imfilter(ImCrops(:,:,n),fspecial('gaussian')),double(prctile(double(ImSmall(:)),[1,99])))
    axis('image')
    colormap('gray')
    %Have user select the desired frame out of the stack
    ImSelect=ginput(1);
    %Convert the user selected point into the integer number of the frame
    ImSNum=ceil(ImSelect(1)/(XLimits(2)-XLimits(1)));
    ImSelected(:,:,n)=ImOR(:,:,ImSNum);
    %Blur the image that will be displayed in figure 3 using default gaussian blur
    Figure3Image2=imfilter(ImSelected(:,:,n),fspecial('gaussian'));
    %Plot the image with a gray colormap
    imagesc(Figure3Image2,double(prctile(double(ImSelected(:)),[1,99])));
    axis('image')
    colormap(gray);
    xlabel('(pixels)')
    ylabel('(pixels)')
    xlim(XLimits); ylim(YLimits)
    %Pan in on image using function I created called "PanImage"
```

```
    title('Pan (to Center Region of Interest), then press enter')
    pan on
    k=0;
    while k~=1
        k=waitforbuttonpress;
    end
    pan off
else
    ImSNum=NaN;
    ImSelected=ImSmall;
end
%User Tracing XXXXXXXXXXXXXXXXXXXXXXXXXXXXXXXXXXXXXXXXXXXXXXXXXXXXXXXXXXXXXX
%XXXXXXXXXXXXXXXXXXXXXXXXXXXXXXXXXXXXXXXXXXXXXXXXXXXXXXXXXXXXXXXXXXXXXXXX
XXX
%Have user specify points around the region of interest
title('Outline Region of Interest...right click on last point in outline')
XLimits2=floor(get(gca,'XLim')); YLimits2=floor(get(gca,'YLim'));
XLimits2(XLimits2==0)=1;YLimits2(YLimits2==0)=1;
[UserPoints(n).X(1),UserPoints(n).Y(1),UserButton]=ginput(1);
%If the user right clicks first, use the entire visible area
if UserButton==3
    Polygon=imrect(gca,[XLimits2(1),YLimits2(1),XLimits2(2)-XLimits2(1),YLimits2(2)-YLimits2(1)]);
else
    %Otherwise have the user defnine a free-form polygonal selection
    j=2;
    UserButton=1;
    %Keep collecting points until the user clicks the right mouse button
    %(Userbutton will then be equal to 2, not 1)
    while UserButton==1
        [UserPoints(n).X(j),UserPoints(n).Y(j),UserButton]=ginput(1);
        %plot a line after each user selected point
        line([UserPoints(n).X(j-1),UserPoints(n).X(j)],[UserPoints(n).Y(j-1),UserPoints(n).Y(j)])
        j=j+1;
    end
    j=j-1;
    %plot the final connecting line a different color after user right-clicks
    line([UserPoints(n).X(1),UserPoints(n).X(end)],[UserPoints(n).Y(1),UserPoints(n).Y(end)],'color','c')
    pause(1)
    %Create a MATLAB polygon from the user-selected points
    Polygon=impoly(Fig3Axis,[UserPoints(n).X',UserPoints(n).Y']);
    setClosed(Polygon,'true')
end
%Use the polygon to create a Black and White image of the region of interest shape
BWStructure(n).BWImage=createMask(Polygon);

%Extract many parameters from the B&W image, and save as a structure
Stats(n)=regionprops(BWStructure(n).BWImage,ImSelected(:,:,n),'all');
%Create Image with only contents of the outlined region of interest plus small border
%Expand the B&W perimeter slightly for use in the diffractogram
BWStructureExp(n).BWImageExp=imdilate(BWStructure(1).BWImage,strel('disk',ceil(BorderWidth/ImSmallScale)));
StatsExp(n)=regionprops(BWStructureExp(n).BWImageExp,ImSelected(:,:,n),'PixelList','PixelIdxList','PixelValues');
%Get list of 2D pixel locations
PListInd=StatsExp(n).PixelList;
%Make the pixel locations begin at 1,1
```

```
PListInd(:,1)=PListInd(:,1)-min(PListInd(:,1))+1; PListInd(:,2)=PListInd(:,2)-min(PListInd(:,2))+1;
%Convert locations to linear indices
PList=sub2ind(max(PListInd),PListInd(:,1),PListInd(:,2));
%Get pixel data
PValues=StatsExp(n).PixelValues;
%Initialize image to contain region of interest image
PImage=zeros([max(PListInd)],class(ImOR));
%Set pixels specified by the linear indices to the pixel data values
PImage([PList])=[PValues];
%Smooth image, then re-set pixels in the outline so that, outside the
%outline, the image is smoothed significantly
PImageSmooth=2*imfilter(PImage,fspecial('average',round(.5*ceil(BorderWidth/ImSmallScale))));
PImageSmooth([PList])=[PValues];
%Show image of region of interest
figure(4)
Fig7NameStr=strcat('Region of Interest Image');
set(gcf,'name',Fig7NameStr)
Figure4Image=imfilter(PImageSmooth',fspecial('gaussian'));
imagesc([1:max(PListInd(:,1))]*ImSmallScale,[1:max(PListInd(:,2))]*ImSmallScale,Figure4Image,prctile(double(PValues(:)),[1,
99]))
axis('image')
colormap('gray')
xlabel('(nm)')
ylabel('(nm)')
%Create Diffractogram XXXXXXXXXXXXXXXXXXXXXXXXXXXXXXXXXXXXXXXXXXXXXXXXXXX
%XXXXXXXXXXXXXXXXXXXXXXXXXXXXXXXXXXXXXXXXXXXXXXXXXXXXXXXXXXXXXXXXXXXXXX
XXX
%Determine the size for the FFT to be a value 2^n just large enough to fit
%the cropped region of interest image shown in Figure 4
FFTsize=2^ceil(log(max(max(PListInd)))/log(2));
%Create a hanning window of the appropriate size to eliminate artifacts
%from the image border
wc=window(@hann,size(PImageSmooth,1));
wr=window(@hann,size(PImageSmooth,2));
[maskr,maskc]=meshgrid(wr,wc);
w=maskr.*maskc;
figure(5)
PImSW=PImageSmooth.*w;
imagesc(PImSW',[0,prctile(double(PImSW(:)),99.9)])
colormap(gray)
axis('image')
xlabel('(pixels)')
ylabel('(pixels)')
title('Selected Area After Hann Window Filter')
fig6=figure(6);
Fig6NameStr=strcat('Diffractogram of Region of Interest Image');
%Fig5NameStr=strcat('Diffractogram of Region of Interest Image, Slice #',num2str(n));
set(gcf,'name',Fig6NameStr)
ScreenSize=get(0,'screensize');
set(fig6,'OuterPosition',[0,round(ScreenSize(4)/20),ScreenSize(3),ScreenSize(4)-round(ScreenSize(4)/20)]);
%Compute the FFT, padding the image to be FFTsize square, and using the
%hanning window jjust defined
Y=fft2(double(PImageSmooth).*w,FFTsize,FFTsize);
%Set the scaling factor for the diffractogram to convert measured distances to nm^-1
```

```
DiffScale=(1/ImSmallScale)/FFTsize;
%Create diffractogram (square of FFT), shift low frequencies to center of image, set log scaling
Diffract=log(fftshift(conj(Y).*Y)+1)';
%set contrast limits
clims=double(prctile(double(Diffract(:)),[.1,99.9]));
%show image of FFT using adjusted gamma
gamma=4;
Diffractgray=mat2gray(Diffract,clims);
imagesc(imadjust(Diffractgray,[0,1],[0,1],gamma))
colormap('gray')
axis('image')
%Diffractogram Indexing XXXXXXXXXXXXXXXXXXXXXXXXXXXXXXXXXXXXXXXXXXXXXXXXXX
%XXXXXXXXXXXXXXXXXXXXXXXXXXXXXXXXXXXXXXXXXXXXXXXXXXXXXXXXXXXXXXXXXXXXXXXXXXXXXXXX
%Have user index points in diffractogram
title('Zoom to Region of Interest, Then Press Enter')
zoom on
k=0;
while k~=1
    k=waitforbuttonpress;
end
zoom off
title('Drag boxes around spots to be indexed... press enter when finished, press D key to delete last box.')
k=0;
i=0;
while k==0
    i=i+1;
    k = waitforbuttonpress;
    if k==0
        point1 = get(gca,'CurrentPoint');    % button down detected
        finalRect = rbbox;                   % return figure units
        point2 = get(gca,'CurrentPoint');    % button up detected
        point1 = point1(1,1:2);              % extract x and y
        point2 = point2(1,1:2);
        p1 = min(point1,point2);             % calculate locations
        offset = abs(point1-point2);         % and dimensions
        x = [p1(1) p1(1)+offset(1) p1(1)+offset(1) p1(1) p1(1)];
        y = [p1(2) p1(2) p1(2)+offset(2) p1(2)+offset(2) p1(2)];
        % extract region of interest
        rowStart=floor(p1(2)); rowEnd=ceil(p1(2)+offset(2));
        colStart=floor(p1(1)); colEnd=ceil(p1(1)+offset(1));
        DRegion = Diffract(rowStart:rowEnd, colStart:colEnd);
        % find max value and get its index
        [DRMax, IND] = max(DRegion(:));
        [Mi, Mj] = ind2sub(size(DRegion), IND);
        % move indexes to correct spot in matrix
        Mi = Mi + rowStart-1;
        Mj = Mj + colStart-1;
        MStruct(i).Mi=Mi;
        MStruct(i).Mj=Mj;
        [~,MaxNPX]=max([Diffract(Mi,Mj-1),-inf,Diffract(Mi,Mj+1)]);
        [~,MaxNPY]=max([Diffract(Mj,Mi-1),-inf,Diffract(Mj,Mi+1)]);
        MaxNPX=MaxNPX-2; MaxNPY=MaxNPY-2;
        xp=MaxNPX*(2*abs(Diffract(Mi,Mj+MaxNPX))-
```

```
abs(Diffract(Mi,Mj)))/(abs(Diffract(Mi,Mj+MaxNPX))+abs(Diffract(Mi,Mj)));
      yp=MaxNPY*(2*abs(Diffract(Mi+MaxNPY,Mj))-
abs(Diffract(Mi,Mj)))/(abs(Diffract(Mi+MaxNPY,Mj))+abs(Diffract(Mi,Mj)));
      DiffMaxPixAbs(i,:)=[Mi,Mj];
      DiffMaxPix=DiffMaxPixAbs-(size(Diffract,1)/2+1);
      DiffMaxPos(i,:)=[Mi+yp,Mj+xp]-(size(Diffract,1)/2+1);
      DiffMaxDistance_nm(i)=1/(norm(DiffMaxPos(i,:))*DiffScale);
      DiffMax(i)=DRMax;
      if i>1
         DiffMaxAngle_deg(i-1)=180/pi*atan2(norm(cross([DiffMaxPos(i,:),0],[DiffMaxPos(i-
1,:),0])),dot(DiffMaxPos(i,:),DiffMaxPos(i-1,:)));
         if DiffMaxAngle_deg(i-1)>90
            DiffMaxAngle_deg(i-1)=180-DiffMaxAngle_deg(i-1);
         end
      end
      hold on
      axis manual
      plot(x,y,'g')                    % redraw in dataspace units
      plot(Mj+xp,Mi+yp,'.b')
      text(x(1),y(1),num2str(i),'color','g','verticalalignment','bottom')
   else
      kchar=get(gcf,'currentcharacter');
      if kchar=='d'
         plot(x,y,'r')
         plot(Mj+xp,Mi+yp,'r.')
         text(x(1),y(1),num2str(i-1),'color','r','verticalalignment','bottom')
         %Reset k to 0, because pressing "d" was a button press, setting k to 1
         k=0;
         i=i-2;
         DiffMaxDistance_nm(end)=[];
         DiffMax(end)=[];
         if exist('DiffMaxAngle_deg','var')
            DiffMaxAngle_deg(end)=[];
         end
      end
   end
end
if ~exist('DiffMaxDistance_nm')
   DiffMaxDistance_nm=[];
   DiffMax=[];
end
if ~exist('DiffMaxAngle_deg')
   DiffMaxAngle_deg=[];
end
%save an image of the diffractogram with the user-selected indexing boxes
print(fig6,'-dpng','Fig3Temp.png')
Fig3Image=imread('Fig3Temp','png');
%Put important values into info structure
info(n).DiffractogramFigure=Fig3Image;
info(n).BWImage=BWStructure(n).BWImage;
info(n).PImageExtended=PImageSmooth;
info(n).OriginalCalibration=MagCalO;
info(n).CalibrationUsed=ImOScale;
info(n).Units=Units;
```

```
info(n).Slice=ImSNum;
info(n).LatticeFringeSpacings=DiffMaxDistance_nm;
info(n).LatticeFringeIntensity=DiffMax;
info(n).LatticeFringeAngles=DiffMaxAngle_deg;
info(n).FileName=FName;
clear DiffMaxDistance_nm DiffMaxAngle_deg
%Fourier Filtering of Image XXXXXXXXXXXXXXXXXXXXXXXXXXXXXXXXXXXXXXXXXXXXXXX
%XXXXXXXXXXXXXXXXXXXXXXXXXXXXXXXXXXXXXXXXXXXXXXXXXXXXXXXXXXXXXXXXXXXXXXX
XXX
%if FFT is set to 1, do fourier filtering
if FFT
    %Take FFT again, but without using the hanning window
    FFTshifted=fftshift(fft2(double(PImageSmooth'),FFTsize,FFTsize));
    %Specify Mask circle Radius
    MaskR=round(FFTsize/512*2);
    MaskSigma=MaskR;
    %create Filter to place in Mask image
    Filter=fspecial('gaussian',MaskR*4+1,MaskSigma);
    NumFiltIm=min(numel(info(n).LatticeFringeSpacings),3);
    for i=1:NumFiltIm
        %Initialize Mask Matrix
        Mask=zeros(FFTsize,FFTsize);
        %Create shift values to use for placing filter in mask image
        MShiftR=MStruct(i).Mi-(MaskR*2+1);
        MShiftC=MStruct(i).Mj-(MaskR*2+1);
        MShiftR2=FFTsize-MStruct(i).Mi-(MaskR*2-1);
        MShiftC2=FFTsize-MStruct(i).Mj-(MaskR*2-1);
        %place filter in mask image at 2 symmetric locations
        Mask(1+MShiftR:size(Filter,1)+MShiftR,1+MShiftC:size(Filter,2)+MShiftC)=Filter;
        Mask(1+MShiftR2:size(Filter,1)+MShiftR2,1+MShiftC2:size(Filter,2)+MShiftC2)=Filter;
        MaskM(:,:,i)=Mask;
        %Apply the mask to the FFT
        FFTfiltered(:,:,i)=(FFTshifted.*MaskM(:,:,i));
        %invert the filtered FFT
        FiltInversedImage(:,:,i)=ifft2(ifftshift(FFTfiltered(:,:,i)));
        InversedImage=ifft2(ifftshift(FFTshifted));
    end
    %in case user selects fewer than 3 fringe spacings, duplicate to make 3 total inversed images
    if NumFiltIm==2
        FiltInversedImage(:,:,3)=FiltInversedImage(:,:,2);
    elseif NumFiltIm==1
        FiltInversedImage(:,:,2)=FiltInversedImage(:,:,1);
        FiltInversedImage(:,:,3)=FiltInversedImage(:,:,2);
    end
    FFTfiltSum=(sum(conj(FFTfiltered).*FFTfiltered,3));
    %Plot the filtered FFT
    fig8=figure(8);
    Fig8NameStr=strcat('Filtered FFT');
    set(gcf,'name',Fig8NameStr)
    hold on
    imagesc(log(FFTfiltSum+1));
    CRadii=[.8,.4,.2,.1,.05];

viscircles(ones(length(CRadii),1)*[FFTsize/2+1,FFTsize/2+1],1./CRadii/DiffScale,'edgecolor','g','drawbackgroundcircle',0,'linewi
```

```
dth',1);
    plot(FFTsize/2+1,FFTsize/2+1,'g')
    axis('ij')
    axis('image')
    [~,I]=min(info(n).LatticeFringeSpacings);
    zoom(FFTsize/norm(DiffMaxPos(I,:))/2.5)
    colormap('gray')
    text(zeros(length(CRadii),1)+FFTsize/2+1,FFTsize/2+1-1./CRadii/DiffScale,{'0.8 nm','0.4 nm','0.2 nm','0.1 nm','0.05
nm'},'color','g','verticalalignment','bottom')
    %Plot 3 filtered images in Red, Green, and Blue images, and link to original image
    fig9=figure(9);
    Fig9NameStr=strcat('Filtered Image Comparison-Individual Fringe Images, Slice #',num2str(n));
    set(gcf,'name',Fig9NameStr)
    ScreenSize=get(0,'screensize');
    set(fig9,'OuterPosition',[0,round(ScreenSize(4)/20),ScreenSize(3),ScreenSize(4)-round(ScreenSize(4)/20)]);
    gamma4=3;
    PVL=prctile(double(PValues(:)),[1,99]);
    F0=subplot(1,4,1);

imagesc([1:FFTsize]*ImSmallScale,[1:FFTsize]*ImSmallScale,imfilter(InversedImage,fspecial('gaussian')),prctile(double(PValu
es(:)),[1,99]));
    axis('image')
    colormap('gray')
    xlabel('(nm)')
    ylabel('(nm)')
    F1=subplot(1,4,2);
    InversedImageM=cat(3,InversedImage,InversedImage,InversedImage);
    FImage1=imadjust(cat(3,mat2gray(FiltInversedImage(:,:,1)),zeros(size(InversedImage)),zeros(size(InversedImage))),[0 1],[0
1],gamma4);
    FImage1(InversedImageM<PVL(1))=0;
    imagesc([1:FFTsize]*ImSmallScale,[1:FFTsize]*ImSmallScale,FImage1);
    axis('image')
    xlabel('(nm)')
    ylabel('(nm)')
    F2=subplot(1,4,3);
    FImage2=imadjust(cat(3,zeros(size(InversedImage)),mat2gray(FiltInversedImage(:,:,2)),zeros(size(InversedImage))),[0 1],[0
1],gamma4);
    FImage2(InversedImageM<PVL(1))=0;
    imagesc([1:FFTsize]*ImSmallScale,[1:FFTsize]*ImSmallScale,FImage2);
    axis('image')
    xlabel('(nm)')
    ylabel('(nm)')
    F3=subplot(1,4,4);

FImage3=imadjust(cat(3,zeros(size(InversedImage)),mat2gray(FiltInversedImage(:,:,3))*.75,mat2gray(FiltInversedImage(:,:,3))),
[0 1],[0 1],gamma4);
    FImage3(InversedImageM<PVL(1))=0;
    imagesc([1:FFTsize]*ImSmallScale,[1:FFTsize]*ImSmallScale,FImage3);
    axis('image')
    xlabel('(nm)')
    ylabel('(nm)')
    title(F0,'Original Image');title(F1,strcat('FringeSpacing= ',num2str(info(n).LatticeFringeSpacings(1),4),' nm'));
    if NumFiltIm>=2
        title(F2,strcat('FringeSpacing= ',num2str(info(n).LatticeFringeSpacings(2),4),' nm'));
```

```
        if NumFiltIm==3
            title(F3,strcat('FringeSpacing= ',num2str(info(n).LatticeFringeSpacings(3),4),' nm'))
        end
    end
    linkaxes([F0,F1,F2,F3])
end
%Diffractogram Processing XXXXXXXXXXXXXXXXXXXXXXXXXXXXXXXXXXXXXXXXXXXXXXXX
%XXXXXXXXXXXXXXXXXXXXXXXXXXXXXXXXXXXXXXXXXXXXXXXXXXXXXXXXXXXXXXXXXXXXXXXX
XXX
if DiffBGS
    MRad=FFTsize/2;
    DiffractC=Diffract;
    for i=1:3
        DiffMean(i)=mean(DiffractC(:));
        DiffractC=DiffractC-DiffMean(i);
        DiffMax=max(DiffractC(:));
        DiffractC(abs(DiffractC)>DiffMax/2)=0;
    end
    DiffractBGS=Diffract-sum(DiffMean);
    DiffractBGS(DiffractBGS<0)=0;
    xDiff=-MRad:MRad-1; yDiff=-MRad:MRad-1;
    [XDiff,YDiff]=meshgrid(xDiff,yDiff);
    R=sqrt(XDiff.^2+YDiff.^2);
    DiffractBGS(R>MRad)=0;
    %Rotational Average XXXXXXXXXXXXXXXXXXXXXXXXXXXXXXXXXXXXXXXXXXXXXXXXXX
    qplot = false;
    [xs,ys] = size(DiffractBGS);
    f2 = -xs/2:xs/2-1;
    f1 = -ys/2:ys/2-1;
    [XX,YY] = meshgrid(f1,f2);
    [~,r] = cart2pol(XX,YY);
    if mod(xs,2)==1 || mod(ys,2)==1
        r = round(r)-1;
    else
        r = round(r);
    end
    RotAvg = zeros(floor(min(xs,ys)/2),1);
    RotMax = zeros(floor(min(xs,ys)/2),1);
    for sfs = 1:floor(min(xs,ys)/2)
        RotAvg(sfs) = mean(DiffractBGS(r==sfs));
        RotMax(sfs) = max(DiffractBGS(r==sfs));
    end
    if qplot
        figure; semilogy(1:floor(min(xs,ys)/2),RotAvg);
        xlabel('Spatial frequency (cycles/image)');
        ylabel('Energy');
    end

%XXXXXXXXXXXXXXXXXXXXXXXXXXXXXXXXXXXXXXXXXXXXXXXXXXXXXXXXXXXXXXXXXXXXXXXX
XXX
    r2=1:floor(min(xs,ys)/2);
    RotAvgFit=fit(r2',RotAvg,'gauss4');
    RotMaxFit=fit(r2',RotMax,'gauss4');
    RotAvgDiff=reshape(RotAvgFit(R),MRad*2,MRad*2);
```

```
    DiffractBGS2=DiffractBGS-RotAvgDiff;
    PositiveDiff=DiffractBGS2(DiffractBGS2>0);
    PositiveDiff(PositiveDiff<=0)=[];
    BGSmin=3*mean(PositiveDiff(:));
    DiffractBGS3=DiffractBGS2;
    DiffractBGS3(DiffractBGS2<BGSmin & DiffractBGS2>0)=0;
    DiffractBGS3(DiffractBGS2<-BGSmin*2)=-BGSmin*2;
    figure(10)
    subplot(2,1,1)
    surf(DiffractBGS2)
    colormap('default')
    shading('interp')
    xlabel('y (pixels)')
    ylabel('x (pixels)')
    title('Background Subtracted Diffractogram')
    subplot(2,1,2)
    semilogx(1./(DiffScale*r2),RotMax-RotAvgFit(r2))
    figure(11)
    set(gcf,'OuterPosition',[0,round(ScreenSize(4)/20),ScreenSize(3),ScreenSize(4)-round(ScreenSize(4)/20)]);
    subplot(1,2,1)
    surf(DiffractBGS3')
    axis('square')
    title('Background Subtracted Diffractogram, Processed')
    xlabel('y (pixels)')
    ylabel('x (pixels)')
    shading('interp')
    subplot(1,2,2)
    imagesc([-FFTsize/2+1:FFTsize/2],[-FFTsize/2+1:FFTsize/2],DiffractBGS3)
    axis('image')
    title('Background Subtracted Diffractogram, Processed')
    xlabel('y (pixels)')
    ylabel('x (pixels)')
    shading('interp')
end
%standard deviation image figure
if ImReg
    figure();
    H1=subplot(1,2,1);
    ImSR=sqrt(ImOR)-mean(mean(sqrt(ImOR)));
    MinMax=prctile(ImSR(:),[.1,99.9]);
    ImSR=ImSR-MinMax(1);
    imagesc(ImSR,prctile(ImSR(:),[.1,99.9]));
    axis('image')
    H2=subplot(1,2,2);
    StDevIm=imfilter(std(ImRegStack,0,3).*(ImSR),fspecial('gaussian'));
    StDevIm=std(ImRegStack,0,3);
    MinMax2=prctile(StDevIm(:),[.1,99.9]);
    StDevIm=(StDevIm-MinMax2(1)).*ImSR;
    imagesc(StDevIm,prctile(StDevIm(:),[.1,99.9]));
    axis('image');
    linkaxes([H1,H2])
end
%Package important data into a single structure and save XXXXXXXXXXXXXXXXXX
%XXXXXXXXXXXXXXXXXXXXXXXXXXXXXXXXXXXXXXXXXXXXXXXXXXXXXXXXXXXXXXXXXXXXXXXXX
```

```
XXX
%Put all the Structures created by the above code into one giant structure,
%and give the fields of that structure useful names
TitlesU=fieldnames(UserPoints);
TitlesS=fieldnames(Stats);
TitlesI=fieldnames(info);
Titles=[TitlesU;TitlesS;TitlesI];
%Convert structures to cells
DataCellU=struct2cell(UserPoints(:))';
DataCellI=struct2cell(info(:))';
DataCellS=struct2cell(Stats(:))';
%Combine Cells
DataCell=[DataCellU,DataCellS,DataCellI];
%Convert back to structure
DataStruct=cell2struct(DataCell,Titles,2);
KeyData=DataStruct;
E=1;
i=1;
%Save the data in a file that doesn't exist, if it does exist, increment
%the filename's numerical suffix
while E>0
   if E==1
      NE=[];
   else
      NE=i;
   end
   if E>0
      E=exist(strcat(Path,FName,'_',num2str(NE),' MATLAB Data.mat'));
   end
   if E==0
      save(strcat(Path,FName,'_',num2str(NE),' MATLAB Data.mat'),'DataStruct','KeyData')
   end
   i=i+1;
end
```

3rd Party Codes Used: ReadDMFile

ImageRegMutualInfo MATLAB Function

```
function [ImMontageReg,ImStackReg,ImDiffMontage]=ImageRegMutualInfo(ImO,Fraction,Scale,RunNum,varargin)
%Reserve figures 1 and 2 for the calling function
figure(1)
figure(2)
%Make a copy of the original image
ImOPlot=ImO;
%get the number of image frames
N=size(ImO,3);
%for each frame, apply a median filter (5x5 kernel) and rescale the image
for i=1:N
   ImOS(:,:,i)=imresize(medfilt2(ImO(:,:,i),[5,5]),Scale);
   %Save a copy of the filtered, scaled image
   ImOSPlot=ImOS;
end
```

```
%if this is the first time the function has been called, do a rough shift
if RunNum==1
    for i=1:N
        %run Phase-correlation code obtained online
        Shift(i,:)=POCShift(ImOS(:,:,1),ImOS(:,:,i));
        %produce an affine transformation matrix for both the original and
        %scaled image stacks
        ShiftTransS(i)=affine2d([1,0,0;0,1,0;-Shift(i,2),-Shift(i,1),1]);
        ShiftTrans(i)=affine2d([1,0,0;0,1,0;-Shift(i,2)/Scale,-Shift(i,1)/Scale,1]);
        %apply the transformations to shift the images into rough alignment
        ImOS(:,:,i)=imwarp_same(ImOS(:,:,i),ShiftTransS(i));
        ImO(:,:,i)=imwarp_same(ImO(:,:,i),ShiftTrans(i));
    end
end
%if a extra argument is past, this should be the fixed image used to align
%others in the stack
if size(varargin)>0
    ImOStationary=varargin{1,1};
    %otherwise, just use the first image in the stack (usual behavior)
else
    ImOStationary=ImOS(:,:,1);
end
%find the intensity range of the original image
ImLimits=prctile(double(ImO(:)),[1,99]);
%Initialize the registration metric
[~,RegMetric]=imregconfig('multimodal');
%Initialize the registration optimizer
RegOptimizer=registration.optimizer.RegularStepGradientDescent();
%Set optimizer parameters
RegOptimizer.RelaxationFactor=.75;
RegOptimizer.MaximumStepLength=RegOptimizer.MaximumStepLength*.5;
%Set metric parameters
if Fraction>1
    RegMetric.UseAllPixels=0;
    RegMetric.NumberOfSpatialSamples=round(numel(ImOS(:,:,1))/Fraction);
elseif Fraction==1
    RegMetric.UseAllPixels=1;
else
    error('"Fraction" should be an integer larger than 1')
end
%for each frame:
for i=1:N
    %register the image
    RegTrans(i)=imregtform(ImOS(:,:,i),ImOStationary,'translation',RegOptimizer,RegMetric,'pyramidlevels',4);
    %Update a counter so the user knows the registration progress
    Fig2String=strcat({'Please Wait. Image Registration in Progress: Frame '},num2str(i),{' of '},num2str(N));
    title(gca,Fig2String)
    %Pause briefly (this seems to help the code function)
    pause(.05)
    %Create the transformation matrix based on the result of imregtform
    RegTrans(i).T=RegTrans(i).T.*[1,1,1;1,1,1;1/Scale,1/Scale,1];
    pause(.05)
    %transform the image using the transformation matrix
    ImStackReg(:,:,i)=imwarp_same(ImO(:,:,i),RegTrans(i));
```

```
    pause(.05)
    %create a small version of the resulting registered image stack
    ImStackRegS(:,:,i)=imresize(medfilt2(ImStackReg(:,:,i),[5,5]),.5);
end
%create a new figure that fills the screen
figure
ScreenSize=get(0,'screensize');
set(gcf,'OuterPosition',[0,round(ScreenSize(4)/20),ScreenSize(3),ScreenSize(4)-round(ScreenSize(4)/20)]);
%wait for the user to hit enter (or any oother key) before showing images
%in the figure
title('Press Enter to see comparison sequence')
waitforbuttonpress()
%set number of times the series of frames is cycled
NN=ceil(50/N);
for T=1:N*NN
    %idex of frame to be displayed
    t=1+mod(T,N);
    %plot the original image on left
    subplot(1,2,1)
    imagesc(ImOSPlot(:,:,t),ImLimits)
    colormap(gray)
    axis('image')
    %plot the registered image on right
    subplot(1,2,2)
    imagesc(ImStackRegS(:,:,t),ImLimits)
    colormap(gray)
    axis('image')
    pause(.1)
end
%create new figure
figure
%show the average registered image so user can select region
imagesc(mean(ImStackReg,3),ImLimits)
%if this is the first time the function has been called, prompt to select a
%region for more precise alignment
if RunNum==1
    title('Select Region for Further Alignment')
    drawnow
    %otherwise, prompt the user to select the region that has been aligned
else
    title('Select Aligned Region')
    drawnow
end
axis('image')
%have user select a region
CropRect=round(getrect());
%update the title so the user knows the region was succesfully selected
title('Please Wait')
%if the limits are just outside the acceptable bounds, fix this
CropRect(CropRect==0)=1; CropRect(CropRect==size(ImStackReg,1)+1)=size(ImStackReg,1);
%create a cropped registered image stack
ImStackCrop=ImStackReg(CropRect(2):CropRect(2)+CropRect(4),CropRect(1):CropRect(1)+CropRect(3),:);
ImStackReg=flip(ImStackCrop,3);
%create a cropped, unregistered image stack
```

```
ImOCrop=ImO(CropRect(2):CropRect(2)+CropRect(4),CropRect(1):CropRect(1)+CropRect(3),:);
%disable warnings about adjusting the magnification (these are just
%annoying)
warning('off','images:initSize:adjustingMag')
for i=1:N
   %create montage matrix from the stack
   MontageIm(:,:,1,i)=ImStackCrop(:,:,i);
   %create a similar montage matrix by duplicating the first frame
   ImOMont(:,:,1,i)=ImStackCrop(:,:,1);
end
%create montage image from montage matrix
Montage=montage(ImOMont);
MontageO=Montage.CData;
%create aligned montage image from montage matrix
Montage=montage(MontageIm);
ImMontageReg=Montage.CData;
%display the aligned montage image
imagesc(ImMontageReg,ImLimits)
%find difference between first frame montage and registered montage
ImDiffMontage=abs(ImMontageReg-MontageO);
```

3rd Party Codes: POCShift imwarp_same

DM3FringeFurtherAnalysis MATLAB Code

```
%Unless the user has just run the DM3FringeAnalysis code, or this code,
%promt them the open a saved data file
if ~exist('DiffractBGS3','var')
   global Path
   if ~exist('Path','var')
      [FName,Path]=uigetfile({'*.mat','MATLAB Data File'},'Select a MATLAB Data File');
   end
   if Path==0
      [FName,Path]=uigetfile({'*.mat','MATLAB Data File'},'Select a MATLAB Data File');
   elseif exist('Path','var')
      [FName,Path]=uigetfile(strcat(Path,'*.mat'),'Select a MATLAB Data File');
   end
   %Extract necessary data from .mat file
   Data=open(strcat(Path,FName));
   try
      DiffractBGS3=Data.DataStruct.DiffractBGS3;
   catch
      error('This data file was not produced by the most recent version of the DM3FringeAnalysis code')
   end
   Diffract=Data.DataStruct.Diffract;
   DiffScale=Data.DataStruct.DiffScale;
   FFTsize=Data.DataStruct.FFTsize;
   MaskR=Data.DataStruct.MaskR;
   Filter=Data.DataStruct.Filter;
   FFTshifted=Data.DataStruct.FFTshifted;
   ImSmallScale=Data.DataStruct.ImSmallScale;
   PVL=Data.DataStruct.PVL;
end
i=1;
Iteration=1;
```

```
%Prompt the user to input information about one or more crystal structures
NumStructures=inputdlg('How many different structures do you want to use for indexing','Number of Structures',1,{'1'});
NumStructures=str2num(NumStructures{1});
global Spacings hkls Names
for ii=1:NumStructures
   MinSpacing=.1;
   Choice = questdlg('Will you enter lattice parameters, or import a CIF file?', ...
      'Structure Input', ...
      'CIF','Lattice Parameters','Use Previous Structures','CIF');
   %calculate crystal spacings from either a CIF or lattice parameters
   switch Choice
      case 'CIF'
         I = 1;
         [Spacings{ii},hkls{ii},Names{ii}]=CrystalSpacings(MinSpacing,I);
      case 'Lattice Parameters'
         I = 2;
         [Spacings{ii},hkls{ii},Names{ii}]=CrystalSpacings(MinSpacing,I);
      case 'Use Previous Structures'
         I = 0;
         Spacings{ii}=Spacings{ii};
         hkls{ii}=hkls{ii};
         Names{ii}=Names{ii};
   end
   SpacingNumber(ii,:)=size(Spacings{ii});
end
SpacingNumbers=SpacingNumber(:,1);
%Create a new, large figure window
Fig12=figure(12);
ScreenSize=get(0,'screensize');
set(gcf,'OuterPosition',[0,round(ScreenSize(4)/20),ScreenSize(3),ScreenSize(4)-round(ScreenSize(4)/20)]);
Ax1=subplot(1,3,1);
%Plot a processed diffractogram
imagesc(DiffractBGS3)
colormap(Ax1,'default')
axis('image')
title('Zoom to Area of Interest, then Press Enter')
xlabel('y (pixels)')
ylabel('x (pixels)')
k=0;
zoom on
while k~=1
   k=waitforbuttonpress;
end
zoom off
zoom reset
%Allow the user to select a spot
title('Background Subtracted Diffractogram, Processed, Select a Spot')
k=0;
while k~=1
   k=waitforbuttonpress;
   if k==1
      Char=get(Fig12,'currentcharacter');
      %allow the user to zoom in on the image
      if Char=='z' && Iteration~=1;
```

```
        Ax1=subplot(1,3,1);
        title('Background Subtracted Diffractogram, Processed')
        AA=Char;
        Ax2=subplot(1,3,2);
        title('Original Image. When Finished Zooming Press Enter')
        zoom on
        kk=0;
        while kk~=1
           kk=waitforbuttonpress;
        end
        zoom off
        title('Original Image.')
        k=0;
    else
        break
    end
    Ax1=subplot(1,3,1);
    title('Background Subtracted Diffractogram, Processed, Select Another Spot, or Press Enter to Stop')
    k=waitforbuttonpress;
    if k==1
        break
    end
end
set(Fig12,'currentcharacter','a');
hold(Ax1,'on')
xlim manual
imagesc(DiffractBGS3)
zoom out
colormap(Ax1,'default')
point1 = get(gca,'CurrentPoint');    % button down detected
finalRect = rbbox;                   % return figure units
point2 = get(gca,'CurrentPoint');    % button up detected
point1 = point1(1,1:2);              % extract x and y
point2 = point2(1,1:2);
title('Background Subtracted Diffractogram, Processed, Please Wait')
p1 = min(point1,point2);             % calculate locations
offset = abs(point1-point2);         % and dimensions
x = [p1(1) p1(1)+offset(1) p1(1)+offset(1) p1(1) p1(1)];
y = [p1(2) p1(2) p1(2)+offset(2) p1(2)+offset(2) p1(2)];
% extract region of interest
rowStart=floor(p1(2)); rowEnd=ceil(p1(2)+offset(2));
colStart=floor(p1(1)); colEnd=ceil(p1(1)+offset(1));
DRegion = Diffract(rowStart:rowEnd, colStart:colEnd);
% find max value and get its index
[DRMax, IND] = max(DRegion(:));
[Mi, Mj] = ind2sub(size(DRegion), IND);
% move indexes to correct spot in matrix
Mi = Mi + rowStart-1;
Mj = Mj + colStart-1;
MStruct(i).Mi=Mi;
MStruct(i).Mj=Mj;
[~,MaxNPX]=max([Diffract(Mi,Mj-1),-inf,Diffract(Mi,Mj+1)]);
[~,MaxNPY]=max([Diffract(Mj,Mi-1),-inf,Diffract(Mj,Mi+1)]);
MaxNPX=MaxNPX-2; MaxNPY=MaxNPY-2;
```

```
    xp=MaxNPX*(2*abs(Diffract(Mi,Mj+MaxNPX))-
abs(Diffract(Mi,Mj)))/(abs(Diffract(Mi,Mj+MaxNPX))+abs(Diffract(Mi,Mj)));
    yp=MaxNPY*(2*abs(Diffract(Mi+MaxNPY,Mj))-
abs(Diffract(Mi,Mj)))/(abs(Diffract(Mi+MaxNPY,Mj))+abs(Diffract(Mi,Mj)));
    DiffMaxPixAbs(i,:)=[Mi,Mj];
    DiffMaxPix=DiffMaxPixAbs-(size(Diffract,1)/2+1);
    DiffMaxPos(i,:)=[Mi+yp,Mj+xp]-(size(Diffract,1)/2+1);
    DiffMaxDistance_nm(i)=1/(norm(DiffMaxPos(i,:))*DiffScale);
    DSpacingMeas=DiffMaxDistance_nm(i);
    %Check the measured spacing against calculated spacings from the
    %structures selected earlier
    SortedSpacingsI=[]; SortedSDiffI=[]; SortedhklsI=[]; SortedNamesI=[];
    NumClose=3;
    if min(SpacingNumbers)<3
       NumClose=min(SpacingNumbers);
    end
    for j=1:NumStructures
       [SDif{j},II{j}]=sort(abs(DSpacingMeas-Spacings{j}));
       SortedSpacingsI=[SortedSpacingsI;Spacings{j}(II{j}(1:NumClose))];
       SortedSDiffI=[SortedSDiffI;SDif{j}((1:NumClose))];
       SortedhklsI=[SortedhklsI;hkls{j}(II{j}(1:NumClose),:)];
       for jj=1:NumClose
          SortedNamesI{(j-1)*NumClose+jj,1}=Names{j};
       end
    end
    [SortedSDiffs,III]=sort(SortedSDiffI);
    SortedSpacings=SortedSpacingsI(III(1:NumClose));
    Sortedhkls=SortedhklsI(III(1:NumClose),:);
    SortedNames=SortedNamesI(III(1:NumClose));
    for jj=1:NumClose
       hkltext{jj}=strcat({'('},num2str(Sortedhkls(jj,:)),{')'});
       MatchingSpacingStr(jj,1)=strcat(sprintf('%7s',SortedNames{jj}),hkltext{jj},{' '},num2str(SortedSpacings(jj),4),{'nm
('},num2str(100*SortedSDiffs(jj)/SortedSpacings(jj),'%.1f'),'% Error)');
    end
    DiffMaxInt(i)=DRMax;
    hold(Ax1,'on')
    axis manual
    plot(x,y,'g')                    % redraw in dataspace units
    plot(Mj+xp,Mi+yp,'.b')
    drawnow
    %Fourier Filtering of Image XXXXXXXXXXXXXXXXXXXXXXXXXXXXXXXXXXXXXXXXXXXXXXXX
    %Initialize Mask Matrix
    Mask=zeros(FFTsize,FFTsize);
    %Create shift values to use for placing filter in mask image
    MShiftR=MStruct(i).Mi-(MaskR*2+1);
    MShiftC=MStruct(i).Mj-(MaskR*2+1);
    MShiftR2=FFTsize-MStruct(i).Mi-(MaskR*2-1);
    MShiftC2=FFTsize-MStruct(i).Mj-(MaskR*2-1);
    %place filter in mask image at 2 symmetric locations
    Mask(1+MShiftR:size(Filter,1)+MShiftR,1+MShiftC:size(Filter,2)+MShiftC)=Filter;
    Mask(1+MShiftR2:size(Filter,1)+MShiftR2,1+MShiftC2:size(Filter,2)+MShiftC2)=Filter;
    MaskM(:,:,i)=Mask;
    %Apply the mask to the FFT
    FFTfiltered(:,:,i)=(FFTshifted.*MaskM(:,:,i));
```

```
    %invert the filtered FFT
    FiltInversedImage(:,:,i)=ifft2(fftshift(FFTfiltered(:,:,i)));
    InversedImage=ifft2(fftshift(FFTshifted));
    InversedImageM=cat(3,InversedImage,InversedImage,InversedImage);
    gamma4=3;
    FImage1=imadjust(cat(3,mat2gray(FiltInversedImage(:,:,i)),zeros(size(InversedImage)),zeros(size(InversedImage))),[0 1],[0
1],gamma4);
    FImage1(InversedImageM<PVL(1))=0;
    FImage(:,:,:,Iteration)=FImage1;
    imwrite(FImage1,'FFT1.png')
    %plot the image
    Ax2=subplot(1,3,2);
    imagesc([1:FFTsize]*ImSmallScale,[1:FFTsize]*ImSmallScale,imfilter(InversedImage,fspecial('gaussian')),PVL);
    axis('image')
    zoom out
    title('Original Image. Press "z" to zoom')
    colormap(Ax2,'gray')
    xlabel('(nm)')
    ylabel('(nm)')
    %plot the filtered image
    Ax3=subplot(1,3,3);
    imagesc([1:FFTsize]*ImSmallScale,[1:FFTsize]*ImSmallScale,imfilter(FImage1,fspecial('gaussian')));
    axis('image')
    zoom out
    title(strcat({'Filtered Image- '},{'Spacing: '},num2str(DSpacingMeas,4),'nm'))
    xlabel(MatchingSpacingStr)
    ylabel('(nm)')
    imwrite(imfilter(FImage1,fspecial('gaussian')),'FilteredImage.png')
    linkaxes([Ax2,Ax3])
    %go back to diffractogram to prepare for next selection
    Ax1=subplot(1,3,1);
    colormap(Ax1,'default')
    title('Background Subtracted Diffractogram, Processed, Select Another Spot, or Press Enter to Stop')
    Iteration=Iteration+1;
end
```

CrystalSpacings MATLAB Function

```
function [d_sorted_nm,hkl_sorted,Name]=CrystalSpacings(SpacingMin,I)
if I==1
    %Select File using dialog box and after first instance keep opening from same
    %folder.
    global Path
    if ~exist('Path','var')
        [FName,Path]=uigetfile({'*.CIF','CIF File'},'Select a CIF File');
    end
    if Path==0
        [FName,Path]=uigetfile({'*.CIF','CIF File'},'Select a CIF File');
    elseif exist('Path','var')
        [FName,Path]=uigetfile(strcat(Path,'*.CIF'),'Select a CIF File');
    end
    path=strcat(Path,FName);
    CIFData=importcif(path);
    Name=inputdlg('Type a Name for this Crystal:');
    Name=Name{1};
```

```
    Alpha_I=structfind(CIFData,'name','cell_angle_alpha');
    Beta_I= structfind (CIFData,'name','cell_angle_beta');
    Gamma_I= structfind (CIFData,'name','cell_angle_gamma');
    Angles=[CIFData(Alpha_I).val,CIFData(Beta_I).val,CIFData(Gamma_I).val;]/180*pi;
    a_I= structfind (CIFData,'name','cell_length_a');
    b_I= structfind (CIFData,'name','cell_length_b');
    c_I= structfind (CIFData,'name','cell_length_c');
    LatticePar=[CIFData(a_I).val,CIFData(b_I).val,CIFData(c_I).val;];
else
    LatticePar=input('Enter a,b,c lattice parameters (in Angstroms) as vector: [a,b,c]');
    Angles=input('Enter alpha, beta, gamma angles (in degrees) as vector: [Alpha,Beta,Gamma]');
    Name=inputdlg('Type a Name for this Crystal:');
    Name=Name{1};
    Angles=Angles/180*pi;
end
a=LatticePar(1); b=LatticePar(2); c=LatticePar(3);
A=Angles(1); B=Angles(2); C=Angles(3);
V2=a^2*b^2*c^2*(1-(cos(A))^2-(cos(B))^2-(cos(C))^2+2*cos(A)*cos(B)*cos(C));
F1=cos(A)*cos(B)-cos(C);
F2=cos(B)*cos(C)-cos(A);
F3=cos(C)*cos(A)-cos(B);
G11=b^2*c^2*(sin(A))^2;
G12=a*b*c^2*F1;
G13=a*b^2*c*F3;
G21=a*b*c^2*F1;
G22=a^2*c^2*(sin(B))^2;
G23=a^2*b*c*F2;
G31=a*b^2*c*F3;
G32=a^2*b*c*F2;
G33=a^2*b^2*(sin(C))^2;
G_Star=[G11,G12,G13;G21,G22,G23;G31,G32,G33];
G_Star=1/V2*G_Star;
N=3;
%max index number
hklmax=3;
V=-hklmax:hklmax;
[Y{N:-1:1}]=ndgrid(1:numel(V)) ;
hkls=V(reshape(cat(N+1,Y{:}),[],N)) ;
IsAll0=(sum(abs(hkls),2)==0);
hkls(IsAll0,:)=[];
for i=1:size(hkls,1)
    hkl=hkls(i,:);
    d_hkl_A(i)=1/sqrt(hkl*G_Star*hkl');
end
d_hkl_nm=d_hkl_A/10;
[d_sort_nm,I_sort]=unique(round(d_hkl_nm,6));
d_sort_A=d_hkl_A(I_sort);
hkl_sort=-hkls(I_sort,:);
d_sorted_nm=d_sort_nm(d_sort_nm>SpacingMin)';
hkl_sorted=hkl_sort(d_sort_nm>SpacingMin,:);
```

3rd Party Codes Used: structfind, importcif

APPENDIX VIII

PARTICLE OUTLINING AND ELLIPSE FITTING CODE

Distinguishing the outlines of nanoparticles in noisy images is a difficult task, and developing fully automated outline tracing would likely be difficult enough to fill an entire PhD. Yet, obtaining accurate outlines from particles is essential to the work described in Chapter 5 of this dissertation. Thus, a code, called ParticleDM3 was written to allow a human observer to carefully but rapidly outline particles, performing some basic analysis, and saving these outlines for future collection.

The original purpose of this code, which was the forerunner to the diffractogram analysis code described in Appendix VII, was to fit the particle outlines with ellipses, testing the method of Takeda (Takeda and Yoshida, 2013; Uchiyama et al., 2011). The code first allows the user to zoom in on a particle of interest in an image; if the DM3 file selected contains multiple images, the user is prompted to select which image has the best view of this particle. The user is then prompted to outline the area of the particle not obscured by the supporting sphere by clicking on points in the image, beginning at the sphere boundary, proceeding around the particle, and right-clicking on the final point, which should lie at the intersection of the particle and support boundaries. This yields a partial outline of the particle, with a straight line connecting the two points where the particle and support boundaries intersect as seen in Figure 4-11 of the text. An ellipse is then fit to this outline, ignoring the straight line along the sphere boundary, as seen in Figure 4-11. The error in this fit is found by measuring the area between the ellipse and the particle outline (shown in green in Figure A 25), and dividing by the total area within the particle outline. (The area between the ellipse and the particle outline is measured by creating binary images, setting pixels outside the ellipse to -1 and inside to 1, but outside the outline to 1 and inside to -1. For all pixels outside one shape, but inside another, the

sum of the two images is 0, and these pixels are counted.) The outline, the image data within the outline, the ellipse fit coefficients, and other important parameters are then saved in a data file, which can be subsequently read by other MATLAB codes, such as the ParticleDataExtract code described in Appendix IX.

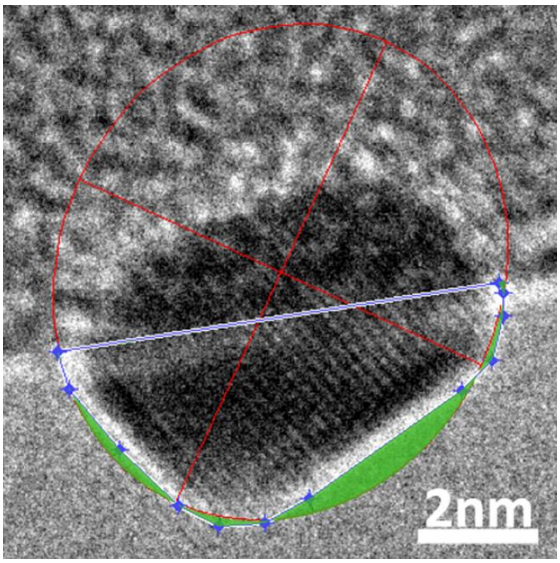

Figure A 25 Ellipse Fit Error. The error in the ellipse fit was calculated by measuring the area shown in green, and dividing by the area within the particle outline (blue).

ParticleDM3 MATLAB Code

```
clear
close all
%Select File using dialog box and after first instance keep opening from same
%folder.
global Path
if ~exist('Path','var')
   [FName,Path]=uigetfile({'*.dm3','DM3 File'},'Select a DM3 File');
end
if Path==0
   [FName,Path]=uigetfile({'*.dm3','DM3 File'},'Select a DM3 File');
elseif exist('Path','var')
   [FName,Path]=uigetfile(strcat(Path,'*.dm3'),'Select a DM3 File');
end
%Read the DM3 file, including the original image calibration
[ImO,MagCalO,Units]=ReadDMFile(strcat(Path,FName));
```

```
global Cal
if isempty(Cal)
   Cal=0;
end
UserCal=[];
%Set the magnification calibration
while isempty(UserCal)
   UserCal=(inputdlg('Type the image scale calibration (nm/pixel), or enter 0 to use calibration found in DM3 file.','Image
Calibration',1,{num2str(Cal)}));
   UserCal=str2num(UserCal{1});
   Cal=UserCal;
   if UserCal==0
      UserCal=double(MagCalO);
   end
end
FName
%Set the number of frames from the Image stack to actually measure
NumFrames=1;
%If the image has fewer frames than the user set, change setting to equal
%actual number of frames
if NumFrames>size(ImO,3)
   NumFrames=size(ImO,3);
end
%Set Scale of Image shown on screen (to speed up display of image)
DispScale=1;
%Specify width of the border (nm) to be used around the outlined particle when
%computing the diffractogram
BorderWidth=1;
%Set the Scale (nm/pixel) for the original image
ImOScale=UserCal;
%Set scale of reduced image to correct value (nm)
ImSmallScale=ImOScale/DispScale;
%Plotting, and Adjusting to center particle in Figure XXXXXXXXXXXXXXXXXXXX
%"n" is the index unique for each image
for n=1:NumFrames
   %Initialize Figure 1
   h=figure(1);
   ScreenSize=get(0,'screensize');
   set(h,'OuterPosition',[0,round(ScreenSize(4)/20),ScreenSize(3),ScreenSize(4)-round(ScreenSize(4)/20)]);
   %Set the name of Figure 1 including the slice number from the image stack
   Fig1NameStr=strcat('TEM Image, Slice #',num2str(n));
   set(h,'name',Fig1NameStr)
   %Read the image file that user specified
   %ImO(:,:,n)=imread(strcat(Path,FName),n,'Info',info);
   %Create a scaled down image, based on DispScale to be used in the rest of the script
   ImSmall(:,:,n)=imresize(ImO(:,:,n)',DispScale);
   %Blur the image that will be displayed in figure 1 using default gaussian blur
   Figure1Image=imfilter(ImSmall(:,:,n),fspecial('gaussian'));
   %Plot the image with the coordinates set to normal x-y mode, rather than
   %standard for images, with a gray colormap
   imagesc(Figure1Image,double(prctile(double(ImSmall(:)),[1,99])));
   %set(gca,'YDir','normal')
   axis('image')
   colormap(gray);
```

```
xlabel('(pixels)')
ylabel('(pixels)')
%Save a handle to this axis for the ellipse fit
AxisIm=gca;
%For the first image, zoom in and pan
if n==1
   title('Zoom in On Particle of Interest (Either Click Once, or Click-and-Drag to Zoom in on Region.)')
   %Zoom in on Just part of the Figure
   zoom on
   waitfor(AxisIm,'XLim')
   %Pan in on image using function I created called "PanImage"
   title('Pan (to Center Particle of Interest)')
   PanImage2(AxisIm,1)
   waitfor(AxisIm,'Tag')
   %Set this as Default Zoom
   zoom reset
   %For the second, and subsequent images, pan only
else
   %set the zoom level to previously defined default
   zoom out
   %Pan in on image using function I created called "PanImage"
   title('Pan (to Center Particle of Interest)')
   PanImage2(AxisIm,1)
   waitfor(AxisIm,'Tag')
end
%Have user select which image from the image stack to use
if size(ImO,3)>1
   XLimits=floor(get(gca,'XLim')); YLimits=floor(get(gca,'YLim'));
   XLimits(XLimits==0)=1;YLimits(YLimits==0)=1;
   for m=1:size(ImO,3)
      if DispScale~=1
         ImS(:,:,m)=imresize(ImO(:,:,m)',DispScale);
         ImCrop(:,:,m)=ImS(YLimits(1):YLimits(2),XLimits(1):XLimits(2),m);
      else
         ImOp(:,:,m)=ImO(:,:,m)';
         ImCrop(:,:,m)=ImOp(YLimits(1):YLimits(2),XLimits(1):XLimits(2),m);
      end
   end
   ImCrops=reshape(ImCrop,size(ImCrop,1),size(ImCrop,2)*size(ImCrop,3));
   clear('ImCrop')
   imagesc(imfilter(ImCrops(:,:,n),fspecial('gaussian')),double(prctile(double(ImSmall(:)),[1,99])))
   axis('image')
   colormap('gray')
   ImSelect=ginput(1);
   ImSNum=ceil(ImSelect(1)/(XLimits(2)-XLimits(1)));
   ImSmall(:,:,n)=imresize(ImO(:,:,ImSNum)',DispScale);
   %Blur the image that will be displayed in figure 1 using default gaussian blur
   Figure1Image=imfilter(ImSmall(:,:,n),fspecial('gaussian'));
   %Plot the image with the coordinates set to normal x-y mode, rather than
   %standard for images, with a gray colormap
   imagesc(Figure1Image,double(prctile(double(ImSmall(:)),[1,99])));
   %set(gca,'YDir','normal')
   axis('image')
   colormap(gray);
```

```
        xlabel('(pixels)')
        ylabel('(pixels)')
        figure(1)
        AxisIm=gca;
        %set the zoom level to previously defined default
        zoom out
        %xlim(XLimits); ylim([size(ImSmall,1)-YLimits(2),size(ImSmall,1)-YLimits(1)]);
        %Pan in on image using function I created called "PanImage"
        title('Pan (to Center Particle of Interest)')
        PanImage2(AxisIm,1)
        waitfor(AxisIm,'Tag')
    end
    if ~exist('ImSelect')
        ImSNum=NaN;
    end
    %User Tracing XXXXXXXXXXXXXXXXXXXXXXXXXXXXXXXXXXXXXXXXXXXXXXXXXXXXXXXXXXXXXXXXXXXXXX
    %Have user specify points along the edge of the particle
    title('Outline Particle...right click on last point in outline')
    [UserPoints(n).X(1),UserPoints(n).Y(1)]=ginput(1);
    j=2;
    UserButton=1;
    %Keep collecting points until the user clicks the right mouse button
    %(Userbutton will then be equal to 2, not 1)
    while UserButton==1
        [UserPoints(n).X(j),UserPoints(n).Y(j),UserButton]=ginput(1);
        %plot a line after each user selected point
        line([UserPoints(n).X(j-1),UserPoints(n).X(j)],[UserPoints(n).Y(j-1),UserPoints(n).Y(j)])
        j=j+1;
    end
    j=j-1;
    %plot the final connecting line a different color after user right-clicks
    line([UserPoints(n).X(1),UserPoints(n).X(end)],[UserPoints(n).Y(1),UserPoints(n).Y(end)],'color','c')
    %Ellipse Fitting XXXXXXXXXXXXXXXXXXXXXXXXXXXXXXXXXXXXXXXXXXXXXXXXXXXXXXXXXXXXXXXXXXXXX
    %call ellipse fitting function
    EllipseFit(n)=fit_ellipse(UserPoints(n).X,UserPoints(n).Y,AxisIm);
    %Get parameters required by residuals function (the angle defined by the
    %ellipse fitting function and the residuals function are different,
    %requiring an if-else statement
    if EllipseFit(n).a<EllipseFit(n).b
        ParamRes=[0,0,EllipseFit(n).long_axis/2,EllipseFit(n).short_axis/2,-EllipseFit(n).phi+pi/2]';
    else
        ParamRes=[0,0,EllipseFit(n).long_axis/2,EllipseFit(n).short_axis/2,-EllipseFit(n).phi]';
    end
    %Call residuals function
    [Residuals(n).RSS,Residuals(n).XYProj]=Residuals_ellipse([UserPoints(n).X'-EllipseFit(n).X0_in,UserPoints(n).Y'-
EllipseFit(n).Y0_in],ParamRes);
    %Compute Root Mean Squared Error
    Residuals(n).RMSE=sqrt(Residuals(n).RSS/j);
    %Normalize RMSE by the quadratic mean of the two semi-axes of the ellipse
    Residuals(n).RMSENorms=Residuals(n).RMSE/sqrt((EllipseFit(n).a^2+EllipseFit(n).b^2)/2);
    %Create a MATLAB polygon from the user-selected points
    Polygon=impoly(AxisIm,[UserPoints(n).X',UserPoints(n).Y']);
    setClosed(Polygon,'true')
    %Pause for 2 seconds so the user can observe the fitted ellipse
```

```
    pause(2)
    %Use the polygon to create a Black and White image of the particle shape
    BWStructure(n).BWImage=createMask(Polygon);
    %Extract many parameters from the B&W image, and save as a structure
    Stats(n)=regionprops(BWStructure(n).BWImage,ImSmall(:,:,n),'all');
    %Expand the B&W perimeter slightly for use in the diffractogram
    BWStructureExp(n).BWImageExp=imdilate(BWStructure(1).BWImage,strel('disk',ceil(BorderWidth/ImSmallScale)));
    StatsExp(n)=regionprops(BWStructureExp(n).BWImageExp,ImSmall(:,:,n),'PixelList','PixelIdxList','PixelValues');
    %Calculate Ellipse Fitting Error XXXXXXXXXXXXXXXXXXXXXXXXXXXXXXXXXXXXXXXXXX
    %Change the black and white image of the particle outline from 1's and 0's
    %to 1's and -1's respectively
    ImageBW=BWStructure(n).BWImage*2-1;
    %Create an image the size of the original image, in which the inside of the
    %elipse is -1 and outside is 1
    EllipseIm=ellipseMatrix(EllipseFit(n).Y0_in,EllipseFit(n).X0_in,EllipseFit(n).a,EllipseFit(n).b,-
EllipseFit(n).phi,ones(size(BWStructure(n).BWImage)),-1,0,0);
    %Adding these two images together, will give 0 between the ellipse and the
    %outline, and either 2 or -2 everywhere else... converting to logical,
    %makes it equal to 1 everywhere else.
    ErrorArea=logical(ImageBW+EllipseIm);
    %Create an X matrix and Y matrix the size of the original image, to calculate the following inequalities
    [BWX,BWY]=meshgrid([1:size(ImageBW,2)],[1:size(ImageBW,1)]);
    %Calculate areas of the image on either side of the line connecting the
    %first and last user-selected points in the particle outline (this is
    %essentially the 2-point-form of the equation of a line)
    BWIneq=UserPoints(n).Y(1)+(UserPoints(n).Y(end)-UserPoints(n).Y(1))/(UserPoints(n).X(end)-UserPoints(n).X(1))*(BWX-
UserPoints(n).X(1))-BWY;
    BWIneq(BWIneq>0)=1; BWIneq(BWIneq<0)=0;
    %Make this a logical matrix
    BWIneq=logical(BWIneq);
    %Find the "middle" user-selected point
    UPXMed=UserPoints(n).X(round(numel(UserPoints(n).X)/2));
    UPYMed=UserPoints(n).Y(round(numel(UserPoints(n).Y)/2));
    %And determine whether that point is below or above the line defined above
    UPMed=UserPoints(n).Y(1)+(UserPoints(n).Y(end)-UserPoints(n).Y(1))/(UserPoints(n).X(end)-
UserPoints(n).X(1))*(UPXMed-UserPoints(n).X(1))-UPYMed;
    %flip the logical matrix depending on whether the point is above or below
    if UPMed<0
        BWIneq=~BWIneq;
    end
    %multiply the image defining the region between the ellipse and the outline
    %by the logical matrix, so that the area in the silica sphere is ignored
    ErrorArea=ErrorArea.*BWIneq;
    %Count the number of pixels inside this area by summing the logical matrix
    EError=sum(ErrorArea(:));
    %Normalize this number of pixels by the number within the outline to form
    %an normalized error in fitting the ellipse
    EErrorNorm=EError/Stats(n).Area;
    %Add this quantity to the Data Structure
    info(n).EllipseErrorNorm=EErrorNorm;
    %Create Image with only contents of the outlined particle plus small border
    %Get list of 2D pixel locations
    PListInd=StatsExp(n).PixelList;
    %PListAbs=sub2ind(size(ImSmall)
```

```
    %Make the pixel locations begin at 1,1
    PListInd(:,1)=PListInd(:,1)-min(PListInd(:,1))+1; PListInd(:,2)=PListInd(:,2)-min(PListInd(:,2))+1;
    %Convert locations to linear indices
    PList=sub2ind(max(PListInd),PListInd(:,1),PListInd(:,2));
    %Get pixel data
    PValues=StatsExp(n).PixelValues;%-min(DataStruct.PixelValues);
    %Initialize image to contain particle image
    PImage=zeros([max(PListInd)],class(ImO));%*min(StatsExp(n).PixelValues);
    %Set pixels specified by the linear indices to the pixel data values
    PImage([PList])=[PValues];
    %Smooth image, then re-set pixels in the outline so that, outside the
    %outline, the image is smoothed significantly
    %PImageSmooth=imfilter(PImage,fspecial('gaussian',[1,1]*2*ceil(BorderWidth/ImSmallScale),7));
    PImageSmooth=2*imfilter(PImage,fspecial('average',round(.5*ceil(BorderWidth/ImSmallScale))));
    %PImageSmooth=PImage;
    PImageSmooth([PList])=[PValues];
    %Show image of particle
    figure(2)
    Fig2NameStr=strcat('Particle Image, Slice #',num2str(n));
    set(gcf,'name',Fig2NameStr)
    Figure2Image=imfilter(PImageSmooth',fspecial('gaussian'));

imagesc([1:max(PListInd(:,1))]*ImSmallScale,[1:max(PListInd(:,2))]*ImSmallScale,Figure2Image,prctile(double(PValues(:)),[1,
99]))
    %set(gca,'YDir','normal')
    axis('image')
    colormap('gray')
    xlabel('(nm)')
    ylabel('(nm)')
    info(n).BWImage=BWStructure(n).BWImage;
    info(n).PImageExtended=PImageSmooth;
    info(n).OriginalCalibration=MagCalO;
    info(n).CalibrationUsed=ImOScale;
    info(n).Units=Units;
    info(n).Slice=ImSNum;
    info(n).FileName=FName;
end
%Put all the Structures created by the above code into one giant structure,
%and give the fields of that structure useful names
TitlesU=fieldnames(UserPoints);
TitlesE=fieldnames(EllipseFit);
TitlesR=fieldnames(Residuals);
TitlesS=fieldnames(Stats);
TitlesI=fieldnames(info);
Titles=[TitlesU;TitlesE;TitlesR;TitlesS;TitlesI];
Titles([1:11])={'OutlineX','OutlineY','a_Elipse','b_Elipse','phi_Elipse','FitX0','FitY0','FitX0in','FitY0in','LongAx_Elipse','ShortAx
_Elipse'};
%Convert structures to cells
DataCellU=struct2cell(UserPoints(:))';
DataCellE=struct2cell(EllipseFit(:))';
DataCellR=struct2cell(Residuals(:))';
DataCellI=struct2cell(info(:))';
DataCellS=struct2cell(Stats(:))';
%Combine Cells
```

```
DataCell=[DataCellU,DataCellE,DataCellR,DataCellS,DataCellI];
%Convert back to structure
DataStruct=cell2struct(DataCell,Titles,2);
if exist('DataStruct')
   NotNeededFields={'FitX0'
      'FitY0';'FitX0in';'FitY0in';'LongAx_Elipse';'ShortAx_Elipse'
      'status';'F';'XYProj';'Centroid';'BoundingBox';'SubarrayIdx'
      'MajorAxisLength';'MinorAxisLength';'Eccentricity';'Orientation'
      'ConvexHull';'ConvexImage';'FilledImage';'FilledArea';'EulerNumber'
      'Extrema';'Solidity';'Extent';'PixelList';'Perimeter'
      'WeightedCentroid';'MinIntensity';'MaxIntensity';'BWImage'};
end
KeyData=DataStruct;
KeyData=rmfield(KeyData,NotNeededFields);
E=1;
i=1;
while E>0
   if E==1
      NE=[];
   else
      NE=i;
   end
   if E>0
      E=exist(strcat(Path,FName,'_',num2str(NE),' MATLAB Particle Data.mat'));
   end
   if E==0
      save(strcat(Path,FName,'_',num2str(NE),' MATLAB Particle Data.mat'),'DataStruct','KeyData')
   end
   i=i+1;
end
```

3rd Party Codes Used: ellipseMatrix, fit_ellipse, PanImage2, ReadDMFile, Residuals_ellipse

APPENDIX IX

PARTICLE ORIENTATION ESTIMATION CODE

Shape signatures are 1D representations of 2D shapes (Costa et al., 2001), and can be used to determine the orientation of 3D objects (Reibacher, 2014) by comparing the shape signatures of a model in a known orientation with shape signatures of a similar object in an unknown orientation.

The automated fitting of experimental outlines to determine particle orientation was achieved using MATLAB. The first step in this process involved a code called WulffSilhouette, which was written to produce shape signatures from a Wulff-shaped CAD model. The 3D CAD model, saved as a .STL file, was first imported into MATLAB using a function found on MATLAB's online File Exchange. Another File Exchange code was used to find 400 randomly, but approximately-uniformly distributed points on a sphere, by minimizing the generalized electrostatic potential energy of a system of charged particles at these points. These points were then used as viewing positions from which to view the 3D model in a MATLAB figure. The silhouette of the particle viewed from each of these 400 points was saved as a binary image. Because the full Wulff shape is never observed, and only the portion of the Ru particles overhanging the vacuum can be reliably used to determine the particle shape, the model images were also cut. The images of the model in each of the 400 orientations were cut off at intervals of 10%, as shown in Figure 4-13. The resulting 3600 cut model images were used to produce shape signatures (described below), and the shape signatures, as well as images of the models were saved in a file for future use.

1D representations of 2D shapes, called shape signatures, can be produced by many different methods (Costa et al., 2001). Here, shape signatures were produced from the cut model images by measuring the distance from the center of the base of each image to the

outline of the particle in 1° increments, and then subtracting the corresponding distance to a circle fit to the particle outline, as shown in Figure A 26 (increments displayed are >1° for clarity). This gives a 1D signal that is sometimes positive (green lines in Figure A 26) and sometimes negative (red lines). The shape signatures shown in Figure A 27 are the result of this process, which was also used to create shape signatures from the experimental images as described below. A lateral shift of this 1D signal is equivalent to a rotation of the original image (Reibacher, 2014).

The main code written for orientation determination was called ParticleDataExtract because it was originally intended to extract the information saved by the ParticleDM3 code described in Appendix VIII. The code begins by prompting the user to open all the .mat data files (which were produced by the ParticleDM3 code) containing images of experimental particles. The particle images are extracted from these files, and rotated so that the interface with the support is always at the bottom of the image. The code then proceeds to compute a shape signature for each of the particle images in the same way as for the models, as shown in Figure A 26 and Figure A 27. A montage of the experimental particle images from the loaded files is displayed, as shown in Figure A 28. Next, the user is prompted to select a data file containing model shape signatures, which was produced using the WulffSilhouette code.

Each of the 3600 cut model shape signatures are then compared to an experimental particle shape signature by calculating the normalized cross correlation of the model and experimental shape signatures, as shown in Figure 4-13. The raw value of each cross correlation is normalized by the autocorrelation of the experimental shape signature with itself at 0 lag, so that the maximum possible value of each normalized cross correlation is

1. After all 3600 cross-correlations are computed, the 5 models giving the highest cross-correlations are plotted, as shown in Figure A 29. (only 3 are shown in the figure). The user must now select whether to manually decide between these top 5 models, or automatically choose the model with the highest cross-correlation. Both options have benefits. The benefit of automatic selection is speed and a complete lack of bias, as no subjective decisions are introduced. However, a human observer can use information in the image which MATLAB does not consider, such as the direction of any lattice fringes present, and may sometimes provide a more accurate determination of the orientation, though this requires more time, is subjective, and may not be consistent if the code is run with the same image several times. Figure A 29 shows a part of the figure presented to the user. The experimental image is shown at the top, and the cut image of the model in the best orientation is in the middle. The number in the bottom-left of this middle window is the normalized cross correlation for this orientation, while the number in the bottom-center is the ideal shift found in the cross-correlation calculation. This shift corresponds directly to an angle in degrees. The bottom plot shows the experimental shape signature (blue) and the model shape signature (orange). This process is repeated for each experimental particle image loaded at the beginning. Once this is complete, the best-matching model images are placed in a montage similar to that shown for the experimental particles in Figure A 28. Finally, results from the code, including the highest cross-correlations for each particle and the montages are saved to a .mat file.

The value of the cross correlation deemed to be a good fit for this study is 0.85. This was determined by running the orientation matching MATLAB code using 100 generated particle images rather than experimental particle images. The generated images were

produced from the Wulff-shaped model exactly as the model shape signatures were; however, since the quasi-random orientations from which the 3D Wulff model is viewed are slightly different each time the WulffSilhouette code is run, the generated particle images will be slightly different than the 400 model images. The cut fraction used for the 100 generated images was randomized. The results of matching the 100 generated images are summarized with a violin plot in Figure A 30. This analysis showed that 98% of the generated images had a maximum cross correlation greater than 0.85 when the model used was also Wulff-shaped. A second model was also used, in which the surface energy of the (101) facets was decreased, giving a related but different 3D shape. The results from orientation matching of the images generated using this model are also shown in Figure A 30; many of these images give a maximum cross correlation less than 0.85.

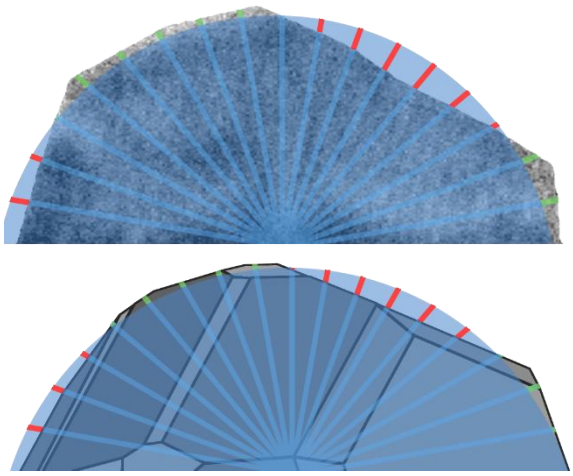

Figure A 26 Shape Signature Production. Visual representation of the method used in this work to produce shape signatures from experimental images (top) and model silhouettes (bottom). Green lines denote angles where the shape signature is positive, and red where it is negative.

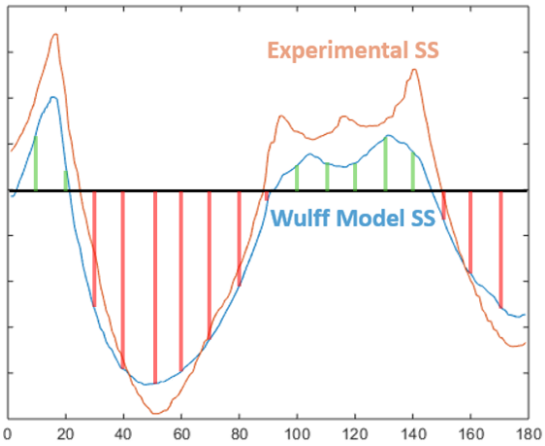

Figure A 27 Shape Signatures. The shape signatures resulting from the experimental and model images shown in Figure A 26, with similar green and red lines drawn for the model shape signature.

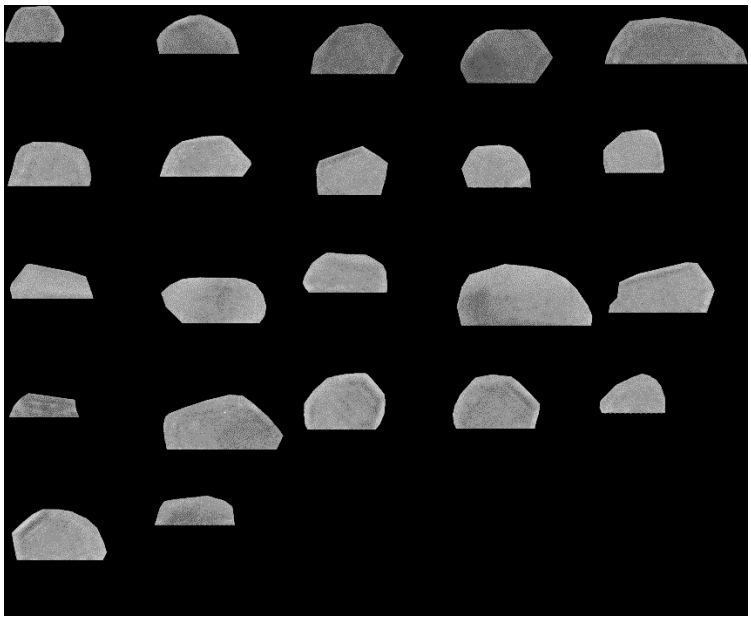

Figure A 28 Particle Image Montage. A montage of experimental particle images, extracted by the ParticleDataExtract code from .mat data files generated by the ParticleDM3 code described in Appendix VIII. The images have been rotated so that the their intersection with the SiO_2 support is always at the bottom.

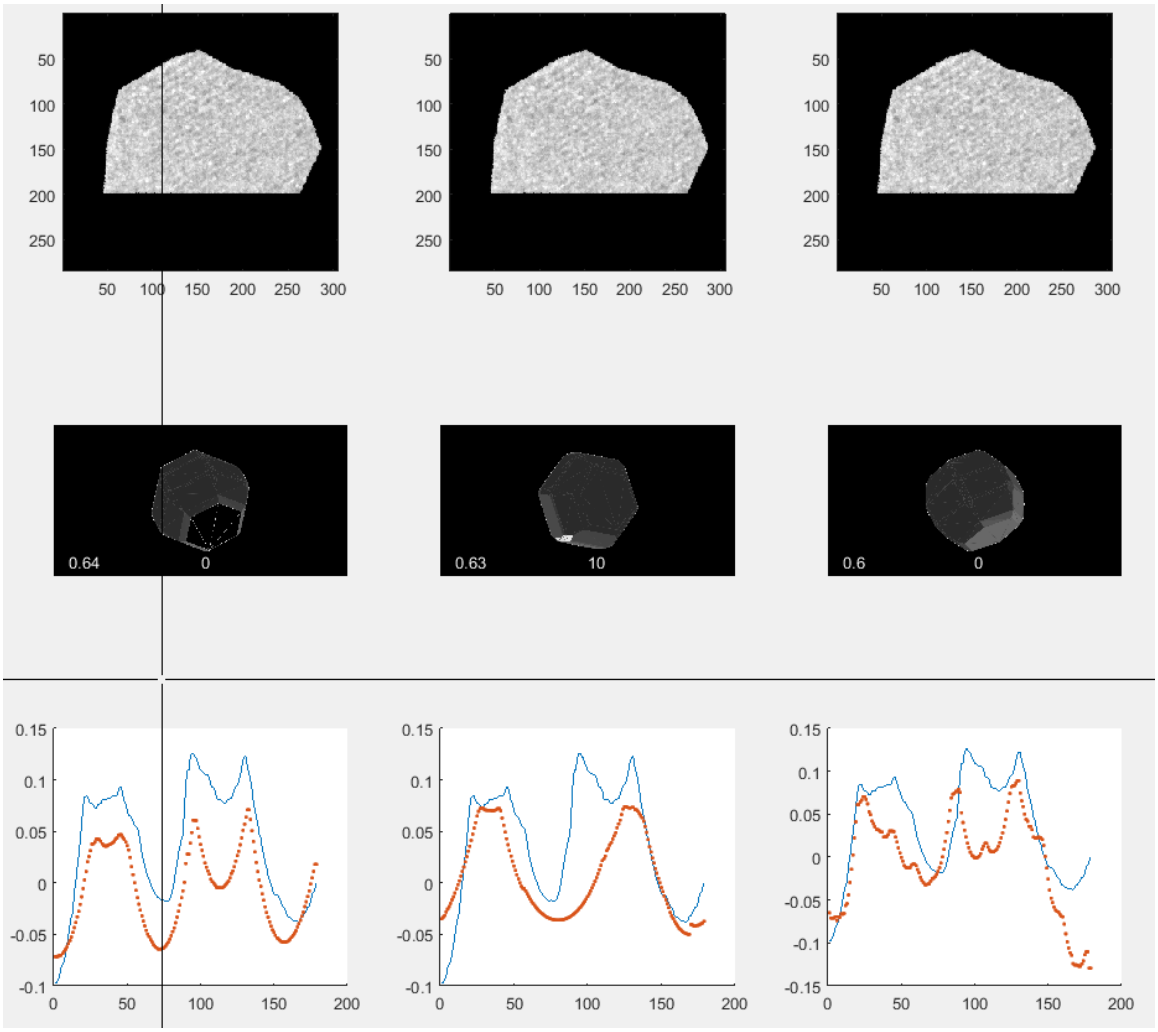

Figure A 29 Orientation Matching Figure. Part of the figure shown to the user so a subjective decision can be made by the user. (Only 3 out of the 5 orientations displayed in MATLAB are shown here to save space.) Top: Experimental image. Middle: Images of the model in the different orientations; the number in the bottom-left of each middle window is the normalized cross-correlation for this orientation, while the number in the bottom-center is the ideal shift found in the cross-correlation calculation. Bottom: Plot of the experimental shape signature (blue) and the model shape signature (orange). The crosshair is used to select the best of the 5 orientations.

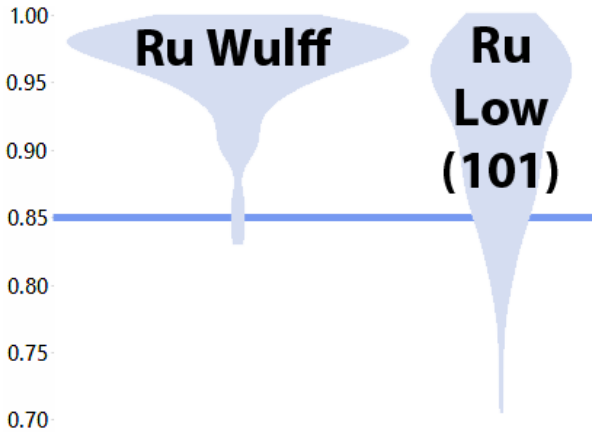

Figure A 30 Violin Plot. summarizing the maximum cross correlation values for 100 generated particle images used to test the ParticleDataExtract MATLAB code.

WulffSilhouette MATLAB Code

```
clear
close('all')
%Number of random viewpoints to create
NumViews=400;
%Open a 3D CAD file in STL format
[FName,Path]=uigetfile({'*.stl','STL File'},'Select an STL File');
%Initialize Figure 1 and set it to fullscreen and white
Fig1=figure(1);
ScreenSize=get(0,'screensize');
set(Fig1,'OuterPosition',[0,round(ScreenSize(4)/20),ScreenSize(3),ScreenSize(4)-round(ScreenSize(4)/20)]);
set(Fig1,'Color',[1 1 1])
%Run a code that converts the STL file to a format MATLAB understands
[F,V,C]=cad2matdemo(strcat(Path,FName));
%Set a propertyof the plot axis
Ax=gca;
set(Ax,'NextPlot','replaceChildren')
%Run a code that finds N randomly, but uniformly dispersed on a sphere
ViewVectors=ParticleSampleSphere('N',NumViews);
%Set the "Up direction" of the camera to be always a different one of the random view directions
UpVect=circshift(ViewVectors,5);
%Get an image of the model from different viewpoints
for i=1:size(ViewVectors,1)
   %For every view direction, set the camera position

set(Ax,'visible','off','cameraposition',ViewVectors(i,:)*.06,'cameraviewangle',170,'cameratarget',[0,0,0],'DataAspectRatio',[1,1,1],'
PlotBoxAspectRatio',[1,1,1],'CameraUpVector',UpVect(i,:))
   %Get an image of the figure plot
   Image=frame2im(getframe(Ax));
   ImageG=rgb2gray(Image);
   %Set any black pixels to white pixels
   ImageG(ImageG==0)=255;
   %Store the gray image in a cell array which will be saved to disk
   ImageM{i}=ImageG;
end
```

```
for i=1:size(ViewVectors,1)
    %convert grayscale image to black and white
    BWImage{i}=~im2bw(ImageM{i},.99999);
    %fill any 'holes' in the image of the particle
    BWImage{i}=imfill(BWImage{i},'holes');
    %determine the extrema of the particle area
    Extrema(i)=regionprops(BWImage{i},'Extrema');
    %Also find the area of the particle
    Area{i}=regionprops(BWImage{i},'area');
    %Use the area to compute an average radius by assuming a circular shape
    Radius(i)=sqrt(Area{i}.Area/pi);
    %Extract the Bottom and top positions of the particle, to find the height
    BWBottom(i)=Extrema(i).Extrema(5,2);
    BWTop=Extrema(i).Extrema(1,2);
    BWHeight(i)=BWBottom(i)-BWTop;
    MaskVars=[BWBottom;BWHeight];
    %Cut the particle shape at 9 heights
    for j=1:9
        %initialize a mask with zeros
        BWMask=zeros(size(BWImage{i}));
        %set some pixels to 1
        BWMask(1:round(BWBottom(i)-j*BWHeight(i)/10),:)=1;
        %Multiply the mask by the BW image to get the cut particle image
        BWImageM=logical(BWImage{i}.*BWMask);
        %Get the centroid and extrema of cut particle
        CentroidS(i,j)=regionprops(BWImageM,'Centroid','Extrema');
        Centroid=CentroidS(i,j).Centroid;
        BWBottom2=CentroidS(i,j).Extrema(5,2);
        %Set the origin for the shape signature to be the cut bottom of the
        %particle, in the horizontal position defined by the centroid
        Origin=[BWBottom2-3,Centroid(1)];
        %Find the boundary of the particle from BW image
        Bounds(i,j)=bwboundaries(BWImageM,8,'noholes');
        Bound=Bounds{i,j};
        %Convert cartesian coordinates of Boundaries to polar coordinates
        RadiiCell{i,j}=sqrt((Bound(:,1)-Origin(1)).^2+(Bound(:,2)-Origin(2)).^2); %sqrt(Y^2+X^2)
        %Calculate the angle around the particle outline, discard flat section
        ThetaCell{i,j}=atan2d((Bound(:,1)-Origin(1)),(Bound(:,2)-Origin(2)));
        %Optionally display the black and white cut particle images
        DiagnosticFigs=0;
        if DiagnosticFigs==1
            figure(3)
            subplot(1,3,1)
            imagesc(BWImageM)
            axis('image')
            pause(.1)
        end
        %Put the polar coordinates together into one matrix
        ShapeSignature{i,j}=[ThetaCell{i,j},RadiiCell{i,j}];
        %remove any duplicate values from MShapeSignature
        MShapeSignature=unique(ShapeSignature{i,j},'rows','stable');
        %Set the angles over which to define the shape signature (SS)
        MThetaNorm=[1:179];
        %Interpolate the values of the SS at the set angles using a cubic spline, smoothing the Radii
```

```
        MRadiiNormO=spline((MShapeSignature(:,1)+180)',smooth(MShapeSignature(:,2))',MThetaNorm);
        %Calculate a nearly parabolic function (the distance which would be
        %obtained as the shape signature of cut cirlces) to be subtracted from
        %each shape signature
        %define the cut percentage
        c=j/10;
        %Make theta go from 0 to 90 and back to 0, rather than 0 to 180
        Theta=90-abs(MThetaNorm-90);
        %Calculate the distance from a point above or below the center of a
        %circle to the circumference of that circle, given an angle with
        %respect to the horizontal (this is the shape signature of a cut circle
        if c==.5
            AB=Radius(i)*ones(size(MThetaNorm));
        elseif c<.5
            Beta=asind(2*abs(.5-c)*sind(90-Theta));
            Gamma=90-Beta+Theta;
            AB=Radius(i)*sind(Gamma)./sind(90-Theta);
        elseif c>.5
            Beta=asind(2*abs(.5-c)*sind(90+Theta));
            Gamma=90-Beta-Theta;
            AB=Radius(i)*sind(Gamma)./sind(90+Theta);
        end
        AB(isnan(AB))=-10000;
        %subtract the circles' shape signatures from the experimental ones (this
        %essentially normalizes the shape signatures)... also median filter the SS
        ShapeSignature{i,j}=[MThetaNorm;medfilt1(MRadiiNormO-AB,3)]';
        %Optionally plot the shape signatures before and after normalization
        if DiagnosticFigs==1
            if mod(j,2)
                subplot(1,3,2)
                hold all
                plot(MRadiiNormO)
                pause(.1)
                subplot(1,3,3)
                hold all
                plot(ShapeSignature{i,j}(:,2))
            end
        end
    end
end

%Save the data needed for the experimental fit code
save('WulffShapeSignatures400Ru7Test.mat','ImageM','ShapeSignature','MaskVars')
ShowMontage=0;
if ShowMontage==1
    for i=1:40
        Size(:,i)=size(ImageM{1,i});
        SMax=max(Size,[],2);
    end
    for i=1:40
        ImageMon(:,:,1,i)=padarray(ImageM{1,i},SMax-Size(:,i),255,'post');
    end
    figure
    montage(ImageMon)
```

```
    for i=1:400
        SSM(i,:)=ShapeSignature{i,1}(:,2);
    end
end
```

3rd Party Codes Used: cad2matdemo, ParticleSampleSphere, RandSampleSphere

ParticleDataExtract MATLAB Code

```
clear
close('all')
global Path
if ~exist('Path','var')
    [FName,Path]=uigetfile({'*.mat','MAT File'},'Select multiple MAT Files','multiselect','on');
end
if Path==0
    [FName,Path]=uigetfile({'*.mat','MAT File'},'Select multiple MAT Files','multiselect','on');
elseif exist('Path','var')
    [FName,Path]=uigetfile(strcat(Path,'*.mat'),'Select multiple MAT Files','multiselect','on');
end
%Calculate a nearly parabolic function (the distance which would be
%obtained as the shape signature of cut cirlces) to be subtracted from
%each shape signature
for j=1:9
    %define the cut percentage
    c=j/10;
    %Make theta go from 1 to 90 and back to 1, rather than 1 to 179
    Theta=90-abs([1:179]-90);
    %Calculate the distance from a point above or below the center of a unit
    %circle to the circumference of that circle, given an angle with
    %respect to the horizontal (this is the shape signature of a cut circle
    if c==.5
        AB=ones([1,179]);
    elseif c<.5
        Beta=asind(2*abs(.5-c)*sind(90-Theta));
        Gamma=90-Beta+Theta;
        AB=sind(Gamma)./sind(90-Theta);
    elseif c>.5
        Beta=asind(2*abs(.5-c)*sind(90+Theta));
        Gamma=90-Beta-Theta;
        AB=sind(Gamma)./sind(90+Theta);
    end
    SSNormO(j,:)=AB;
end
%XXXXXXXXXXXXXXXXXXXXXXXXXXXXXXXXXXXXXXXXXXXXXXXXXXXXXXXXXXXXXXXXXXXXXXXXXXX
%Load the Data Structures Specified by User, and Extract the BW Images,
%Rotating them so that the Sphere Side is Always Down
%XXXXXXXXXXXXXXXXXXXXXXXXXXXXXXXXXXXXXXXXXXXXXXXXXXXXXXXXXXXXXXXXXXXXXXXXXXX
for i=1:size(FName,2)
    %Load the datastructure from file
    Data.F(i)=load(strcat(Path,FName{i}),'DataStruct');
```

```
   Cal(i)=Data.F(i).DataStruct.OriginalCalibration;
   %If the data structure has them, extract the fringe spacings
   if isfield(Data.F(i).DataStruct,'LatticeFringeSpacings')
       FringeSpacings{i}=Data.F(i).DataStruct.LatticeFringeSpacings;
   end
   %Also extract the fringe intensity, if this data exists in the data-structure
   if isfield(Data.F(i).DataStruct,'LatticeFringeIntensity')
       FringeIntensity{i}=Data.F(i).DataStruct.LatticeFringeIntensity;
   else
       FringeIntensity{i}=NaN;
   end
   %Extract the particle outline as a B&W (logical) image, tightly cropped
   FilledImage{i}=Data.F(i).DataStruct.FilledImage;
   %Using the Outline Data saved in the data structure,
   %Calculate the angle of the interface with the support
   BaseAngle(i)=180/pi*atan((Data.F(i).DataStruct.OutlineY(end)-
Data.F(i).DataStruct.OutlineY(1))/(Data.F(i).DataStruct.OutlineX(end)-Data.F(i).DataStruct.OutlineX(1)));
   %Rotate the particle outline B&W Image based on the angle
   FilledImageR{i}=imrotate(FilledImage{i},BaseAngle(i));
   %If the particle outline is now upside-down, fix this
   %Find the horizontal edges in the B&W image using a sobel
   %filter...make this into an image
   [HEdge,~]=edge(FilledImageR{i},'sobel',[],'horizontal');
   %Sum this edge image in the x direction
   YEProfile=sum(HEdge,2);
   %Find the maximum in this summed profile, which is the position of
   %the horizontal edge
   [~,YEMax]=max(YEProfile);
   %Similarly sum the B&W image in the X direction
   YProfile=sum(FilledImageR{i},2);
   %Integrate the YProfile above and below the horizontal edge
   YAbove=sum(YProfile(1:YEMax));
   YBelow=sum(YProfile(YEMax:end));
   %If the Integration below the edge is larger than that above the
   %edge, the particle is up-side-down and must be rotated 180o
   if YBelow>YAbove
       %Rotate the original image by the BaseAngle+180 degrees
       BaseAngle(i)=BaseAngle(i)+180;
       FilledImageR{i}=imrotate(FilledImage{i},BaseAngle(i));
   end
   %Find the size of each rotated B&W Image of the particle
   FilledImageSize(:,i)=size(FilledImageR{i});

%XXXXXXXXXXXXXXXXXXXXXXXXXXXXXXXXXXXXXXXXXXXXXXXXXXXXXXXXXXXXXXXXXXXXXX
   %Find the Shape Signature (SS) of the Particle Images

%XXXXXXXXXXXXXXXXXXXXXXXXXXXXXXXXXXXXXXXXXXXXXXXXXXXXXXXXXXXXXXXXXXXXXX
   %Find the Centroid, and extrema of the rotated particle outline
   RegionS(i)=regionprops(FilledImageR{i},'Centroid','Extrema','Area','Eccentricity');
   RegionProps(i)=regionprops(FilledImageR{i},'all');
   %Use the centroid and extrema to place an origin for the particle at
   %the 'center' of the bottom
   Origins(i,:)=[RegionS(i).Extrema(5,2)-3,RegionS(i).Centroid(1)];
   %Find the boundary of the particle from B&W image
```

```
Bounds(i)=bwboundaries(FilledImageR{i});
%Extract the boundary of the current particle from the "Bounds" cell
Bound=Bounds{i};
BoundY=Bound(:,1);
%Estimate the particle cut by fitting a circle
BoundCutL=BoundY<(max(BoundY)-5);
BoundCut=Bound(BoundCutL,:);
CirclePar=CircleFitByPratt(circshift(BoundCut,1,2));
x=ceil(CirclePar(1)-CirclePar(3)):1:floor(CirclePar(1)+CirclePar(3));
Radius(i)=CirclePar(3);
CStDev=1/sqrt(2*log(2));
CCF=10*(1-(max(BoundCut(:,1))-CirclePar(2))/CirclePar(3))/2;
Cut=1:9;
CutProbCF=sqrt(log(2)/pi)*exp(-(Cut-CCF).^2/(1/log(2)));
%Estimate the particle cut using the eccentricity
ECC=RegionS(i).Eccentricity;
CE=round(-10.454+18.466*ECC+24.247*(ECC-.7976)^2);
CutProbE=sqrt(log(2)/pi)*exp(-(Cut-CE).^2/(1/log(2)));
CutProb=CutProbCF+CutProbE;
[~,ECut]=max(CutProb);
%Calculate the radius from the origin to the particle outline
ERadiiCell{i}=sqrt((Bound(:,1)-Origins(i,1)).^2+(Bound(:,2)-Origins(i,2)).^2); %sqrt(Y^2+X^2)
%Calculate the angle from the origin to the particle outline
EThetaCell{i}=-atan2d((Bound(:,1)-Origins(i,1)),(Bound(:,2)-Origins(i,2)));
%Save the Experimental Shape Signature as a cell in a cell array
EShapeSignatureCell{i}=[EThetaCell{i},ERadiiCell{i}];
%Extract the current particle's Shape Signature (SS), make sure all
%theta values are unique
EShapeSignature=unique(EShapeSignatureCell{i},'rows','stable');
%Define theta for the experimental SS at interval of 1 degree,
%excluding 0 and 180 degrees
EThetaNorm=[1:179];
%Use cubic spline to get a radius value for the SS at every one degree
ERadii=spline((EShapeSignature(:,1))',smooth(EShapeSignature(:,2))',EThetaNorm);
%Save this original ERadii for every image
ERadiiO{i}=ERadii;
for j=1:9
   %Calculate a nearly parabolic function (the distance which would be
   %obtained as the shape signature of cut cirlces) to be subtracted from
   %each shape signature
   %define the cut percentage
   c=j/10;
   %Make theta go from 0 to 90 and back to 0, rather than 0 to 180
   Theta=90-abs(EThetaNorm-90);
   %Calculate the distance from a point above or below the center of a
   %circle to the circumference of that circle, given an angle with
   %respect to the horizontal (this is the shape signature of a cut circle
   if c==.5
      AB=Radius(i)*ones(size(EThetaNorm));
   elseif c<.5
      Beta=asind(2*abs(.5-c)*sind(90-Theta));
      Gamma=90-Beta+Theta;
      AB=Radius(i)*sind(Gamma)./sind(90-Theta);
   elseif c>.5
```

```
            Beta=asind(2*abs(.5-c)*sind(90+Theta));
            Gamma=90-Beta-Theta;
            AB=Radius(i)*sind(Gamma)./sind(90+Theta);
        end
        AB(isnan(AB))=-10000;
        SSNormM(j,:)=AB;
        MF(j,:)=medfilt1(ERadii-SSNormM(j,:),3,1);
    end
    SMF(:,i)=sum(abs(MF),2);
    [SSNMin,SSNMinI]=min(SMF(:,i));
    Ji{i}=[SSNMinI-1,SSNMinI,SSNMinI+1];
    if SSNMinI==1
        Ji{i}=Ji{i}(2:3);
    elseif SSNMinI==9
        Ji{i}=Ji{i}(1:2);
    end
    %subtract the circles' shape signatures from the experimental ones (this
    %essentially normalizes the shape signatures)... also median filter the SS
    ERadiiNormCell{i}=medfilt1(ERadii-SSNormM(SSNMinI,:),3)/Radius(i);
    %Put the theta values into a cell array
    EThetaNormCell{i}=EThetaNorm;
    %Finally, put Theta and the normalized radius into a SS cell
    EShapeSignatureCell{i}=[EThetaNormCell{i};ERadiiNormCell{i}]';
end
save('ParticleShapeData','Bounds','RegionProps')
Dispersion=mean(1.2953./(2*Radius.*Cal));
%Determine the maximum size of the rotated particle images
FISizeMax=max(FilledImageSize,[],2);
%Now pad the images, so they are all the same size, and put them all in
%a 4D matrix, so they can be shown as a montage
for i=1:size(FName,2)
    FilledImageRP(:,:,1,i)=padarray(FilledImageR{i},[FISizeMax-FilledImageSize(:,i)],0,'post');
    %Shift the images, so that the origin of the shape is at the bottom
    %center of the image
    %Find the pixel indices of the bottom-center of the image
    BottomCenter=round([FISizeMax(1),FISizeMax(2)/2]);
    %Determine the shift needed to translate the particle origin to the
    %bottom-center of the image
    ShiftVect(i,:)=(BottomCenter-(ceil(Origins(i,:))+[3,0]));
    %Translate the Filled image using circshift, first padding the Filled
    %image with zeros, so that the resulting images are all one size
    FITrans(:,:,i)=circshift(padarray(FilledImageR{i},[FISizeMax-FilledImageSize(:,i)],0,'post'),ShiftVect(i,:));
    %Calculate a distance transform IN from the particle outline
    FIDistIn(:,:,i)=bwdist(FITrans(:,:,i));
    %Calculate a distance transform OUT from the particle outline
    FIDistOut(:,:,i)=bwdist(~FITrans(:,:,i));
    %Sum the two distance transforms to yield the average distance from all
    %the particle outlines, then add the IN and OUT transforms to give a
    %distance from the outline over the entire image area
    FilledImageDistSum=sum(FIDistIn,3)+sum(FIDistOut,3);
    %Smooth the final distance transform with a gaussian filter (default parameters
    FilledImageDistSum=imfilter(FilledImageDistSum,fspecial('gaussian'));
end
%If FilledImageMontage is set to 1, plot a figure with a montage of all the
```

```
%filled particle images
FilledImageMontage=0;
if FilledImageMontage
    figure(1)
    FM=montage(FilledImageRP);
    axis('image')
end
%XXXXXXXXXXXXXXXXXXXXXXXXXXXXXXXXXXXXXXXXXXXXXXXXXXXXXXXXXXXXXXXXXXXXXXX
XXX
%Distance Transform Code
%XXXXXXXXXXXXXXXXXXXXXXXXXXXXXXXXXXXXXXXXXXXXXXXXXXXXXXXXXXXXXXXXXXXXXXX
XXX
%If DistanceTransform is set to 1, plot the distance transform, etc
DistanceTransform=0;
if DistanceTransform
    FilledImageDistSum=imfilter(FilledImageDistSum,fspecial('gaussian'));
    figure(2)
    FIMinLake=ones(size(FilledImageDistSum));
    NRegions=1;
    i=0;
    while NRegions==1
        i=i+1;
        FIMinLake(FilledImageDistSum<=min(min(FilledImageDistSum))+i*2)=0;
        NR=bwconncomp(FIMinLake);
        Areas=regionprops(NR,'Area');
        if numel(Areas)>1
            if Areas(2).Area>200
                NRegions=2;
            end
        end
    end
    [FX,FY]=gradient(double(FilledImageDistSum(3:end-3,3:end-3)));
    FIM=imregionalmax(FilledImageDistSum);
    NNN=2;
    figure(3)
    subplot(1,3,2)
    surf(sqrt((FX.^2)+(FY.^2)))
    shading('interp')
    colormap('jet')
    P1=subplot(1,3,1);
    imagesc(double(FilledImageDistSum))
    axis('image')
    subplot(1,3,3)
    imagesc(FIM)
    subplot(1,3,1);
    axis('image')
    IslandMax=round(ginput(1));
    [X,Y]=meshgrid(1:size(FIMinLake,2),1:size(FIMinLake,1));
    X=X-IslandMax(1);
    Y=Y-IslandMax(2);
    [Theta,Rho]=cart2pol(X,Y);
    for T=1:360*2;
        Thetai(T)=(T-360)/360*pi;
        FIDistSumVi=FilledImageDistSum(Theta>Thetai(T)-pi/180 & Theta<Thetai(T)+pi/180);
```

```
        RhoVi=Rho(Theta>Thetai(T)-pi/180 & Theta<Thetai(T)+pi/180);
        [~,Mini]=min(FIDistSumVi);
        MinRhoi(T)=RhoVi(Mini);
    end
    [Xmin,Ymin]=pol2cart(Thetai,MinRhoi);
    Xmin=Xmin+IslandMax(1);
    Ymin=Ymin+IslandMax(2);
    figure(4)
    scatter(Xmin,Ymin,'.')
    axis('image')
    axis('ij')
    FIMin=bwmorph(~FIMinLake,'skel',Inf);
    figure(5)
    imshow(FIMin)
end
%XXXXXXXXXXXXXXXXXXXXXXXXXXXXXXXXXXXXXXXXXXXXXXXXXXXXXXXXXXXXXXXXXXXXXXX
XXX
%Create GrayScale (Pixel) Images of the Particles Based on Data in the
%DataStructure and display them in a montage
%XXXXXXXXXXXXXXXXXXXXXXXXXXXXXXXXXXXXXXXXXXXXXXXXXXXXXXXXXXXXXXXXXXXXXXX
XXX
for i=1:size(FName,2)
    %In case the code has not begun from the beginning, clear PImageS
    clear PImageS
    %Get list of 2D pixel locations
    PListInd=Data.F(i).DataStruct.PixelList;
    %Make the pixel locations begin at 1,1
    PListInd(:,1)=PListInd(:,1)-min(PListInd(:,1))+1; PListInd(:,2)=PListInd(:,2)-min(PListInd(:,2))+1;
    %Convert locations to linear indices
    PList=sub2ind(max(PListInd),PListInd(:,1),PListInd(:,2));
    %Get pixel data
    PValues=Data.F(i).DataStruct.PixelValues;
    %Initialize image which will contain particle image
    PImage=zeros([max(PListInd)],class(PValues));
    %Set pixels specified by the linear indices to the pixel data values
    PImage([PList])=[PValues];
    %Smooth the image, and transpose it to get the correct orientation
    PImage=imfilter(PImage',fspecial('gaussian'));
    %Rotate the image, using the same angle used previously for the B&W Images
    PImageR=imrotate(PImage,BaseAngle(i));
    %Determine the size of this rotated image
    PImageSize(:,i)=size(PImageR);
    %Put the rotated image into a cell array
    PImages{i}=PImageR;
end
%Determine the maximum size of the rotated images
PIMaxSize=max(PImageSize,[],2);
%Now pad the images, so they are all the same size, and put them all in
%a 4D matrix, so they can be shown as a montage
for i=1:size(FName,2)
    PImageS(:,:,1,i)=padarray(PImages{i},[PIMaxSize-PImageSize(:,i)],0,'post');
end
%If PixelImageMontage is set to 1, plot a figure with a montage of all the
%filled particle images
```

```
PixelImageMontage=1;
if PixelImageMontage
    figure(6)
    %Get all the pixel values that are not 0 and put them into a vector, so
    %that the prctile function can create useful gray limits for the plot
    PImagePositive=PImageS(:);
    PImagePositive(PImagePositive==0)=[];
    %Plot the montage of all the particle images
    PM=montage(PImageS,'displayrange',prctile(double(PImagePositive(:)),[5,99]));
end
%XXXXXXXXXXXXXXXXXXXXXXXXXXXXXXXXXXXXXXXXXXXXXXXXXXXXXXXXXXXXXXXXXXXXX
XXX
%Model Shape Signatures Code
%XXXXXXXXXXXXXXXXXXXXXXXXXXXXXXXXXXXXXXXXXXXXXXXXXXXXXXXXXXXXXXXXXXXXX
XXX
%Load the Model Shape Signatures 'ShapeSignature' cell array as well as
%'ImageM' (which contains corresponding images of the model) from a MAT file
[FNameSS,PathSS]=uigetfile({'*.mat','MAT File'},'Select MAT File with Particle ShapeSignatures');
load(strcat(PathSS,FNameSS))
%For one out of every 10 model shape signatures, plot aspect ratio and
%degree of clipping in a scatter plot
SSScatter=0;
if SSScatter
    for s=1:10:numel(ShapeSignature)
        %Create a vector of s values, (for scatter plot)
        SIndex(s)=s;
        %Based on the Shape Signature cell array, get the number betweeen 1 and
        %400 of the orientation, and between 1 and 9 of the degree of clipping
        %of the silhouette
        [OrientationNum(s),Clipping(s)]=ind2sub(size(ShapeSignature),s);
        %Get single shape signature from the cell array
        ShapeSignatures=ShapeSignature{s};
        %I only need the radii... discard the theta column
        ShapeSignatures=ShapeSignatures(:,2);
        %Shift the shape signatures so they are positive, with a non-zero mean
        SSPositive{s}=ShapeSignatures-min(ShapeSignatures);
        %Find the max of each shape signature
        SSPosMax(s)=max(SSPositive{s});
        %Find the mean of each shape signature
        SSPosMean(s)=mean(SSPositive{s});
        %Calculate the ratio between the max and mean of the shape signatures
        SSAspectRatio=SSPosMax./SSPosMean;
    end
    figure(7)
    scatter(SIndex,SSAspectRatio,[],Clipping/max(Clipping),'filled')
end
%Find the sizes and maximum size of the model images contained in the shape
%signatures MAT file
for II=1:numel(ImageM)
    %Change the background of the Model images to black
    IM=ImageM{II};
    IM(IM==255)=0;
    ImageM{II}=IM;
    MImageSize(:,II)=size(ImageM{II});
```

```
end
MImageMaxSize=max(MImageSize,[],2);
%XXXXXXXXXXXXXXXXXXXXXXXXXXXXXXXXXXXXXXXXXXXXXXXXXXXXXXXXXXXXXXXXXXXXXXXXXX
%Shape Matching Based on Cross-Correlation of Shape Signatures
%XXXXXXXXXXXXXXXXXXXXXXXXXXXXXXXXXXXXXXXXXXXXXXXXXXXXXXXXXXXXXXXXXXXXXXXXXX
CCorVMaxGV=[];
for Im=1:numel(PImages)
    for i=1:size(ShapeSignature,1)
        Ji{Im}=[1:9];
        for j=Ji{Im}
            %Extract each Model SS from the SS cell array
            MShapeSignature=ShapeSignature{i,j};
            Rad=226;
            %Place Radii values in a new cell array
            MRadiiNormCell{i,j}=MShapeSignature(:,2)/Rad;
            %All theta vectors will be identical, call it MThetaNorm
            MThetaNorm=MShapeSignature(:,1);
            %If PlotAllMSS is set to one, this will sequentially plot all
            %the Model SSs (this takes a long time to complete)
            PlotAllMSS=0;
            if PlotAllMSS
                figure(8)
                hold all
                plot(MThetaNorm,MRadiiNormCell{i,j},'o')
                plot(MShapeSignature(:,1),MShapeSignature(:,2))
            end
            %XXXXXXXXXXXXXXXXXXXXXXXXXXXXXXXXXXXXXXXXXXXXXXXXXXXXXXXXXXXXXX
            %Perform the cross-correlation to determine the goodness of fit
            %of each model with each experimental image, as well as the
            %shift (conceptually, a rotation) needed to align the two.
            %(This is the core of the shape matching code!)
            %XXXXXXXXXXXXXXXXXXXXXXXXXXXXXXXXXXXXXXXXXXXXXXXXXXXXXXXXXXXXXXX
            [CCorV,CCShift]=xcorr(MRadiiNormCell{i,j},ERadiiNormCell{Im},10,'coeff');
            %XXXXXXXXXXXXXXXXXXXXXXXXXXXXXXXXXXXXXXXXXXXXXXXXXXXXXXXXXXXXXX
            %Find the value and index of the Cross-Correlation (CC) which
            %is the best fit based on shifting the SS
            [CCorVMax(i,j),CCVMInd(i,j)]=max(CCorV);
            %Find the shift value for which the CC shows the best fit
            CCShiftMax(i,j)=CCShift(CCVMInd(i,j));
            %Plot the shifts versus the CC for each combination of model
            %and experimenatal image (this takes a long time!)
            PlotCCShift=0;
            if PlotCCShift
                figure(9)
                hold all
                plot(CCShift,CCorV,'.')
                hold all
                %Also plot the maximum CC for each combination of model and
                %experimental image, with an open circle
                scatter(CCShiftMax(i,j),CCorVMax(i,j),[],i,'o')
            end
        end
```

```
end
[NumR,NumC]=meshgrid([1:size(ShapeSignature,1)],Ji{Im});
NumC=NumC'; NumR=NumR';
CCorVMaxJ=CCorVMax(:,Ji{Im});
CCorVMaxGV=cat(1,CCorVMaxGV,[ones(numel(CCorVMaxJ),1)*Im,NumC(:),NumR(:),CCorVMaxJ(:)]);
%After computing all the CCs for each of the model SSs, find the
%largest CC value... indicating the best-fitting model
[~,Match]=max(CCorVMax(:));
%Sort the CCs for all the model SSs, so the best n fits can be chosen
[CCVMaxSorted,MatchesSortInd]=sort(CCorVMax(:),'descend');
CCorVMax=zeros(size(CCorVMax));
%Extract the shift that was used for this best-fitting model
MatchShift=CCShiftMax(Match);
%Shift the matching model SS by the best-fitting shift
MatchingSS=[circshift(MThetaNorm,MatchShift),MRadiiNormCell{Match}];
%Allow the user to manually select the  best match from among the top 5
%matches automatically determined using the CC
H=figure(11);
clf(11)
for p=1:5
   subplot(3,5,p)
   imagesc(PImages{Im},prctile(PImages{Im}(:),[5,99.9]))
   axis('image')
   %Get the subscript value needed to extract the correct 5 images
   %from the ImageM cell array
   [Sub1,Sub2]=ind2sub(size(MRadiiNormCell),MatchesSortInd(p));
   %Get the shift that was used to get the largest CC for the 5 model
   %SSs that were best
   CCShiftSort(p)=CCShiftMax(Sub1,Sub2);
   %Show the matching model image directly below the experimental
   %image, rotated by the value of the CC shift
   subplot(3,5,p+5)
   BWImage=~im2bw(ImageM{Sub1},.99999);
   %initialize a mask with zeros
   BWMask=ones(size(BWImage));
   %Multiply the mask by the BW image to get the cut particle image
   BWImageM=logical(BWImage.*BWMask);
   ImageMCut=ImageM{Sub1}.*uint8(BWImageM);
   imshow(imrotate(ImageMCut,CCShiftSort(p),'nearest','crop'))
   set(gca,'Xdir','reverse')
   %Also display the CC values
   text(.05,.1,num2str(CCVMaxSorted(p),2),'color','w','units','normalized')
   %Also display the shift values
   text(.5,.1,num2str(CCShiftSort(p)),'color','w','units','normalized')
   subplot(3,5,10+p)
   hold on
   plot(EThetaNormCell{Im},ERadiiNormCell{Im})
   plot(circshift(MThetaNorm,CCShiftMax(MatchesSortInd(p))),MRadiiNormCell{MatchesSortInd(p)},'.')
end
%If this is the first image, ask the user whether they would like to
%manually selet the best match from the top 5 matches selected by
%MATLAB, or just use the match with the highest cross correlation (default)
if Im==1
   MatchMeth=questdlg('Would You Like to Manually Select from Top 5 Matches?', ...
```

```
        'Final Match Method', ...
        'Manually Match','Use Highest Cross-Correlation','Use Highest Cross-Correlation');
    end
    % Handle response
    switch MatchMeth
        case 'Manually Match'
            %Have the user click on the model image they think is the best fit
            UserMatchiO=ginput(1);
            UserMatchiO=[127.848101265823,0.00276442307692321];
            set(H,'units','normalized')
            CP(Im,:)=get(H,'CurrentPoint');
            Fig11Lims=[0.1145;0.2697;0.43177;0.59583;0.76197;0.91927];
            %Convert the clicked coordinates to an index between 1 and 5
            UserMatchi=ceil(5*(CP(Im,1)-Fig11Lims(1))/(Fig11Lims(end)-Fig11Lims(1)));
        case 'Use Highest Cross-Correlation'
            UserMatchi=1;
    end
    %Select the Matching SS and save the indices of this match to a vector
    %with one element for each experimental image
    UserMatchInd(Im)=MatchesSortInd(UserMatchi);
    %Extract the CC value for the user selected match
    UserCCMatch(Im)=CCVMaxSorted(UserMatchi);
    UserCCMatchNorm(Im)=CCVMaxSorted(UserMatchi)/CCVMaxSorted(1);
    UserCCShift(Im)=CCShiftSort(UserMatchi);
    %Find the subscript value of the user-selected match (only need the first subscript)
    [SubUser1(Im),SubUser2(Im)]=ind2sub(size(MRadiiNormCell),UserMatchInd(Im));
    %Place the matching model image for each experimental image into a 4D
    %array for creating a montage
    ImageMS(:,:,1,Im)=flipdim(imrotate(ImageMCut,CCShiftSort(p),'nearest','crop'),2);
end
%Create a figure to compare the model images with the experimental images
figure(16)
CompareFig=gcf;
%Plot a montage of the experimental (pixel) images
subplot(1,2,1)
PM=montage(PImageS,'displayrange',prctile(double(PImagePositive(:)),[5,99]));
%Calculate the size of the montage just created
PMX=get(PM,'XData');
NumCol=PMX(2)/PIMaxSize(2);
%Plot a montage of the model images, with the same number of columns (and
%therefore rows) as the experimental image montage
subplot(1,2,2)
MM=montage(ImageMS,'size',[NaN,NumCol]);
figure(14)
clf(gcf)
for im=1:numel(UserMatchInd)
    subplot(1,2,1)
    plot(MThetaNorm,MRadiiNormCell{UserMatchInd(im)})
    subplot(1,2,2)
    plot(EThetaNormCell{im},ERadiiNormCell{im})
    pause(.1)
end
MRadNCSum=zeros(size(ERadiiNormCell{1}));
ERadNCSum=zeros(size(ERadiiNormCell{1}));
```

```
MERadNCSum=zeros(size(ERadiiNormCell{1}));
%Shape Averaging based on Shape Signatures
for im=1:numel(UserMatchInd)
    hold all
    subplot(1,2,1)
    plot(MThetaNorm,MRadiiNormCell{UserMatchInd(im)})
    SSMatches(:,im)=MRadiiNormCell{UserMatchInd(im)};
    hold all
    subplot(1,2,2)
    plot(EThetaNormCell{im},ERadiiNormCell{im})
    SSExp(:,im)=ERadiiNormCell{im};
    MRadNCSum=MRadNCSum+MRadiiNormCell{UserMatchInd(im)}';
    ERadNCSum=ERadNCSum+ERadiiO{im};
    MERadNCSum(im,:)=MRadiiNormCell{UserMatchInd(im)}'+ERadiiNormCell{im};
end
%Plot the Sum of all matched SS's and that of all experimental SS's
figure(15)
subplot(1,3,1)
plot(MThetaNorm,MRadNCSum,'r')
subplot(1,3,2)
plot(EThetaNormCell{1},ERadNCSum,'k')
subplot(1,3,3)
[x,y]=pol2cart(EThetaNorm/180*pi,ERadNCSum/im);
plot(x,y)
axis('equal')
%XXXXXXXXXXXXXXXXXXXXXXXXXXXXXXXXXXXXXXXXXXXXXXXXXXXXXXXXXXXXXXXXXXXXXXX
XXX
%Save relevant data to DataFile and Figure File
%XXXXXXXXXXXXXXXXXXXXXXXXXXXXXXXXXXXXXXXXXXXXXXXXXXXXXXXXXXXXXXXXXXXXXXX
XXX
ShapeMatchData.SSMatchIndex=UserMatchInd;
ShapeMatchData.SSMatchModelNum=SubUser1;
ShapeMatchData.SSMatchModelCut=SubUser2;
ShapeMatchData.SSMatchCrossCor=UserCCMatch;
ShapeMatchData.SSMatchCrossCorNorm=UserCCMatchNorm;
ShapeMatchData.SSMatchShift=UserCCShift;
ShapeMatchData.SSMatches=SSMatches;
ShapeMatchData.SSExp=SSExp;
ShapeMatchData.SSMatchesSum=MRadNCSum;
ShapeMatchData.SSExpSum=ERadNCSum';
ShapeMatchData.FileName=FName;
ShapeMatchData.XCorrValues=CCorVMaxGV;
ShapeMatchData.FileNames=FName(CCorVMaxGV(:,1))';
save(strcat(Path,'ShapeMatchDataFile',FName{1}),'ShapeMatchData')
savefig(CompareFig,strcat(Path,'ParticleShapeMatchFig_',FName{1},'.fig'))
```

3rd Party Codes Used: CircleFitByPratt

APPENDIX X

IMAGE REFERENCE TABLES

Over 5,400 DM3 files were produced as part of this work and contain original, unprocessed, TEM image and EELS data. Many of these files include multiple image frames, or multiple spectra. Thus, it would be extremely difficult for someone unfamiliar with the project to find the original data for any of the images displayed in the figures of this dissertation without the information in Table A 2, which gives the original DM3 filenames (without the .dm3 extension). Table A 1 additionally lists the basic conditions under which each image was acquired, including the temperature, gas composition, accelerating voltage, and microscope. An image name is also given, which is composed of the date of the experiment found in the image's filename and the numeric designation also in the filename. Generally, image files given here consist of 5 images, unless the Image Name given in Table A 1 contains a decimal value (e.g. 041.5) in which case this is the 5th image frame of a series, which has been saved in separate files, rather than a single file. Letters in the Image name indicate that the same particle or region of interest has been captured using multiple series of 5 image frames. Thus, image 2015-12-02 017j is the 11th set of 5 frames acquired from region of interest 17 during the experiment which began on 2015-12-02.

Table A 1 Selected Conditions for TEM Images Contained in this Dissertation by Figure

Dissertation Figure	Image Name	TEM	kV	Gas Pressures (Torr)	Temp (°C)
3-11a	2014-04-23 12	Tecnai	200	-	25
3-11b	2015-03-25 009	Titan	80	0.75 H2	495
3-24 (Top)	2015-04-24 001f	Titan	80	2.67 CO + 1.33 O2	200
3-24 (Bottom)	2015-04-24 002m	Titan	80	2.67 CO + 1.33 O2	215
4-5 (Left)	2013-10-25 041.5	Tecnai	200	0.66 CO + 0.33 O2	380
4-5 (Right)	2013-10-25 59.3	Tecnai	200	0.66 CO + 0.33 O2	450
4-6, 4-8, 4-9	2015-12-02 017i	Titan	300	2 CO + 0.7 O2	300
4-11	2015-12-02 021j	Titan	300	2 CO + 0.7 O2	200

4-12	2014-05-21 065d	Tecnai	200	0.66 CO + 0.33 O2	215
4-13	2013-10-25 59.3	Tecnai	200	0.66 CO + 0.33 O2	450
4-14	2014-05-28 029a	Tecnai	200	0.53 CO + 0.27 O2	200
5-4a	2014-01-23 015.1	Tecnai	200	1.33 CO + 0.67 O2	200
5-4b	2014-01-23 004b.3	Tecnai	200	1.33 CO + 0.67 O2	350
5-4c	2014-01-23 033a.1	Tecnai	200	1.33 CO + 0.67 O2	450
5-4d	2014-01-23 45.2	Tecnai	200	1.33 CO + 0.67 O2	200
5-4e	2014-01-23 45a.4	Tecnai	200	1.33 CO + 0.67 O2	200
5-7a	2014-05-20 018a	Tecnai	200	0.66 CO + 0.33 O2	25
5-7b	2014-05-20 045	Tecnai	200	0.66 CO + 0.33 O2	200
5-7c	2014-05-20 056f	Tecnai	200	0.66 CO + 0.33 O2	200
5-7d	2014-05-20 066b	Tecnai	200	0.66 CO + 0.33 O2	200
5-7e	2014-05-20 065c	Tecnai	200	0.66 CO + 0.33 O2	200
5-12 (Upper Right)	2014-05-28 033	Tecnai	200	0.66 CO + 0.33 O2	205
5-12 (Lower Left)	2014-05-28 018a	Tecnai	200	0.66 CO + 0.33 O2	195
5-14 (Upper Right)	2014-05-28 033	Tecnai	200	0.66 CO + 0.33 O2	205
5-14 (Upper Left)	2014-06-16 035	Tecnai	200	1 O2	200
5-14 (Center Left)	2014-06-11 062	Tecnai	200	1 CO2	200
5-14 (Lower Left)	2014-06-10 043a	Tecnai	200	1 CO	200
5-18 (Upper Left)	2014-05-28 033	Tecnai	200	0.66 CO + 0.33 O2	205
5-18 (Upper Right)	2014-06-16 031	Tecnai	200	1 O2	200
5-18 (Lower Left)	2014-06-11 062	Tecnai	200	1 CO2	200
5-18 (Lower Right)	2014-06-10 033	Tecnai	200	1 CO	200
6-1	2014-05-28 033	Tecnai	200	0.66 CO + 0.33 O2	205
6-2a	2015-02-09 0058	Titan	80	2 H2	200
6-2b	2015-02-09 0098	Titan	80	2 H2 + 0.01 O2	200
6-3	2015-12-02 221i	Titan	300	2 CO + 0.7 O2	225
6-4	2015-04-24 002l	Titan	80	2.67 CO + 1.33 O2	214
6-5	2015-12-02 017i	Titan	300	2 CO + 0.7 O2	300
6-8	2015-12-02 021x	Titan	300	2 CO + 0.7 O2	200
6-9	2015-12-02 018d	Titan	300	2 CO + 0.7 O2	200
6-11	2015-12-02 011zc	Titan	300	2 CO + 0.7 O2	215
6-13a	2015-12-02 614g	Titan	300	2 CO + 3.6 O2	225
6-13b	2015-12-02 714c	Titan	300	2 CO + 0.7 O2	225
A 20	2015-12-02 017i	Titan	300	2 CO + 0.7 O2	300
A 21	2015-12-02 021x	Titan	300	2 CO + 0.7 O2	200
A 23	2015-12-02 017i	Titan	300	2 CO + 0.7 O2	300
A 25	2014-05-21 065d	Tecnai	200	0.66 CO + 0.33 O2	215

Table A 2 Original DM3 Filenames for TEM Images Contained in this Dissertation

Dissertation Figure	Filename
3-11a	2014-04-23 Ru-SiO2 On Fiber 350kx 25C Grid and Pellet 12
3-11b	009 2015-03-25 Ru-SiO2 Oper 380kx 495C .75T H2
3-24 (Top)	001f 2015-04-24 Ru-SiO2 Operando 200C 2CO+O2 4 Torr 380kx
3-24 (Bottom)	002m 2015-04-24 Ru-SiO2 Operando 200C 2CO+O2 4 Torr 380kx
4-5 (Left)	2013-10-25 Ru-SiO2 376C 041.5
4-5 (Right)	2013-10-25 Ru-SiO2 450C 59.3
4-6, 4-8, 4-9	017i 2015-12-02 Ru-SiO2 Operando RT 2 Torr CO 410kx
4-11	021j 2015-12-02 Ru-SiO2 Operando RT 2 Torr CO 410kx
4-12	065d 2014-05-21 Ru-SiO2 CO Oxidation Pre-Red 350kx 215C 1Torr 2CO+O2 Area 03002
4-13	2013-10-25 Ru-SiO2 450C 59.3
4-14	029a 2014-05-28 Ru-SiO2 CO Oxidation Pre-Red 350kx 203C 0.8 Torr 2CO O2 Area 08
5-4a	2014-01-23 CO Ox 350C 015.1
5-4b	2014-01-23 CO Ox 200C 004b.3
5-4c	2014-01-23 CO Ox 450C 033a.1
5-4d	2014-01-23 CO Ox 200C 45.2
5-4e	2014-01-23 CO Ox 200C 45a.4
5-7a	018a 2014-05-20 Ru-SiO2 CO Oxidation Pre-Red 350kx 20C 1Torr 2CO+O2 Area 02
5-7b	045 2014-05-20 Ru-SiO2 CO Oxidation Pre-Red 350kx 200C 1Torr 2CO+O2 Area 03
5-7c	056f 2014-05-21 Ru-SiO2 CO Oxidation Pre-Red 350kx 200C 1Torr 2CO+O2 Area 03
5-7d	066b 2014-05-21 Ru-SiO2 CO Oxidation Pre-Red 350kx 215C 1Torr 2CO+O2 Area 03

5-7e	065c 2014-05-21 Ru-SiO2 CO Oxidation Pre-Red 350kx 215C 1Torr 2CO+O2 Area 03
5-12 (Upper Right)	033 2014-05-28 Ru-SiO2 CO Oxidation Pre-Red 350kx 203C 0.8 Torr 2CO O2 Area 11
5-12 (Lower Left)	018a 2014-05-28 Ru-SiO2 CO Oxidation Pre-Red 350kx 193C 1.0 Torr 2CO O2 Area 08
5-14 (Upper Right)	033 2014-05-28 Ru-SiO2 CO Oxidation Pre-Red 350kx 203C 0.8 Torr 2CO O2 Area 11
5-14 (Upper Left)	035 Ru-SiO2 Pre-Red .93Torr O2 196C 250kx
5-14 (Center Left)	062 Ru-SiO2 Pre-Red .81Torr CO2 199C 250kx
5-14 (Lower Left)	043a Ru-SiO2 Pre-Red .85Torr CO 196C 250kx
5-18 (Upper Left)	033 2014-05-28 Ru-SiO2 CO Oxidation Pre-Red 350kx 203C 0.8 Torr 2CO O2 Area 11
5-18 (Upper Right)	031 Ru-SiO2 Pre-Red .93Torr O2 196C 250kx
5-18 (Lower Left)	062 Ru-SiO2 Pre-Red .81Torr CO2 199C 250kx
5-18 (Lower Right)	033 Ru-SiO2 Pre-Red .85Torr CO 196C 250kx
6-1	033 2014-05-28 Ru-SiO2 CO Oxidation Pre-Red 350kx 203C 0.8 Torr 2CO O2 Area 11
6-2a	2015-02-09 Ru-SiO2 H2, O2-380000X-0058
6-2b	2015-02-09 Ru-SiO2 H2, O2-380000X-0098
6-3	221i 2015-12-03 Ru-SiO2 Operando 200C 3 Torr CO+O2 410kx
6-4	002l 2015-04-24 Ru-SiO2 Operando 200C 2CO+O2 4 Torr 380kx
6-5	017i 2015-12-02 Ru-SiO2 Operando RT 2 Torr CO 410kx
6-8	021x 2015-12-02 Ru-SiO2 Operando RT 2 Torr CO 410kx
6-9	018d 2015-12-02 Ru-SiO2 Operando RT 2 Torr CO 410kx
6-11	011zc 2015-12-02 Ru-SiO2 Operando RT 2 Torr CO 410kx
6-13a	614g 2015-12-03 Ru-SiO2 Operando 226C 4.3 Torr CO+O2 410kx

6-13b	714c 2015-12-03 Ru-SiO2 Operando 226C 2.3 Torr CO+O2 410kx
A 20	017i 2015-12-02 Ru-SiO2 Operando RT 2 Torr CO 410kx
A 21	021x 2015-12-02 Ru-SiO2 Operando RT 2 Torr CO 410kx
A 23	017i 2015-12-02 Ru-SiO2 Operando RT 2 Torr CO 410kx
A 25	065d 2014-05-21 Ru-SiO2 CO Oxidation Pre-Red 350kx 215C 1Torr 2CO+O2 Area 03002